Fluidized Bed Selective Oxidation and Sulfation Roasting of Nickel Sulfide Concentrate

by

Dawei Yu

A thesis submitted in conformity with the requirements
for the degree of Doctor of Philosophy

Department of Materials Science and Engineering
University of Toronto

Fluidized Bed Selective Oxidation and Sulfation Roasting of Nickel Sulfide Concentrate

Dawei Yu

Doctor of Philosophy

Department of Materials Science and Engineering
University of Toronto

2014

Abstract

Selective oxidation and sulfation roasting of nickel concentrate followed by leaching was investigated as a novel route for nickel production. In the oxidation roasting stage, the iron species in the nickel concentrate was preferentially oxidized to form iron oxides, leaving non-ferrous metals (Ni, Cu, Co) as sulfides. The roasted product was then sulfation roasted to convert the sulfides of the latter metals into water-soluble sulfates. The sulfates were then leached into solution for further recovery and separation from iron oxides.

The oxidation of nickel concentrate was firstly studied by means of thermogravimetric and differential thermal analysis over a wide temperature range. A reaction scheme was deduced, in which preferential oxidation of iron sulfide species occurred over a wide temperature range up to about 700 ºC, forming a $Ni_{1-x}S$ core with iron oxide shell. A batch fluidized bed roaster was then constructed to study the oxidation and sulfation roasting of nickel sulfide concentrate. Oxidation roasting tests were carried out at temperatures between 650 °C and 775 °C. It was found that low temperatures (e.g. 650 °C) are favorable for the preferential oxidation of iron sulfide species while minimizing the formation of nickeliferous oxides, i.e. trevorite and NiO. Several parameters were varied in the sulfation roasting experiments, including the sulfation gas

flowrate, sulfation roasting temperature, the addition of Na_2SO_4, sulfation roasting time, and the oxidation roasting temperature. Under optimized conditions of sulfation gas composition (95% air, 5% SO_2), temperature (700 °C), Na_2SO_4 addition (10 wt%) and time (150 min), the conversions to sulfates were 79% Ni, 91% Cu, and 91% Co. Only 5% Fe forms water-soluble sulfate. The residue from the leaching of calcine in water contained 49% Fe and 10% Ni, which is a suitable feedstock for the production of ferronickel alloys. Therefore, further studies were also conducted to evaluate the reduction behavior of the residue with CO, H_2 and graphite.

Acknowledgments

I would like to express my deepest gratitude to the late Professor Torstein A. Utigard for introducing me to this exciting topic and his continuous supervision even after he was diagnosed with cancer. I am always grateful that he offered me the opportunity to pursue the Ph.D. degree after I studied on this project for a year as a MASc candidate.

My sincere gratitude also goes to Professor Mansoor Barati as my co-supervisor. The completion of this thesis would not have been possible without the patience, enthusiasm, encouragement, and immense knowledge of him as well as of late Professor Utigard.

I would like to thank the rest of my thesis committee: Professor Doug D. Perovic, Professor Charles Q. Jia, Professor Ramamritham Sridhar and Professor Christopher A. Pickles for their insightful and constructive comments and advice.

I would like to thank George Kretschmann and Yanan Liu of the Geology Department of the University of Toronto for their assistance in the characterization of some of the samples. The assistance from Mingqian Zhu during the summer of 2012 is gratefully acknowledged. I would also like to thank my colleague and friend Mark Li for the stimulating discussions and support.

I wish to thank Xstrata Process Support (Sudbury, Ontario, Canada) for providing the nickel concentrate and both Xstrata and Vale for sponsoring the project. The funding for this research was provided by the Natural Sciences and Engineering Research Council (NSERC) of Canada and the Centre for Chemical Process Metallurgy.

Last but not least, I like to thank my mother Aihua Liu and my father Haijiang Yu for their love, encouragement and support.

Table of Contents

List of Tables

List of Figures

List of Appendices

1 Introduction

1.1 Pyrometallurgical Routes of Nickel Extraction

Since the commercial production of nickel from the laterite deposits of New Caledonia in 1875, and later from the great sulfide deposits of the Sudbury district of Canada in 1885 [1], nickel extraction is carried out by several flowsheets. The processing routes to treat these two types of nickel minerals are largely different, determined by their individual mineralogy. Laterites are not amenable to concentration by physical means [2] and can only be upgraded by a factor of 1.3–2 [3]. Production of nickel from saprolite (low-Fe laterite) is through reduction in rotary kilns followed by smelting in electric furnaces. The feed to a laterite smelter contains 35% to 47% water in the form of free moisture and crystalline water. In addition, production of ferronickel from laterite requires high temperatures due to the high melting temperature of both the ferronickel and the slag. As a result of these, the production of nickel from laterite by smelting is highly energy intensive [2]. Limonite and smectite (high-Fe laterite) are treated by high-pressure acid leaching process (*HPAL* process) [4]. Limonite-type laterite is also treated in the Caron process which comprises pyrometallurgical reduction followed by leaching with an aqueous NH_3+CO_2+O_2 solution [4]. On the other hand, nickel sulfide minerals are amenable to concentration by efficient and cost-effective milling and flotation [5], with a concentration factor of approximate 20 times [3]. Contrary to the laterite smelting, pyrometallurgical processing of nickel sulfide minerals is relatively energy efficient, due mainly to the effective utilization of heat from the oxidation of sulfides, as well as the ease of beneficiation of the sulfide ores by mineral dressing techniques. As a result, the exploitation of sulfide ores has predominated historically, despite the geographical predominance of the laterite ores [1]. In the year 2004, the nickel output of the world nickel sulfide smelters was around 740,000 tonnes, representing about 59% of the world primary nickel production, the rest being from the laterite smelters and hydrometallurgical-plants [5].

There are two routes for the processing of the nickel sulfide concentrate, namely flash smelting and electric furnace smelting, as schematically shown in Figure 1.1 [3]. These two processing routes share the same principle: 1) partial sulfur removal by oxidizing gas (air, oxygen-rich air or industrial oxygen) forming gaseous SO_2; 2) oxidation of Fe forming iron oxides which report

to the slag phase along with the gangue materials by combining with the siliceous flux, and 3) separation of the matte from the slag due to their immiscible nature and the density difference. The product from the smelting process is a Ni-rich and Fe-lean matte, which requires further refining.

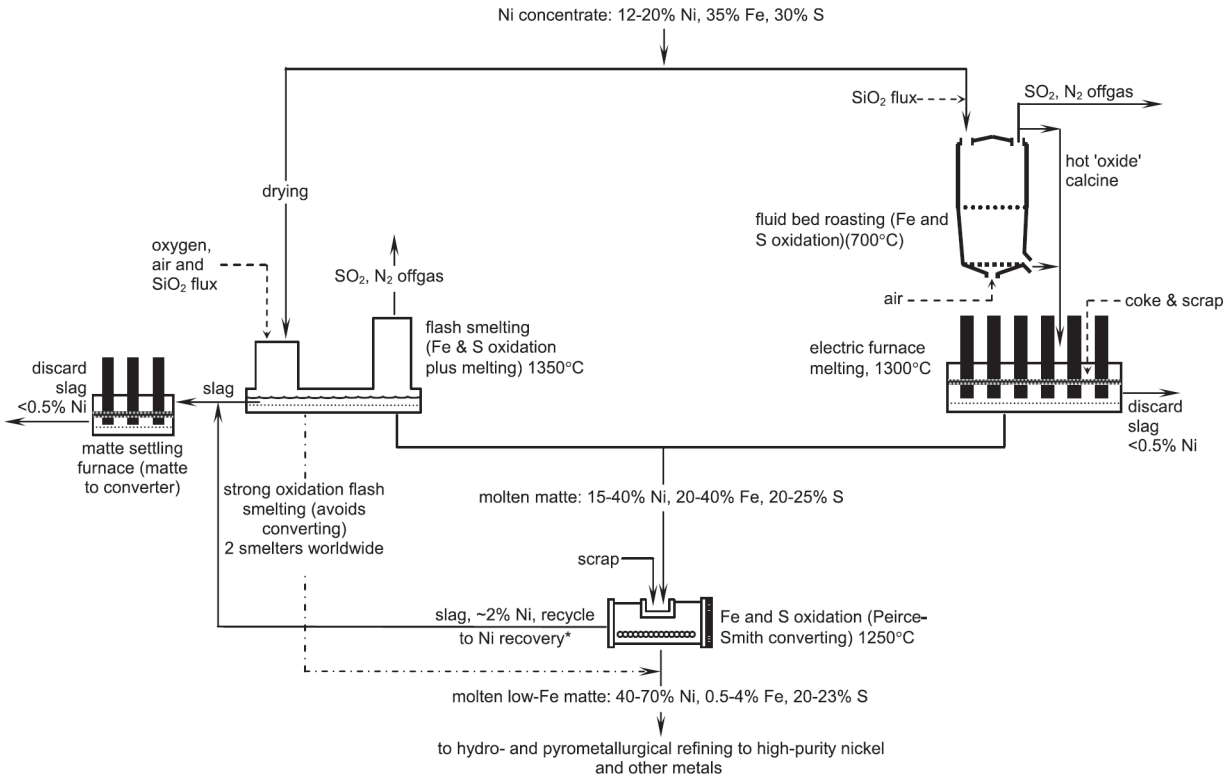

Figure 1.1. Schematic of two routes for producing a Ni-rich matte from nickel sulfide concentrate [3].

The electric furnace smelting route to treat nickel concentrate comprises the following steps: roasting, smelting and converting. Partial oxidation of the concentrate is performed in a fluidized bed roaster to form iron oxide and nickel sulfide, the oxidation reactions being represented by Reactions (1.1) and (1.2). In the oxidative atmosphere, a certain amount of Ni is also oxidized to nickel oxide (NiO) and nickel ferrite ($Ni_xFe_{3-x}O_4$). Separation of the iron oxide from the sulfide is achieved by melting the calcine and fluxing with siliceous materials in the electric furnace under a reducing atmosphere. The main reactions occurring in the electric furnace are represented by Reactions (1.3) to (1.5). The recovery of Ni can be as high as 98%

due to the reducing environment in the electric furnace [3]. Converting is usually performed in the Pierce-Smith converter to further reduce the Fe content in the electric furnace matte to 1–4 wt% as well as the sulfur content by blowing air or oxygen-enriched air.

$$Fe_{4.5}Ni_{4.5}S_8 + 7.25O_2 = 4.5FeO + 1.5Ni_3S_2 + 5SO_2 \quad (1.1)$$

$$Fe_7S_8 + 11.5O_2 = 7FeO + 8SO_2 \quad (1.2)$$

$$2C + O_2 = 2CO \quad (1.3)$$

$$2FeO + SiO_2 = Fe_2SiO_4 \quad (1.4)$$

$$NiO + FeS = NiS + FeO \quad (1.5)$$

Flash smelting combines roasting and smelting in one smelter. Compared with electric furnace smelting, it greatly reduces the fuel or electricity consumption by utilizing the heat released from the oxidation of iron and sulfur in the concentrate. However, the nickel loss to the slag is higher due to the more oxidizing atmosphere employed in the flash furnace, necessitating further slag cleaning to recover the entrapped and oxidized Ni. Converting is also an integral part of the flash smelting route to reduce the iron and sulfur contents of the matte.

1.2 Environmental Issues of the Pyrometallurgical Routes

In the year 2006, the total SO_2 emissions reached 1.97 million tonnes in Canada. The non-ferrous smelting and refining continued to be the largest single source sector of SO_2 emissions, which can be seen from Figure 1.2 [6]. With the more stringent environmental regulations, it is of paramount importance to reduce the SO_2 emissions from the non-ferrous metal smelters through technological improvement and innovation.

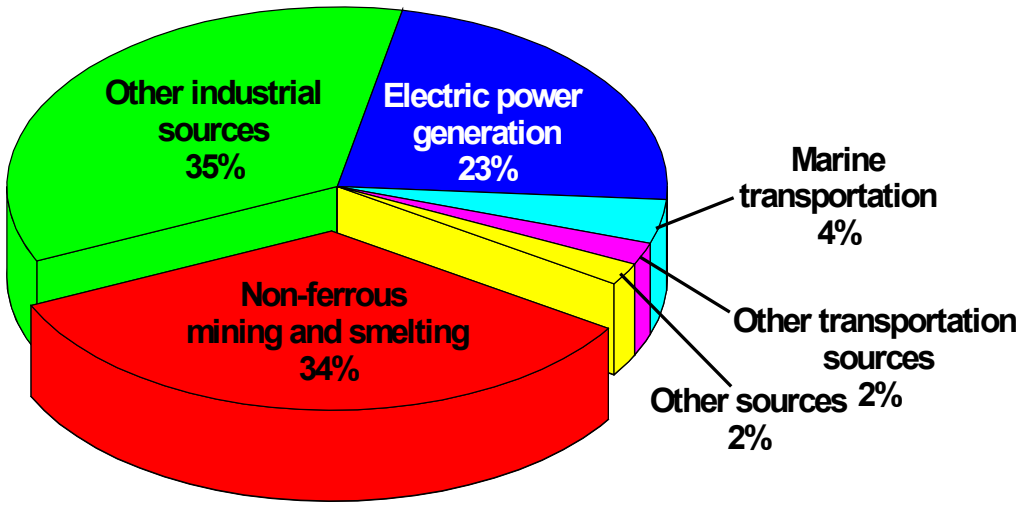

Figure 1.2. Canadian emission sources of sulfur dioxide in 2006 [6].

As for the nickel industry, sulfur rejection in the pyrometallurgical routes of nickel extraction always involves gaseous SO_2 as a by-product. SO_2 fixation is necessary in order to meet the more stringent environmental regulations. This is performed by converting it to sulfuric acid (H_2SO_4) in the acid plant. The sulfuric acid plant requires the optimum SO_2 concentration of the gas input to be between 10% and 12% [3]. Generally speaking, the flash furnace and the fluidized bed roaster would produce a continuous offgas stream with suitable SO_2 concentration for efficient production of sulfuric acid. On the other hand, the SO_2 content in the offgas from an electric furnace is too weak for this purpose. Usually this offgas is emitted to the atmosphere without SO_2 capture. The Pierce-Smith converter offgas is discontinuous and relatively weak, which makes it difficult to capture. SO_2 can be emitted to the environment during charging and skimming, as well as from the interface between the hood and the converter during blowing [3].

The dependence of the SO_2 disposition method on the SO_2 concentration of the offgas can be revealed by the nickel smelters' practices worldwide. Table 1.1 and Table 1.2 provide a summary of the SO_2 production and its disposal in nickel smelters of both the flash smelting and the electric furnace smelting routes [5]. These 11 smelters investigated and listed in these two tables account for approximately 55.5% of the annual world primary Ni production in the year

2004, and the balance was mainly produced by the laterite processing plants. Based on the data presented here, the amount of SO_2 emitted to the atmosphere was some 900,000 tonnes per year from the flash smelters, and 300,000 tonnes per year from the electric furnace smelters, assuming the smelters operate 90% of the time. About 53% of the SO_2 produced from the smelting stage in the flash smelters was captured to make acid, while the value was only 8% captured from the converting stage. As for the electric furnace smelters, only 33% of the SO_2 produced from the roasting stage was captured for acid making, which is mainly due to the weak SO_2 produced by the traveling grates employed in the two nickel smelters in Russia. Although the Vale nickel smelter in Thompson, Manitoba, Canada produces offgas with strong SO_2 from the fluidized bed roaster which is suitable for acid making, it is vented to the atmosphere through stacks instead due mainly to the high cost of transportation of sulfuric acid to the market. This makes it difficult for the company to meet the environmental regulations. Because of this situation, as well as a lack of the raw materials, Vale will shut down the smelter in Thompson in the year 2015 [7]. As for the Pierce-Smith converters in the electric furnace smelters, 47% of the SO_2 produced from them was fixed as sulfuric acid. This number is relatively high compared to that of the flash smelters, which is mainly attributed to the capture of SO_2 from the converters for acid making practiced by the Pechenganickel smelter in Russia, although its concentration in the offgas is very low.

Apart from the SO_2 issues, the electric furnace smelters are also large consumers of electricity, which is revealed in Table 1.3. This is a major drawback of the electric furnace smelters compared with the flash smelters in which heat released from the exothermic oxidation of the concentrate is utilized to melt the feed. The electric furnace uses consumable carbon paste electrodes to conduct current, and create a more reducing environment with the addition of coke. Substantial amounts of CO_2 are emitted as a result, which can be seen in Table 1.3. Also a large amount of heavy metals are emitted to the atmosphere from the smelters.

Table 1.1. SO_2 production and disposition for nickel flash smelters [5].

Plant		BCL Smelter, BCL Limited, Selebi Phikwe, Botswana	Kalgoorlie, BHP Billiton Nickel West, Kalgoorlie, Australia	Jinchuan, Jinchuan Group Ltd. Gansu Province, China	Nadezda Matallurgical Plant, Norilsky Nickel, Norilsk, Russia	DON Flash Smelters		Inco Oxygen Flash Smelter, Copper Cliff, CVRD Inco, Sudbury, Ontario, Canada
						Harjavalta, Boliden Harjavalta Oy (Smelter), Harjavalta, Finland	Fortaleza de Minas, Votorantim Metais, Brazil	
Annual Ni Production (t)		27400	100000	65000	140000	38000	7000	133400
Smelting	Off-gas Volume (Nm^3/h)	87152	_____	60000	56000	16000	13100	24000-28000
	SO_2 Dry Basis (vol.%)	7.2	_____	8	30-35	30	26	55 Dry basis
	Off-gas Disposition	Atmosphere	Acid Plant	Acid Plant	Atmosphere	Acid Plant	Acid Plant	To liquid SO_2 plant and to acid plant
Converting	Off-gas Volume (Nm^3/h)	80000 one converter	41000 to acid plant	50000-60000	140000	N/A	N/A	140000
		160000 two converters in stack	60000 to stack			_____	_____	
	SO_2 Dry Basis (vol.%)	5.2	4% to acid plant	2.5-3.5	2.5	_____	_____	3-5% during regular blows
			2.7% to stack			_____	_____	
	Off-gas Disposition	To stack	To acid plant or stack	Acid Plant	Atmosphere	_____	_____	To stack
Slag Cleaning	Off-gas Disposition	Atmosphere	See flash furnace off-gas disposition	Atmosphere	Atmosphere after dust recovery	Baghouse and stack	_____	_____

Table 1.2. SO_2 production and disposition for nickel electric furnace smelters [5].

Plant		Sudbury Smelter Xstrata Nickel Sudbury, ON, Canada	Thompson CVRD Inco Manitoba, Canada	Nickel Plant Norilsky Nickel Norilsk, Russia	Pechenganickel Norilsky Nickel Pechenga, Russia
Annual Ni Production (t)		63000	50000	40000	35000
Roasting	Off-gas Volume (Nm^3/h)	40000	17819	280000	46000
	SO_2 Dry Basis (vol.%)	11 to 13	25	1 to 2	2.2
	Off-gas Disposition	Acid Plant	Stack	Stack	Stack
Smelting	SO_2 Dry Basis (vol.%)	1	3.3	0.01	<0.3
	Off-gas Disposition	Stack	Stack	Stack	Stack
Converting	Off-gas Volume (Nm^3/h)	_____	75000	140000	180000
	SO_2 Dry Basis (vol.%)	_____	3.6	1-2.5	2.5
	Off-gas Disposition	Off-gas from slag-cleaning vessel, slag-making converter, and finish converter to stack	Stack	Stack	To acid Plant
Slag Cleaning	Off-gas Disposition	Stack	_____	Stack	_____

Table 1.3. Summary of 2004 energy consumption and emissions for the Xstrata nickel smelter in Sudbury and Vale smelter in Thompson*.

Nickel Smelters	Annual Electric Energy ($x10^6$ kW·h)	Furnace CO_2 Emissions (tonnes/year)	SO_2 Emissions (tonnes/year)	Heavy Metal Atmospheric Emissions (tonnes/year)		
				Pb	As	Ni
Xstrata, Sudbury	317	69,000	40,000	___	___	___
Vale, Thompson	253	52,000	190,000	2.7	3.6	190
Total	570	121,000	230,000			

* Data estimated based on published information [5, 8, 9]. Assume electric furnaces operate 90% of the time. The furnace CO_2 emissions do not include indirect emissions due to electricity generation.

1.3 Proposed Process and Objectives

The thesis project aims at developing a new and more environmentally friendly process to treat nickel sulfide concentrate. The ultimate objectives are to decrease the electric energy consumption, decrease SO_2, CO_2 and heavy metal emissions from nickel smelters.

This investigation aims at developing a process where the electric furnace and the converters are eliminated. Instead, roasting will be modified to make water-soluble nickel, copper and cobalt sulfates so that leaching followed by various hydrometallurgical steps are used. Such a process could potentially eliminate all the emissions and decrease the use of electric energy dramatically. The roasting process would include two roasters in series, one oxidizing followed by one sulfating. Both of these processes will be continuous with all gases captured and passed through an acid plant, for nearly 100% capture of SO_2 and heavy metals. The fuel value of the sulfides will be maximized to dramatically decrease the use of electric energy and with no need for coke or any other fossil fuel.

In the process to be investigated, iron sulfides are firstly oxidized selectively to iron oxides, and the remaining metal sulfides are then roasted to form water soluble sulfates, thus eliminating

electric furnace smelting and converting. The valuable metal sulfates formed will then be leached, purified and recovered. The process steps would be:

Oxidation roasting → Sulfation roasting → Leaching

The main advantages are: 1) Eliminating the use of electric energy by the electric furnaces; 2) Avoiding the use of coke as a reductant thereby reducing the CO_2 emissions; 3) Significant reduction of SO_2 emissions; 4) Reducing heavy metals atmospheric emissions; 5) Decreasing fugitive emission of gases and dust, improving work place conditions; 6) Simplified flowsheet with lower capital cost. Since all the gases from the roasters will pass through various gas cleaning steps and then enter a sulfuric acid plant, heavy metal emissions will also be minimal.

Summary of the steps in the proposed process:

1) Roast Ni/Cu concentrate selectively to oxidize most of the iron sulfides to magnetite and hematite, maintaining nearly all nickel and copper as sulfides.

2) Take the partially oxidized product from step one and sulfatize it further to form nickel, copper and cobalt sulfates from the sulfides. The sulfation atmosphere has to be determined.

3) Leach product from step 2). The nickel, copper and cobalt sulfates are soluble while the iron oxides do not dissolve.

4) Precipitation of any dissolved iron from the separated leach liquor by air oxidation after the adjustment of pH and temperature.

5) Recovery of copper from the iron-free liquor by pH adjustment and liquid-liquid extraction.

6) Recovery of nickel and cobalt from the purified liquor by pH adjustment and liquid-liquid extraction.

7) Electrowinning or precipitation of valuable metals.

This thesis will be mainly focused on steps 1) and 2) since they are the main technical challenges. Steps 3) to 7) should be fairly standard hydrometallurgical processes, except

possibly iron oxide filtration and removal as well as effluent treatment to meet the water discharge regulations.

1.4 Fluidized Bed Roasting Technology

Fluidized bed roaster (Figure 1.3) is an efficient unit for roasting a sulfide in terms of energy recovery, temperature control, oxygen efficiency, and SO_2 capture. Roasting of a sulfide is a process involving mainly gas-solid two-phase exothermic reactions. Due to the extremely high reaction surface area, high oxygen efficiency can be achieved. As a result, the SO_2 in the offgas is strong, and the volume of the feeding gas (usually air) required to roast a unit amount of solid material is minimal. Therefore, the latent heat carried away by the gas phase is minimized, thus maximizing the energy efficiency. In fact, the fluidized bed roasting process could be autogenous, meaning the heat released from the exothermic reactions is high enough to maintain the roasting temperature without the input of external fuels. More often than not, cooling is required to prevent the fluidized bed from overheating. Due to the quick heat and mass transfer, the fluidized bed tends to be uniform, rendering a relatively easy temperature control. Therefore, the fluidized bed roaster is a reaction vessel especially suitable for the process where precise control of reaction temperature is critical.

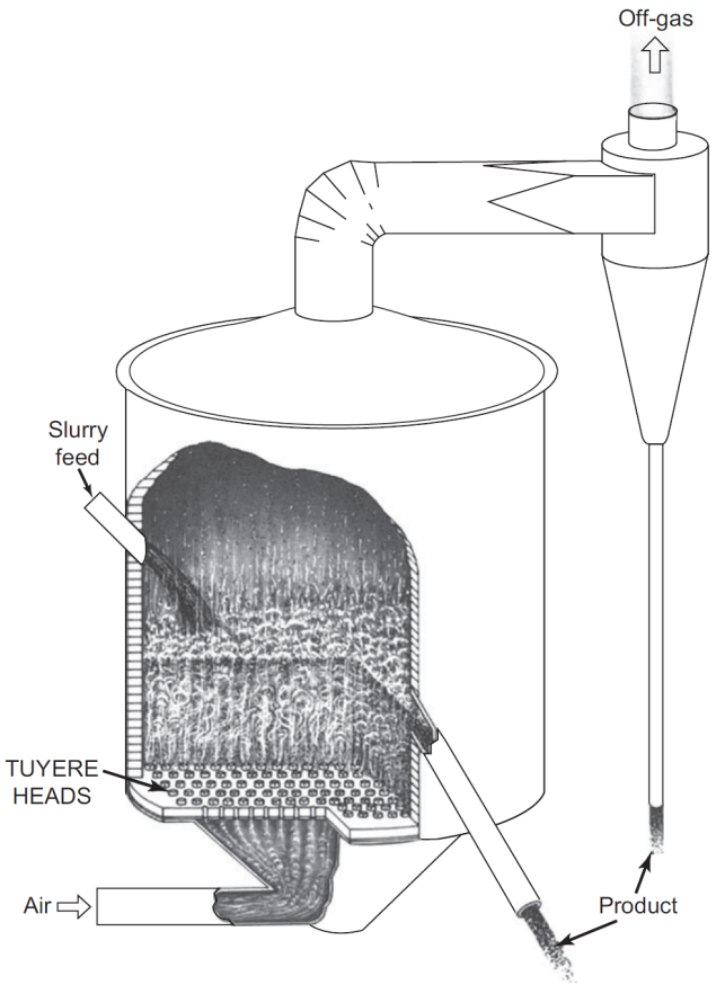

Figure 1.3. Fluidized bed roaster [10].

Fluidized bed technology is widely used for drying, calcining, roasting, and catalyzing, etc. Its wide application draws a lot of interest in research in this area, resulting in a large amount of literature. Some basic yet important aspects of the fluidized bed technique are briefly discussed below.

1.4.1 Geldart Classification of Powders

Based on the mean particle size and the density difference between the fluid and solid, Geldart [11] classified the powders into four groups, which are shown as Figure 1.4. In Group A, the particles have a small mean particle size (30–100 μm) and density (<1400 kg/m^3). Mixing is

rapid even with a few bubbles. Group B has particles with mean sizes between 40 μm and 500 μm, and with density between 1400 and 4000 kg/m^3. A typical example of this group is sand. Mixing is poor in the absence of bubbles. Group C are fine and cohesive particles, which are difficult to fluidize. This difficulty arises because the inter-particular forces are greater than the forces exerted by the fluid. As a result, the powder is lifted as a plug in small diameter tubes, or channels badly. Group D is comprised of coarse (d_p>500 μm) and dense particles, which is spoutable.

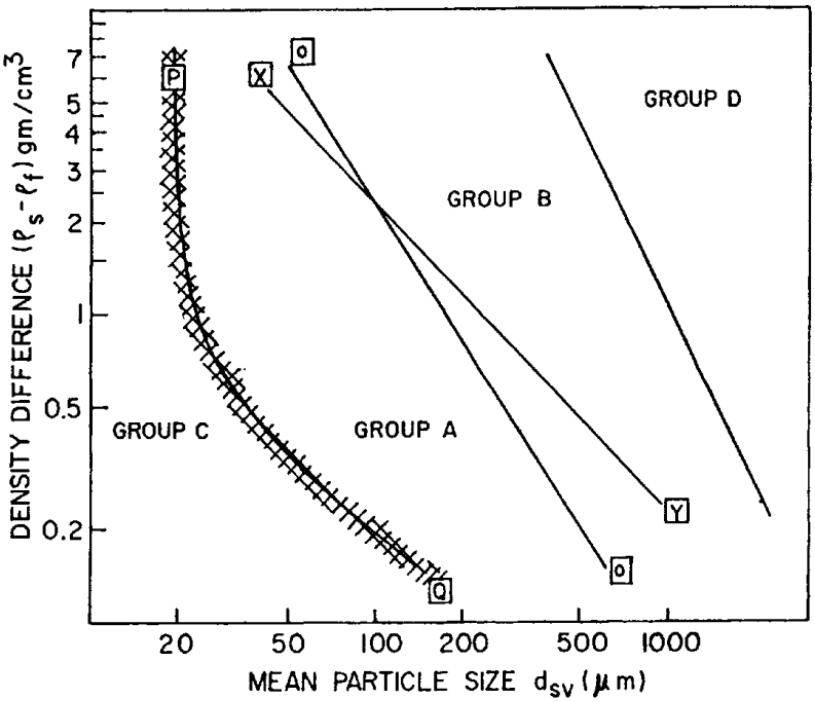

Figure 1.4. Geldart classification of powders [11].

1.4.2 Minimum Fluidization Velocity (V_{mf})

This is the minimum superficial velocity of the fluid required to form a fluidized bed. This V_{mf} could be experimentally determined by plotting the pressure drop (ΔP) across the powder bed as a function of the fluid velocity (V), as illustrated in Figure 1.5. In the AB region, ΔP increases with the increase of the fluid velocity through the fixed bed. V_{mf} marks the transition point after

which the pressure drop becomes relatively constant, which is because the drag force exerted on the bed equals the gravitational force less the buoyancy.

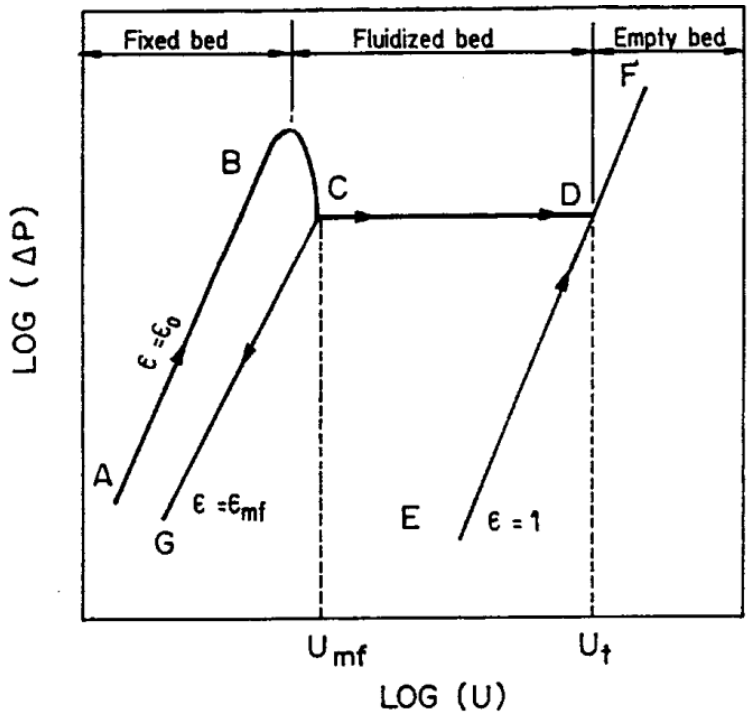

Figure 1.5. Bed pressure drop vs. superficial velocity [12].

The minimum fluidization velocity can also be theoretically predicted. For example, Thonglimp et al. [13] developed a correlation for Re_{mf} derived from the pressure drop principles, which is shown as Equation (1.6).

$$Re_{mf} = (31.6^2 + 0.0425 * Ar)^{1/2} - 31.6 \quad (1.6)$$

where Re_{mf} is the Reynolds number with minimum fluidization velocity, and Ar is the Archimedes number. They are shown as Equations (1.7) and (1.8), respectively.

$$Re_{mf} = d_p V_{mf} \rho_g / \mu_g \quad (1.7)$$

$$Ar = {d_p}^3 \rho_g (\rho_s - \rho_g) g / {\mu_g}^2 \quad (1.8)$$

where d_p is the diameter of the particle, V_{mf} is the minimum fluidization velocity, ρ_g is the density of the fluid, μ_g is the dynamic viscosity of the fluid, ρ_s is the density of the particle, g is the gravitational acceleration.

1.4.3 Terminal Velocity (V_t)

Terminal velocity is the maximum allowable velocity for operation of a fluidized bed, at which entrainment of the particles starts to occur [12]. This velocity marks another transition in Figure 1.5, where the pressure drop across the bed starts to increase again. Terminal velocity of a single particle could be theoretically calculated based on the force balance, which constitutes the gravitational force, the buoyant force, and the drag force by the fluid. In the case of a spherical particle, the terminal velocity could be determined based on Equation (1.9) [12].

$$C_D {Re_t}^2 = \frac{4}{3} Ar \tag{1.9}$$

where C_D is the drag coefficient, Re_t is the Reynolds number calculated with terminal velocity, and Ar is the Archimedes number.

The drag coefficient could be determined from Re by Equation (1.10), in which *a* and *b* are constants which are given in Table 1.4 for three flow regimes.

$$C_D = {a}/{Re^b} \tag{1.10}$$

Table 1.4. Constants for evaluating drag coefficient for three flow regimes [12].

Range	a	b	Range $(Ar)^{1/8}$=K
Re<2, Stokes	24	1	<3.3
2<Re<500, intermediate	18.5	0.6	3.3–48.6
500<Re<200,000, Newton	0.44	0	43.6–2360

1.4.4 Heat Transfer between a Fluidized Bed and an Immersed Surface

Heat transfer between a fluidized bed and an immersed surface is relatively fast due to the fluid-like nature of the fluidized bed. It mainly involves the convective heat transfer associated with the gas and the heat transfer associated with the contact between the fluidized particles and the immersed surface [14]. Borodulya et al. [15] investigated the heat transfer between a surface and a fluidized bed using a two-zone model. Considering the heat transfer coefficient as the sum of the conductive (h_{cond}), convective (h_{conv}), and radiative (h_r) components, Equation (1.11) was obtained for computing the overall heat transfer coefficient. Thermophysical properties are evaluated at $(T_\infty - T_s)/2$.

$$Nu = 0.85Ar^{0.1}\left(\frac{\rho_p}{\rho_g}\right)^{0.14}\left(\frac{C_p}{C_g}\right)^{0.24}(1-\omega)^{2/3} + 0.046RePr\frac{(1-\omega)^{2/3}}{\omega}$$

$$+\frac{\bar{D}}{k_g}\sigma^*(T_\infty^2 + T_s^2)(T_\infty + T_s) \quad (1.11)$$

where ρ_p and ρ_g are the densities of fluidized particles and gas, respectively; C_p and C_g are the heat capacities of the particles and gas; ω is the porosity or voidage of the fluidized bed; $\bar{D}$ is the mean diameter of the particles; k_g is the thermal conductivity of the gas; T_∞ is the temperature of the fluidized bed core; T_s is the temperature of the immersed surface;

$Nu = \frac{h\bar{D}}{k_g}$; where h is the overall heat transfer coefficient;

$Ar = \frac{g\bar{D}^3\rho_g(\rho_p-\rho_g)}{\eta_g{}^2}$;

$Re = \frac{\bar{D}V_0}{\nu_g}$; where V_0 is the superficial velocity of the gas; ν_g is the kinematic diffusivity of the gas;

$Pr = \frac{\nu_g}{\alpha_g}$; where α_g is the thermal diffusivity of the gas;

$\sigma^* = \frac{\sigma}{\left(\frac{1}{\varepsilon_s}+\frac{1}{\varepsilon_e}-1\right)}$; where σ=5.670*10^{-8} W·m^{-2}·K^{-4}; ε_s is the emissivity of the immersed solid; ε_e is the emissivity of the bed.

1.5 Oxidation Roasting of Nickel Concentrate

1.5.1 Thermodynamics

The main reactions in the oxidation roasting are the oxidation of the metal sulfide(s), which can be generally represented by Reaction (1.12). The Gibbs free energies of formation (ΔG_f) for metal sulfides and oxides of interests are plotted in Figure 1.6 as a function of temperature. It represents the relative affinities of metal elements for sulfur and oxygen: the lower the ΔG_f, the higher the affinity would be. In the roasting temperature range which is 500 ºC to 800 ºC, the metal elements have similar affinities for sulfur, and have much higher affinities for oxygen, meaning the oxidation of sulfides (Reaction (1.12)) would occur in the presence of oxygen. Of all the four oxides, Fe_3O_4 has the lowest ΔG_f. This indicates that if limited amount of O_2 is supplied to roast the mixture of sulfides, the iron sulfides (e.g. Fe_7S_8) would be preferentially oxidized to form oxides, leaving the non-ferrous metal sulfides unoxidized. A typical example of this type of preferential oxidation is the oxidation of pentlandite $(Ni,Fe)_9S_8$, which is represented by Reaction (1.13) [16].

$$MeS(s)+2/3O_2(g)\rightarrow MeO(s)+SO_2(g) \quad (1.12)$$

$$(Ni,Fe)_9S_8+O_2\rightarrow Fe_2O_3+Ni_{1-x}S+SO_2 \quad (1.13)$$

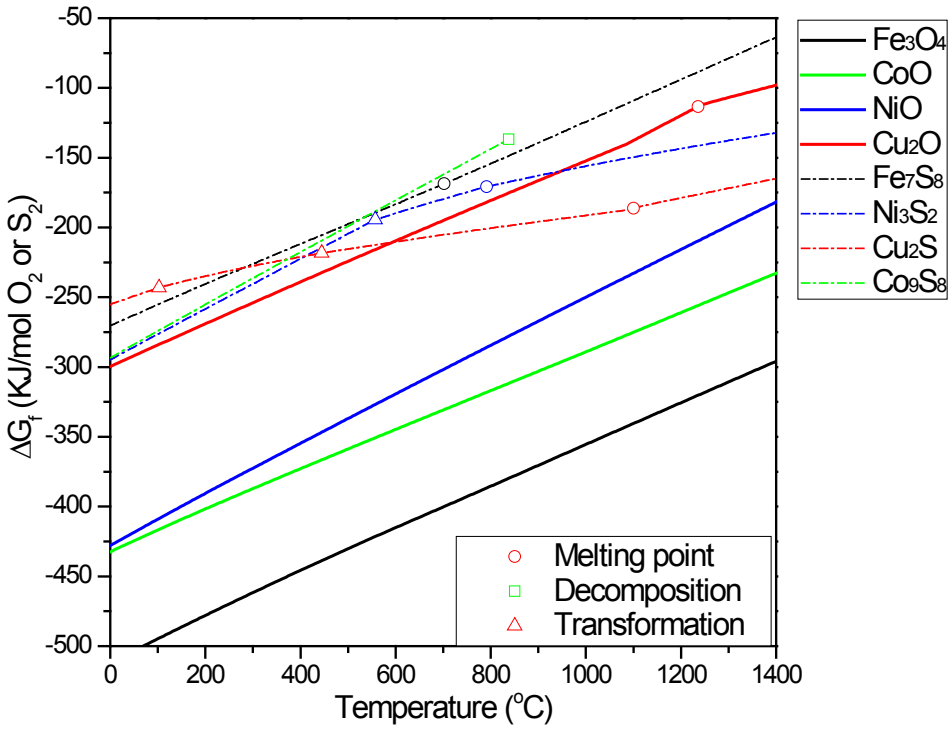

Figure 1.6. Gibbs free energy of formation vs. temperature for oxides and sulfides calculated using HSC Chemistry [17].

Thermodynamically, the stabilities of sulfide and oxide species depend not only on the temperature, but also on the gas environment in the roaster. Therefore the roasting parameters must be carefully chosen in order to achieve a good quality of the roasting product. Predominance diagrams (Figure 1.7 and Figure 1.8) could provide guidance for the appropriate selection of roasting conditions, such as roasting temperature and the roasting gas composition. The roasting temperature of a fluidized bed could be adjusted by the water content of the feeding slurry and by water cooling. The roasting gas composition could be indirectly controlled by adjusting the gas to feed ratio as well as the feeding gas composition. Figure 1.7 and Figure 1.8 indicate that thermodynamically, sulfides are not stable under an oxidative environment at normal roasting temperatures. Sulfates could form at relatively lower temperatures (e.g. 500 ^{o}C) and with high partial pressure of SO_2. Most probably the dead roasting product of a nickel-iron sulfide concentrate would be Fe_2O_3 and NiO. A lower extent of the oxidation of NiS species could be achieved by limiting the O_2 supply, based on the theory of preferential oxidation of iron species mentioned above.

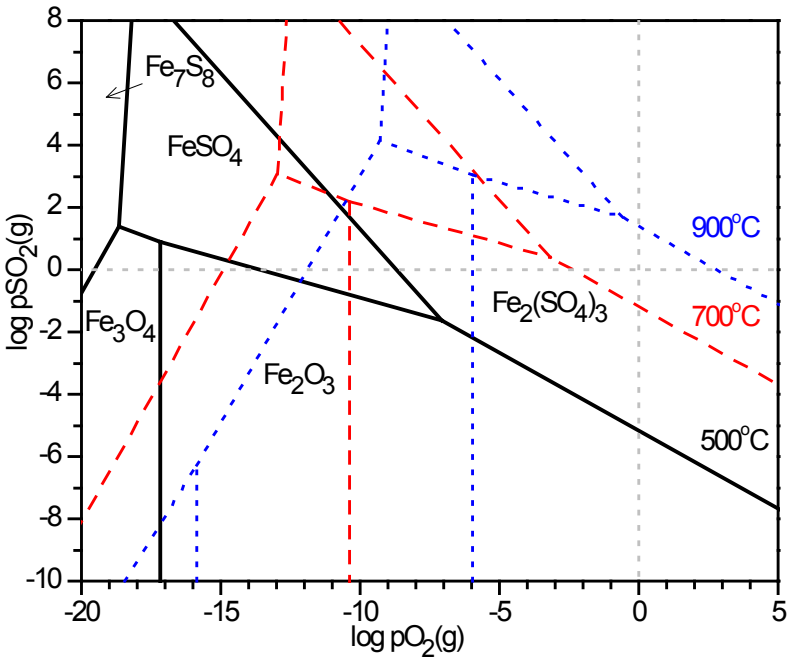

Figure 1.7. Superimposed Fe-S-O predominance diagrams for 500 ºC, 700 ºC and 900 ºC calculated using HSC Chemistry [17].

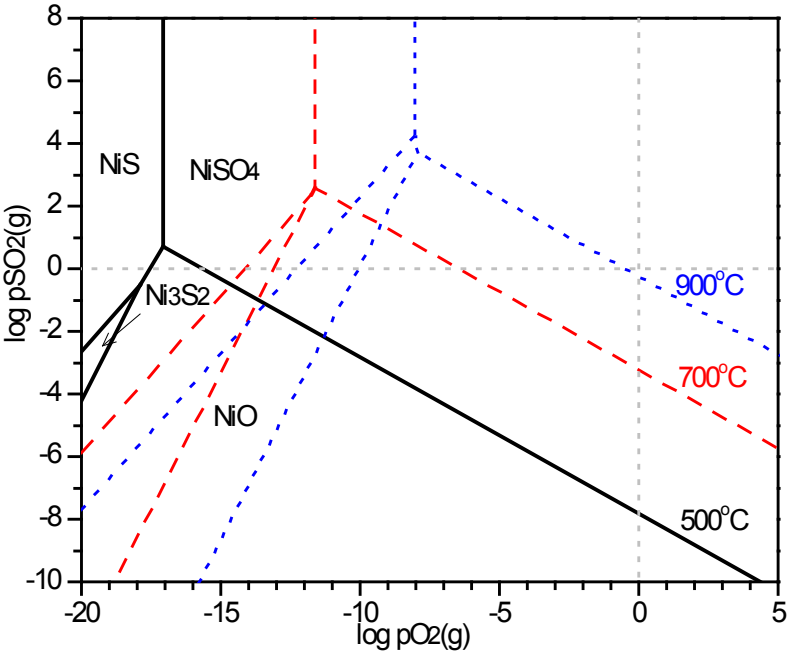

Figure 1.8. Superimposed Ni-S-O predominance diagrams for 500 °C, 700 °C and 900 °C calculated using HSC Chemistry [17].

1.5.2 Kinetics

Reaction (1.12) which represents the main reactions occurring in a sulfide roasting process indicates that solid and gas phases are involved both as reactants and as products. Figure 1.9 shows the shrinking core model for the oxidation roasting of a sulfide particle, illustrating schematically the process of roasting. There are several steps involved in the oxidation roasting mechanism of a sulfide mineral: 1) Oxygen diffusion through a thin gas film to the surface of the particle; 2) Oxygen diffusion to the unreacted core (MeS) surface through the layer of solid product (MeO); 3) Oxygen adsorption onto the surface of the sulfide core; 4) Electron transfer from a sulfide ion to a nearby oxygen, and incorporation of the ions into the mineral lattice; 5) Binding of the neutralized sulfur with another oxygen molecule adsorbed beside it; 6) Desorption of the SO_2 molecule and diffusion away through the MeO layer and the gas thin film into the main gas stream, leaving a vacant sulfide ion site on the mineral surface; 7) Diffusion of another sulfur ion from the interior of the sulfide core to occupy this site and continue the reaction [18], or this site is occupied by another oxygen ion, forming a bond of the solid product MeO.

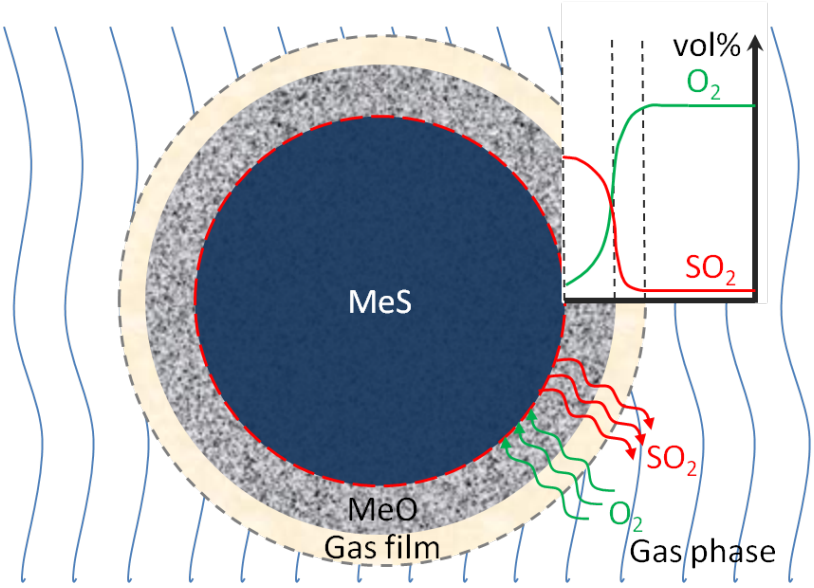

Figure 1.9. Shrinking core model for the oxidation roasting of a sulfide particle.

Depending on the roasting conditions and the nature of the sulfide itself, any step during the above process could control the overall rate of the oxidation reaction. As is shown in Figure 1.9,

the gaseous oxidant has to diffuse inward through the MeO layer before reacting with the sulfide core, and the gaseous product has to diffuse out through the MeO layer. This diffusion of gases through the solid product layer could be the rate determining step depending on the diffusivity of the gas in MeO as well as the morphology of MeO. If the solid product MeO is porous in nature, the gas can easily access the surface of the unreacted core through the pores. It would less likely be the rate controlling step. The porosity of the solid product is largely dependent on the reaction mechanism and the volume change of the solid for a certain reaction. Table 1.5 summarizes the volume changes of the solids for the roasting reactions that might be involved which are calculated based on the densities of the solids. The general rule is that oxidation of sulfides leads to a volume decrease, meaning the space originally occupied by the sulfides cannot be fully occupied by the solid product. This gives the solid product a potential to be porous, which will result in an accelerated roasting reaction. This is particularly true for the oxidation of pyrrhotite. Figure 1.10 is an optical microscopy image of a roasted pyrrhotite particle, featuring its characteristic columnar structure. This particular morphological feature results from its particular oxidation mechanism, i.e. the preferential oxidation proceeding along certain crystallographic planes [19], as well as the occupied volume decrease illustrated in Table 1.5.

Table 1.5. Volume changes for oxidation and sulfate formation reactions.

Reactions	Volume change
$2Fe_{0.88}S+3.32O_2=0.88Fe_2O_3+2SO_2$	-24.1%
$4Fe_{4.5}Ni_{4.5}S_8+45.5O_2=9Fe_2O_3+6Ni_3S_2+32SO_2$	-19.0%
$4Fe_3O_4+O_2=6Fe_2O_3$	+1.8%
$NiS+2O_2=NiSO_4$	+155%
$2NiS+3O_2=2NiO+2SO_2$	-34.4%
$2Ni_3S_2+7O_2=6NiO+4SO_2$	-21.3%
$Fe_{0.88}S+1.88O_2=0.88FeSO_4+0.12SO_2$	+108%
$4CuFeS_2+13O_2=4CuO+2Fe_2O_3+8SO_2$	-37.0%
$4CuFeS_2+15O_2=4CuSO_4+2Fe_2O_3+4SO_2$	+36.2%
$2Fe_{0.88}S+0.64SO_2+4.64O_2=0.88Fe_2(SO_4)_3$	+223%

Note: Densities of sulfides and oxides are cited from Reference [20] and those of sulfates are cited from Reference [21].

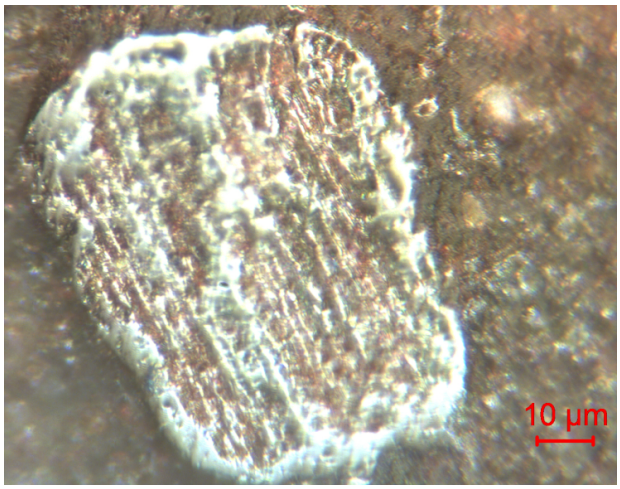

Figure 1.10. Columnar structure of a roasted pyrrhotite particle.

1.6 Sulfation Roasting of Nickel Concentrate

1.6.1 Thermodynamics

Figure 1.11 depicts the predominance area diagrams in Me-S-O (Me = Fe, Ni, Cu, Co) system at 680 °C calculated using HSC Chemistry [17]. The shaded area shows the window of opportunity in which the non-ferrous metal sulfates are stable, while the iron sulfate is not. As a result, the roasting conditions should fall within this window in order to achieve the selective sulfation roast. In practice, the roasting mechanism is rather complicated due to the complexity of the mineralogical composition, the complex heat and mass transfer involved in the multi-phase reactions, and the kinetics of various reactions that may not allow establishment of equilibrium conditions. Although the fluidized bed roaster has the merit of relatively easy temperature and atmosphere control, the in-situ conditions (i.e. temperature, local gas environment) under which the roasting reactions take place could be largely different from one position to another or even within individual particles. This may result in the formation of unwanted by-products such as non-ferrous metal oxides. The formation of nickel ferrite

($NiFe_2O_4$), a by-product possibly from the solid-solid reaction between iron oxides and nickel oxide due to local overheating in the fluidized bed, is typically detrimental to the sulfation roast. Once formed, it is difficult to sulfatize, which would lead to the nickel loss into the residue during the following leaching step [22-24].

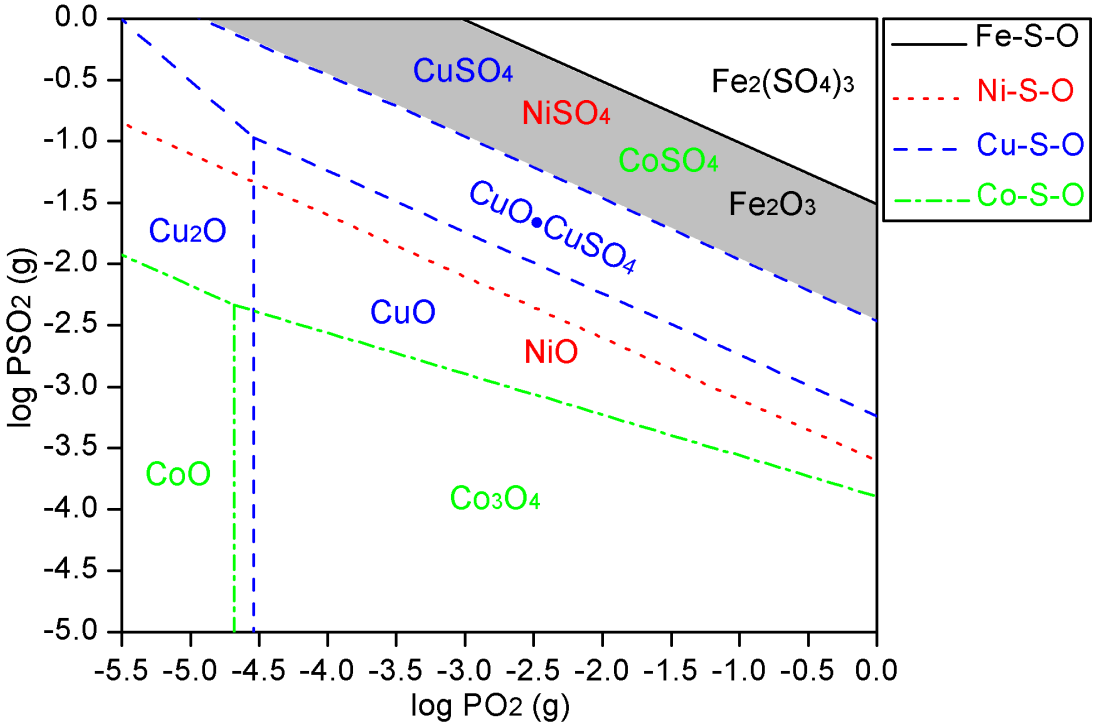

Figure 1.11. Predominance area diagram by superimposing Fe-S-O, Ni-S-O, Cu-S-O and Co-S-O predominance area diagrams at 680 °C (calculated using data from HSC Chemistry [17]).

1.6.2 Kinetics

Sulfate formation can take place by two possible reaction routes, which are represented by Reactions (1.14) to (1.16). The former is the direct sulfation of sulfide (e.g. oxidation of nickel sulfide and iron (II) sulfide), and the latter is the sulfation of oxide with sulfur trioxide (e.g. formation of $CuSO_4$) [25]. The sulfation of nickel sulfide is an extremely slow process due to the rather dense nature of the nickel sulfate layer formed which inhibits further sulfation [26]. The formation of $NiSO_4$ from NiS requires 2.5 times the space occupied by the original NiS by calculation, which can be seen from Table 1.5. This volume increase leads to the dense nature of

the $NiSO_4$ [27]. As a result, sulfation of nickel sulfide is so slow that it is impossible to be employed in commercial production. To address the slow-kinetics problem, previous studies have investigated the effect of Na_2SO_4 addition that could accelerate the reactions by one or a combination of the following mechanisms [23, 28-33]:

1). Na_2SO_4 forms solid solution (β) or binary sulfates (ε,δ,γ) with $NiSO_4$, which could be seen from the $NiSO_4$-Na_2SO_4 binary phase diagram in Figure 1.12 [34]. The formation of any of these phases increases the stability of $NiSO_4$ by lowering its activity, thus preventing the sulfate decomposition [23]. Na_2SO_4 could also destroy the impervious $NiSO_4$ layer by forming a melt possibly below the roasting temperature [35]. As can be seen from Figure 1.12, the lowest melting temperature is the eutectic at approximately 670 °C, which could be below the normal roasting temperature (650–750 °C).

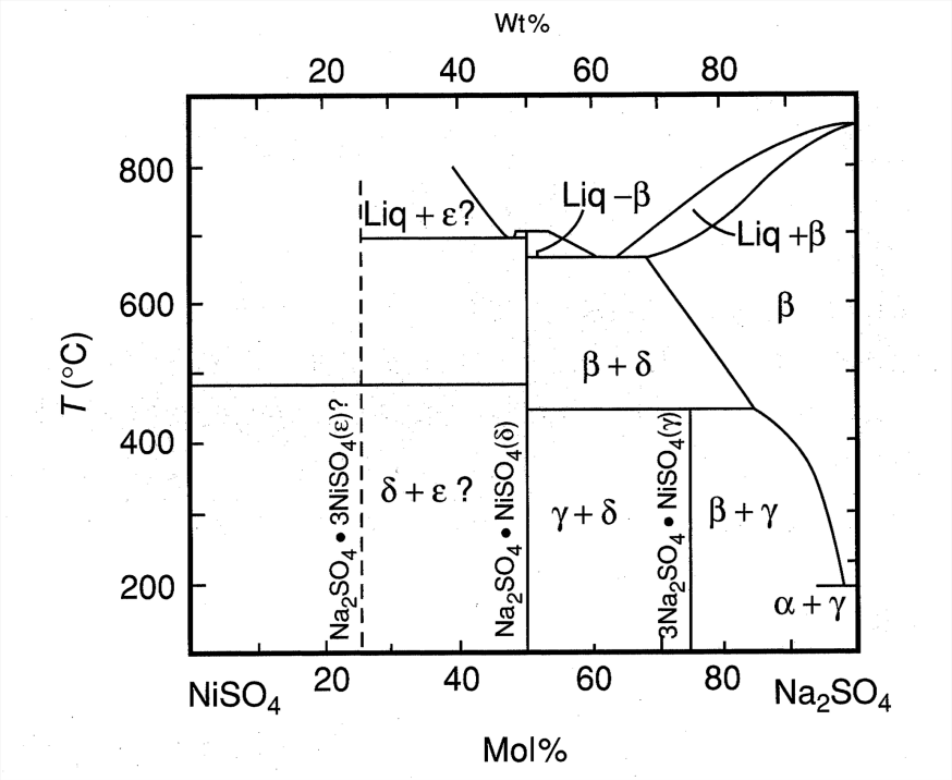

Figure 1.12. $NiSO_4$-Na_2SO_4 phase diagram [34].

2). Na_2SO_4 destroys the nickel ferrite formed via Reaction (1.17) [22, 36]. If the Na_2SO_4 melt contains Fe^{3+} ions, Reaction (1.18) will take place, in which the role of Na_2SO_4 is to provide the melt conditions for the reactive Fe^{3+} ions [26, 37, 38].

3). Na_2SO_4 acts as a reservoir of SO_3 for the sulfation of NiO via Reactions (1.19) and (1.20) [22, 36, 39].

$$MeS + 2O_2 = MeSO_4 \quad (1.14)$$

$$SO_2 + 1/2O_2 = SO_3 \quad (1.15)$$

$$MeO + SO_3 = MeSO_4 \quad (1.16)$$

$$NiFe_2O_4 + Na_2SO_4 = Na_2Fe_2O_4 + NiSO_4 \quad (1.17)$$

$$3NiFe_2O_4(s) + Fe_2(SO_4)_3(melt) = 4Fe_2O_3(s) + 3NiSO_4(melt) \quad (1.18)$$

$$Na_2SO_4(s) + SO_3(g) \leftrightarrow Na_2S_2O_7(l) \quad (1.19)$$

$$SO_3 + NiO = NiSO_4 \quad (1.20)$$

Most of the work on sulfation roasting was conducted between 1950 and 1990. The overall technical challenges seem to be the low Ni yield (maximum around 80%) after leaching due largely to the formation of nickel ferrite during roasting, as well as the slow kinetics which made it economically unattractive at the time. Today, however, environmental regulations are more stringent, to an extent that meeting the imposed limits on emissions is forcing the closure of smelters. Energy conservation is more important than ever and emissions of heavy metals are also coming under increasing scrutiny. Therefore, sulfation roasting today could be much more attractive from energy, environmental and economic points of view if technical and economic solutions can be found for the above mentioned problems.

1.7 References

[1] B. Terry, A.J. Monhemius, A.R. Burkin, General introduction, in: A.R. Burkin (Ed.) Extractive Metallurgy of Nickel, John Wiley & Sons, New York, 1987, pp. 1-6.

[2] A.E.M. Warner, C.M. Diaz, A.D. Dalvi, P.J. Mackey, A.V. Tarasov, JOM World Nonferrous Smelter Survey, Part III: Nickel: Laterite, Journal of Metals, 58 (2006) 11-20.

[3] F.K. Crundwell, M.S. Moats, V. Ramachandran, T.G. Robinson, W.G. Davenport, Extractive Metallurgy of Nickel, Cobalt and Platinum-Group Metals, Elsevier Ltd., Great Britain, 2011.

[4] F.K. Crundwell, M.S. Moats, V. Ramachandran, T.G. Robinson, W.G. Davenport, Overview of the Hydrometallurgical Processing of Laterite Ores, in: Extractive Metallurgy of Nickel, Cobalt and Platinum-Group Metals, Elsevier Ltd., Great Britain, 2011, pp. 117-122.

[5] A.E.M. Warner, C.M. Diaz, A.D. Dalvi, P.J. Mackey, A.V. Tarasov, R.T. Jones, JOM World Nonferrous Smelter Survey, Part IV: Nickel: Sulfide, Journal of Metals, 59 (2007) 58-72.

[6] 2006-2007 Progress Report on The Canada-Wide Acid Rain Strategy for Post-2000, Canadian Council of Ministers of the Environment, 2008.

[7] Thompson refinery shutting down, CBC News, 2010, http://www.cbc.ca/news/canada/manitoba/story/2010/2011/2017/mb-thompson-smelter-refinery-close.html.

[8] Xstrata, Xstrata Sustainability Report 2006, 2006.

[9] Moving Towards Sustainability, 2005 Good Neighbours Report on Health, Safety, Environment and Community, Inco Limited, Toronto, Canada, 2005, pp. 93.

[10] J. Joseph R. Boldt, P. Queneau, Roasting, in: The Winning of Nickel, Longmans, Toronto, 1967, pp. 231-237.

[11] D. Geldart, Types of Gas Fluidization, Powder Technology, 7 (1973) 285-292.

[12] C.K. Gupta, D. Sathiyamoorthy, Generalities and Basics of Fluidization, in: Fluid Bed Technology in Materials Processing, CRC Press, 1999, pp. 1-6.

[13] V. Thonglimp, N. Hiquily, C. Laguerie, Vitesse minimale de fluidisation et expansion des couches fluidisées par un gaz, Powder Technology, 38 (1984) 233-253.

[14] D.R. Poirier, G.H. Geiger, Correlations and Data for Heat Transfer Coefficients, in: Transport Phenomena in Materials Processing, The Minerals, Metals and Materials Society, Pennsylvania, 1994, pp. 248-279.

[15] V.A. Borodulya, Y.S. Teplitsky, I.I. Markevich, A.F. Hassan, T.P. Yeryomenko, Heat transfer between a surface and a fluidized bed: consideration of pressure and temperature effects, International Journal of Heat and Mass Transfer, 34 (1991) 47-53.

[16] D. Yu, T.A. Utigard, TG/DTA study on the oxidation of nickel concentrate, Thermochimica Acta, 533 (2012) 56-65.

[17] A. Roine, HSC Chemistry, Outokumpu Research Oy, Pori, Finland, 2007.

[18] H.Y. Sohn, R.P. Goel, Principles of Roasting, Minerals Sci.Engng, 11 (1979) 137-153.

[19] P.G. Thornhill, L.M. Pidgeon, Micrographic Study of Sulfide Roasting, Journal of Metals, 9 (1957) 989-995.

[20] J.W. Anthony, R.A. Bideaux, K.W. Bladh, M.C. Nichols, Handbook of Mineralogy, Mineralogical Society of America, Chantilly, VA 20151-1110, USA.

[21] P. Patnaik, Handbook of Inorganic Chemicals, McGraw-Hill, 2003.

[22] P.G. Thornhill, U.S. Patent 2,813,016, Method of Roasting Nickeliferous Sulfide Concentrates in a Fluidized Bed, United States, 1957.

[23] A.W. Fletcher, M. Shelef, The Role of Alkali Sulphates in Promoting the Sulphation Roasting of Nickel Sulphides, in: Unit Process in Hydrometallurgy. Group C: Plant Operating Practice - Economics - General, New York Gordon and Breach Science Publishers, 1963, pp. 946-970.

[24] A.W. Fletcher, M. Shelef, A Study of the Sulfation of a Concentrate Containing Iron, Nickel, and Copper Sulfides, Transactions of the Metallurgical Society of AIME, 230 (1964) 1721-1724.

[25] J.G. Dunn, The oxidation of sulphide minerals, Thermochimica Acta, 300 (1997) 127-139.

[26] P.J. Saikkonen, U.S. Patent 4,464,344, Process for Recovering Non-ferrous Metal Values From Ores, Concentrates, Oxidic Roasting Products or Slags, United States, 1984.

[27] M.C.B. Hotz, T.R. Ingraham, The Sulphation of Tricobalt Tetroxide and Nickel Monoxide with Fused Sodium Hydrogen Sulphate, Canadian Metallurgical Quarterly, 4 (1965) 295-302.

[28] W.K. Sproule, P.E. Queneau, G.C. Nowlan Jr, Canadian Patent CA 593622, Method for producing high grade hematite from nickeliferous iron sulfide ore, Canadian Intellectual Property Office (CIPO), Canada, 1960.

[29] P.G. Thornhill, U.S. Patent 2,930,604, Fluidized Bed Roasting of Metal Sulfide Concentrates, Unites States, 1960.

[30] K.L. Luthra, Mechanism of Oxidation-Sulfation reactions of CoO in the Presence of Na_2SO_4, Metallurgical Transactions A, 13A (1982) 1647-1654.

[31] N. Zubryckyj, D.J.I. Evans, V.N. Mackiw, Preferential sulfation of nickel and cobalt in lateritic ores, Journal of Metals, 17 (1965) 478-486.

[32] P.G. Thornhill, The Falconbridge Iron Ore Process, AIME Transactions, LXIV (1961) 337-344.

[33] J.R. Boldt, Jr., Falconbridge Pyrrhotite Process, in: P. Queneau (Ed.) The Winning of Nickel, Longmans Canada, Toronto, 1967, pp. 331-336.

[34] N. Birks, G.H. Meier, F.S. Pettit, Hot Corrosion, in: Introduction to The High-Temperature Oxidation of Metals, Cambridge University Press, United States of America, 2006, pp. 205-252.

[35] J.M. Toguri, A review on the methods of treating nickel-bearing pyrrhotite; with special reference to the Sudbury Area pyrrhotite, Canadian Metallurgical Quarterly, 14 (1975) 323-338.

[36] M.C.B. Hotz, R.C. Kerby, T.R. Ingraham, The sulphation of nickel and cobalt ferrites and sulphides by molten sodium pyrosulphate and sodium bisulphate, Canadian Metallurgical Quarterly, 7 (1968) 205-210.

[37] P.J. Saikkonen, J.K. Rastas, The Role of Sulfate Melts in Sulfating Roasting, in: 25th Annual Conference of Metallurgists, Toronto, Ontario, Canada, 1986, pp. 278-290.

[38] K.T. Jacob, Kinetics of Sulphation of Nickel and Cobalt Ferrites with Na_2SO_4 Melt Containing Fe^{3+} Ions, Transactions of the Indian Institute of Metals, 40 (1987) 383-388.

[39] M.C.B. Hotz, T.R. Ingraham, Fused Sodium Pyrosulphate as a Sulphation Catalyst for NiO and Co_3O_4, Canadian Metallurgical Quarterly, 5 (1966) 237-244.

2 TG/DTA Study on the Oxidation of Nickel Concentrate

2.1 Introduction

In the proposed selective oxidation-sulfation roasting route for nickel processing, the objective of the first step, i.e. oxidation roasting, is to preferentially oxidize the iron sulfide species from the nickel concentrate to form oxides. Therefore, it is of critical importance to understand the oxidation roasting mechanisms of the nickel concentrate. Experiments were therefore conducted to achieve this end by means of thermogravimetric (TG) and differential thermal analysis (DTA).

Oxidizing roasting mechanisms of metal sulfide minerals are quite complex because they vary depending on the sulfide species in the minerals, the roasting conditions employed, and the interactions among all species present. Lab scale thermogravimetric and differential thermal analysis studies on the oxidation of sulfide minerals have much milder oxidative conditions than the industrial scale fluidized bed roasting in terms of the effective gas-solid contact area and the heating rate. However, TG/DTA studies yield valuable information on the chemical reaction routes and the kinetics of gas-solid reactions during roasting due to its ability to precisely control the experimental conditions and to monitor the variables. In this investigation, attempts were made to reveal the reaction sequences during the oxidation of a nickel concentrate by TG/DTA. Gas analyzer was employed to continuously measure the offgas SO_2 and O_2 contents during the TGA runs. X-ray powder diffraction (XRD), scanning electron microscopy (SEM), energy dispersive X-ray spectroscopy (EDS), electron probe microanalysis (EPMA) and inductively coupled plasma optical emission spectroscopy (ICP-OES) were employed to characterize the concentrate and the oxidation products, namely calcines. The rate controlling step in the TGA tests was also investigated.

Many researchers have studied the oxidation of various metal sulfides on a laboratory scale. Studies on the oxidation of nickel, iron, and copper containing sulfide minerals, as well as studies on the thermal decomposition of metal sulfates that could be formed during the roasting of the nickel concentrate, are briefly reviewed in this section.

The oxidation of a natural pentlandite $(Fe,Ni)_9S_8$ was studied by Dunn and Kelly [1] using TG and DTA. In their study, an exothermal event was detected by the DTA at 520 ºC which was claimed to be due to the oxidation of iron sulfide (FeS) forming iron oxide (Fe_2O_3). Another exothermal event at 575 ºC was suggested to be caused by the oxidation of the $Fe_{8\pm x}Ni_{8\pm y}S_{16\pm z}$ phase which forms upon heating the natural pentlandite. Upon reaching 800 ºC, the temperature is in the vicinity of the melting point of the unquenchable compound $Ni_{3\pm x}S_2$, which leads to its accelerated oxidation. This thermal event was also suggested in [2, 3]. And a reaction scheme was deduced, Table 2.1 [1]. The oxidation of synthetic millerite ($Ni_{0.994}S$) was also investigated by Dunn and Kelly [2] with the same apparatuses in a dynamic oxygen atmosphere (0.2 L/min) up to 1000 ºC. Under these conditions, a reaction scheme was proposed and is shown in Table 2.2.

Table 2.1 Various reactions occurring during the oxidation of pentlandite at 10 ºC/min in an air/oxygen flow of 0.2 L/min [1].

<460 ºC	$(Ni,Fe)_{9\pm x}S_{8\pm y} \rightarrow Fe_{8\pm x}Ni_{8\pm y}S_{16\pm z} + NiS + FeS$
460-640	$FeS + 2O_2 \rightarrow FeSO_4$
460-715	$NiS + 2O_2 \rightarrow NiSO_4$
520	$2FeS + 3.5O_2 \rightarrow Fe_2O_3 + 2SO_2$
575	$Fe_{8\pm x}Ni_{8\pm y}S_{16\pm z} + O_2 \rightarrow Ni_2FeO_4 + SO_2 + NiO + Fe_2O_3$
640-760	$2FeSO_4 \rightarrow Fe_2O_3 + (2SO_2 + 0.5O_2)$
	$(Ni,Fe)_{9\pm x}S_{8\pm y} \rightarrow Ni_{3\pm x}S_2 + Fe_{8\pm x}Ni_{8\pm y}S_{16\pm z}$
700-740	$Fe_{8\pm x}Ni_{8\pm y}S_{16\pm z} + O_2 \rightarrow Ni_2FeO_4 + SO_2$
	$NiS + 1.5O_2 \rightarrow NiO + SO_2$
775-805	$Ni_{3\pm x}S_2 \xrightarrow{O_2} NiO + (SO_2 + 0.5O_2)$
>800	$NiSO_4 \rightarrow NiO + (SO_2 + 0.5O_2)$

Table 2.2. Various reactions occurring in the oxidation of $Ni_{0.994}S$ [2].

400-785 ºC	$NiS+2O_2 \rightarrow NiSO_4$
500-785	$NiO+SO_2+0.5O_2 \rightarrow NiSO_4$
540-552 and 682-692	$NiS+1.5O_2 \rightarrow NiO+SO_2$
682-692 and possibly	$3NiS+2NiSO_4 \rightarrow Ni_3S_2+2NiO+3SO_2$
682-692	$10NiS+2O_2 \rightarrow Ni_7S_6+Ni_3S_2+2SO_2$
682-780 and/or	$Ni_7S_6+9.5O_2 \rightarrow 7NiO+6SO_2$
	$Ni_7S_6+12.5O_2 \rightarrow 6NiSO_4+NiO$
793	$Ni_3S_{2(s)} \rightarrow Ni_3S_{2(l)}$
793	$Ni_3S_{2(l)}+3.5O_2 \rightarrow 3NiO+2SO_2$
>800	$NiSO_4 \rightarrow NiO+SO_2+1/2O_2$

Kennedy and Sturman [4] investigated the oxidation of iron(II) sulfide $Fe_{1-x}S$ in air and oxygen atmospheres using TG, DTA, XRD and chemical analysis. A reaction scheme reported in this study is shown in Table 2.3. The rate of oxidation of ferrous sulfide in a tiny bucket was examined by means of a spring balance and X-ray powder diffraction analysis [5]. The bulk of sample in the bucket had a disk-type shape, with several millimeters thickness. By varying the sample sizes, the conclusion was drawn that the rate was controlled by the diffusion of oxygen and/or gaseous products through the bed of the sample.

The oxidation of chalcopyrite was studied by means of TG, DTA, XRD and colorimetry techniques [6]. The results indicate that in the range between 350 ºC and 440 ºC, the sample surface, which had free access to oxygen, was oxidized into iron sulfate, $CuSO_4$ and Fe_2O_3. On the other hand, below the surface where oxygen was relatively starved, bornite (Cu_5FeS_4) could be formed as an inert atmosphere product along with the formation of FeS and elemental sulfur. Between 440 ºC and around 500 ºC these inert atmosphere products were oxidized significantly.

Iron sulfate was fully decomposed at 700 ºC, after which $CuSO_4$ would be decomposed to CuO with the formation of an intermediate compound $CuO \cdot CuSO_4$. In the temperature range between 800 ºC and 850 ºC, CuO, $CuFe_2O_4$ and Fe_3O_4 were the only stable species.

Table 2.3. Reaction scheme for the oxidation of iron sulfide ($Fe_{1-x}S$) [4].

425–520 ºC	$Fe_{1-x}S+(2-x)O_2 \rightarrow (1-x)FeSO_4+xSO_2$
	$3Fe_{1-x}S+(5-2x)O_2 \rightarrow (1-x)Fe_3O_4+3SO_2$
	$4Fe_{1-x}S+(7-3x)O_2 \rightarrow (2-2x)Fe_2O_3+4SO_2$
	$8Fe_{1-x}S+(2-4x)SO_2 \rightarrow (1-2x)Fe_3O_4+(5-2x)FeS_2$
520–572 ºC	$4Fe_{1-x}S+(7-3x)O_2 \rightarrow (2-2x)Fe_2O_3+4SO_2$
575–625 ºC	$FeS_2+3O_2 \rightarrow FeSO_4+SO_2$
	$12FeSO_4+3O_2 \rightarrow 2[Fe_2(SO_4)_3]_2 \cdot Fe_2O_3$
	$4Fe_3O_4+O_2 \rightarrow 6Fe_2O_3$
625–725 ºC	$[Fe_2(SO_4)_3]_2 \cdot Fe_2O_3 \rightarrow 3Fe_2O_3+6SO_3$

Thermal decomposition of nickel (II), copper (II), iron (II and III), and cobalt (II) sulfates have been investigated by many researchers [7-13]. The decomposition temperatures of $Fe_2(SO_4)_3$, $CuSO_4$, $NiSO_4$ and $CoSO_4$ in air were reported to be 575 ºC, 625 ºC, 675 ºC and 720 ºC respectively by TG/DTA [7]. The thermal decomposition process of copper(II) sulfate consisted of two steps, which are shown as Reactions (2.1) and (2.2) [7, 10, 13].

$$2CuSO_4 = CuO \cdot CuSO_4 + SO_3 \quad (2.1)$$

$$CuO \cdot CuSO_4 = 2CuO + SO_3 \quad (2.2)$$

2.2 Experimental

2.2.1 Sample

The nickel concentrate investigated was Raglan concentrate from the Xstrata Sudbury Smelter. The XRD analysis show that it is mainly composed of three minerals, i.e. pentlandite $(Fe,Ni)_9S_8$, chalcopyrite $CuFeS_2$ and pyrrhotite $Fe_{1-x}S$, Figure 2.1. The chemical composition and estimated mineral contents are presented in Table 2.4. Electron Probe Microanalysis (EPMA) was employed to evaluate the stoichiometry of pentlandite, chalcopyrite, pyrrhotite, and pyrite in different individual grains. The results of analysis are exhibited in Table 2.5. Figure 2.2 shows the BSE image of the Raglan concentrate. Most of the sulfide grains in this image with particle size larger than around 3 µm were analyzed by EDS for their mineralogical composition to estimate the relative particle population of these four sulfides. 68 pentlandite grains (56.2%), 20 chalcopyrite grains (16.5%), 32 pyrrhotite grains (26.4%) and 1 pyrite grain (0.8%) were identified in the image. The particle size of Raglan concentrate was determined by means of sieve analysis using a Ro-Tap RX-29 type mechanical sieve shaker. The results of particle size analysis are shown in Table 2.6. Particle size distribution of the material was also obtained using a Laser Particle Size Analyzer (Hydro 2000S, Malvern Instruments) with the results shown in Figure 2.3.

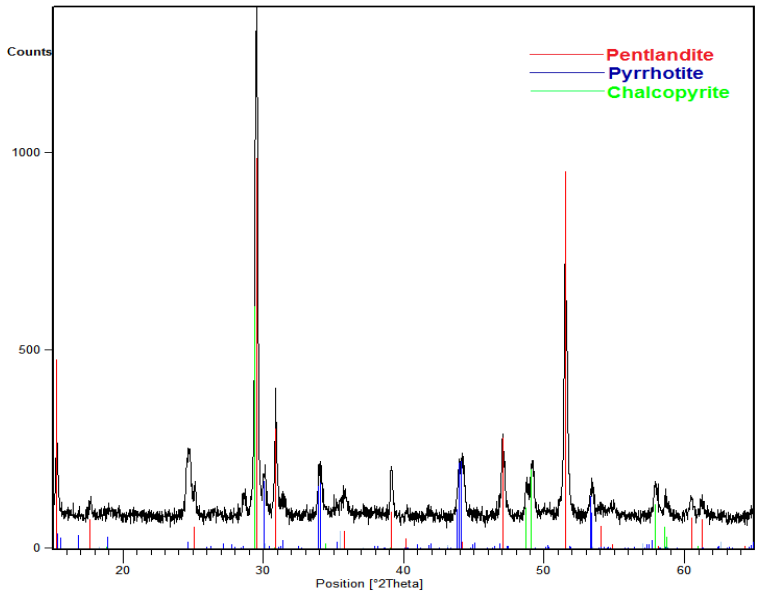

Figure 2.1. XRD pattern for the Raglan concentrate.

Table 2.4. Chemical composition and estimated mineral contents of the Raglan concentrate.

Chemical composition (wt%)		Mineral contents (wt%)	
Ni	17.9	$Fe_{4.5}Ni_{4.5}S_8$	52.3
Fe	30.8	$Fe_{4.5}Co_{4.5}S_8$	1.05
Cu	4.54	Fe_7S_8	15.6
Co	0.36	$CuFeS_2$	13.1
S	27.6	MgO	5.43
MgO	5.43	Al_2O_3	0.76
Al_2O_3	0.76	SiO_2	8.69
SiO_2	8.69	Total	97.0

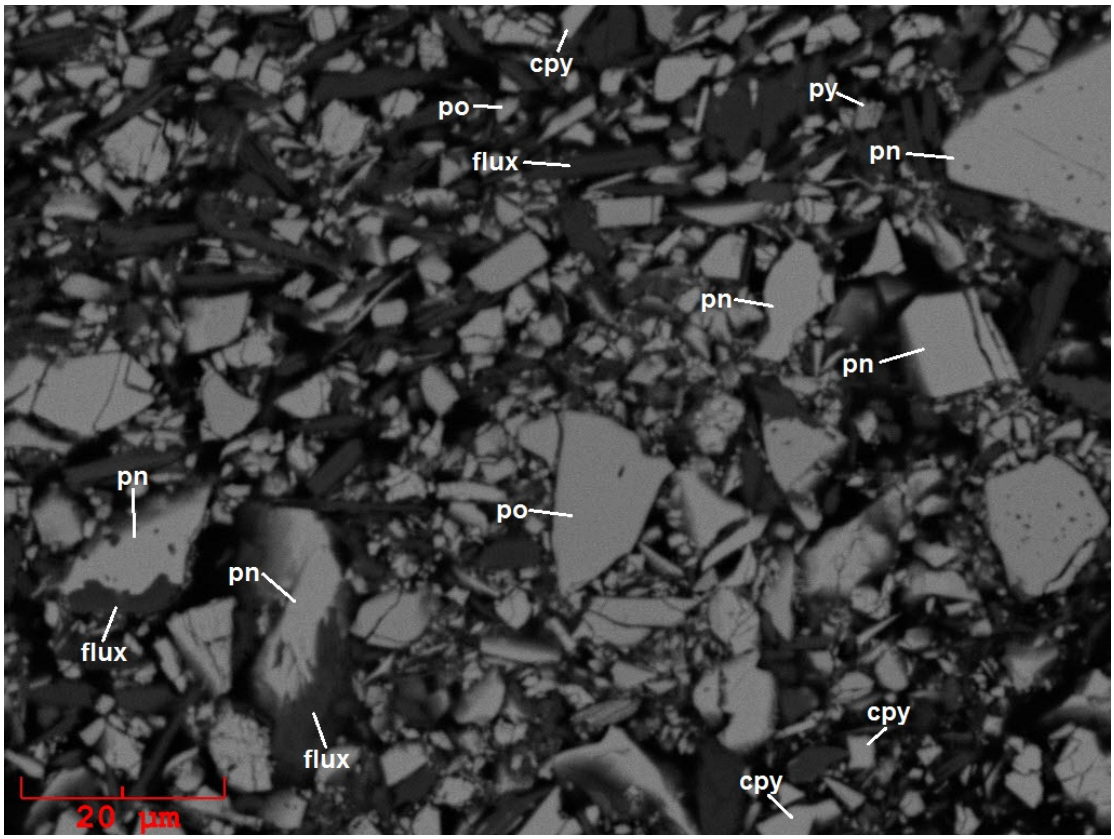

Figure 2.2. BSE image of the Raglan concentrate (pn: pentlandite; cpy: chalcopyrite; po: pyrrhotite; py: pyrite; flux: silicate flux).

Table 2.5. EPMA compositional analysis of individual grains of the Raglan concentrate and their calculated stoichiometry, which shows the composition difference between particles of the same mineral.

Raglan concentrate		Composition (wt%)						Stoichiometry				
Minerals	Grain #	Fe	Ni	Cu	Co	S	Total	Fe	Ni	Cu	Co	S
Pentlandite $(Fe,Ni)_9S_8$	1	27.8	36.8	0.058	0.609	34.2	99.5	3.73	4.70	0.0069	0.0775	8
	2	32.1	33.7	0.050	0.657	33.0	99.5	4.47	4.47	0.0062	0.0867	8
	3	31.3	35.1	0.063	0.346	33.6	100.4	4.29	4.57	0.0075	0.0449	8
	4	31.2	34.5	0.051	0.575	33.0	99.3	4.34	4.57	0.0062	0.0758	8
	5	30.3	35.7	0.022	0.633	33.2	99.9	4.19	4.70	0.0026	0.0829	8
	6	31.3	34.7	0.040	0.366	32.9	99.3	4.38	4.61	0.0049	0.0485	8
	7	30.5	35.2	0.121	0.455	33.1	99.4	4.24	4.65	0.0148	0.0598	8
	8	31.8	34.3	0.010	0.575	33.0	99.7	4.43	4.54	0.0012	0.0759	8
	9	31.2	35.0	0.033	0.460	32.9	99.7	4.36	4.65	0.0041	0.0608	8
	10	31.0	35.2	0.033	0.624	33.2	100.0	4.29	4.63	0.0040	0.0818	8
Chalcopyrite $CuFeS_2$	11	30.8	0.247	34.0	0.000	34.8	99.8	1.02	0.0077	0.986	0.0000	2
	12	30.5	0.164	34.2	0.000	35.2	100.0	0.994	0.0051	0.979	0.0000	2
	13	30.5	0.123	34.1	0.000	35.0	99.7	1.00	0.0038	0.986	0.0000	2
	14	30.6	0.216	34.0	0.000	34.9	99.6	1.01	0.0068	0.985	0.0000	2
Pyrrhotite $Fe_{1-x}S$	15	59.6	0.342	0.035	0.000	39.7	99.6	0.862	0.0047	0.0004	0.0000	1
	16	59.2	0.693	0.004	0.000	39.4	99.3	0.862	0.0096	0.0001	0.0000	1
	17	59.5	0.792	0.142	0.000	38.8	99.2	0.879	0.0111	0.0019	0.0000	1
	18	59.9	0.824	0.080	0.000	38.7	99.5	0.888	0.0116	0.0010	0.0000	1
	19	59.7	0.646	0.054	0.000	38.7	99.1	0.887	0.0091	0.0007	0.0000	1
	20	59.4	0.352	0.087	0.000	39.4	99.2	0.865	0.0049	0.0011	0.0000	1
Pyrite FeS_2	21	45.3	0.183	1.69	0.168	53.8	101.1	0.966	0.0037	0.0316	0.0034	2
	22	45.0	0.284	0.096	0.896	54.3	100.5	0.951	0.0057	0.0018	0.0180	2
	23	46.2	0.084	0.000	0.789	53.4	100.5	0.994	0.0017	0.0000	0.0161	2
	24	44.5	0.111	0.067	2.25	53.2	100.2	0.960	0.0023	0.0013	0.0459	2
	25	45.7	0.139	0.041	1.31	53.1	100.2	0.987	0.0029	0.0008	0.0268	2
	26	44.2	0.101	0.080	1.90	53.1	99.3	0.956	0.0021	0.0015	0.0390	2

Table 2.6. Particle size analysis of Raglan concentrate by sieving.

Sieve	Weight % Passing
106 µm	99.4
75 µm	93.3
53 µm	82.3
38 µm	76.7

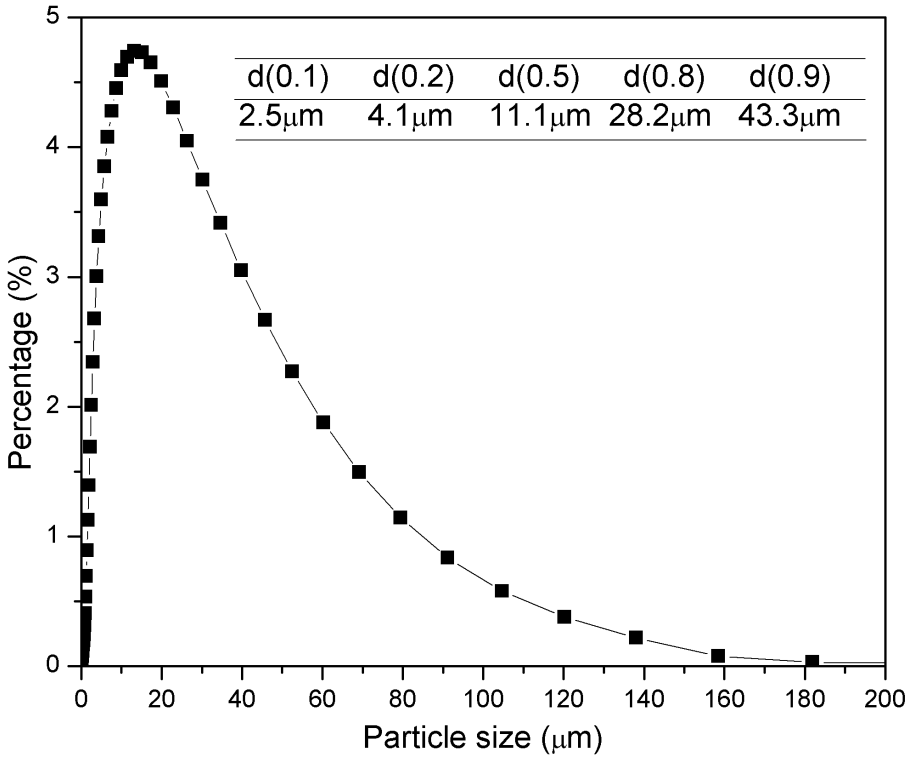

Figure 2.3. Particle size distribution of the Raglan concentrate.

2.2.2 TG/DTA Study

All the oxidation tests were conducted in a Setaram TG-DTA 92 unit (SETARAM Inc, Newark, CA). The experimental setup of its TGA mode is shown schematically in Figure 2.4. Uncertainty analysis of the experimental measurements using this unit was firstly performed. TGA measurements give an uncertainty limit of ±0.041 mg with 95% confidence level based on the repeated experiments, which are the thermal decomposition of $CuSO_4 \cdot 5H_2O$ in air at 15 ºC/min heating to 1300 ºC. One of the repeated tests is shown in Figure 2.5, illustrating the stepwise decomposition of the $CuSO_4 \cdot 5H_2O$. DTA analysis has an uncertainty limit of ±1.0 ºC with 95% confidence level by repeatedly measuring the melting temperature of 99.999% pure silver, which is shown in Figure 2.6. For TGA runs, Raglan concentrate of 100 mg was put in an alumina crucible (I.D. 7.20 mm, Depth 5.39 mm). The crucible was suspended from the microbalance on top of the TGA unit by platinum wires. The temperature profile was set prior to each run. During each run, the atmosphere was controlled by introducing either extra dried air,

O_2, or argon gas into the TGA chamber from the top, with the gas flowrate being adjusted by a rotameter (OMEGA FL-3402C). The flowrate of the offgas was measured by a digital flowmeter (OMEGA FMA-5610). The offgas was analyzed continuously by a two-channel gas analyzer (ABB EL3020) for its SO_2 and O_2 contents. A computer controlled data acquisition system (FLUKE Hydra Series II) was used to record the data from both the gas analyzer and the digital gas flowmeter. Most of the samples were air-quenched by lifting the crucible out of the TGA chamber once the heating was completed. The TG-DTA unit setting was switched to DTA mode for DTA runs, which was done by replacing the platinum wires with a DTA rod and plugging necessary connections for the DTA thermocouples. Raglan concentrate of 30 mg was put in an alumina crucible (I.D. 4.08 mm, Depth 8.07 mm) which was then mounted on the DTA rod. Calcined alumina powder of 30 mg was put in the other crucible as a reference.

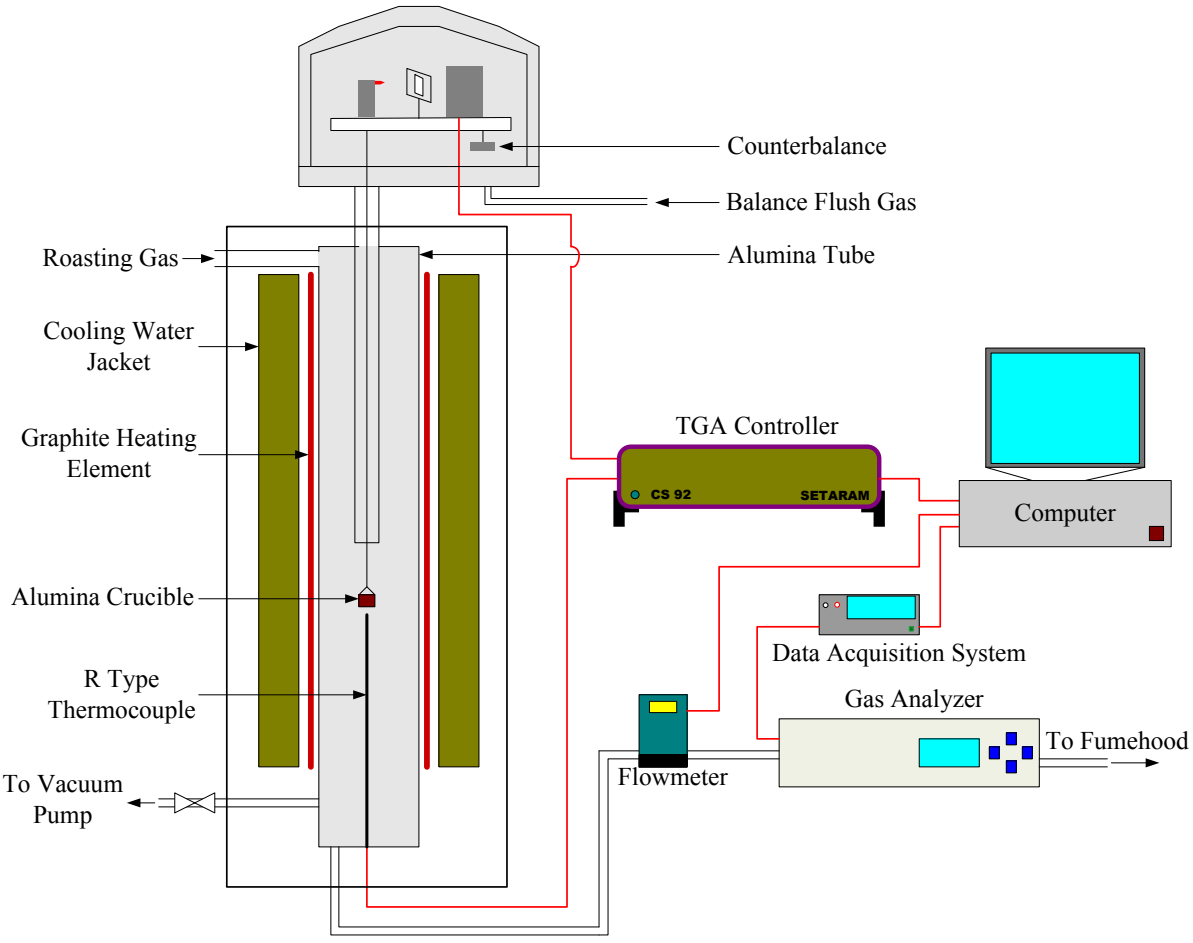

Figure 2.4. Schematic of the TG-DTA unit (TGA mode).

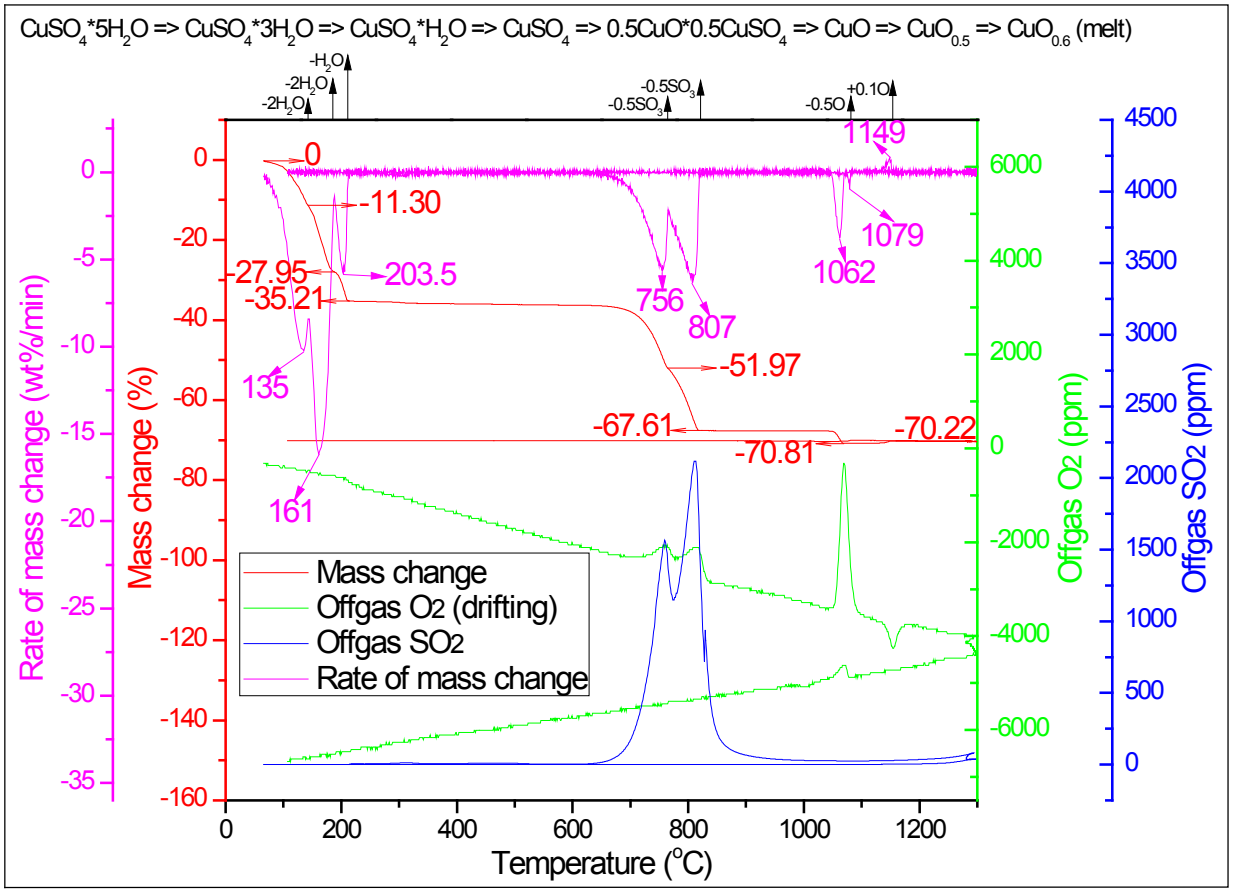

Figure 2.5. Stepwise decomposition of $CuSO_4 \cdot 5H_2O$ in air by TGA.

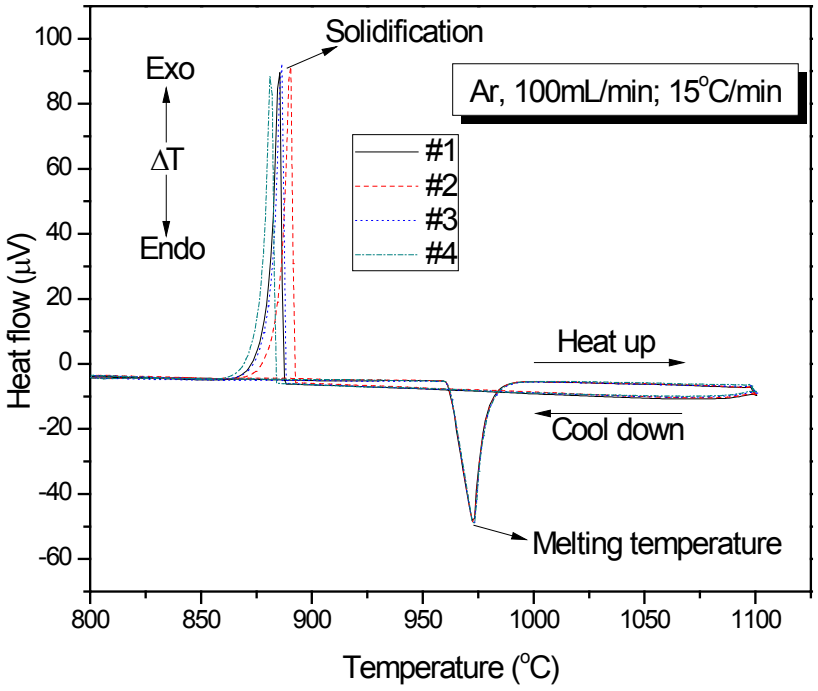

Figure 2.6. Repeated tests for the determination of the melting temperature of Ag by DTA.

2.2.3 Analytical Methods

XRD - Quenched samples were subjected to XRD analysis for qualitative mineral composition. The X-ray patterns were obtained using a Philips PW2273/20 diffractometer covering 15º to 65º in terms of 2θ angle using Cu-K_α radiation. Due to the limited amount of sample available, a single crystalline silica slide was used as the sample holder. The sample powder was mixed with acetone to make a slurry that was spread onto the silica slide.

SEM/EDS – The sample powders were mounted in an epoxy resin. After the epoxy was cured, the surface was ground with silicon carbide papers with abrasive sizes of 180, 400, 600, 800, and 1200 sequentially. Final surface preparation was made on a polishing pad with water based 0.3 μm alumina suspension as the polishing media. For samples which contain water soluble sulfate species, oil based 1μm diamond suspension was used instead. The surface was then coated with carbon to render it electrically conductive. The SEM used is a JEOL, JSM-840, complemented by a PGT/AAT EDS detector (thin window) and an IXRF 500 digital pulse

processor, allowing both X-ray microanalysis and digital imaging, via SE, BSE and X-ray signals.

EPMA - Compositional analyses were acquired on a Cameca SX50 electron probe x-ray microanalyzer equipped with 3 tunable wavelength dispersive spectrometers. Operating conditions were 40 degrees takeoff angle, and a beam energy of 20 keV. The beam current was 20 nA, and the beam diameter was 1 μm. Elements were acquired using analyzing crystals LiF for Fe Kα, Ni Kα, Cu Kα, Co Kα, PET for S Kα, and PC1 for O Kα. The standards were hematite for O Kα, cobaltite for Co Kα, pentlandite for S Kα, Fe Kα, Ni Kα, and chalcopyrite for Cu Kα. The counting time was 20 seconds for Fe Kα, Ni Kα, Cu Kα, S Kα, 40 seconds for O Kα, and 60 seconds for Co Kα.

ICP-OES – Air-quenched samples of around 60 mg were water-leached at 90 ºC for 30 minutes. Leachates were analyzed using ICP-OES (PerkinElmer Optima 7200 DV) for Fe, Ni, Cu, Co, S, Mg, Al, and Si contents.

2.3 Results and Discussion

Figure 2.7 displays the sample mass change, the rate of mass change, SO_2 concentration and O_2 consumption in the offgas for the TGA run in which 100 mg of Raglan concentrate was heated in a 1 L/min air stream from room temperature to 950 ºC at 15 ºC/min. The DTA curve for the oxidation of 30 mg Raglan concentrate under the same experimental conditions is shown in Figure 2.8. In order to evaluate the effects of oxygen partial pressure change on the possible thermal events, a DTA run was also conducted in pure oxygen atmosphere for comparison, its results being illustrated in Figure 2.9. Due to the geometrical difference of the crucibles used in the TGA and DTA runs, the TGA and DTA curves may not necessarily correlate well with each other. The powder nature of the sample tends to delay heat transfer and leads to a drift of temperature range in which a specific thermal event occurs. As a result, the combined effect of the powder sample size and the geometry of the sample which is dictated by the geometry of the crucible should also contribute to the discrepancy between TGA and DTA results. Samples air-quenched from intermediate temperatures in the TGA runs were analyzed by XRD for their

mineralogical compositions. Their XRD patterns are provided in Figure 2.10. Due to the complex nature of the system, assignments of some of the peaks were only tentatively suggested. Results of the wet chemical analysis of the quenched samples by hot water leaching and ICP is illustrated in Figure 2.11 as the percentages of water soluble sulfates calculated on the basis of the content of each element in the calcines. In order to better understand the oxidation mechanism of pentlandite in the concentrate, EPMA was applied to investigate the chemical composition change of the pentlandite sulfide cores during the dynamic heating period. The results are plotted in the Fe-Ni-S ternary diagram as shown in Figure 2.12.

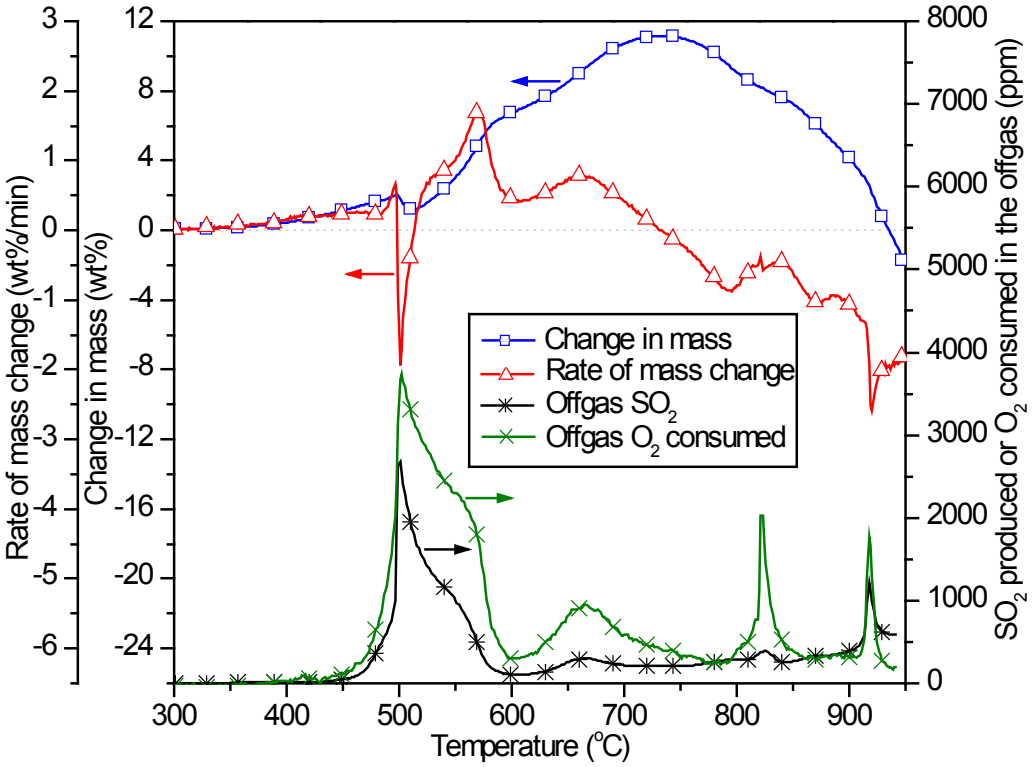

Figure 2.7 Sample mass change, rate of mass change, SO_2 concentration and O_2 consumption in the offgas for the TGA run in which 100 mg concentrate was heated to 950 ºC at 15 ºC/min in air.

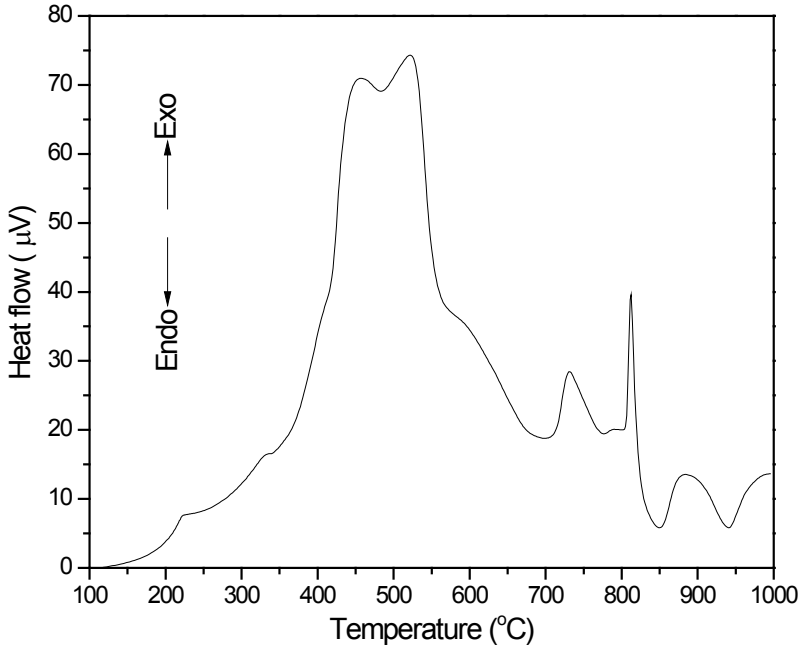

Figure 2.8. DTA curve of Raglan concentrate heated at 15 ºC/min in air.

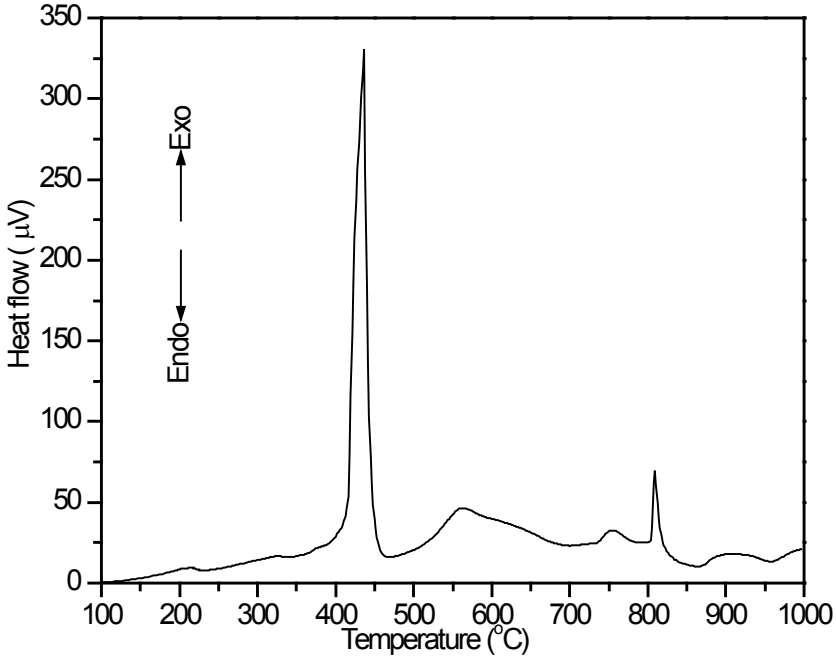

Figure 2.9. DTA curve of Raglan concentrate heated at 15 ºC/min in O_2.

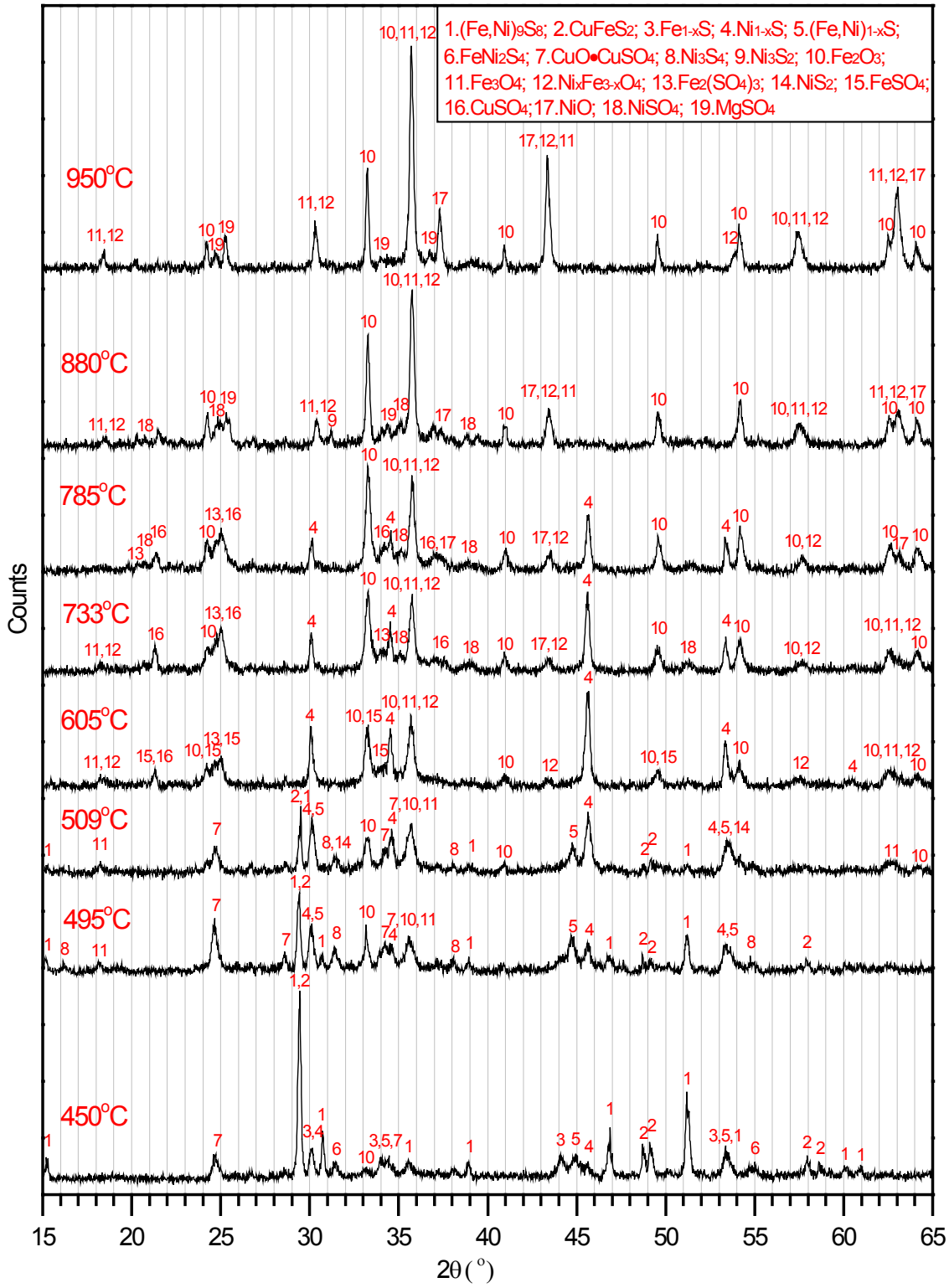

Figure 2.10. XRD patterns for calcines quenched from intermediate temperatures after heating at 15 ºC/min in air in TGA runs.

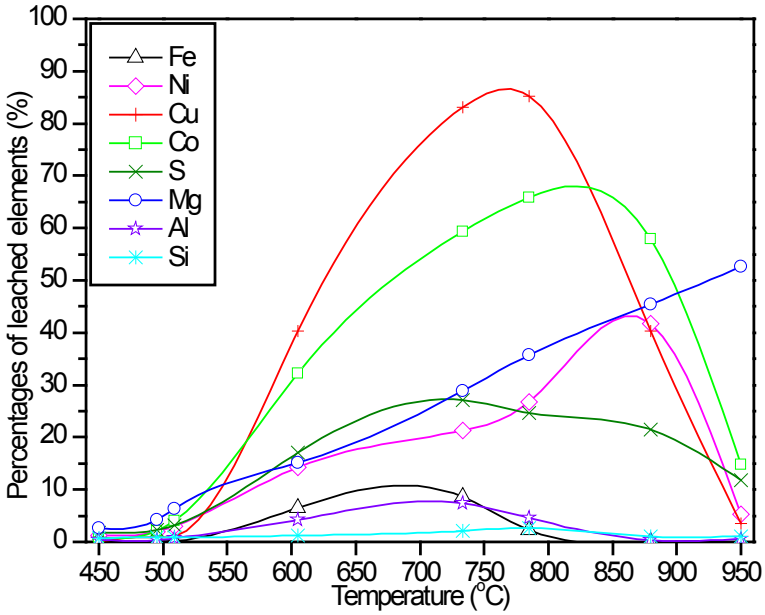

Figure 2.11. Chemical analysis results for the contents of the water soluble sulfates in the calcines quenched from intermediate temperatures after heating at 15 ºC/min in air in TGA runs.

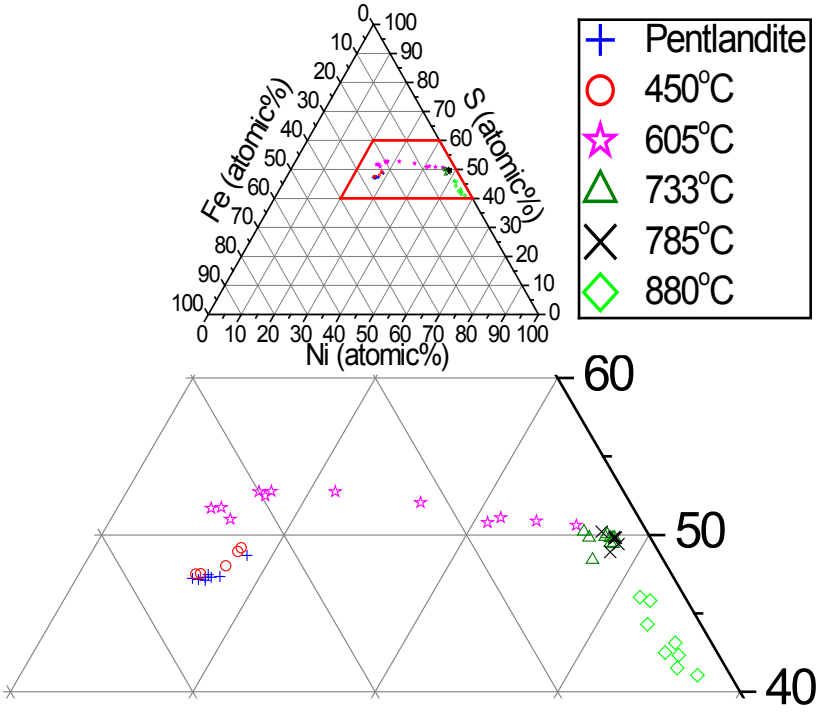

Figure 2.12. Fe-Ni-S diagram showing the change of chemical compositions during non-isothermal heating in TGA runs analyzed by EPMA. The bottom part is the magnified area of the trapezoid in the top ternary diagram.

Mass changes are barely seen below 350 ºC from Figure 2.7. Afterwards, there is a gradual increase in mass till 498 ºC, where the mass reaches a small peak and starts to decrease. Correspondingly, O_2 in the feeding gas was consumed intensively and SO_2 was emitted, which is denoted by the intensive SO_2 and O_2 peaks in Figure 2.7, indicating the occurrence of vigorous oxidation reactions. This is further confirmed by two partly overlapped exotherms in the vicinity of 500 ºC in Figure 2.8, indicating the presence of at least two exothermic reactions leading to the mass change and SO_2 emission. These two reactions were greatly promoted by increasing the oxygen partial pressure shown as a much stronger single peak at 437 ºC in Figure 2.9, which confirms the oxygen involvement in these two exotherms. The mass change between 450 ºC and 509 ºC in Figure 2.7 is mainly due to two competing reactions, which are the oxidation of chalcopyrite forming $CuO{\cdot}CuSO_4$ and the oxidation of pyrrhotite forming Fe_2O_3. These two reactions are expressed as Reaction (2.3) and Reaction (2.4), the former leading to the mass gain while the latter leading to the mass loss. Reaction (2.3) dominates below 498 ºC, causing an increase in the mass while the mass loss above 498 ºC is primarily due to Reaction (2.4).

$$2CuFeS_2+7O_2\rightarrow CuO{\cdot}CuSO_4+Fe_2O_3+3SO_2 \quad (2.3)$$

$$2Fe_{1-x}S+(3.5-1.5x)O_2\rightarrow(1-x)Fe_2O_3+2SO_2 \quad (2.4)$$

The evidence to Reaction (2.3) is the XRD patterns, showing the dramatic reaction of chalcopyrite and the formation of Fe_2O_3 and $CuO{\cdot}CuSO_4$ between 450 ºC and 509 ºC. The assignment of Reaction (2.4) is based on the fact that pyrrhotite disappeared between 450 ºC and 509 ºC and that a substantial amount of Fe_2O_3 was formed at 509 ºC, as suggested by the XRD patterns in Figure 2.10. Dunn and Kelly [1] observed the same reaction at 520 ºC. This disagreement of temperature under which the oxidation of $Fe_{1-x}S$ occurs is partly caused by the difference between the experimental conditions employed in the two studies. Another factor that may contribute to the disagreement is the difference in the samples being studied. Since their sample is a natural pentlandite, there would be no $Fe_{1-x}S$ unless it is formed from the decomposition of pentlandite. While the sample in this study is a concentrate containing not only pentlandite, but also around 16 wt% pyrrhotite, 13 wt% chalcopyrite and some siliceous gangue. Figure 2.13, Figure 2.14, and Figure 2.15 illustrate the morphological features of the

oxidized pyrrhotite air-quenched from 605 ºC, 733 ºC and 880 ºC, respectively. Reaction (2.4) would result in the volume reduction of 24% (calculated based on the densities of Fe_2O_3 and Fe_3O_4). From this, one would expect a porous micro-structure of the oxidized pyrrhotite particles. However, the pyrrhotite particle seems to be rather dense in Figure 2.13. It became porous after heating to higher temperatures as shown in Figure 2.14 and Figure 2.15. We resort to the Fe-S-O predominance diagram to help understand the change of micro-structure as a function of temperature. Figure 1.7 is the Fe-S-O predominance diagram at 500 ºC, 700 ºC and 900 ºC calculated using HSC Chemistry [14]. The pyrrhotite particles experienced an oxidative atmosphere with the O_2 partial pressure of approximately 0.21 atm at the beginning of oxidation. The propagation of the oxidation reaction as Reaction (2.4) in the bulk of the sample bed consumed O_2 from the local gas environment and released SO_2, which in turn lead to a drop in the partial pressure of O_2 and an increase in the partial pressure of SO_2. Once the partial pressure of SO_2 exceeded 10^{-5} atm, the gas environment in the bulk of sample bed would favor the formation of $Fe_2(SO_4)_3$ at 500 ºC. Indeed around 2.5 wt% S was detected in the oxidized pyrrhotite particle in Figure 2.13 by EDS. This is indicative of the presence of $Fe_2(SO_4)_3$ which is disseminated in Fe_2O_3. The formation of $Fe_2(SO_4)_3$ alone from pyrrhotite would result in a volume increase by 223%. It is thus easy to imagine that even a small fraction of $Fe_2(SO_4)_3$ would offset the volume reduction caused by the formation of Fe_2O_3. This formation of $Fe_2(SO_4)_3$ along with Fe_2O_3 resulted in the rather dense nature of the oxidized pyrrhotite at relatively low temperature as seen in Figure 2.13. The formation of $Fe_2(SO_4)_3$ became more difficult with the increase of temperature indicated by the shrinkage of the predominant area for $Fe_2(SO_4)_3$ in Figure 1.7 as temperature increases. The particles became porous at higher temperature as can be seen in Figure 2.14 and Figure 2.15 since $Fe_2(SO_4)_3$ is no longer stable. This characteristic columnar reaction interface with distinct orientations in these two figures was reported to be due to the inward preferential oxidation along certain crystallographic plains [15, 16].

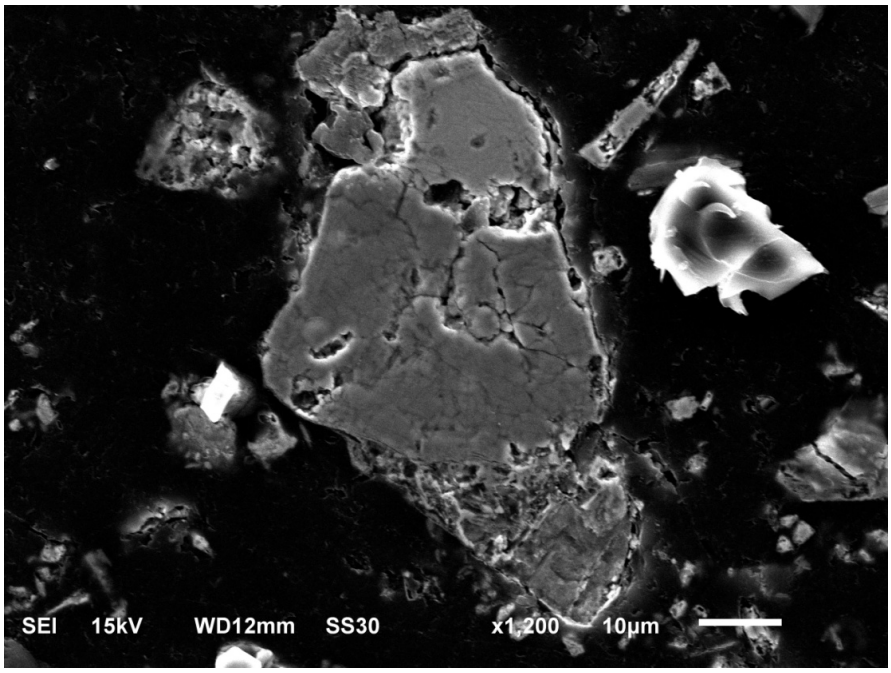

Figure 2.13. SE image of an oxidized pyrrhotite particle quenched from 605 ºC in the TGA run.

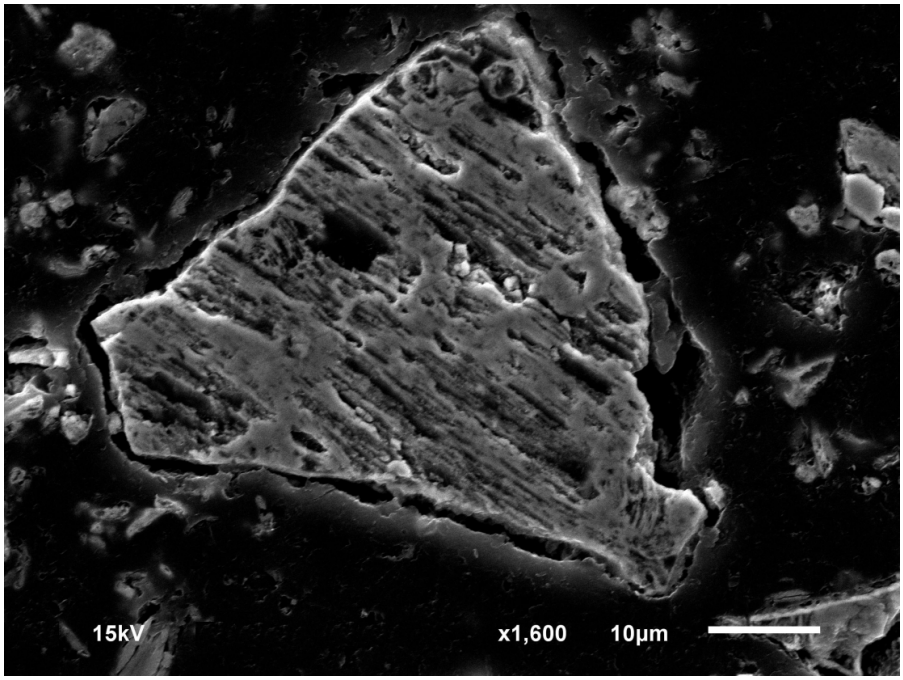

Figure 2.14. SE image of an oxidized pyrrhotite particle quenched from 733 ºC in the TGA run showing its characteristic columnar structure.

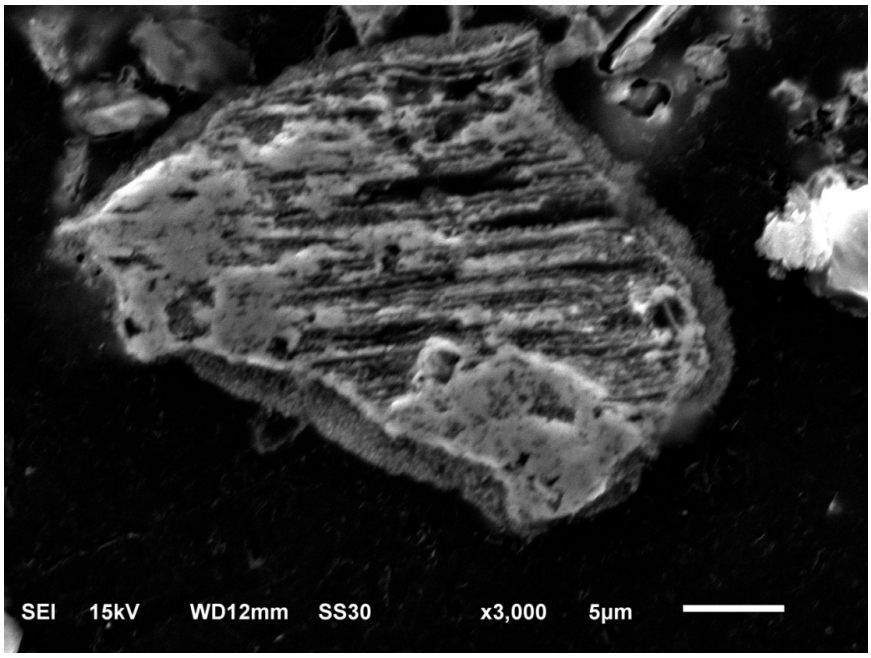

Figure 2.15. SE image of an oxidized pyrrhotite particle quenched from 880 ºC in the TGA run.

Below 495 ºC, very little sulfates were formed, illustrated by the profiles in Figure 2.11. But an increase in the content of water-insoluble $CuO{\cdot}CuSO_4$ is shown in the XRD patterns till 495 ºC. Decomposition of chalcopyrite would result in the formation of bornite (Fe_5CuS_4), as indicated by previous studies [6, 16]. This phase was not detected by XRD in any of the quenched samples in this study, probably because the content of this phase was too low to be identified by XRD. However, bornite was identified by SEM/EDS. As illustrated in the backscattered electron (BSE) image of Figure 2.16, bornite formed around the chalcopyrite core with a clear boundary between them. The porous surface layer is Fe_2O_3 formed by the preferential oxidation of iron species from chalcopyrite. The intensity of the peaks for $CuO{\cdot}CuSO_4$ decreased after 495 ºC, meaning its content was decreasing as the heating proceeded. While at the same time, the content of $CuSO_4$ started to increase. This suggests that $CuO{\cdot}CuSO_4$ is a precursor for the formation of $CuSO_4$, which has also been reported by other researchers [17].

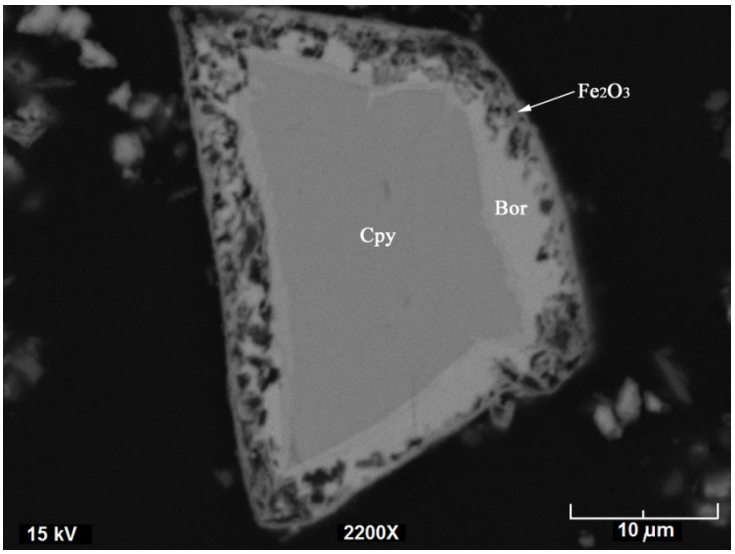

Figure 2.16. BSE image of a chalcopyrite particle after heating the Raglan concentrate in air at 450 ºC for 1 hour (Cpy: chalcopyrite, $CuFeS_2$; Bor: bornite, Cu_5FeS_4).

Another reaction possibly has occurred up to 605 ºC based on the XRD patterns. The consumption of pentlandite and formation of monosulfide solid solution (Mss), $Ni_{1-x}S$, and Fe_2O_3 are obvious and illustrated by the XRD patterns at 450 ºC, 495 ºC and 509 ºC in Figure 2.10. As a result, this reaction is suggested to be the oxidation of pentlandite forming $(Ni,Fe)_{1-x}S$, $Ni_{1-x}S$, and Fe_2O_3 with the assignment of Reaction (2.5). SO_2 produced from Reaction (2.5) and the O_2 in the feeding gas provide suitable atmosphere for sulfate formation, which is revealed by the massive metal sulfate formation between 509 ºC and 605 ºC in Figure 2.11. This, as a result, gives rise to an accelerating mass increase, indicated by the peak in the rate of mass change curve in Figure 2.7, corresponding to the right uplifting shoulders of the offgas curves. $(Ni,Fe)_{1-x}S$ in Reaction (2.5) represents the non-stoichiometric iron nickel sulfide, Mss with hexagonal pyrrhotite structure [18]. Apart from the XRD observation, some other evidence also supports the occurrence of Reaction (2.5). Firstly, Raglan concentrate was heated in argon at 450 ºC for 1 hour and was quickly cooled down to room temperature with $(Ni,Fe)_{1-x}S$, $Ni_{1-x}S$ and $Fe_{1-x}S$ found in the product. Dunn and Kelly [1] also found $(Fe,Ni)_{1-x}S$, NiS and FeS as the decomposition product of pentlandite in a dynamic oxygen atmosphere below 460 ºC. Secondly, Raglan concentrate was oxidized isothermally at 450 ºC for 1 hour and its product was examined under microscope, a thin layer of iron oxide was found to have formed on the surface of the pentlandite particle, with its core being converted to Mss. This suggests iron cations in

pentlandite are oxidized preferentially via outward diffusion mechanism. Preferential oxidation of iron species from pentlandite has been studied by many researchers and is well recognized [15, 16, 19, 20]. Iron cations tend to migrate out from the pentlandite particles towards the oxygen/oxide interface close to the surface of the particles where they combine with O_2 forming Fe_2O_3.

$$(Ni,Fe)_9S_8+O_2\rightarrow(Ni,Fe)_{1-x}S+Ni_{1-x}S+Fe_2O_3+SO_2 \quad (2.5)$$

Violarite solid solution $(Ni,Fe)_3S_4$ was also formed in the TGA samples quenched from 450 ºC, 495 ºC and 509 ºC, which is denoted by two stoichiometric forms $FeNi_2S_4$ and Ni_3S_4. Although $(Ni,Fe)_3S_4$ was reported to be stable only below 461±3 ºC in the presence of an equilibrium sulfur vapor [21], the dynamic heating conditions applied in the present study sustained its presence up to 509 ºC. In nature, violarite is often intimately associated with pentlandite. Violarite forms readily from pentlandite because the pentlandite structure can be easily converted to that of violarite with a minimum reorganization, by removal of excess metal atoms and redistribution of the remainder [22]. Based on this, violarite in the present study is considered to be produced by the transformation of pentlandite. The removal of the excess Fe atoms was accelerated by the oxidizing condition forming Fe_2O_3 as a by-product. The transformation reaction is represented as Reaction (2.6). This reaction coincides with the mild mass increase and no significant SO_2 release up to 500 ºC. Thermal decomposition of violarite occurred above 509 ºC as indicated by the XRD results showing the disappearance of its peaks at 605 ºC. Dunn and Howes [23] studied the oxidation of violarite and reported that its decomposition in the oxidizing atmosphere leads to the formation of Mss and SO_2 in the temperature range 405–475 ºC. As Mss was also formed in the present study and significant SO_2 release was occurring above 509 ºC, Reaction (2.7) is tentatively suggested.

$$(Ni,Fe)_9S_8 + O_2 \rightarrow (Ni,Fe)_3S_4 + Fe_2O_3 \quad (2.6)$$

$$(Ni,Fe)_3S_4 + O_2 \rightarrow (Ni,Fe)_{1-x}S + SO_2 \quad (2.7)$$

The following thermal event is indicated by the spiking shoulder of the DTA curve from 550 ºC to 690 ºC in Figure 2.8, corresponding to the wide peaks in the rate of mass change curve and offgas curves at 660 ºC. In Figure 2.9, this exotherm is shown as a wide peak from 468 ºC to

700 ºC peaking at 562 ºC. This reaction can be deduced based on the XRD patterns in Figure 2.10 along with the change in composition of the pentlandite sulfide cores in Figure 2.12. Although no Mss at 605 ºC was detected by XRD (Figure 2.10), its presence was confirmed by EPMA in Figure 2.12. At 650 ºC, the points correspond to the sulfur-excess compound of $(Fe,Ni)_{1-x}S$ with various Fe:Ni ratios. There was a relationship between the Fe:Ni ratios and the size of the particles analyzed, which was that a smaller particle tended to have a lower Fe/Ni ratio. This is expected because in a smaller particle which has a larger surface to volume ratio, the average path for the Fe^{2+} ion to diffuse out of the sulfide core and be preferentially oxidized was shorter, which means a shorter time was needed for the depletion of Fe^{2+} ion from the sulfide core. This phenomenon also suggests that smaller particles usually have higher oxidation rates, provided other conditions remain unchanged. At 733 ºC, all the pentlandite sulfide cores were transformed into $Ni_{1-x}S$ containing around 2.5 atm% Fe whose percentages reached a minimum and did not go any lower with the increase of temperature. XRD patterns also show the increasing contents of $Ni_{1-x}S$ and Fe_2O_3, as well as the full consumption of the intermediate product Mss from 495 ºC to 733 ºC. All of these suggest that this thermal event is the oxidation of Mss forming $Ni_{1-x}S$ and Fe_2O_3, represented by Reaction (2.8). The mechanism behind this reaction is also the preferential oxidation of iron species from Mss via diffusion, forming an iron oxide shell and a nickel sulfide core in each pentlandite grain. Figure 2.17 is a BSE image of a pentlandite particle quenched from 733 ºC showing its particular structure of a nickel sulfide core surrounded by a porous layer of iron oxide. EDS analysis indicated the iron sulfates were disseminated in the iron oxide. There is a discrepancy in the temperature range in which Reaction (2.8) occurs in the TGA and DTA modes, which is probably caused by the geometrical difference of the crucibles used in these two modes, as well as a larger sample size used in the TGA mode.

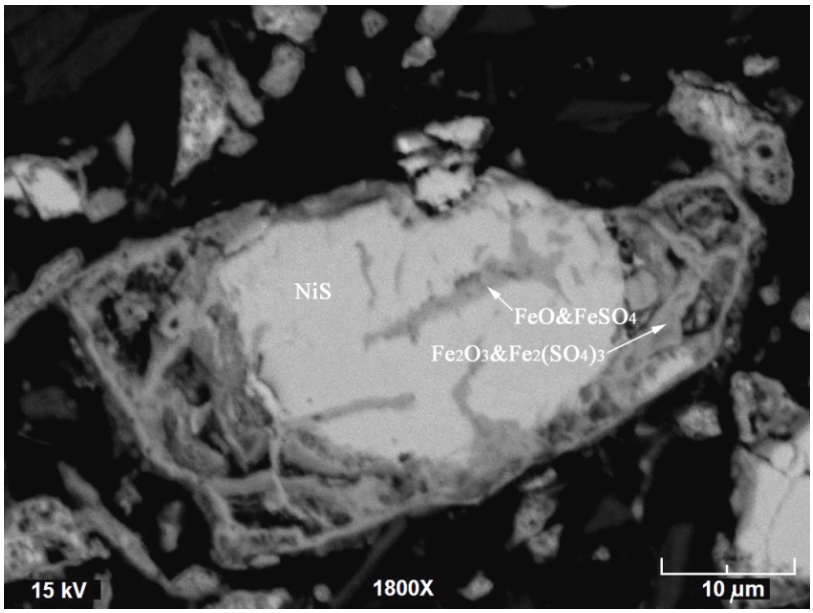

Figure 2.17. BSE image of a partly oxidized pentlandite particle air-quenched from 733 ºC in the TGA run.

$$(Ni,Fe)_{1-x}S+O_2 \rightarrow Ni_{1-x}S+Fe_2O_3+SO_2 \quad (2.8)$$

Previously formed $Ni_{1-x}S$ was further oxidized giving rise to another exotherm peaking at 731 ºC in Figure 2.8. Quenched samples from 695 ºC and 785 ºC in the DTA runs were analyzed by XRD to evaluate this exotherm, with their XRD patterns shown in Figure 2.18. The disappearance of $Ni_{1-x}S$ and formation of heazlewoodite (Ni_3S_2) can be clearly seen on the basis of these two XRD patterns. The formation of Ni_3S_2 is indicative of the unquenchable compound $Ni_{3\pm x}S_2$, which was suggested by Dunn and Kelly [1], and was further confirmed in this study using SEM/EDS. As a result, this exotherm is suggested to be the oxidation of $Ni_{1-x}S$ forming $Ni_{3\pm x}S_2$, represented by Reaction (2.9). The temperature discrepancy between TGA and DTA runs can be observed by comparison between the XRD patterns for TGA runs in Figure 2.10 and those for DTA runs in Figure 2.18. The XRD patterns for 695 ºC in the DTA mode fit well with that for 733 ºC in the TGA mode. The formation of Ni_3S_2 is only observed in the TGA sample quenched from 880 ºC, which resemble the DTA sample quenched from 785 ºC. Due to this temperature discrepancy, Reaction (2.9) did not occur by 785 ºC in the TGA mode, which can be seen from the TGA curves and XRD results in Figure 2.7 and Figure 2.10, respectively.

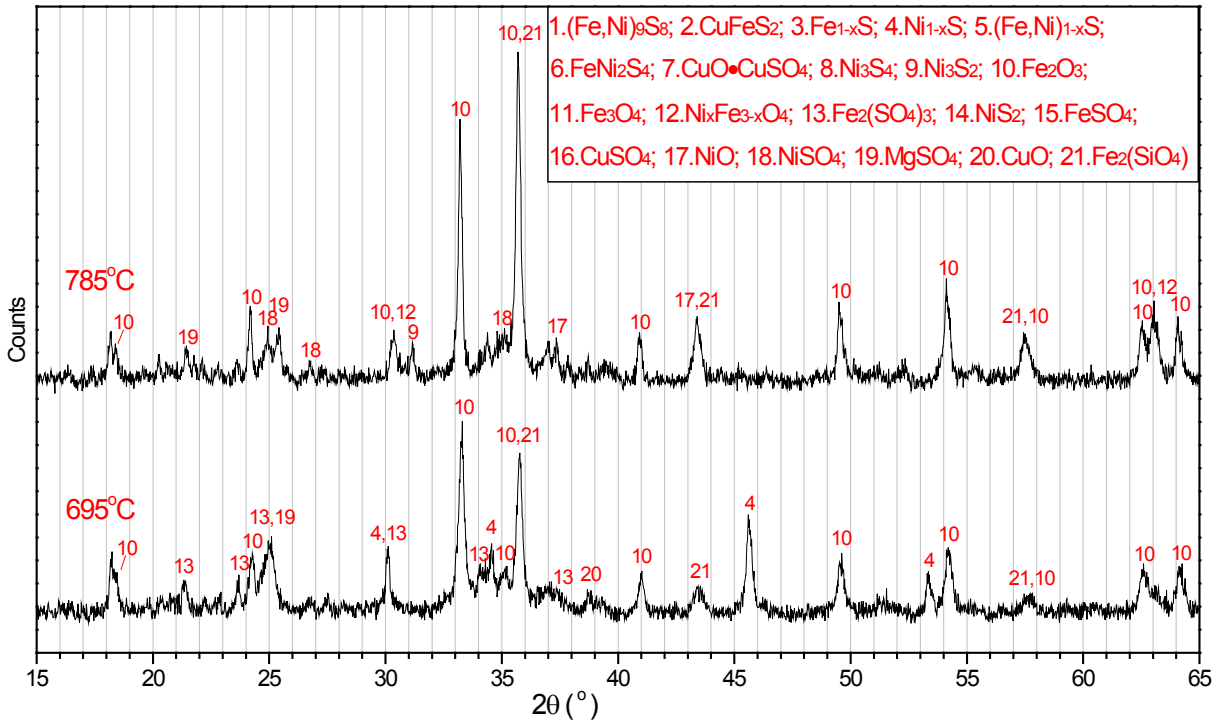

Figure 2.18. XRD patterns for calcines quenched from intermediate temperatures after heating at 15 ºC/min in air in DTA runs.

$$(3\pm y)Ni_{1-x}S+(1+2x\pm y)O_2\rightarrow(1-x)Ni_{3\pm y}S_2+(1+2x\pm y)SO_2 \quad (2.9)$$

The next thermal event appears as a sharp peak at 813 ºC in the DTA curve in Figure 2.8, corresponding to a large O_2 consumption peak at 822 ºC in Figure 2.7. This exotherm is believed to be the oxidation of $Ni_{3\pm x}S_2$ which has an incongruent melting point in the vicinity of 800 ºC. Ion diffusion in the sulfide was greatly increased after $Ni_{3\pm x}S_2$ melted, resulting in the accelerated oxidation reaction rate. This exotherm was also reported by others [1, 2]. Along with NiO, a substantial amount of $NiSO_4$ was also formed in this exotherm, which can be clearly seen in the XRD pattern at 880 ºC in Figure 2.10 and its chemical analysis results in Figure 2.11. The very weak emission of SO_2 at 822 ºC in Figure 2.7 compared with its corresponding intensive O_2 consumption peak also indirectly suggests the occurrence of sulfation rather than SO_2 formation. As a result, this exotherm is tentatively suggested as Reaction (2.10).

$$Ni_{3\pm x}S_{2(s)}\rightarrow Ni_{3\pm x}S_{2(l)}, \text{ and } Ni_{3\pm x}S_{2(l)}+O_2\rightarrow NiO+NiSO_4+SO_2 \quad (2.10)$$

Figure 2.19 and Figure 2.20 are BSE images of two partly oxidized pentlandite particles air-quenched from 880 ºC, showing their morphological features. It comprises of complex layers of iron oxides and a nickel sulfide core. It is difficult to determine the stoichiometry of the iron oxides layers by EDS or EPMA when the oxide layers are either porous or too thin. Their stoichiometries were tentatively suggested based on other observations as follows. The outer dark porous layer of iron oxide shown in Figure 2.19 and Figure 2.20 was not seen in any partly oxidized pentlandite particles quenched from below 880 ºC. The same phenomenon occurred for pyrrhotite. As illustrated in Figure 2.14 and Figure 2.15, a similar dark porous layer of iron oxide was formed on the surface when the sample was heated to 880 ºC. By noting XRD patterns, it is obvious that magnetite reoccurred at 880 ºC. Thus this porous layer is believed to be magnetite formed from the decomposition of hematite represented by Reaction (2.11). There were conditions causing the decomposition of hematite between 785 ºC and 880 ºC. As is depicted in Figure 1.7, the formation of Fe_3O_4 is easier at higher temperature since the predominant area for Fe_3O_4 expands to the right with the increase of temperature. It suggests that the already formed Fe_2O_3 would thermally decompose to Fe_3O_4 if the O_2 partial pressure drops to a level at which Fe_3O_4 is thermodynamically stable. The melting of nickel sulfide core above 800 ºC accelerated its oxidation and would have lowered the oxygen partial pressure within the bulk of the sample bed to a level that gives rise to the decomposition of Fe_2O_3, forming Fe_3O_4. The porous nature of the Fe_3O_4 is possibly due to the volume reduction of around 2% for Reaction (2.11).

The top right corner of Figure 2.19 shows the isolated sulfide core with enhanced contrast. This sulfide core is composed of alternating layers of two nickel sulfide phases, one of which is Ni_3S_2, the other is possibly Ni_7S_6. These two phases were probably formed by the exsolution of the molten sulfide core during quenching, which provides evidence for the presence of the unquenchable compound $Ni_{3\pm x}S_2$ in Reactions (2.9) and (2.10). On the surface of the sulfide core where O_2 is accessible, a layer of $NiSO_4$ was formed via Reaction (2.10). The extent of Reaction (2.10) was eventually retarded by the $NiSO_4$ layer formed on the surface of the molten sulfide core due to the limited O_2 diffusion rate through this dense sulfate layer to reach the surface of the sulfide where the reaction proceeded.

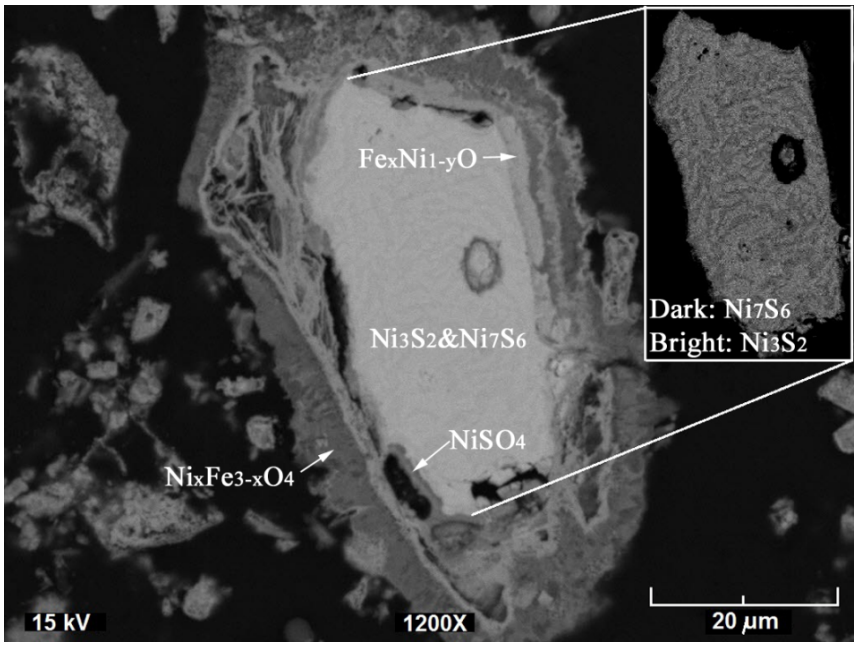

Figure 2.19. BSE image of an oxidized pentlandite particle air-quenched from 880 ºC in the TGA run. Textures of the sulfide core are exhibited with enhanced contrast.

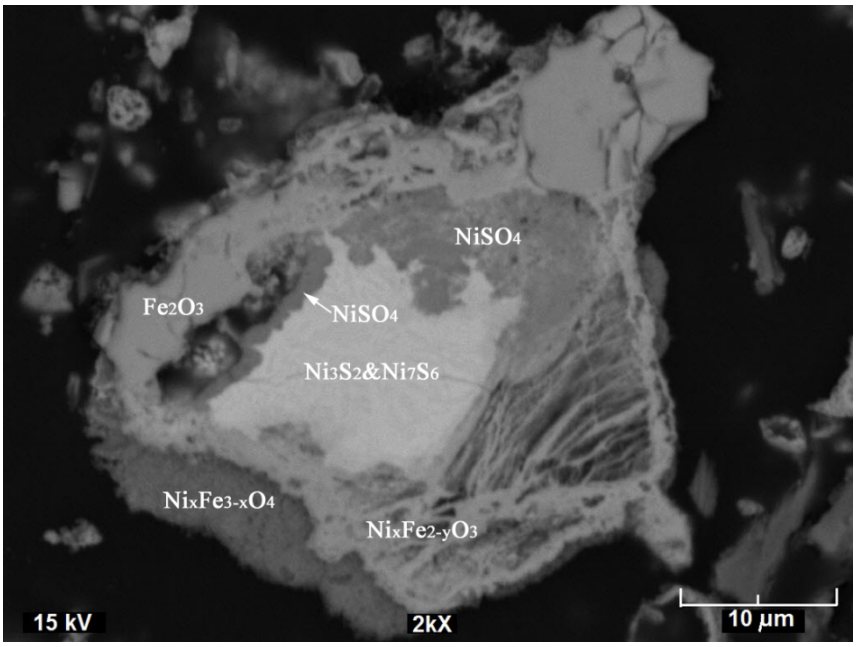

Figure 2.20. BSE image of an oxidized pentlandite particle air-quenched from 880 ºC in the TGA run.

$$6Fe_2O_3 \rightarrow 4Fe_3O_4 + O_2 \qquad (2.11)$$

An endotherm occurred at 942 ºC, represented by a valley in the DTA curve in Figure 2.8. It correlates to a quick mass loss and offgas peaks at 917 ºC. This endotherm is easily deduced on the basis of the chemical analysis results in Figure 2.11, to be the thermal decomposition of $NiSO_4$. This is based on the fact that the amount of water-soluble species, $NiSO_4$, dropped significantly between 800–950 ºC, as shown in Figure 2.11. Decomposition of $NiSO_4$ at higher temperatures (942 ºC) results in mass loss and SO_2 emissions, according to Reaction (2.12). Evidence also suggests the occurrence of another reaction along with the decomposition of $NiSO_4$, which is expressed as Reaction (2.13). The $NiSO_4$ layer, which covered the remaining molten sulfide core and protected the core from being oxidized, was decomposed and exposed the molten sulfide core to the oxidative atmosphere, leading to the complete oxidation of the remaining sulfide through Reaction (2.13). The assignment of this reaction is supported by the occurrence of the corresponding O_2 consumption peak in Figure 2.7, as well as the disappearance of Ni_3S_2 at 950 ºC in the XRD patterns. Figure 2.21 is a BSE image of an oxidized pentlandite particle air-quenched from 950 ºC, showing the outcome of Reactions (2.12) and (2.13). Without the shield of the $NiSO_4$ layer, the molten sulfide core was oxidized, leaving a pore in the oxidized pentlandite particle.

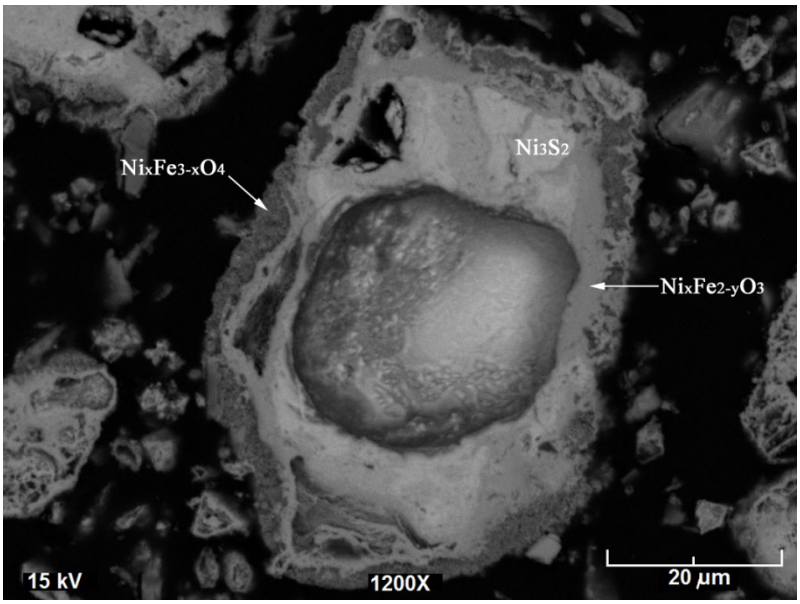

Figure 2.21. BSE image of an oxidized pentlandite particle air-quenched from 950 ºC in the TGA run.

$$NiSO_4 \rightarrow NiO + SO_2 + 1/2O_2 \quad (2.12)$$

$$Ni_{3\pm x}S_{2(l)} + (3.5\pm 0.5x)O_2 \rightarrow (3\pm x)NiO + 2SO_2 \quad (2.13)$$

There is another endotherm at 850 ºC after Reaction (2.10). Samples were collected at 825 ºC and 885 ºC from DTA runs for XRD analysis in order to evaluate this endotherm. XRD patterns indicate the increase of NiO and decrease of $NiSO_4$ contents after this endotherm. It becomes then clear that this endotherm is also the thermal decomposition of $NiSO_4$. This means a single reaction, which is represented by Reaction (2.12), gave rise to two endotherms in this test. The explanation for this is tentatively interpreted as follows. The melting of $Ni_{3\pm x}S_2$ and the following intensive thermal oxidation represented by Reaction (2.10) raised the temperature of the sulfide core dramatically well above the furnace temperature, even higher than 942 ºC. Meanwhile, the formation of $NiSO_4$ layer on the molten sulfide core from Reaction (2.10) eventually terminates the oxidation reaction by inhibiting the O_2 diffusion. The local temperature of the sulfide core is already high enough for the quick decomposition of the $NiSO_4$ layer around the core, leading to the endotherm at 850 ºC. With the proceeding of the DTA run, while the furnace temperature was increasing, the local temperature of the sulfide core drops due to the termination of the exothermic Reaction (2.10) as well as the occurrence of the endothermic Reaction (2.12). Reaction (2.12) stopped as a consequence due to this temperature drop, which is indicated by the termination of the endotherm at 850 ºC. The decomposition of $NiSO_4$ resumes when the temperature is increased to 942 ºC, which gives rise to the second endotherm.

Sulfate formation and decomposition is the second focus of this study. As can be seen in Figure 2.11, sulfation and sulfate decomposition which played a key role in the sample mass change, spanned over a wide temperature range. Massive sulfation started from around 500 ºC, leading to the increase of mass till 733 ºC. Sulfate decomposition prevailed at relatively higher temperatures, resulting in the mass loss after 733 ºC. It is surprising to see that the sulfation for Cu is over 85% at 785 ºC. It is also worth mentioning that Mg containing species, which is siliceous gangue materials in the concentrate, is also prone to sulfation. This is illustrated by the increasing sulfation for Mg to over 50% at 950 ºC. $NiSO_4$ is relatively hard to produce, which is due to its dense nature tending to inhibit further sulfation. The quick increase in $NiSO_4$ from 785

ºC to 880 ºC is because of the melting of nickel sulfide that leads to the acceleration of the kinetics for sulfation, as discussed earlier. The percentage of iron sulfate formation is low, which is probably caused by the low stability of the sulfates. Sulfate formation can take place by two possible reaction routes, which can be shown by Reactions (2.14) and (2.15) in general [20]. The first reaction represents the direct oxidation of sulfide, whereas in the second reaction the sulfate is formed by SO_2 and O_2. No attempts have been made to determine by which route these various sulfates were formed in this study. Sulfate decomposition can be generally represented by Reaction (2.16). Temperature ranges for sulfates formation and decomposition for various species can be seen in Figure 2.11 and will be summarized later.

It is also found from this study that at relatively high temperatures, various metal sulfates tended to form sulfate mixtures. Figure 2.22 illustrates a particle of $NiSO_4$-$MgSO_4$ mixture in the calcine quenched from 880 ºC. Mixtures of $CuSO_4$-$MgSO_4$, $NiSO_4$-$CuSO_4$-$MgSO_4$, and even $Fe_2(SO_4)_3$-$NiSO_4$-$CuSO_4$-$MgSO_4$ were also found to have formed. This is possibly because sulfates of individual particles which have physical contact tend to diffuse into each other and form mixtures. The formation of sulfates mixture increases the thermal stability of each individual sulfate by lowering its activity, resulting in an increase in its decomposition temperature.

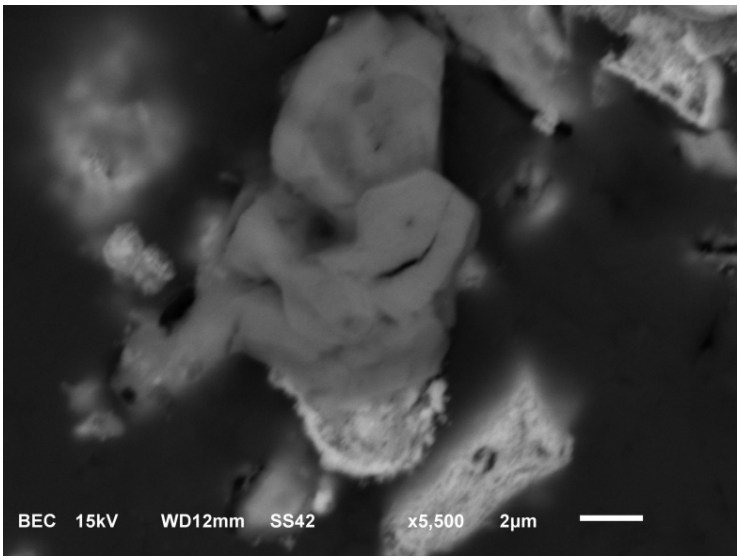

Figure 2.22. BSE image of a particle composed of a mixture of $NiSO_4$ and $MgSO_4$ quenched from 880 ºC.

$$MeS+2O_2 \rightarrow MeSO_4 \quad (2.14)$$

$$MeO+SO_2+1/2O_2 \rightarrow MeSO_4 \quad (2.15)$$

$$MeSO_4 \rightarrow MeO+SO_2+1/2O_2 \quad (2.16)$$

For the oxidation of the Raglan concentrate at 15 ºC/min in air, the reaction scheme is summarized in Table 2.7 based on this study.

Table 2.7. Summary of the reaction sequence for the oxidation of the Raglan concentrate at 15 ºC/min in air.

450 ºC~498 ºC [a]	$2CuFeS_2+7O_2 \rightarrow CuO \cdot CuSO_4+Fe_2O_3+3SO_2$
450 ºC~509 ºC [a]	$2Fe_{1-x}S+(3.5-1.5x)O_2 \rightarrow (1-x)Fe_2O_3+2SO_2$
350 ºC~605 ºC [a]	$(Ni,Fe)_9S_8+O_2 \rightarrow (Ni,Fe)_{1-x}S+Ni_{1-x}S+Fe_2O_3+SO_2$
350 ºC~509 ºC [a]	$(Ni,Fe)_9S_8+O_2 \rightarrow (Ni,Fe)_3S_4+Fe_2O_3$
509 ºC~605 ºC [a]	$(Ni,Fe)_3S_4+O_2 \rightarrow (Ni,Fe)_{1-x}S+SO_2$
468 ºC~700 ºC [b]	$(Ni,Fe)_{1-x}S+O_2 \rightarrow Ni_{1-x}S+Fe_2O_3+SO_2$
509 ºC~733 ºC [c] for Fe 509 ºC~785 ºC [c] for Cu 509 ºC~785 ºC [c] for Co 509 ºC~880 ºC [c] for Ni	$MeS+2O_2 \rightarrow MeSO_4$ or $MeO+SO_2+1/2O_2 \rightarrow MeSO_4$
>495 ºC [c]	$MgO+SO_2+1/2O_2 \rightarrow MgSO_4$
731 ºC [b]	$(3\pm y)Ni_{1-x}S+(1+2x\pm y)O_2 \rightarrow (1-x)Ni_{3\pm y}S_2+(1+2x\pm y)SO_2$
733 ºC~785 ºC [c] for Fe >785 ºC [c] for Co 785 ºC~950 ºC [c] for Cu 942 ºC [b] for Ni	$MeSO_4 \rightarrow MeO+SO_2+1/2O_2$
813 ºC [b]	$Ni_{3\pm x}S_{2(s)} \rightarrow Ni_{3\pm x}S_{2(l)}$, and $Ni_{3\pm x}S_{2(l)}+O_2 \rightarrow NiO+NiSO_4+SO_2$
>813 ºC [b]	$6Fe_2O_3 \rightarrow 4Fe_3O_4+O_2$
942 ºC [b]	$Ni_{3\pm x}S_{2(l)}+(3.5\pm0.5x)O_2 \rightarrow (3\pm x)NiO+2SO_2$

[a] Temperature determined from TGA results.

[b] Temperature determined from DTA results.

[c] Temperature determined from ICP results.

A set of TGA runs was also performed to evaluate the effect of sample size on its oxidation kinetics. Samples were heated in argon to 760 ºC and oxidized by switching the feeding gas to 1 L/min air and maintaining this temperature. Mass changes in weight percent were plotted against oxidation time, as shown in Figure 2.23. At the onset of the oxidation, mass changes were normalized to 0. The initial rates of mass change at the onset of oxidation in both mg/second and weight%/second were plotted as a function of both the sample size and the sample bed thickness in the crucible in Figure 2.24. For the runs with sample sizes larger than 5 mg, the initial rate of mass change (mg/sec) is roughly the same and independent of the sample size. This indicates that reactions did not take place uniformly within the bulk of the sample, but instead occurred gradually downward from the top surface of the sample. This is because diffusion of O_2 through the bed plays an essential part in the progress of reactions. Due to the O_2 consumption reactions taking place at a certain depth in the bed, the O_2 partial pressure must have dropped to near zero in the area below the reaction level. As a result, the reaction front where most oxidation reactions were taking place propagated downwards, leaving the oxide products above and the materials below unaffected. The thickness of the reaction front must be thin compared with that of the whole sample bed.

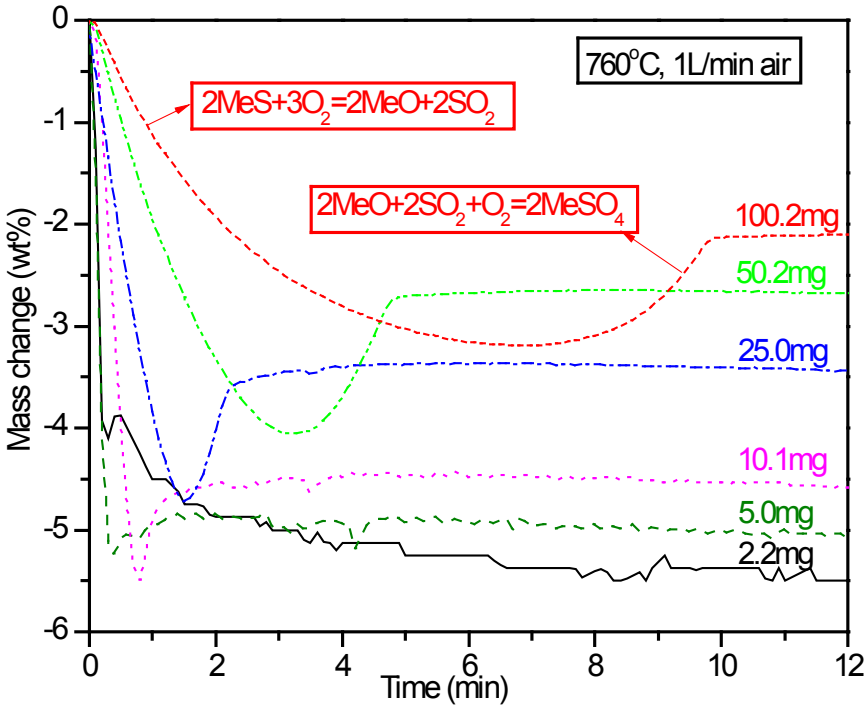

Figure 2.23. Mass change in wt% vs. time with the variation of sample size.

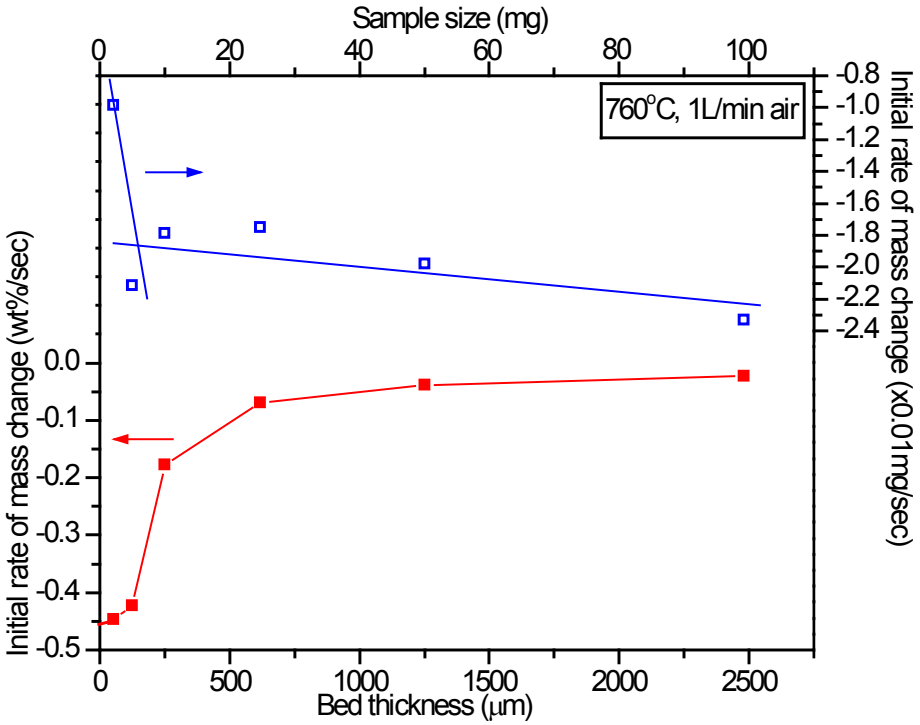

Figure 2.24. Initial rate of mass change vs. sample size and bed thickness.

The progress of reactions can be envisioned on the basis of the mass change curves in Figure 2.23. At the beginning of oxidation, the reactions occurring are mostly oxidation reactions releasing considerable amounts of SO_2, leading to the initial quick mass loss. O_2 from above the sample bed diffuses through the oxidized bed and reaches the reaction front, where most of it is consumed, releasing SO_2 as a gaseous product. The resulting SO_2 needs to diffuse upwards through the oxidized bed before it is swept away by the feeding gas. The resulting counter diffusion action of SO_2 and O_2, as well as the presence of the oxides as catalysts for the oxidation of SO_2 forming SO_3, provides an ideal atmospheric environment for the sulfation of oxides. With the downward propagation of the reaction front, the thickness of the oxidized bed increases, giving rise to the prevalence of the sulfation reactions as opposed to the oxidation reactions, resulting in the mass increase. Most of the oxidation stops when the reaction front reaches the bottom of the crucible. Without the presence of SO_2, the sulfation reactions stop immediately, indicated by the sudden transition of the mass change curves in Figure 2.23. Regarding this scenario, it is reasonable that the duration of this oxidation process is proportional to the sample size, as shown in Figure 2.23. A sample size of 5 mg marks a transition in the kinetics of oxidation, because the slopes of the mass change curves of 5 mg and 2.2 mg are identical. For the runs with sample sizes no larger than 5 mg in Figure 2.24, the initial rate of mass change (mg/sec) becomes proportional to the sample size, indicating that the O_2 diffusion through the bed of the sample did not control the reaction rate. Probably in this case, the diffusion in the particle became the rate controlling step. The sample size of 5 mg, with the bed depth of around 125 μm, should roughly be the size of the reaction front. Given the particle size of the Raglan concentrate, it is fair to say that even around 5 layers of the concentrate particles would reduce most of the O_2 partial pressure during the oxidation of the concentrate at 760 ºC.

2.4 Conclusions

The oxidation mechanism of a nickel concentrate was investigated by means of TG/DTA. Reaction products at intermediate temperatures were analyzed by XRD, SEM/EDS, EPMA and chemical analysis. A reaction scheme was deduced for its oxidation in air from ambient up to

1000 ºC at 15 ºC/min. Between 350 ºC and 550 ºC, the main reaction was the decomposition of pentlandite forming monosulfide solid solution, as well as the oxidation of iron sulfide. Violarite is also involved as a transitional by-product from the decomposition of pentlandite at around 500 ºC. Preferential oxidation of iron sulfide species from the resulting monosulfide solid solution occurred over a wide temperature range up to around 700 ºC, forming $Ni_{1-x}S$ core with iron oxide shell. The $Ni_{1-x}S$ core was then transformed into $Ni_{3\pm x}S_2$ at around 730 ºC. The melting of the nickel sulfide core at 813 ºC accelerated further oxidation as well as the formation of nickel sulfate, which lowered the O_2 partial pressure in the bulk of the sample bed, leading to the decomposition of Fe_2O_3 forming Fe_3O_4. Decomposition of $NiSO_4$ at 942 ºC exposed the remaining nickel sulfide core to the oxidative atmosphere, leading to the complete oxidation of the sulfide. Sulfates of various metals started to form at around 500 ºC probably due to the emission of SO_2 which favors the sulfation by providing a suitable atmosphere. These sulfates tended to decompose at higher and varying temperatures, depending on their individual thermal stability. Mixtures of sulfates were formed at relatively high temperature, which increased their individual thermal stability.

The reaction rate controlling step was the O_2 diffusion through the bed of sample for TGA runs with sample sizes larger than 5 mg. Most of the oxidation reactions took place in a reaction front of around 125 μm in depth which propagated downwards in the sample bed due to the limited access of O_2.

2.5 References

[1] J.G. Dunn, C.E. Kelly, A TG/MS and DTA study of the oxidation of pentlandite, Journal of Thermal Analysis, 18 (1980) 147-154.

[2] J.G. Dunn, C.E. Kelly, A TG/DTA/MS study of the oxidation of nickel sulphide, Journal of Thermal Analysis, 12 (1977) 43-52.

[3] A.C. Chamberlain, The effect of stoichiometry on the thermal properties of violarite and pentlandite, Ph.D. thesis, Curtin University, Perth, Australia, 1997.

[4] T. Kennedy, B.T. Sturman, The oxidation of iron (II) sulphide, Journal of Thermal Analysis and Calorimetry, 8 (1975) 329-337.

[5] K. Niwa, T. Wada, Y. Shiraishi, Roasting Reaction of Ferrous Sulfide, JOM, 9 (1957) 269-273.

[6] M. Aneesuddin, P.N. Char, M.R. Hussain, E.R. Saxena, Studies on thermal oxidation of chalcopyrite from Chitradurga, Karnataka State, India, Journal of Thermal Analysis, 26 (1983) 205-215.

[7] G.A. Kolta, M.H. Askar, Thermal decomposition of some metal sulphates, Thermochimica Acta, 11 (1975) 65-72.

[8] T.R. Ingraham, Thermodynamics of the Thermal Decomposition of Nickel(II) Sulfate: The Ni-S-O System from 1000º to 1150º K, Transactions of the Metallurgical Society of AIME, 236 (1966) 1064-1067.

[9] T.R. Ingraham, P. Marier, Kinetics of the Formation and Decomposition of Nickelous Sulfate, Transactions of the Metallurgical Society of AIME, 236 (1966) 1067-1071.

[10] T.R. Ingraham, P. Marier, Kinetics of the Thermal Decomposition of Cupric Sulfate and Cupric Oxysulfate, Transactions of the Metallurgical Society of AIME, 233 (1965) 363-367.

[11] P. Masset, J.Y. Poinso, J.C. Poignet, TG/DTA/MS Study of the thermal decomposition of $FeSO_4 \cdot 6H_2O$, Journal of Thermal Analysis and Calorimetry, 83 (2006) 457-462.

[12] P.G. Coombs, Z.A. Munir, The decomposition of iron(III) sulfate in air, Journal of Thermal Analysis, 35 (1989) 967-976.

[13] R.V. Siriwardane, J.A. Poston Jr, E.P. Fisher, M.-S. Shen, A.L. Miltz, Decomposition of the sulfates of copper, iron (II), iron (III), nickel, and zinc: XPS, SEM, DRIFTS, XRD, and TGA study, Applied Surface Science, 152 (1999) 219-236.

[14] A. Roine, HSC Chemistry, Outokumpu Research Oy, Pori, Finland, 2007.

[15] P.G. Thornhill, L.M. Pidgeon, Micrographic Study of Sulfide Roasting, Journal of Metals, 9 (1957) 989-995.

[16] M. Zamalloa, T.A. Utigard, The behaviour of Ni-Cu concentrate in an industrial fluid bed roaster, Canadian Metallurgical Quarterly, 35 (1996) 435-449.

[17] S. Prasad, B.D. Pandey, Thermoanalytical Studies on Copper—Iron Sulphides, Journal of Thermal Analysis and Calorimetry, 58 (1999) 625-637.

[18] G. Kullerud, Thermal stability of pentlandite, The Canadian Mineralogist, 7 (1963) 353-366.

[19] T. Tanabe, K. Kawaguchi, Z. Asaki, Y. Kondo, Oxidation Kinetics of Dense Pentlandite, Transactions of the Japan Institute of Metals, 28 (1987) 977-985.

[20] J.G. Dunn, The oxidation of sulphide minerals, Thermochimica Acta, 300 (1997) 127-139.

[21] J.R. Craig, Violarite Stability Relations, The American Mineralogist, 56 (1971) 1303-1311.

[22] K.C. Misra, M.E. Fleet, Chemical Composition and Stability of Violarite, Economic Geology, 69 (1974) 391-403.

[23] J.G. Dunn, V.L. Howes, The oxidation of violarite, Thermochimica Acta, 282–283 (1996) 305-316.

3 Leaching Behavior of the Roasted Nickel Calcine

3.1 Introduction

It is known from the previous chapter that the roasting mechanism could be rather complicated due to the complex mineralogy of the nickel concentrate, the heterogeneous nature of the reactions, as well as the varying local roasting conditions. Therefore, it is expected that after sulfation roasting, some unwanted by-products (e.g. $NiFe_2O_4$, NiO) could co-exist with the non-ferrous metal sulfates in the calcine. A leach procedure therefore needs to be developed to maximize the non-ferrous metal recovery and minimize the dissolution of iron species from the calcine.

The main minerals in the nickel sulfide concentrate are: pentlandite $(Fe,Ni)_9S_8$, pyrrhotite $Fe_{1-x}S$, chalcopyrite $CuFeS_2$, and siliceous gangue materials. The main species that the roasted calcine may contain are: hematite (Fe_2O_3), magnetite (Fe_3O_4), nickel oxide (NiO), nickel ferrite ($NiFe_2O_4$), cupric oxide (CuO), pyrrhotite (hexagonal type Fe_9S_{10}, monoclinic type Fe_7S_8), heazlewoodite (Ni_3S_2), iron nickel monosulfide solid solutions ($(Fe,Ni)_{1-x}S$), NiS, bornite (Cu_5FeS_4), and chalcocite ($Cu_{2-x}S$), as well as the water soluble sulfates [1-3]. The leaching of water soluble sulfates is rather straightforward without the involvement of chemical transformations. However, there is a possible scenario where the sulfates formed are enclosed in the oxides and cannot be accessed by the leach solution. This would lead to the loss of metal sulfates into the leach residue after the leach process. The major focus of this study is, as a result, to investigate the leaching behavior of the minerals in the calcine and the possible interactions among the species present in the leaching system.

Extensive studies have been done to investigate the leachability of some of the species involved in this work. The leaching behavior of sulfide and oxide minerals of interest can be mainly affected by the following conditions.

1. pH

In non-oxidative acid leaching, protons provided by the acidic leachants are used to attack the solid. An example is the Falconbridge matte leach process, in which Ni_3S_2 in the smelter matte

is dissolved in concentrated HCl as shown as Reaction (3.1) [4, 5]. The effect of the acidity on the dissolution rate can be generally described by Equation (3.2). Majima et al. [6] found the leaching rate of hematite (Fe_2O_3) is first order with respect to $a(H^+)$ in hydrolic acid or perchloric acid solutions, and is of half order in sulfuric acid solutions. While the leaching rate of NiO has an order of 0.66 with respect to the H_2SO_4 acid concentration [7].

$$Ni_3S_2+6H^+ \rightarrow 3Ni^{2+}+2H_2S+H_2 \quad (3.1)$$

$$\text{Dissolution rate} \propto a_{(H^+)}{}^n \quad (3.2)$$

2. Redox potential (addition of oxidizing or reducing agents)

Leaching reactions involving the transfer of electrons or the change of the valence state of components could respond to the change of redox potential of the leaching system. Copper concentrate could be leached under acidic oxidizing conditions, which can be expressed as Reaction (3.3) [8]. Another commercialized oxidative leaching example is the Sherritt Gordon Ammonia leach process to treat nickel sulfide concentrate, shown as Reactions (3.4) and (3.5) [9]. Redox potentials are observed to have large effects on the leaching of oxides of the transition elements Fe, Co, Ni, and Cu, because they are capable of forming oxides of variable stoichiometry [10]. For the leaching of iron oxides, dissolution rate could be increased by the addition of a small amount of reducing agents (including sulfide ions) [10-14], and the presence of oxidizing agents can significantly reduce its dissolution rate [15]. On the contrary, the dissolution rate of NiO tends to decrease if the leaching solution contains reductive ions, and the ion with stronger reducing ability has larger effects on decreasing the dissolution rate of NiO [7]. A study conducted by Rodenas et al. [16] revealed that the dissolution of nickel ferrite ($NiFe_2O_4$) could be accelerated by both reductants (Fe^{2+}) and oxidants (O_2) because of the presence of appreciable amounts of both Ni(II) and Fe(III) in the dissolving interface of the particles.

$$CuFeS_2+4O_x \rightarrow Cu^{2+}+Fe^{2+}+2S^o+4O_x^- \quad (3.3)$$

$$NiS+5H_2O+8O_x \rightarrow NiO+SO_4^{2-}+10H^++8O_x^- \quad (3.4)$$

$$NiO+2NH_4^++4NH_3 \rightarrow Ni(NH_3)_6^{2+}+H_2O \text{ (with ammonia)} \quad (3.5)$$

3. Temperature

The temperature dependence of the dissolution rate of certain mineral could be quantitatively described by the Arrhenius correlation. Table 3.1 summarizes the apparent activation energy for the acid leaching of some minerals of interest.

Table 3.1. Activation energies for the acid dissolution of some minerals.

Minerals	Acid	Normality (N)	Activation Energy (kJ/mol)	References
Fe_2O_3	HCl	1	77.7	[6]
Fe_2O_3	H_2SO_4	2	104	[6]
pyrrhotite	HCl	2.87	29.3±2.9	[17]
CuO	HCl	0.2	50.6	[18]
NiO prepared at 873K	H_2SO_4	0.02	75.7	[7]
NiO prepared at 1273K	H_2SO_4	2	64.8	[7]

4. History of the minerals

Both the thermal history and the storage conditions may have a great impact on the leachability of certain minerals. This especially applies to the leaching behavior of NiO. Studies have shown that the dissolution behavior of NiO is sensitive to the conditions of preparation [7, 19, 20]. They found that NiO samples heated to higher temperature were less reactive towards both acid and ammoniacal solutions. This phenomenon was tentatively explained by a decrease in the surface area as well as a change in defect (e.g. dislocation) concentration near the surface, because the dissolution of NiO begins from the defect site (Ni^{2+} vacancy) on the surface of the oxide particle [20, 21]. Astonishingly, the dissolution rate of fresh NiO is found to be over 40 times faster than that of the stored NiO powder [19], which is due to the change on its surface during storage by the adsorption of foreign atoms or molecules [20].

5. Elemental sulfur formed on the surface of the particle

Elemental sulfur is, to some extent, resistant to oxidation in spite of high oxidizing potentials in the direct leaching of sulfide minerals [8]. The formation of elemental sulfur could detrimentally

affect the dissolution of sulfide minerals. Pyrrhotite is a non-stoichiometric mineral with an Fe:S ratio smaller than 1. Due to the excess of sulfur contained in pyrrhotite, elemental sulfur tends to form on the surface of the particle as part of the acid leaching product, apart from H_2S. And the fraction of elemental sulfur in the product is dependent on the stoichiometry of the pyrrhotite itself. This sulfur layer formed on the surface of particles inhibits the progress of leaching. If the minimum leaching conditions, i.e. temperature and acidity of the leachant, are not met, leach would pause as a result of the refractory effect of the sulfur layer, leaving a fraction of the pyrrhotite undissolved [17]. In the leaching of NiS (millerite) using HCl solution, H_2S gas would be oxidized to elemental sulfur if oxidizing conditions were present, resulting in a reduced dissolution rate [22].

6. Anions or Cations in the leaching solution

In some cases of acid leaching of oxides, aside from the hydrogen ions, anions from the leachants also play an important role. The mechanism of such effect may be the complexation of metal ions, enhancement of proton co-adsorption, or labilization of vicinal Me-O bonds [16]. Majima et al. [6] found that due possibly to the adsorption of anions of the leachants onto the mineral surface which determines the leaching rate, the dissolution rate of hematite differed greatly when leached with different acids although $a(H^+)$ were adjusted to the same value. The study conducted by K. Nut [20] shows that in the acid dissolution of NiO, the presence of Co^{2+} could promote the dissolution of NiO, while the cations with stronger reducing ability tend to have a larger effect in decreasing the leaching rate of NiO. In the same study, it was also found that the reducing ion (e.g. Fe^{2+}) present in the solution would preferentially be adsorbed on the sites where the dissolution of NiO initiates. As a result, the dissolution rate is largely affected by only a small coverage of the surface by reducing ions due to this preferential adsorption behavior. Majima and Awakura [23] found the acid leaching of hematite as well as cupric oxide could be enhanced by the addition of NaCl to HCl solution or $NaClO_4$ to $HClO_4$ solution. Rather than employing the adsorption theory, they explained this enhancement of leaching as a result of an increase of $a(H^+)$ by the addition of the appropriate salts.

7. Pressure

An example is the Dynatec Process developed by Sherritt Gordon in Canada. The main reaction is shown as Reaction (3.6), taking place at 115–150 ºC and about 2000 kPa oxygen pressure [24]. Pyrrhotite is insoluble in water under normal conditions, but can be slowly dissolved in water at 110 ºC and 200 kPa oxygen pressure via Reaction (3.7) [24].

$$2CuFeS_2+4H^+ +5/2O_2 \rightarrow 2Cu^{2+}+2FeOOH+4S+H_2O \quad (3.6)$$

$$FeS+2O_2(aq) \rightarrow FeSO_4(aq) \quad (3.7)$$

8. Stoichiometry of the mineral

As an intrinsic property of the mineral, the stoichiometry has a great impact on its leachability. Take iron oxides as an example, the reactivity of the oxides in HCl solution is of the order $FeO>Fe_3O_4>Fe_2O_3$ [10]. By taking advantage of this effect of stoichiometry on the leachability, Dyson and Scott [25] devised an activation procedure which renders the nickel concentrate more acid reactive by eliminating excess sulfur from it in a reducing atmosphere (natural gas) under high temperature. With no excess sulfur in the system, the possibility of forming a protective sulfur coating on the particles is eliminated.

3.2 Experimental

Nickel concentrate as received is Raglan concentrate from Xstrata Nickel's smelter in Sudbury (see Section 2.2.1 for more information on this material). Roasting of the nickel concentrate was conducted in the experimental setup illustrated in Figure 3.1. In each roasting test, Raglan concentrate of 5 grams was put in a porcelain boat. In order to maximize the heat and mass transfer rate between the sample and its local surroundings, the concentrate was spread evenly in the boat to cover an area of 28 cm^2 with a thickness of 1.5 mm. The boat was then placed in a sealed tube inside a resistance heating furnace. The samples were heated under flowing argon and were subsequently subjected to the roasting gas (dried air and/or SO_2 mixed with N_2). The offgas was analyzed for its SO_2 content before it was scrubbed to eliminate the SO_2 and SO_3 for purging to the atmosphere. The SO_2 concentration of the off-gas was measured using a gas analyzer (ABB EL3020) and was recorded using a computer controlled data acquisition system

(FLUKE Hydra Series II). After roasting, the tube was withdrawn from the electric furnace to ensure a fast cooling rate.

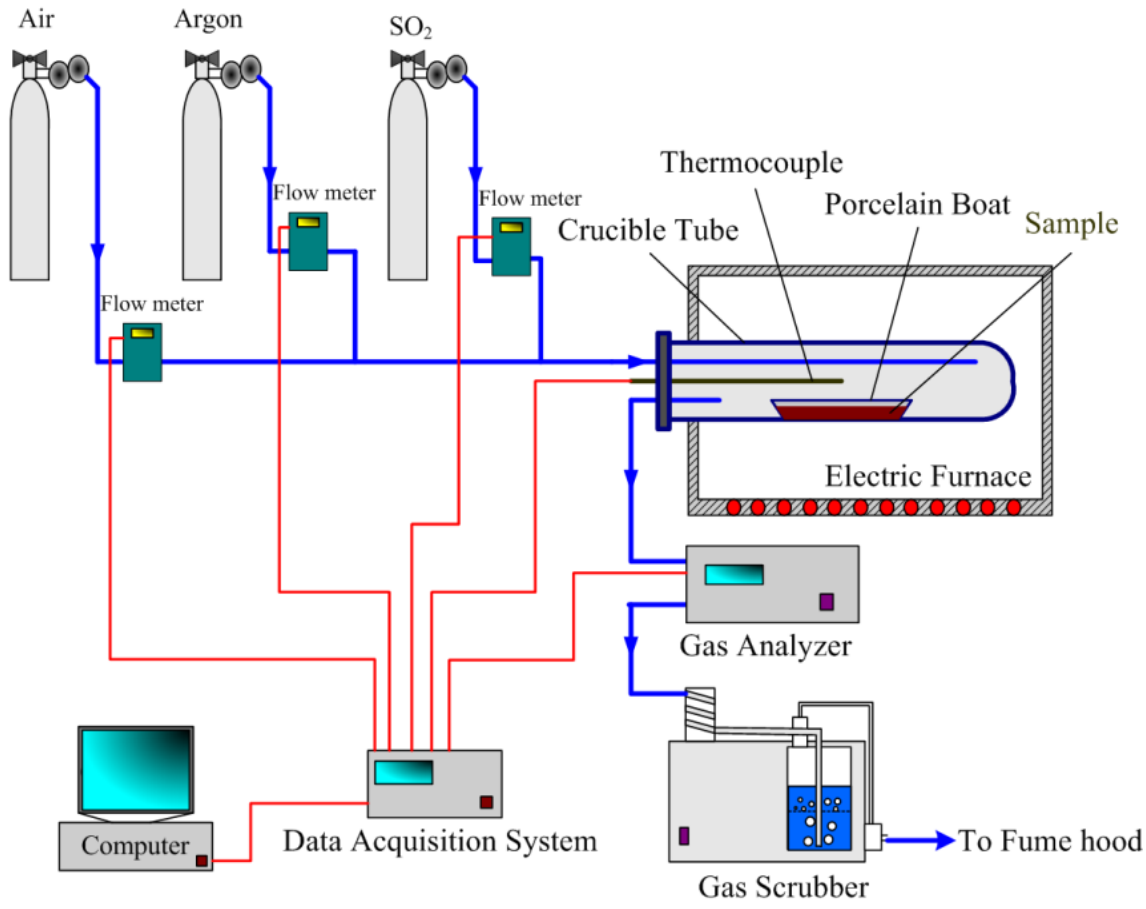

Figure 3.1. Experimental setup for the roasting of nickel concentrate.

In order to investigate the effects of both the roasting and leaching conditions on the leaching behaviors of calcines, three types of leaching tests were conducted: Dilute Acid Leaching (DAL), Hot Water Leaching (HWL), and Concentrated Acid Leaching (CAL). Conditions of the leaching experiments are summarized in Table 3.2. Leaching took place in a 250 mL flask equipped with a water condenser on exhaust to minimize the vaporization losses of the solution. For precise temperature control within ±1 ºC, the flask was placed in a hot water bath. 1 mL aliquot samples of leach liquor were drawn from the flask after predetermined time intervals. After leaching, the pulp was filtrated and the residue was dried. Roughly 0.079 g residue was taken and digested in aqua regia. Both the leach liquor samples and the solutions from residue

digestion were analyzed by ICP-OES after appropriate dilution. Calcines and leach residues were analyzed by optical microscopy, SEM/EDS, and XRD.

Table 3.2. Leaching conditions of three types of leaching tests.

	DAL	HWL	CAL
Calcine mass (g)	1.5	1.5	4.0
Leaching temperature (ºC)	90	90	100
Leachant	HCl	H_2O	HCl
Normality	0.57	N/A	5.00
Volume (mL)	200	200	200
Leaching time (hours)	48.00	5.00	12.75
Stirring rate (rpm)	600	600	600

3.3 Results and Discussion

3.3.1 Calcine Preparation

Three calcines were prepared for leaching by roasting the Raglan concentrate under various conditions. The first calcine (named **Calcine650**) was prepared by roasting 5 gram Raglan concentrate at 650 ºC with 500 mL/min air stream until the SO_2 concentration in the offgas dropped to near zero. The temperature and SO_2 profiles and the switching time of the feeding gas are shown in Figure 3.2. This calcine was examined using SEM/EDS. Figure 3.3 illustrates a backscattered electron (BSE) image of this calcine and the elemental maps of Fe, Ni, and S of the same area. It shows that even the largest pyrrhotite particles were completely oxidized, indicating the complete oxidation of pyrrhotite in the sample, forming iron oxides by Reaction (3.8) [3]. Relatively large pentlandite particles have a characteristic microstructure of a nickel sulfide core and an iron oxide rim, indicating the preferential oxidation of iron sulfide from the pentlandite via Reaction (3.9) [3]. The degree of sulfur elimination of this calcine is 69.9% by chemical analysis.

$$2Fe_{1-x}S + (3.5-1.5x)O_2 \rightarrow (1-x)Fe_2O_3 + 2SO_2 \quad (3.8)$$

$$(Ni,Fe)_9S_8 + O_2 \rightarrow Fe_2O_3 + Ni_{1-x}S + SO_2 \quad (3.9)$$

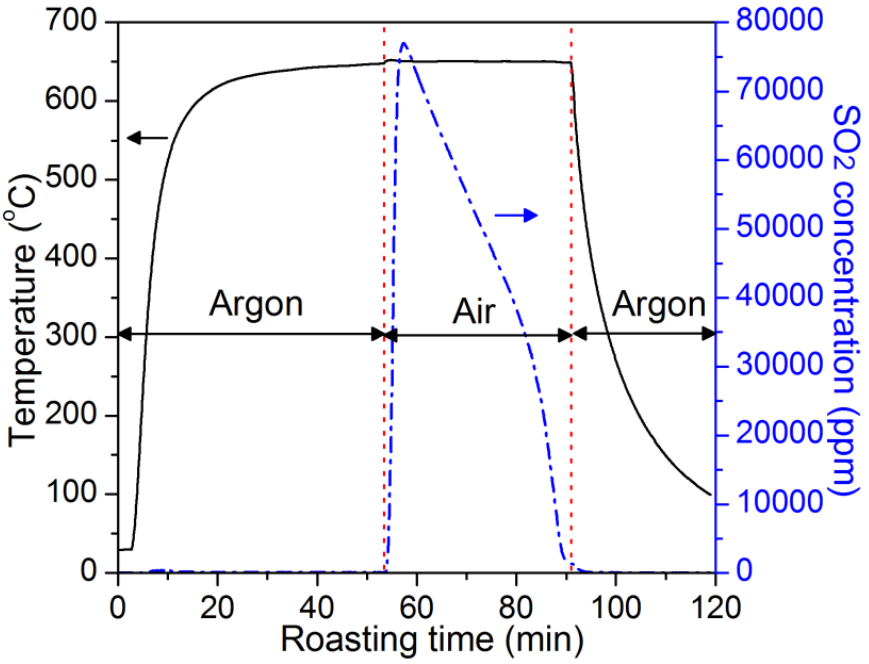

Figure 3.2. Temperature and SO_2 concentration in the offgas during roasting of sample **Calcine650**.

One partially roasted calcine (named **Calcine650S**) was prepared by roasting the Raglan concentrate at 650 ºC under a gas mixture of 500 mL/min air and 500 mL/min 10% SO_2 (balance N_2) until no apparent SO_2 was emitted from the sample. The last calcine (named **Calcine750**) was produced by roasting the concentrate at 750 ºC with air, aiming to investigate how the roasting temperature would affect the leaching behavior of the calcine. The degree of sulfur elimination for **Calcine750** is 91.8%. The temperature and the SO_2 concentration in the offgas are plotted against roasting time in Figure 3.4 and Figure 3.5 for **Calcine650S** and **Calcine750**, respectively.

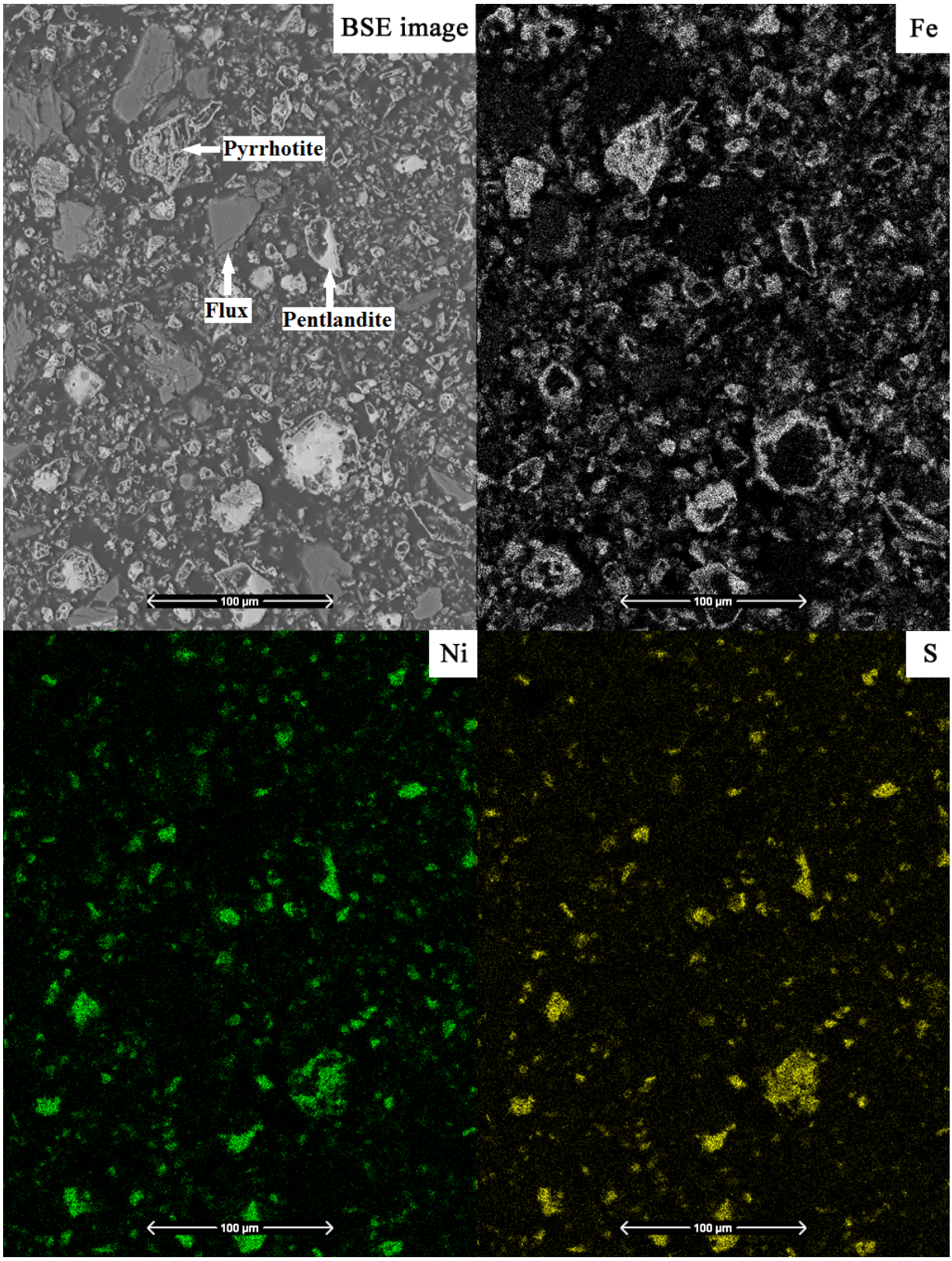

Figure 3.3. BSE image and elemental maps of Fe, Ni, and S of sample **Calcine650**.

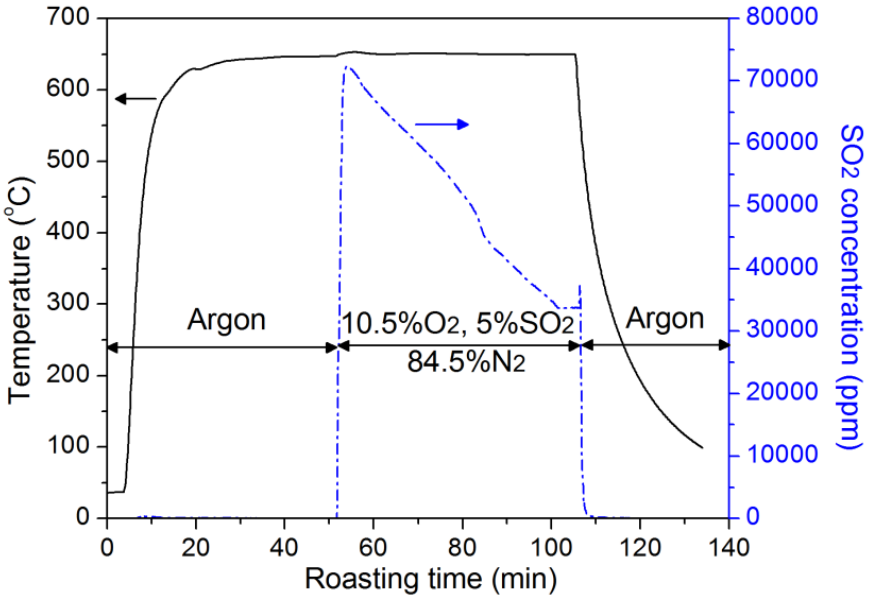

Figure 3.4. Temperature and SO_2 concentration during roasting of sample **Calcine650S**.

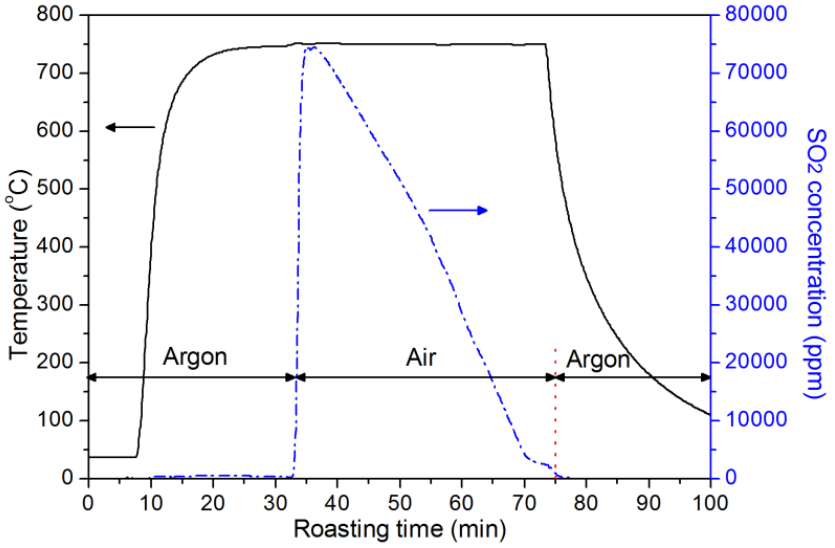

Figure 3.5. Temperature and SO_2 concentration during roasting of sample **Calcine750**.

3.3.2 Leaching Tests

3.3.2.1 Leaching Test 1: DAL of **Calcine650**

Dilute HCl acid leaching of sample **Calcine650** was conducted in this test for 48 hours. The progression of leaching for various elements is shown in Figure 3.6. The degree of sulfur elimination is 69.9% during roasting. The sulfur curve levels off immediately after 0.5 hour leaching and remains constant at 63%. This 63% sulfur that was leached out within very short time most likely existed as sulfates, as sulfates have fast leaching rate due to their direct dissolution into the leachate without chemical transformations involved. In order to further prove that the 63% sulfur is from sulfates, a thermogravimetric analysis (TGA) test was conducted on the sample **Calcine650**. The calcine was heated up to 950 ºC at 15 ºC/min in argon. After the temperature was held at 950 ºC for 10 min, it was lowered to room temperature at 15 ºC/min. The SO_2 concentration in the offgas was analyzed by the gas analyzer. The result is illustrated in Figure 3.7. The weight loss and the emission of SO_2 are due to the decomposition of sulfates, which can be generally described as Reaction (3.10). The weight change is -7.6 mg for 50.5 mg sample. Based on the weight change, the weight fraction of the sulfur as sulfates in the calcine can then be calculated to be 6.00%. While in the leaching test, the weight of the sulfur that was leached into the solution is calculated to be 5.26% of the calcine sample. These two values are in good agreement with each other, indicating the initially removed 63% sulfur has been present in the form of sulfates.

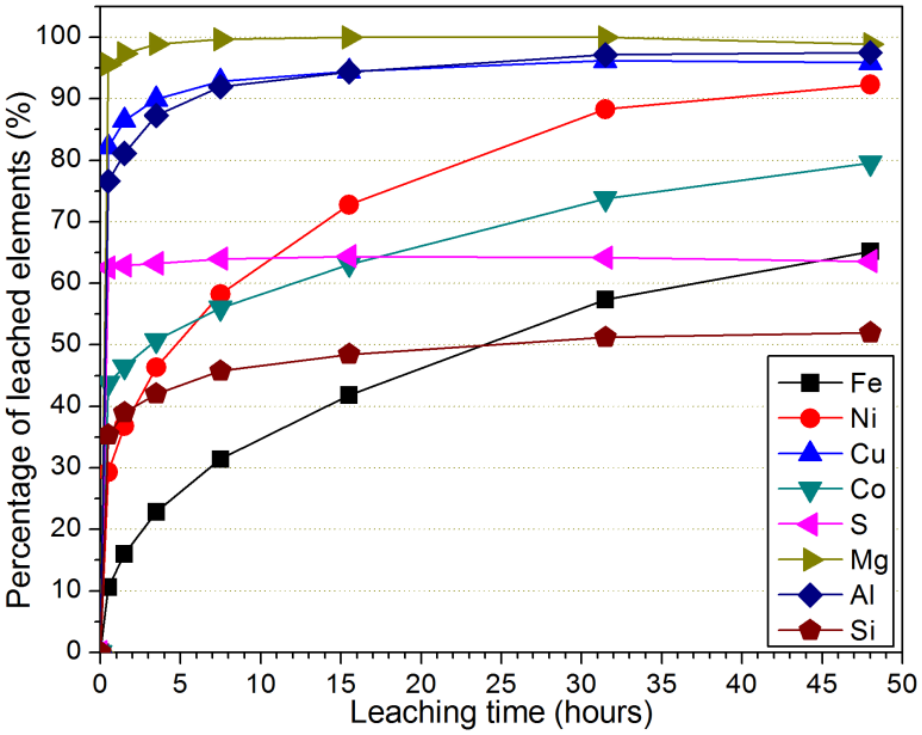

Figure 3.6. Progression of leaching for DAL of **Calcine650**.

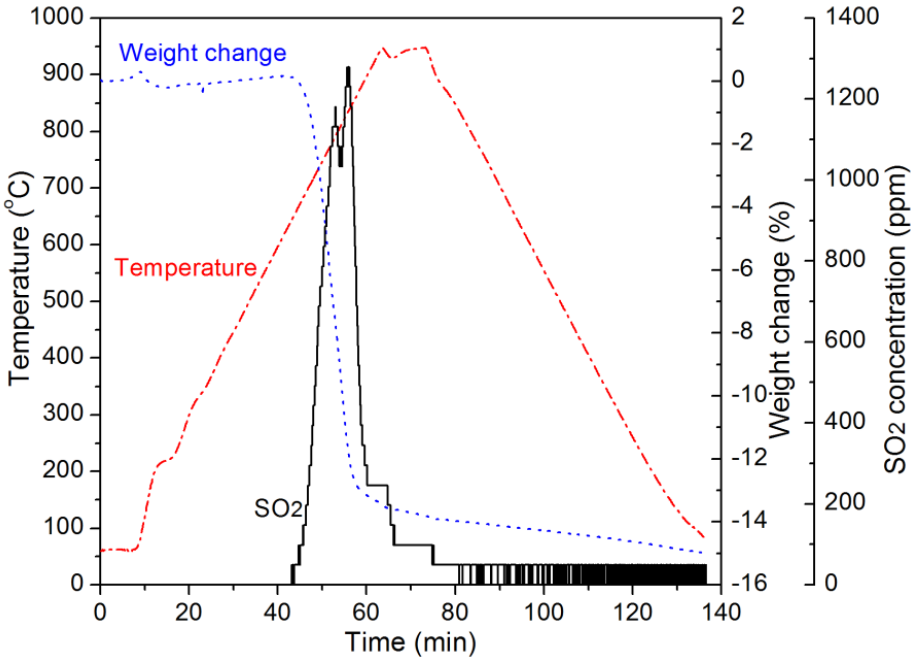

Figure 3.7. Mass change, temperature and the SO_2 concentration in the TGA test for sample **Calcine650**.

$$MeSO_4 \rightarrow MeO + SO_2 + 1/2O_2 \quad (3.10)$$

Based on the EDS analysis of the Raglan concentrate and the calcines, all the Mg and Al are in the siliceous gangue materials. As is shown in Figure 3.6, almost all the Mg was leached in 4 hours. A large portion of Al was also leached although it only weighs 0.40% in the concentrate. However, only around 50% Si was dissolved. This shows that the Mg and Al in the siliceous gangue materials were preferentially attacked by the acid. The percentage of Cu that was leached was also very high, and the dissolution took place primarily in the first 30 minutes, corresponding to the sulfate leaching period. This points to the formation of a large amount of copper sulfate during roasting. The major portion of the Ni was still in the sulfide cores in the calcine based on the EDS analysis. After 48 hours leaching, over 90% of Ni was leached out, indicating that the nickel sulfide cores were gradually attacked by HCl acid. Apart from nickel sulfide, NiO and $NiFe_2O_4$ could also be leached, contributing to the high percentage of Ni extraction. However, the leached percentage of sulfur remains constant although the nickel sulfide core was gradually attacked. The possible reason is the formation of elemental sulfur during the acid leaching of the nickel sulfide cores, which can be represented by Reactions (3.11) and (3.12). These two reactions require the presence of oxidants in the leaching solution (e.g. Fe^{3+}, Cu^{2+}). The leaching profile of Co is similar to that of Ni because of the similarity of these two elements as well as the co-presence of Co as impurities with Ni in the pentlandite. Of all the elements of interests, Fe has the least extent of leaching, which can be seen in Figure 3.6. In sample **Calcine650**, most of the iron is in the form of Fe_2O_3 and $NiFe_2O_4$, accounting for its low dissolution rate. The formation of iron sulfates is limited under the examined conditions due to their relatively low decomposition temperature. Figure 3.8 shows the BSE and optical images of the leach residue. The remains are mainly nickel ferrous ferrite ($Ni_xFe_{3-x}O_4$) and siliceous gangue materials. Most of the oxide rims in the partly oxidized pentlandite particles were broken down into fragments as can be seen in the BSE image. In the optical image, the oxide rim was seen to be relatively intact, in which the sulfide core is mostly leached with very little remains (shown as the white yellow part).

$$Ni_3S_2 \rightarrow Ni^{2+} + 2NiS + 2e^- \quad (3.11)$$

$$NiS \rightarrow Ni^{2+} + S + 2e^- \quad (3.12)$$

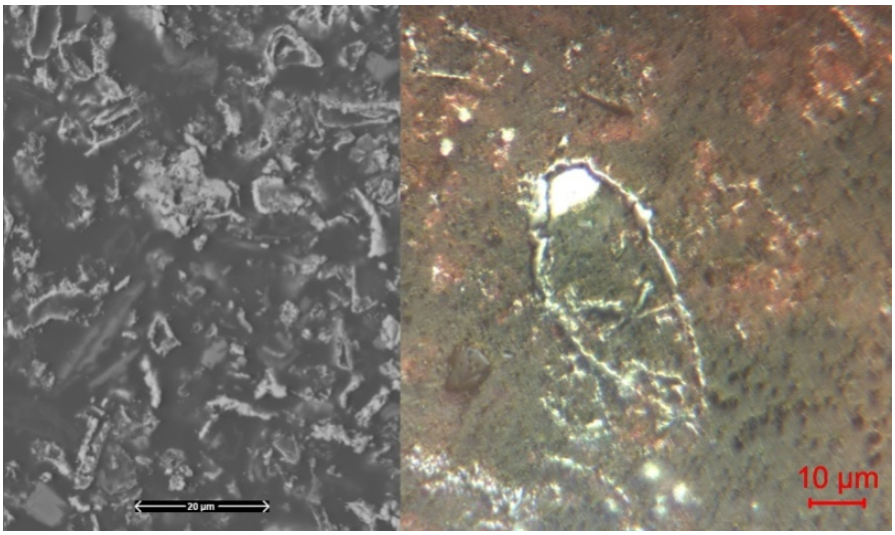

Figure 3.8. BSE and optical images of the leach residue from the DAL of **Calcine650**.

3.3.2.2 Leaching Test 2: HWL of **Calcine650**

Sample **Calcine650** was leached in water at 90 ºC for 5 hours, with the leaching results shown in Figure 3.9. The only water-soluble species in the calcine should be sulfates. The results show that 30 min is long enough to leach all the sulfates into water. After 30 min, the content of most of the species, except Cu and Si, stay relatively constant. Around 63% sulfur was leached after 30 min water leaching, which is consistent with the results from the CAL of **Calcine650**. No sulfates of Fe and Al were formed in the calcine since these two elements were not found in the leaching solution. The content of Cu^{2+} in the leaching solution decreased after 30 min, indicating the Cu^{2+} started to precipitate out. Cu^{2+} precipitation has also been reported in the heap leaching of copper–nickel sulfide ore. Maley, Bronswijk, and Watling [26, 27] studied the interactions of Cu with selected sulfide minerals and the effect of aeration and pH on the Cu recovery. It was claimed that the copper deposition is partly caused by the reaction $Cu^{2+}+H_2S \rightarrow CuS+2H^+$, in which the hydrogen sulfide is the product of the dissolution of pyrrhotite. This copper deposition can occur in the solution with a pH range of 1 to 5, preferentially with pH higher than 2.3. pH plays an important role in the Cu precipitation. When pH is higher than 2.3, Cu^{2+} is precipitated by absorption on or reaction with the sulfide minerals. In the present study, the precipitation of Cu^{2+} is believed to be caused by its reaction with the

sulfide in the calcine, which is represented by Reaction (3.13). Nickel sulfide (Ni_3S_2) in the calcine acts as a source of electrons and sulfur for the reduction of Cu^{2+} and formation of Cu_2S. The slight increase in the content of Ni^{2+} in the leaching solution after 30 min in Figure 3.9 coincides with Reaction (3.13), which produces Ni^{2+} as one product.

$$2Cu^{2+} + Ni_3S_2 \rightarrow NiS + 2Ni^{2+} + Cu_2S \quad (3.13)$$

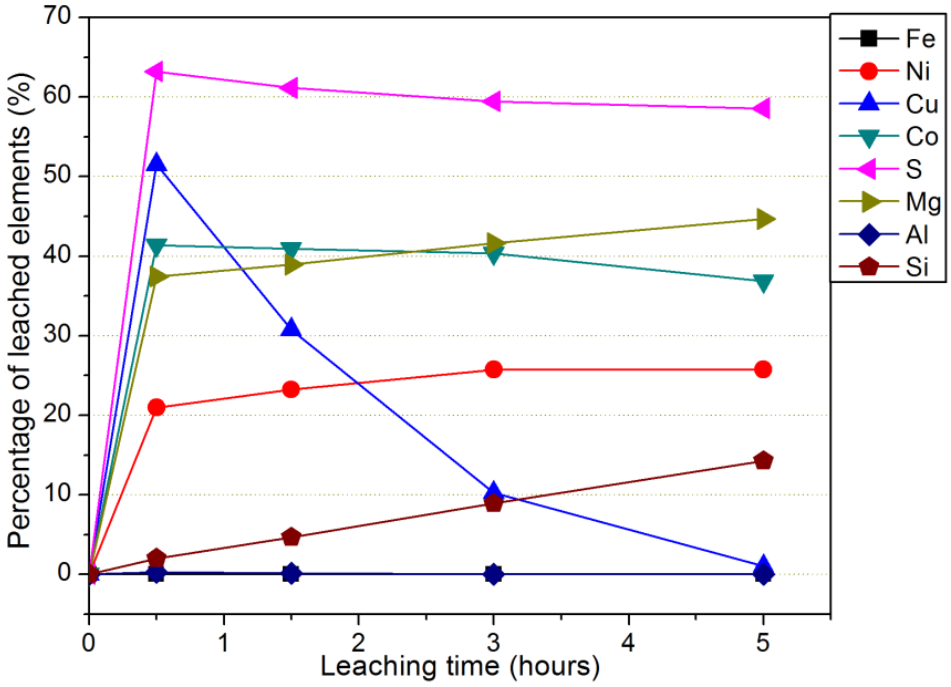

Figure 3.9. Hot water leaching results of sample **Calcine650**.

3.3.2.3 Leaching Test 3: CAL of **Calcine650**

Sample **Calcine650** was leached with concentrated HCl acid (5N) at boiling temperature for 12.75 hours, the results being shown in Figure 3.10. As can be seen, the leaching by concentrated HCl acid is less selective but much faster compared with the DAL results. Most of the species, except Ni and S, were leached into the solution after 2 hours. It is known that the iron compounds in the calcine are mainly hematite Fe_2O_3, magnetite Fe_3O_4, and nickel ferrite $Ni_xFe_{3-x}O_4$. The complete dissolution of iron species shown in Figure 3.10 demonstrates that these three iron-containing compounds are readily attacked by concentrated HCl solution. The

leaching rate of Ni is relatively slow due to the protective elemental sulfur layer formed on the sulfide surface, which diminished further dissolution of the nickel sulfide cores. As can be seen in Figure 3.11, the main minerals in the leach residue are siliceous gangue materials, nickel sulfide and elemental sulfur. Small particles of nickel sulfide cores were completely leached forming elemental sulfur particles. For larger sulfide particles in which the leaching was incomplete, an elemental sulfur layer can be clearly observed on the surface of the sulfide.

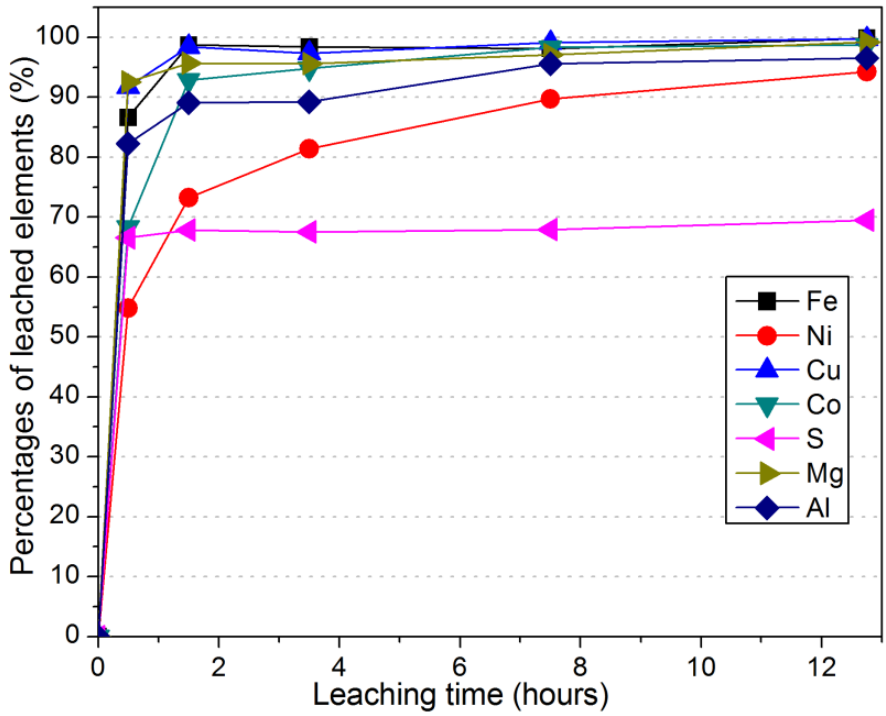

Figure 3.10. Concentrated HCl acid leaching behavior of sample **Calcine650**.

XRD analysis was used to determine the mineralogical composition of the leach residue, with the spectrum shown in Figure 3.12. The formation of elemental sulfur is confirmed by the dominant peaks of S_8 in the XRD pattern. It also shows the presence of another phase Ni_xS_6 as a by-product. Based on its stoichiometry, this phase should be an intermediate product during the oxidative transformation of nickel sulfide Ni_3S_2 to Ni^{2+} and elemental sulfur S_8. The dissolution of Ni_3S_2 forming Ni^{2+} and S_8 requires an oxidant. It is clear that the main oxidant in the leaching solution should be Fe^{3+} from the dissolution of iron oxides. In this scenario, Reactions (3.14) and (3.15) are tentatively suggested as the mechanism of the dissolution of nickel sulfide in the present study: nickel sulfide core (Ni_3S_2) is first oxidized by Fe^{3+} in the highly acidic solution

with the preferential dissolution of metallic ions into the solution, forming solid Ni_xS_6 on the surface of the sulfide; the Ni_xS_6 is then further oxidized by the Fe^{3+} forming elemental sulfur. Figure 3.13 schematically illustrates the dissolution of a Ni_3S_2 particle with the presence of the oxidant Fe^{3+} in the HCl solution. Ni_xS_6 should be found as a layer beneath the elemental sulfur rim. The non-stoichiometry of Ni_xS_6, as well as the rate controlling step which should be ionic diffusion through the solid product, suggest a decreasing content of Ni in Ni_xS_6 from the sulfide core to the surface, which is exhibited in Figure 3.13. The morphological feature of the incompletely leached nickel sulfide with elemental sulfur rim is shown in Figure 3.14. The Ni_xS_6 layer could not be clearly differentiated from elemental sulfur using EDS due to its low content of Ni.

$$3Ni_3S_2 + (18-2x)Fe^{3+} \rightarrow Ni_xS_6 + (9-x)Ni^{2+} + (18-2x)Fe^{2+} \quad (3.14)$$

$$Ni_xS_6 + 2xFe^{3+} \rightarrow 3/4S_8 + xNi^{2+} + 2xFe^{2+} \quad (3.15)$$

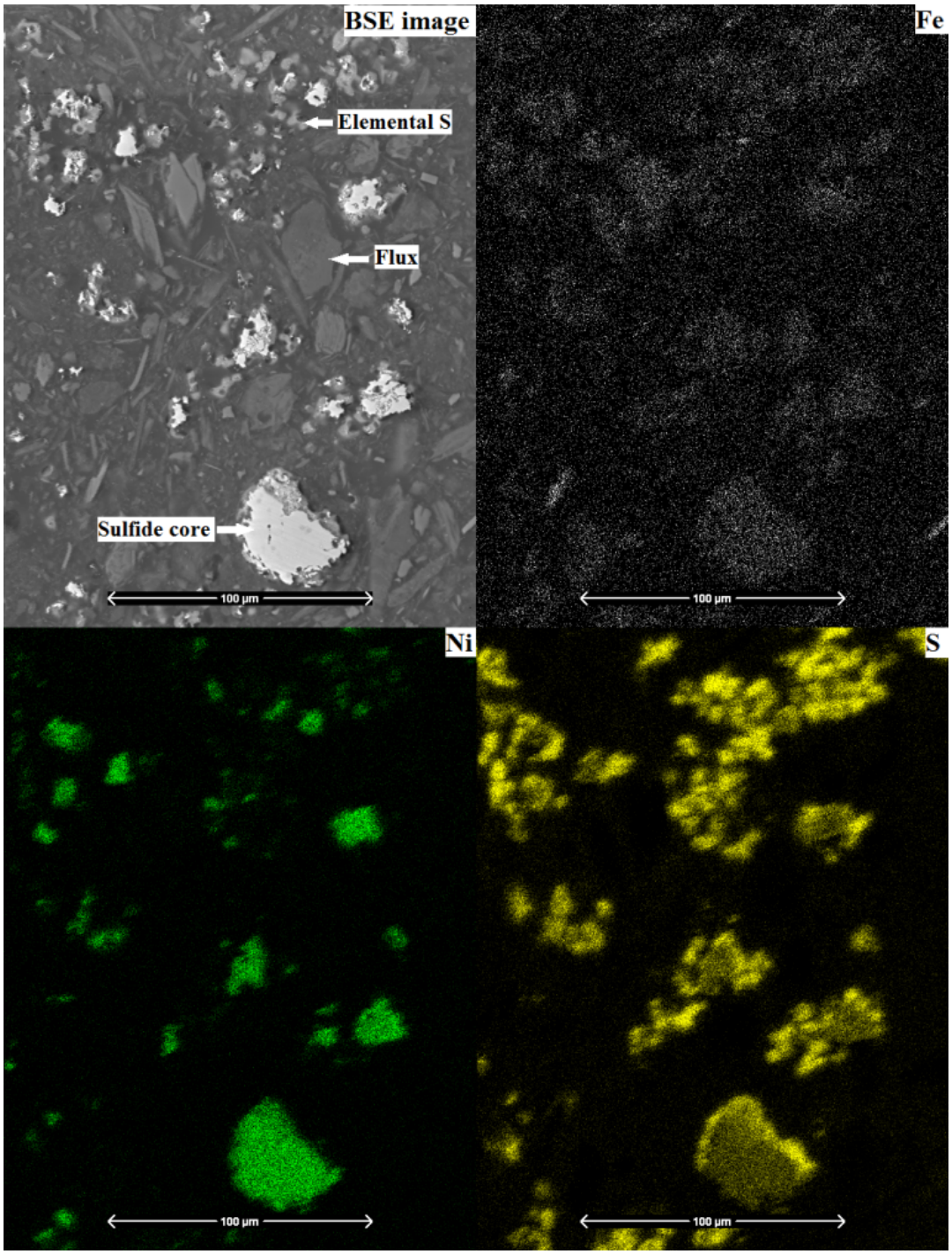

Figure 3.11. BSE image and elemental maps of Fe, Ni, and S of the leach residue from the CAL of **Calcine650**.

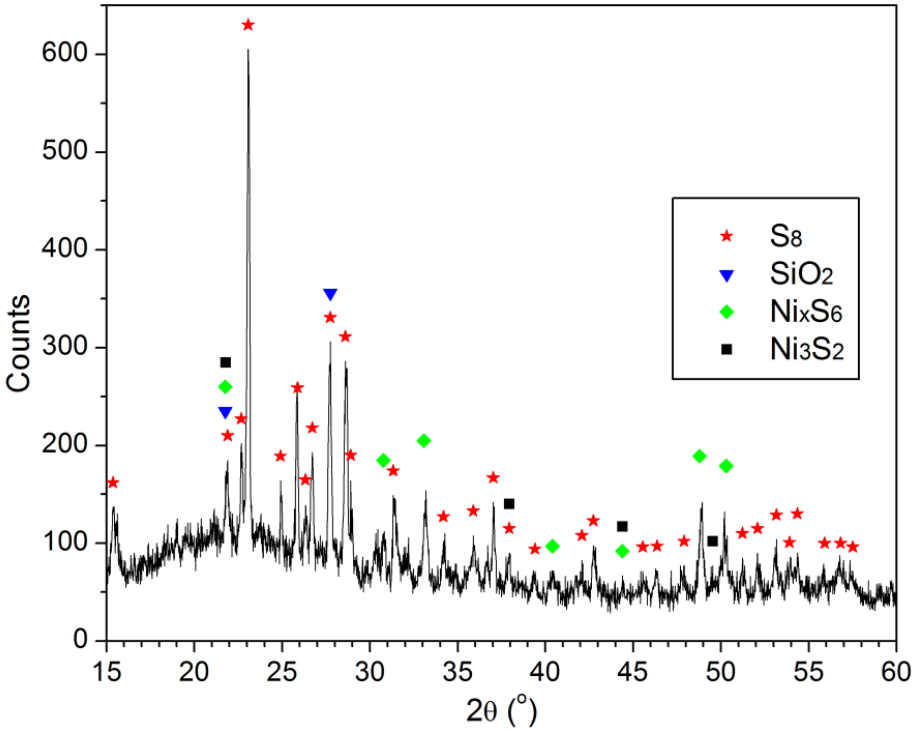

Figure 3.12. XRD pattern for the residue from the CAL of **Calcine650**.

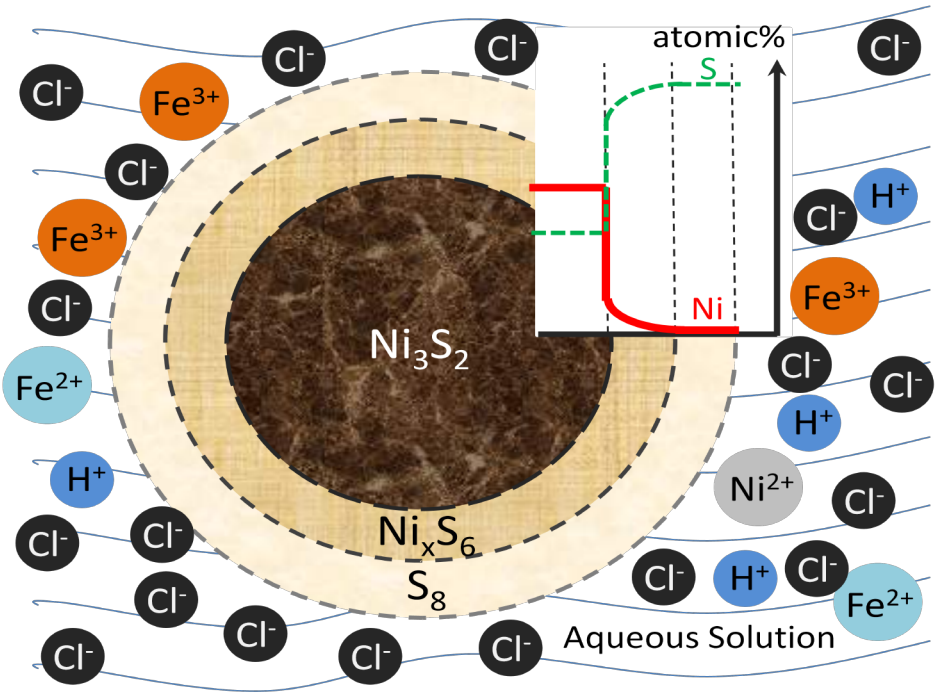

Figure 3.13. Schematic representation of the oxidative dissolution of Ni_3S_2 in HCl solution with the presence of Fe^{3+}.

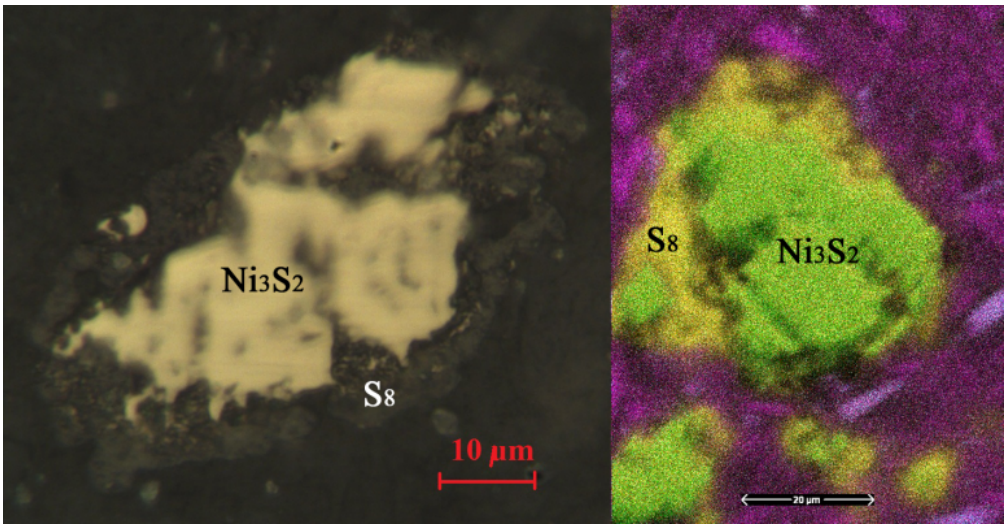

Figure 3.14. Optical and elemental mapping images showing the morphological features of the nickel sulfide core covered with elemental sulfur rim.

3.3.2.4 Leaching Test 4: DAL of **Calcine650S**

Partly sulfation roasted sample **Calcine650S** was leached with dilute HCl solution, the results being shown in Figure 3.15. The profiles of the leaching curves are similar to those of the DAL of **Calcine650**. The sulfur dissolution is approximately 72%, which is 9% higher than that of the DAL of **Calcine650**, indicating the higher amount of sulfate formation. The amount of sulfate formation of Ni, Co, and Cu, which could be estimated based on the 30 min data in Figure 3.15, are all higher than in Figure 3.6. The formation of $NiSO_4$ is still very low (34%) after the sulfation roasting for 56 min, due to the protective layer of $NiSO_4$ formed which inhibited further sulfation [3]. It can also be observed that the dissolution of Si increased from 52% (in Figure 3.6) to 87% (in Figure 3.15), showing higher susceptibility of Si in the form of silicate to acid leaching after sulfation roasting. Elemental sulfur must also have formed from the dissolution of the nickel sulfide, indicated by the constant percentage of sulfur dissolution after 0.5 hour in Figure 3.15.

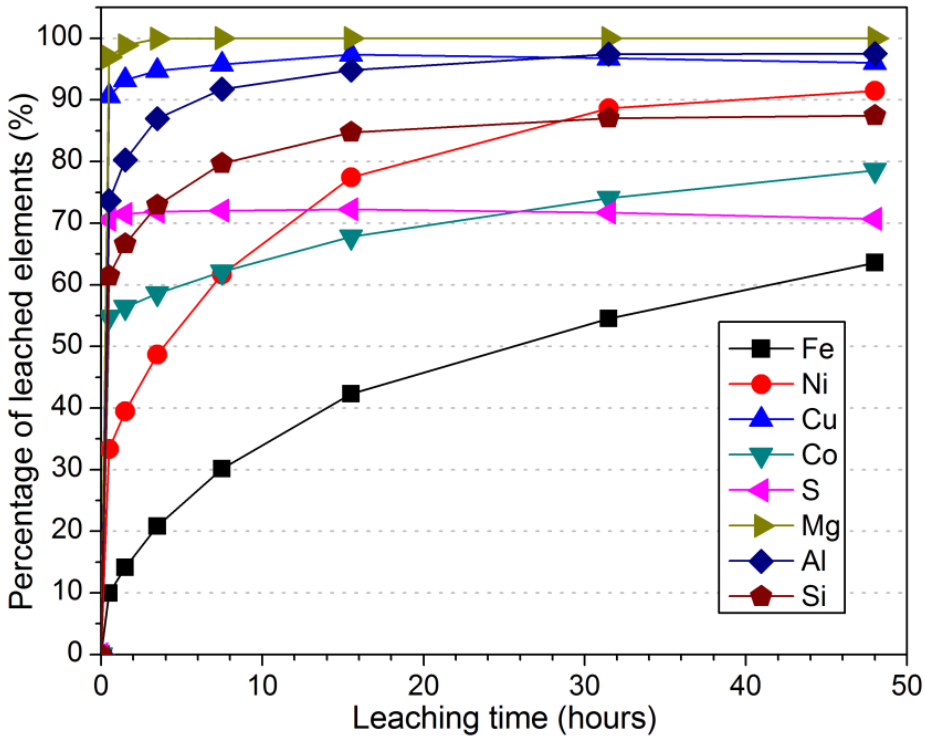

Figure 3.15. Dilute HCl acid leaching results of the sample **Calcine650S** based on the ICP analysis.

3.3.2.5 Leaching Test 5: DAL of **Calcine750**

In order to investigate the leaching behavior of calcine roasted at higher temperature, the calcine, generated by roasting the Raglan concentrate at 750 ºC, was leached with dilute HCl acid. The degree of sulfur elimination of this calcine is 91.8%, much higher than that of the **Calcine650**. As is shown in Figure 3.16, 98% of sulfur in the calcine was leached as sulfates within 0.5 hour, and the balance is sulfides, which indicates that the weight ratio of sulfates to sulfides in the calcine increases with the increase of roasting temperature. Compared with the results of the Leaching test 1, much lower percentages of elements of interest, i.e., Ni, Cu, and Co, were dissolved at the beginning of the leaching process, because of the lower percentages of these elements existing as sulfates in the **Calcine750**. The iron profile in Figure 3.16 is lower than that in Figure 3.6, especially at the beginning. Apparently, this has no relation with the formation of sulfates, since no iron sulfates were formed in both calcines. But at higher degree

of roast, a larger amount of the iron species in the concentrate would be oxidized to Fe_2O_3 than to Fe_3O_4. A previous study by other researchers demonstrated the relative reactivity of hematite, magnetite, and nickel ferrite in HCl solution is in the order Fe_3O_4>>Fe_2O_3>$NiFe_2O_4$ [19], in other words, the leaching rates of these three compounds would be in the same order. The lower fraction of magnetite in the **Calcine750** than in the **Calcine650** is partially responsible for the lower leaching rate of iron in Figure 3.16 than that in Figure 3.6. Similarly, more nickel ferrite forms when the concentrate is roasted at higher temperature, especially above 700 ºC. The leaching rate of nickel ferrite is rather slow, which is another factor that contributes to the slower leaching rate of nickel in this leaching test, apart from the fact that less fraction of nickel sulfate exists in the **Calcine750**.

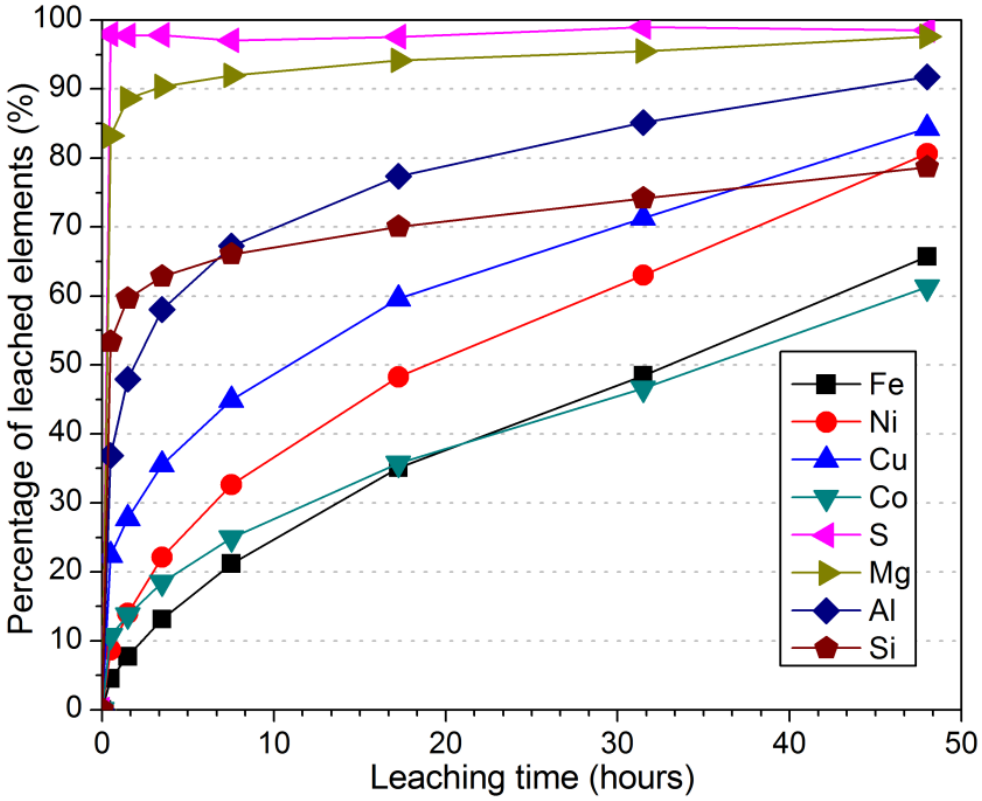

Figure 3.16. Dilute HCl acid leaching results of sample **Calcine750**.

3.4 Conclusions

Water leaching and non-oxidative HCl leaching tests were performed on the calcines produced by roasting the nickel concentrate under various conditions. Results show that all sulfates could be leached by water within 30 min. Longer leaching time results in the slow precipitation of Cu^{2+} possibly due to its reaction with the nickel sulfide in the calcine. In acid leaching of calcine, the formation of elemental sulfur would inhibit the dissolution of the nickel sulfide in the calcine. Substantial amount of iron species was also leached along with the dissolution of non-ferrous metal species in the non-oxidative acid leaching of the calcine. Leaching the calcine with stronger HCl solution is much faster but less selective. Calcine produced at higher temperature was less susceptible to acid leaching due to the formation of more acid-resistant compounds, such as $NiFe_2O_4$ and Fe_2O_3.

3.5 References

[1] V.M. Zamalloa, Mechanisms of roasting, reduction and smelting of Ni-Cu concentrates, Ph.D. thesis, University of Toronto, Toronto, Ontario, Canada, 1995.

[2] M. Zamalloa, T.A. Utigard, The behaviour of Ni-Cu concentrate in an industrial fluid bed roaster, Canadian Metallurgical Quarterly, 35 (1996) 435-449.

[3] D. Yu, T.A. Utigard, TG/DTA study on the oxidation of nickel concentrate, Thermochimica Acta, 533 (2012) 56-65.

[4] P.G. Thornhill, E. Wigstol, G.V. Weert, The falconbridge matte leach process, JOM, 23 (1971) 13-18.

[5] G.N. Lewis, M. Randall (Eds.) Thermodynamics, McGraw Hill Book Company, Toronto, 1961, pp. 316-317.

[6] H. Majima, Y. Awakura, T. Mishima, The Leaching of Hematite in Acid Solutions, Metallurgical Transactions B, 16 (1985) 23-30.

[7] K. Bhuntumkomol, K.N. Han, F. Lawson, The leaching behaviour of nickel oxides in acid and in ammoniacal solutions, Hydrometallurgy, 8 (1982) 147-160.

[8] E. Peters, Direct Leaching of sulfides: Chemistry and applications, Metallurgical Transactions B, 7 (1976) 505-517.

[9] F.A. Forward, Ammonia pressure leach process for recovering nickel, copper, and cobalt from Sherritt Gordon nickel sulfide concentrates, Transactions C.I.M., 56 (1953) 373.

[10] M.J. Nicol, The non-oxidative leaching of oxides and sulphides: an electrochemical approach, in: K.Osseo-Asare, J.D. Miller (Eds.) Hydrometallurgy: Research, Development and Plant Practice, Proc 3rd Int Symp Hydrometall, 112th AIME Annu Meet, Atlanta, Georgia, 1983, pp. 177-195.

[11] N. Valverde, Investigation on the rate of dissolution of metal oxide in aqueous solutions with addition of redox couples and complexing agents, Berichte der Bunsen-Gesellschaft für Physikalische Chemie, 80 (1976) 333-340.

[12] M.J. Pryor, The reductive dissolution of ferric oxide in acid. Part III. The mechanism of reductive dissolution, Journal of the Chemical Society (Resumed), 0 (1950) 1274-1276.

[13] M.J. Pryor, U.R. Evans, The reductive dissolution of ferric oxide in acid. Part I. The reductive dissolution of oxide films present on iron, Journal of the Chemical Society (Resumed), 0 (1950) 1259-1266.

[14] M.J. Pryor, U.R. Evans, The reductive dissolution of ferric oxide in acid. Part II. The reductive dissolution of powdered ferric oxide, Journal of the Chemical Society (Resumed), 0 (1950) 1266-1274.

[15] K. Jibicki, Acid decomposition reactions on compounds and minerals in the Fe-Ni-Sulphide system, Ph.D. thesis, University of British Columbia, Vancouver, Canada, 1974.

[16] L.A. García Rodenas, M.A. Blesa, P.J. Morando, Reactivity of metal oxides: Thermal and photochemical dissolution of MO and MFe_2O_4 (M=Ni, Co, Zn), Journal of Solid State Chemistry, 181 (2008) 2350-2358.

[17] T.R. Ingraham, H.W. Parsons, L.J. Cabri, Leaching of pyrrhotite with hydrochloric acid, Canadian Metallurgical Quarterly, 11 (1972) 407-411.

[18] I.H. Warren, G.I.D. Roach, Physical aspects of the leaching of goethite and hematite, Transactions of the Institution of Mining and Metallurgy, 80 (1971) C152-155.

[19] Z.-Y. Lu, D.M. Muir, Dissolution of metal ferrites and iron oxides by HCl under oxidising and reducing conditions, Hydrometallurgy, 21 (1988) 9-21.

[20] K. Nut, On the dissolution behavior of NiO, Corrosion Science, 10 (1970) 571-583.

[21] J.M. Diggle, Dissolution of oxide phases, in: J.M. Diggle (Ed.) Oxides and oxide films, Marcel Dekker, New York, 1973, pp. 285-386.

[22] M.C. Jha, J.R. Carlberg, G.A. Meyer, Hydrochloric acid leaching of nickel sulfide precipitates, Hydrometallurgy, 9 (1983) 349-369.

[23] H. Majima, Y. Awakura, Leaching of oxides and sulphides in acidic chloride media, in: Extraction Metallurgy '85 Symposium, Institution of Mining and Metallurgy, London, UK, 1985, pp. 607-627.

[24] F. Habashi, A textbook of hydrometallurgy 2nd ed., Laval University, Quebec, Canada, 1999.

[25] N.F. Dyson, T.R. Scott, Acid leaching of nickel sulphide concentrates, Hydrometallurgy, 1 (1976) 361-372.

[26] M. Maley, W. van Bronswijk, H.R. Watling, Leaching of a low-grade, copper–nickel sulfide ore: 2. Impact of aeration and pH on Cu recovery during abiotic leaching, Hydrometallurgy, 98 (2009) 66-72.

[27] M. Maley, W. van Bronswijk, H.R. Watling, Leaching of a low-grade, copper–nickel sulfide ore. 3. Interactions of Cu with selected sulfide minerals, Hydrometallurgy, 98 (2009) 73-80.

4 Fluidized Bed Oxidation Roasting

4.1 Introduction

In an attempt to lower the environmental footprint of nickel processing, and as an alternative process to treat nickel sulfide concentrate, a two-stage oxidation-sulfation roasting process followed by leaching was proposed and investigated. Sulfation roasting to treat nickeliferous sulfide ores or low grade concentrates was investigated in the period from 1960s to 1990s [1-10]. In general, the sulfation roasting process suffers from the drawbacks of slow kinetics and low recovery of non-ferrous metals, Ni in particular, due to the formation of nickel ferrite ($NiFe_2O_4$) at high temperatures (>700 °C) which is resistant to sulfation. These studies in general lack detailed investigation on the kinetics and mechanisms of the sulfation roasting of nickel sulfide concentrate. In addition, with more stringent environmental regulations, a renewed interest in further studying the prospects of the proposed technology is warranted. The scope of the thesis includes two-stage oxidation-sulfation roasting, leaching of the calcines, and further recovery of Ni from the leach residue through high temperature reduction. This chapter and the following one focus on the optimization of the roasting steps using the fluidized bed technique with the aim of maximizing recovery of valuable metals into the leach solution. The recovery of Ni from the leach residue was also studied and will be discussed later. This chapter presents an overview of the methods and findings from fluidized bed oxidation roasting of nickel concentrates. The results from the investigation of the second stage, i.e. sulfation roasting, are presented in the next chapter.

4.2 Materials and Methods

4.2.1 Materials

Raglan concentrate from Xstrata Nickel's smelter in Sudbury, Canada was used in the experiments. Please refer to Section 2.2.1 for the characteristics of the concentrate.

4.2.2 Experimental

Compared to oxidation roasting, sulfation roasting is characterized by slow kinetics and strong dependence on temperature [11]. In order to achieve the highest possible reaction rates and accurate temperature control during the roasting process, fluidized bed technique was employed. A laboratory scale, batch-operated fluidized bed roaster was designed and constructed to allow conducting both the oxidation and sulfation roasting experiments (Figure 4.1).

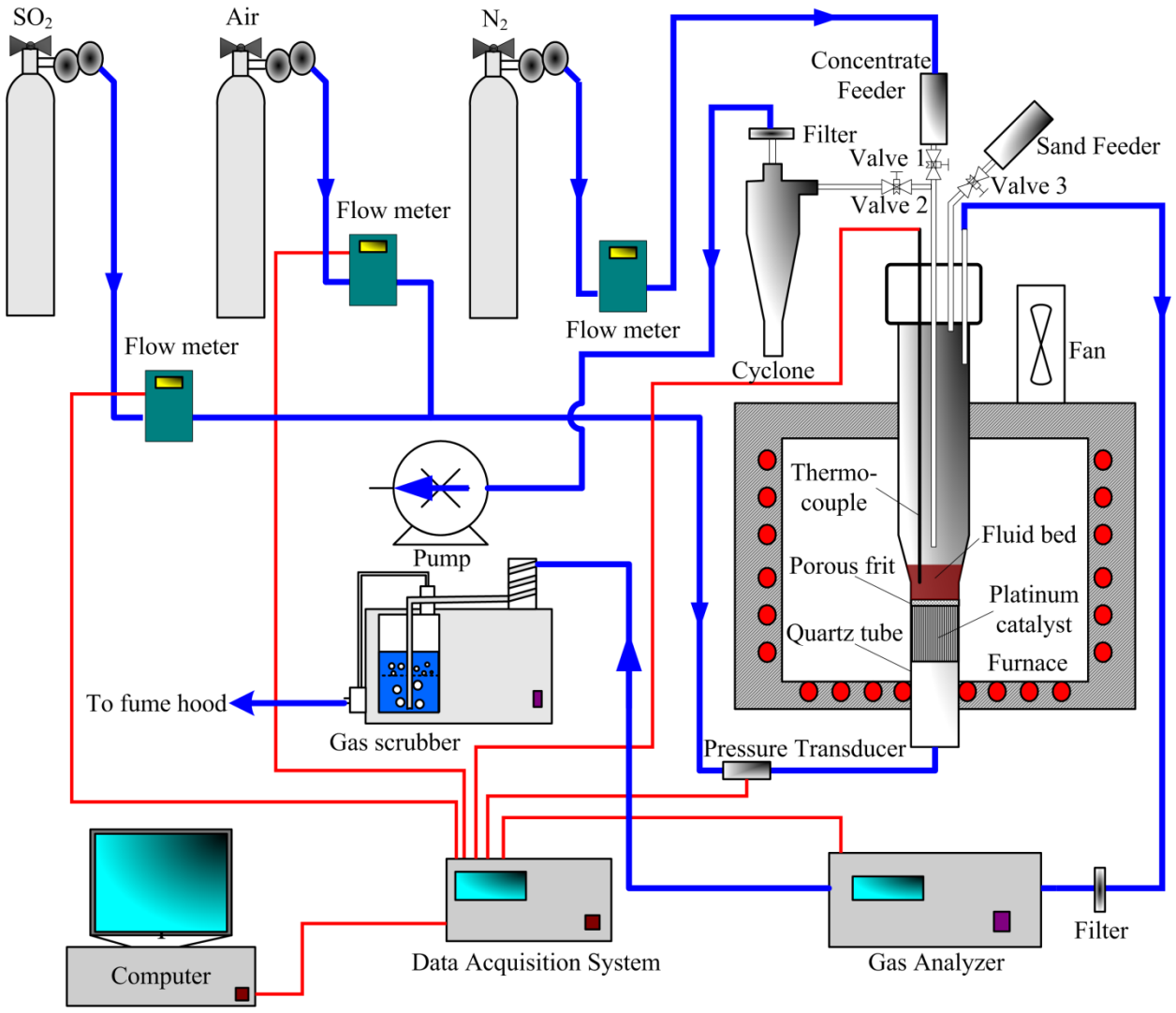

Figure 4.1. Schematic of the batch-wise fluidized bed experimental setup.

The diameter of the lab scale fluidized bed roaster is a very important parameter partly due to the wall effect, part of the fluidized bed near the roaster wall being less mobile than the centre

due to the uneven distribution of the feeding gas [10]. If the diameter of the fluidized bed is too small, the wall effect would be so prominent that it would result in poor fluidization and prevent smooth operation [12]. On the other hand, the gas consumption would be higher with higher fluidized bed diameter, given the same gas flow velocity in the bed. In the present work, a clear quartz tube with inner diameter of 36mm with an expanded top (66 mm inner diameter) was used as the roasting reaction vessel. All dimensions are shown in Figure 4.2. A porous frit was fused in the quartz tube acting as the gas distributor. The purpose of this design is to lower the velocity of the gas in the freeboard above the fluidized bed, thus alleviating the gas entrainment of solid particles. The quartz tube was mounted vertically in an electric furnace as shown in Figure 4.1. Its top opening was sealed with a brass cap to prevent the leakage of the offgas.

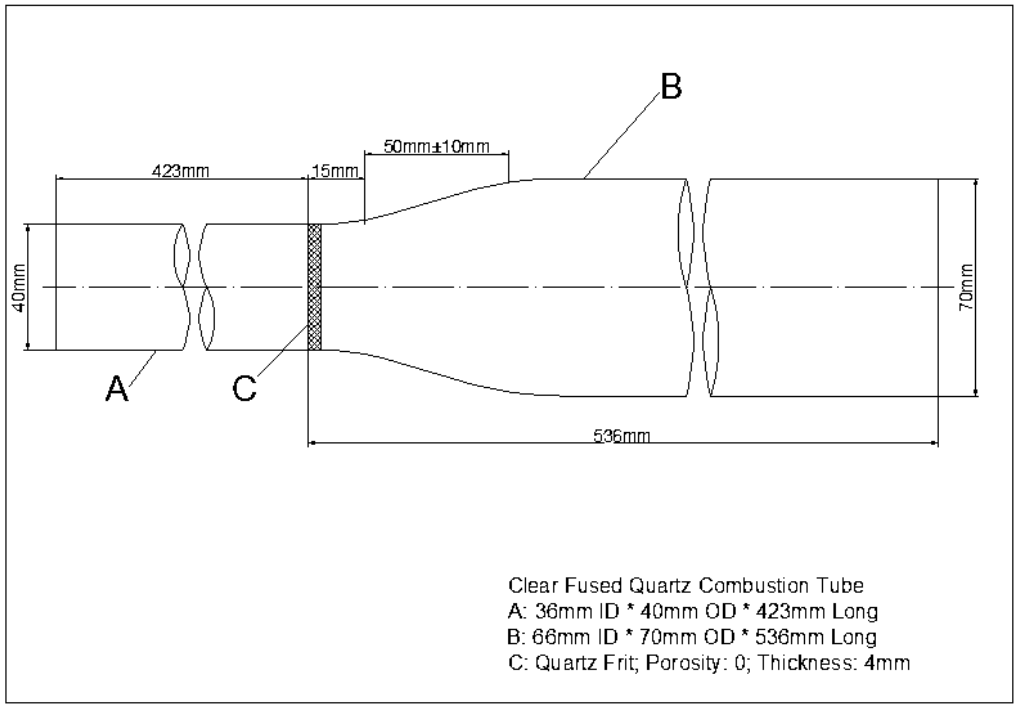

Figure 4.2. Dimensions of the fused quartz combustion tube.

Roasting gas was fed from the bottom of the quartz tube. The offgas was cleaned in a gas scrubber (Buchi Scrubber B-414) to eliminate SO_2 before venting to the fume hood. A pneumatic dispenser was used to feed the concentrate to the sealed chamber using nitrogen as the carrier gas. During the roasting experiment, the temperature of the fluidized bed was measured using a K-type thermocouple. The pressure drop across the bed and the porous frit

was measured by a pressure transducer (OMEGA PX302-015GV). The offgas was directed to a multi-channel gas analyzer (ABB EL3020) to measure its SO_2 and O_2 contents. These above data along with the feeding gas flowrate were recorded using a computer controlled data acquisition system (FLUKE Hydra Series II). A platinum catalyst was mounted beneath the porous frit only for the sulfation roasting experiments. Once the fluidized bed roasting experiment was completed, the calcine was withdrawn from the quartz tube immediately. This was accomplished using a vacuum pump which collects the calcine into a cyclone via a long ceramic tube. Quick collection of calcine out of the quartz tube was necessary to prevent decomposition of sulfates at high temperature.

Preliminary experiments were carried out to fluidize the Raglan concentrate but all failed. Channels were formed within the bed through which the feeding gas escaped. The concentrate was then fused together due to the immobility of the bed and the highly exothermic reactions occurring in the bed. This failure of fluidization is due to the fact that the Raglan concentrate falls into Group C in the Geldart classification of powders according to the particle size distribution of the Raglan concentrate in Figure 2.3 and the Geldart classification in Figure 1.4. The interparticle forces are greater than the force exerted by the up-flowing gas, resulting in the formation of channels instead of the concentrate being fluidized. On the contrary, sand can be easily fluidized and is classified in Group B. It is reasonable to believe that the fluidity of the concentrate could be enhanced by mixing it with sand. The particle size range of the sand should be different from that of the Raglan concentrate to render the effective separation of calcine from the sand after roasting by sieving. Trial experiments were performed to maximize the fluidity of the mixture of the Raglan concentrate and sand. The results showed that the particle size range of the sand should be as close to that of the Raglan concentrate as possible, to avoid the appreciable physical separation of sand and concentrate into separate layers during roasting. As a result, the particle size range of the sand was 150–212 μm. In addition, the weight ratio of sand to concentrate should be no less than around 4 to render a fluidized bed with enough mobility to avoid large agglomeration due to local overheating. Based on these results, a batch of 5 gram Raglan concentrate was mixed with 20 gram sand with the particle size range between 150 μm and 212 μm before roasting tests. Separation between the resulting calcine and the sand can be conducted based on the particle size range difference between these two simply by sieving.

Two series of oxidizing roasting tests were performed to study the effect of temperature and roasting time on the extent of oxidation and reaction products. In the first series of tests, the temperature was varied in the range 650–775 °C. The roasting was terminated by withdrawing the calcine (and sand) when the SO_2 concentration of the offgas dropped below 0.3 vol%, which is an indication of the near-completion of the roasting reactions. While in the second set, the temperature was maintained at 750 °C and roasting times from 1 to 13 minutes were examined. The collected calcines were subjected to various analyses to evaluate the roasting performances.

4.2.3 Analytical Methods

The calcines were leached in water at 90 ºC for 30 min to evaluate the amount of sulfate formation during roasting. The hot water leaching tests were conducted in the following way.

(1) Raise the temperature of the water bath to 90 ºC. Set the stirring rate to be 250 rpm.

(2) Measure 15 mL deionized water and put it into a 150 mL flask. Put a magnetic stirrer in the flask. Heat it in the water bath while stirring.

(3) Weigh around 100 mg calcine to be leached and grind it using the mortar and pestle for 10 minutes.

(4) Weigh 60 mg calcine that was grinded and put it into the deionized water for leaching for 30 minutes.

(5) After 30 minutes leaching, cool the leachate in tap water and filter it. Wash the flask and the residue.

(6) Dilute the solution to 25 mL using volumetric flask.

(7) Collect 14 mL solution for ICP analysis.

The leach residues were fully digested in water by firstly fusing them in sodium peroxide (Na_2O_2). And the procedure is as follows:

(1) Weigh 4 gram Na_2O_2 and put it in a 20 mL zirconium crucible.

(2) Weigh 0.5 gram sample to be fused and spread it on top of the Na_2O_2 in the crucible.

(3) Blend the Na_2O_2 and the sample thoroughly using a platinum wire.

(4) Weigh 1 gram of Na_2O_2 and spread it on top of the mixture as a thin layer.

(5) Cover the crucible with a zirconium cover.

(6) Heat the crucible with a propane blow torch using the outer flame with a distance of around 0.5 cm between the bottom of the crucible and the tip of the inner flame, and time it.

(7) Swirl the sample after it melts. After around 3 minutes when no solid residue can be observed, cool the crucible by taking it away from the flame and putting it on a clean Al plate.

(8) Put a Teflon beaker with a cover on a hotplate, and put the Zr crucible into the Teflon beaker.

(9) Add water slowly using syringe needle drop by drop into the Zr crucible until no evident sputtering can be seen when water is added.

(10) Slowly add 30 mL 18 wt% HCl into the Zr crucible drop by drop to avoid sputtering. When water or acid is added into the Zr crucible, Teflon cover should always be placed on top of the beaker to prevent the solution from splashing out.

(11) Wash the underside of the Teflon cover and the inner wall of the Teflon beaker, and also the entire Zr crucible. (At this time, no residue should be seen.)

(12) Take the Teflon beaker away from the hotplate and allow it to cool. Transfer the solution into a 100 mL volumetric flask and take to the volume.

(13) Take 0.67 mL solution with pipette and transfer it into a 10 mL volumetric flask and take to volume for ICP analysis.

Solutions from both leaching and Na_2O_2 fusion were properly diluted and analyzed by inductively coupled plasma optical emission spectrometry (ICP-OES) for chemical composition determination and calculation of the percentages of the formation of water-soluble species based

on Eq. (4.1), in which $W_{(Me,\ leach\ solution)}$ represents the weight of species Me in the leach solution and $W_{(Me,\ leach\ residue)}$ represents the weight of species Me in the residue calculated based on the ICP results.

$$wt\%_{(Me,\ water\text{-}soluble)} = \frac{W_{(Me,\ leach\ solution)}}{W_{(Me,\ leach\ solution)} + W_{(Me,\ leach\ residue)}} \times 100 \quad (4.1)$$

Samples were also analyzed by XRD using a Philips PW2273/20 diffractometer. Calcines were further examined by scanning electron microscopy (SEM, JEOL JSM6610-Lv) equipped with EDS detector (Oxford/SSD) for characterization of the morphology and the mineralogy of the phases formed. Composition of the sulfide cores of the calcines was determined by a Cameca SX50 electron probe microanalyzer (EPMA) equipped with 3 tunable wavelength dispersive spectrometers. Operating conditions were 40º takeoff angle, and a beam energy of 20 keV. The beam current was 20 nA, and the beam diameter was 1 μm. Elements were acquired using analyzing crystals LiF for Fe K_α, Ni K_α, Cu K_α, Co K_α, PET for S K_α, and PC1 for O K_α. The standards were hematite for O K_α, cobaltite for Co K_α, pentlandite for S K_α, Fe K_α, Ni K_α, and chalcopyrite for Cu K_α. The counting time was 20 seconds for Fe K_α, Ni K_α, Cu K_α, S K_α, 40 seconds for O K_α, and 60 seconds for Co K_α.

4.3 Results and Discussion

4.3.1 Characterization of the Fluidized Bed Roaster

4.3.1.1 Determination of the Minimum Fluidization Velocity (V_{mf})

In order to determine the minimum allowable flowrate of the feeding gas, the V_{mf} needs to be determined first. Figure 4.3 shows the calculated V_{mf} from Equations (1.6) to (1.8) as a function of the particle size and the roasting temperature using air as the roasting gas to roast a mixture of 20 g sand and 5 g Raglan concentrate. The density of the solid is taken as the average density of the solid mixture, which is 2872 kg/m^3. As can be seen, larger particles require a larger velocity of air to fluidize. Because the thermophysical properties of air are functions of the temperature, V_{mf} is also affected by the roasting temperature as a result, showing as a decreasing trend with

the increase of temperature. The average particle size of the fluidized bed is in the vicinity of 170 µm. The V_{mf} is approximately 0.013 m/s given the roasting temperature of 700 ºC.

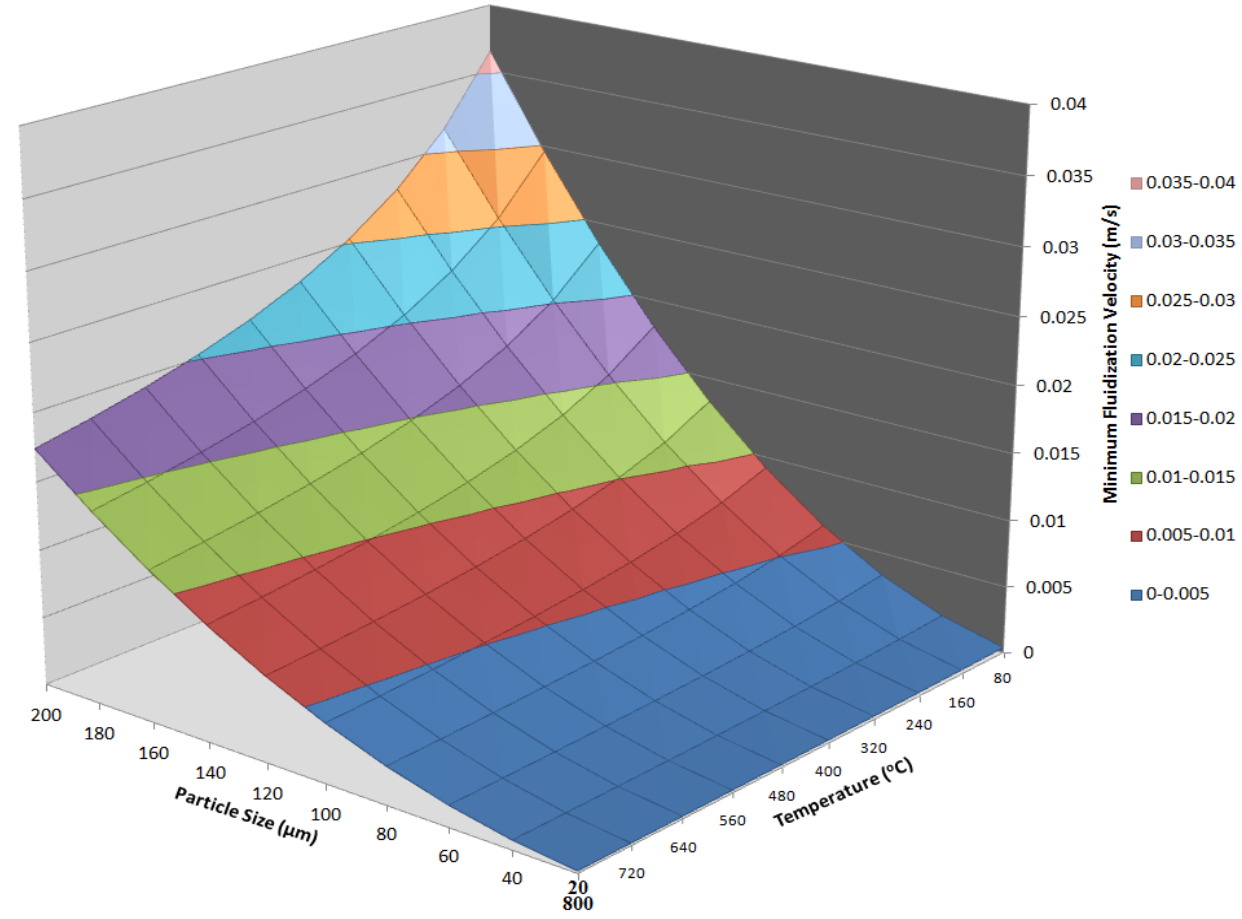

Figure 4.3. Calculated minimum fluidization velocity as a function of particle size and temperature for the roasting of 20 g sand + 5 g Raglan concentrate using air.

The V_{mf} is further determined experimentally using the pressure drop method at 700 ºC. During roasting, the pressure measured beneath the porous frit has two components: the pressure drop across the bed and the pressure drop across the porous frit. In Figure 4.4, the pressure drop across the porous frit is plotted as a function of the gas velocity when no feeding material is added. 20 g sand and 5 g Raglan concentrate was then put in the quartz tube, and the pressure beneath the frit was measured again and was also plotted in Figure 4.4. The pressure drop across the bed was calculated by taking the difference of the two curves in Figure 4.4, which is shown in Figure 4.5. As can be seen, the pressure drop across the fixed bed increases with the increase

of gas velocity. The transition from fixed bed to fluidized bed is denoted by the sudden drop in the pressure drop. The experimentally determined V_{mf} is 0.06 m/s at 700 ºC read from Figure 4.5. This minimum fluidization velocity corresponds to a feeding gas flowrate of 1.1 L/min.

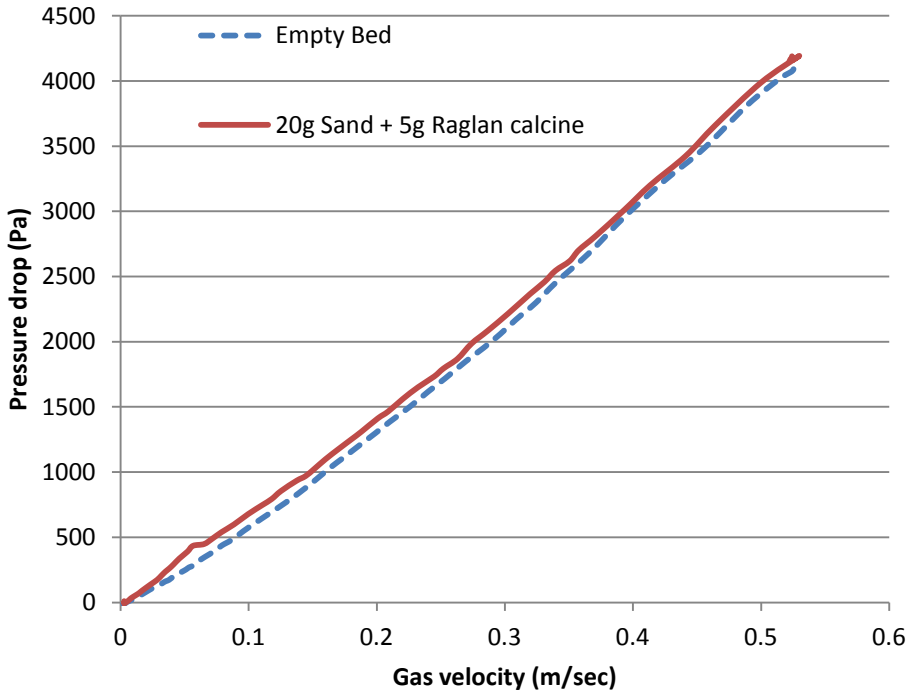

Figure 4.4. Pressure drop method for the determination of V_{mf}.

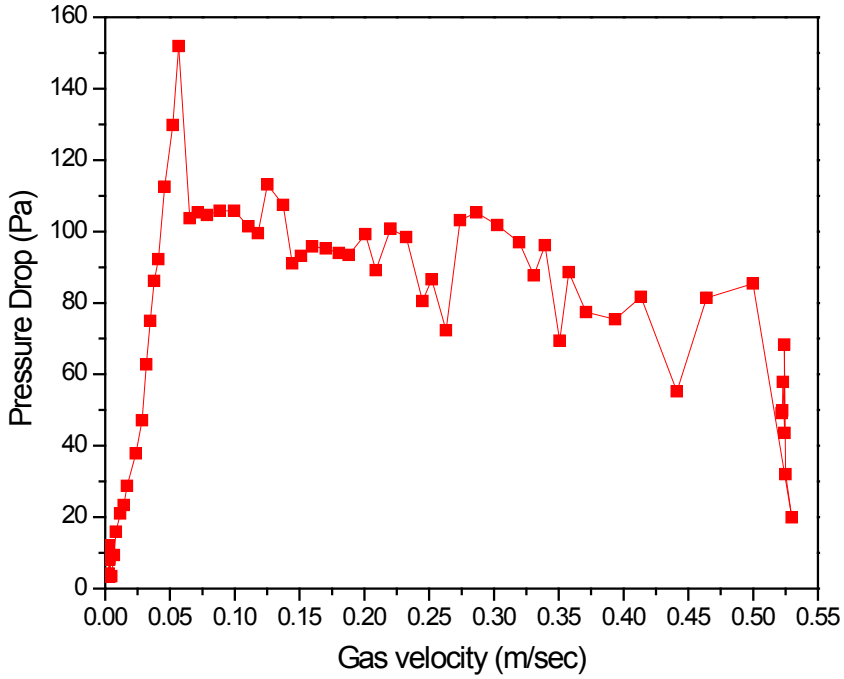

Figure 4.5. Pressure drop across the bed vs. gas velocity.

4.3.1.2 Determination of the Terminal Velocity (V_t)

Terminal velocity for the roasting of a mixture of 20 g sand and 5 g Raglan concentrate using air was calculated as a function of particle size and the roasting temperature using Equations (1.9) and (1.10). The dependence of V_t on roasting temperature is because the properties of air (i.e. density, dynamic viscosity) are dependent on temperature. The density of the solid was taken as the average density of the Raglan concentrate. As can be seen in Figure 4.6, the terminal velocity is more dependent on the particle size than on the roasting temperature. Larger particles have larger terminal velocities. V_t is approximately 100 times higher than V_{mf} given the same particle size and temperature from the comparison between Figure 4.3 and Figure 4.6. A wide particle size range will narrow down the allowable range of operating gas flowrate. As a result, efforts should be made to widen the allowable range of operating gas flowrate.

Apparent terminal velocity is plotted against particle size and temperature in Figure 4.7. Apparent terminal velocity is calculated by converting the terminal velocity at that particular temperature to the velocity at room temperature (25 ºC) using PV=nRT. This graph provides

more information since at any given time, the apparent velocity (converted velocity at 25 ºC) in the quartz tube is constant, which is determined by the flowrate of the feeding gas, regardless of the temperature variation along the longitudinal axis of the quartz tube. From Figure 4.7, it is obvious that the apparent terminal velocity is largely affected by the temperature. Figure 4.8 illustrates the temperature profile measured along the height of the quartz tube above the fluidized bed maintained at 700 ºC. The temperature gradually decreases from the fluidized bed temperature at 700 ºC to around 100 ºC with the increase of height above the bed, because, as can be seen in Figure 4.1, the top part of the quartz tube is out of the electric furnace and is cooled by a fan. The movement pattern of particles above the fluidized bed could be envisaged based on Figure 4.7 and Figure 4.8. If the flowrate of the gas is fixed to result in an apparent velocity (at 25 ºC) of 0.1 m/s for instance, the relationship between the temperature and the size of the particles which just experience their terminal velocity at that specific temperature can be described by the curve a–b in Figure 4.7. In the fluidized bed at 700 ºC, particles smaller than 72 μm (read from the a–b curve) experience a gas flow velocity which is larger than their terminal velocity. These particles flow upwards as a result. When they reach a cooler region in the freeboard, the larger particles among them start to drop because the gas velocities they experience drop below their individual terminal velocities due to this temperature drop. Smaller particles are still carried upwards until a much cooler region is reached. This phenomenon continues until the particles reach the top of the quartz tube where only particles smaller than 35 μm exit the quartz tube. Larger particles fall back to a region where the temperature is hot enough to result in the ascent of the particles again. This upward-downward circulation occurs to the particles within certain particle ranges. Relatively smaller particles circulate in the upper part of the freeboard, while larger ones do in the lower part. This idealized regular circulation could be compromised by the natural convection brought about by the temperature gradient in the freeboard as well as the forced convection resulting from the turbulence of the fluidized bed. Overall, the temperature gradient of the freeboard helps alleviate the gas entrainment problem.

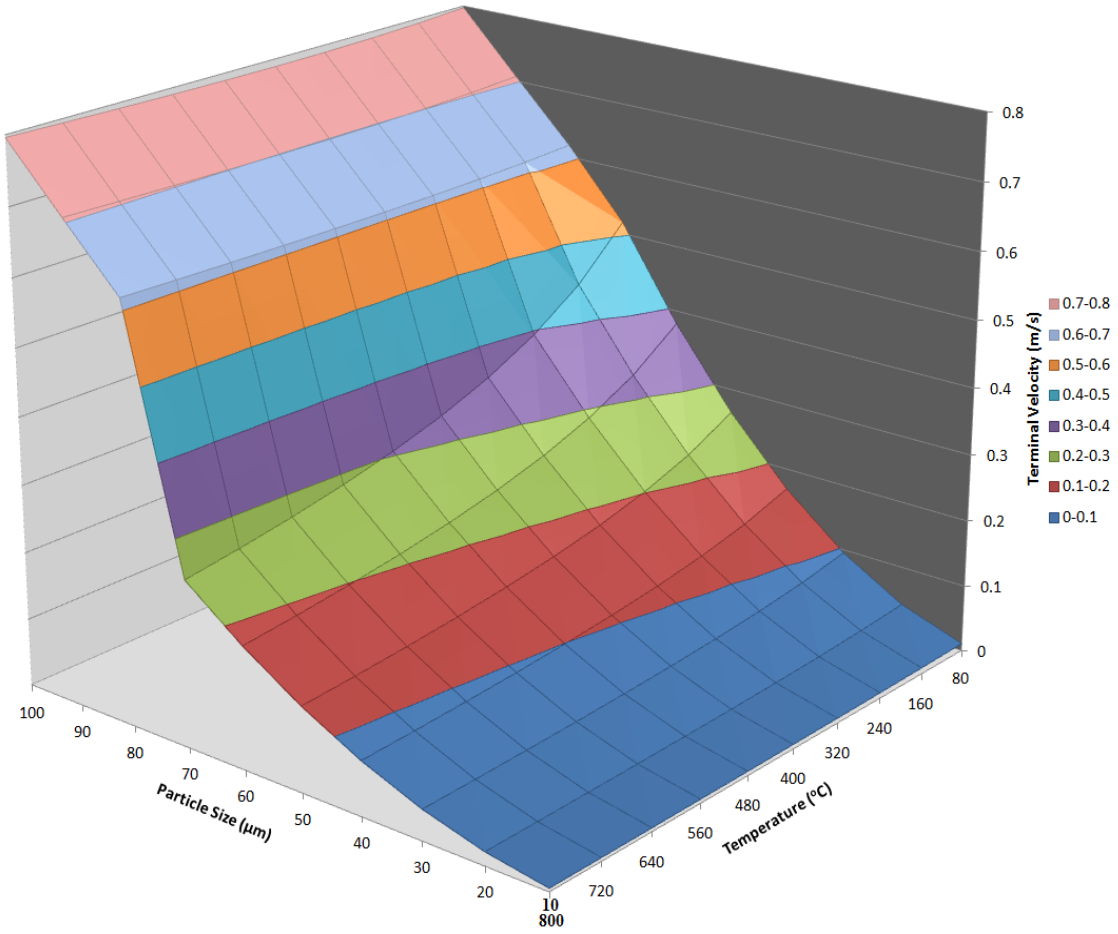

Figure 4.6. Terminal velocity vs. particle size and temperature for the roasting of Raglan concentrate with air.

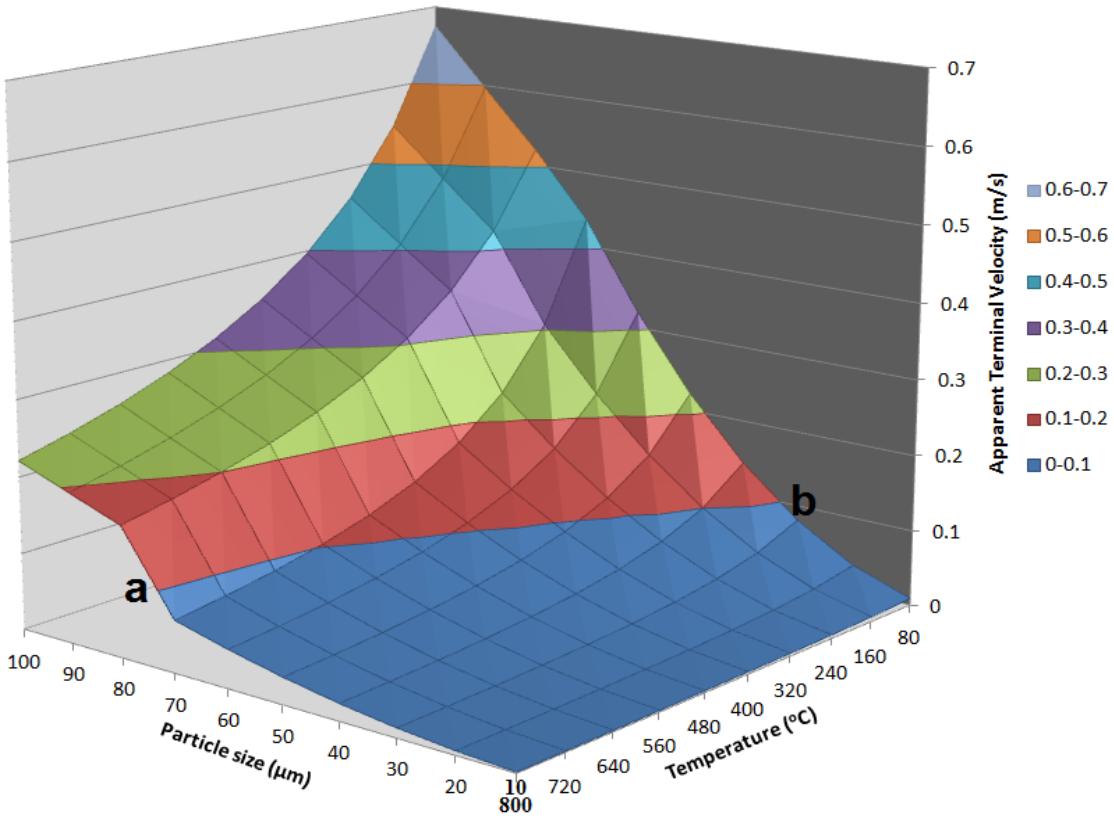

Figure 4.7. Apparent terminal velocity (25 ºC) vs. particle size and temperature for the roasting of Raglan concentrate using air.

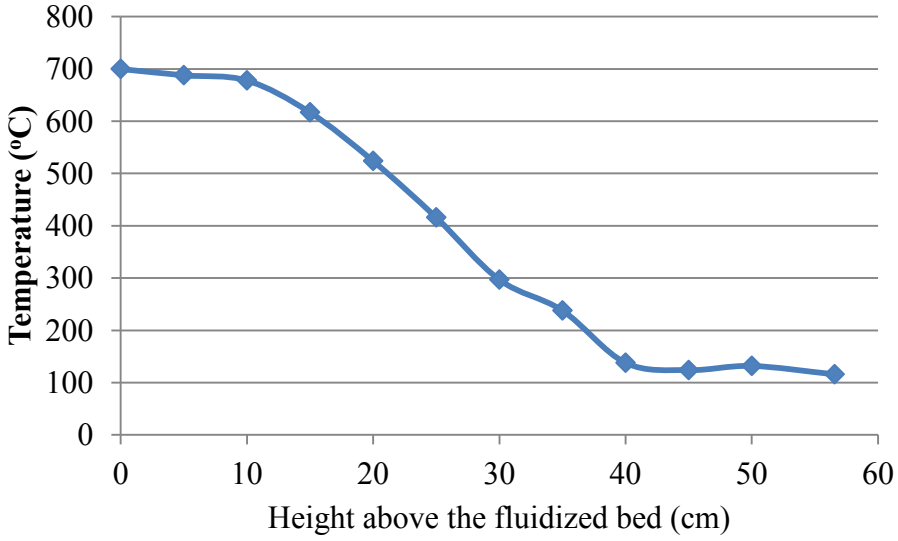

Figure 4.8. Temperature profile above the fluidized bed.

4.3.1.3 Heat Transfer Calculation

A fluidized bed oxidation roasting test was performed by processing a mixture of 20 g sand and 5 g Raglan concentrate in the apparatus at 700 ºC with 3 L/min air for 10 min. The fluidized bed temperature, pressure beneath the porous frit and the SO_2 concentration in the offgas were measured and are plotted against the roasting time in Figure 4.9. Figure 4.10 (a–h) displays the development of the fluidized bed in the quartz tube and the collection of calcine at the end of roasting. Figures (a) and (b) exhibit the feeding process of the mixture of concentrate and sand into the quartz tube. At the onset when only a small amount of sulfide particles was ejected from the thin ceramic tube into the quartz tube, the sulfide particles were ignited as shown in Figure 4.10 (a) due to the extreme high heating rate and the oxygen present in the chamber. Oxygen in the chamber was quickly consumed and the supply of oxygen through the porous frit is not quick enough to sustain the ignition before the chamber was cooled down substantially by the feeding material. During this oxygen deficient period when the temperature is still high enough, some sulfur vapor was formed from the decomposition of sulfide minerals at high temperature. A portion of this sulfur vapor was blown downwards through the porous frit by concentrate carrier gas (N_2). Beneath the frit where the temperature is very high, the sulfur vapor mixed with the up-flowing oxygen and caused a small pulse of explosion which was captured by the video and shown in Photo (c) in Figure 4.10. The remaining sulfur vapor travelled with the up-flowing roasting gas and was condensed on the upper wall of the quartz tube, which was shown as yellowish elemental sulfur particles in Figure 4.11. After all the powders were fed into the chamber, a steady fluidized bed was developed as shown in Photo (d). Temperature of the fluidized bed was very low right after the feeding process and it increased quickly afterwards, which could be seen in Figure 4.9. Due to the extremely exothermic nature of the reactions occurring in the fluidized bed as well as the radiation received from the furnace, the temperature of the fluidized bed exceeded 800 ºC, more than 100 ºC higher than the set point of the electric furnace. The fluidized bed became visibly radiative as shown in Figure 4.10 (e) and (f), indicating the involvement of vigorous exothermic reactions. The temperature dropped due to the gradually weakening roasting reactions. The roasted product was finally drawn from the

chamber via the ceramic tube by the vacuum pump and was collected into the cyclone, which is shown in Figure 4.10 (g) and (h).

A heat transfer and energy balance calculation for the fluidized bed system were carried out using the recorded data from this oxidation roasting test. Four heat transfer components were involved in the fluidized bed system:

1. Heat transfer between the feeding gas and the fluidized bed;
2. Radiative heat transfer between the electric furnace and the fluidized bed;
3. Heat generated within the fluidized bed by exothermic reactions;
4. Conductive heat transfer through the wall of the quartz tube.

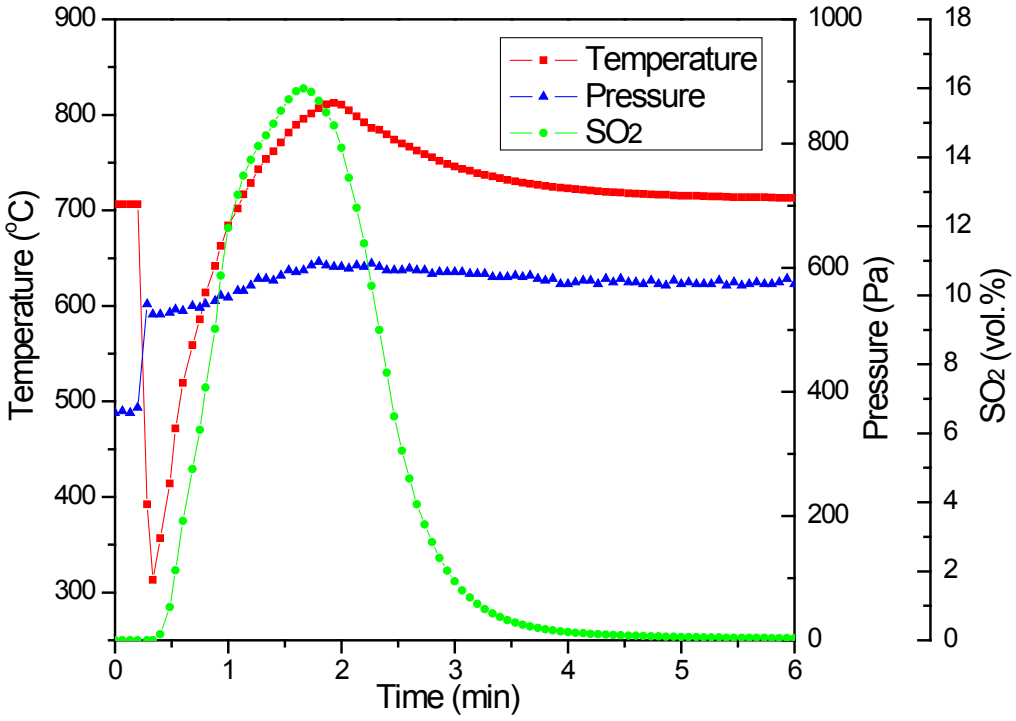

Figure 4.9. Fluidized bed roasting test without cooling.

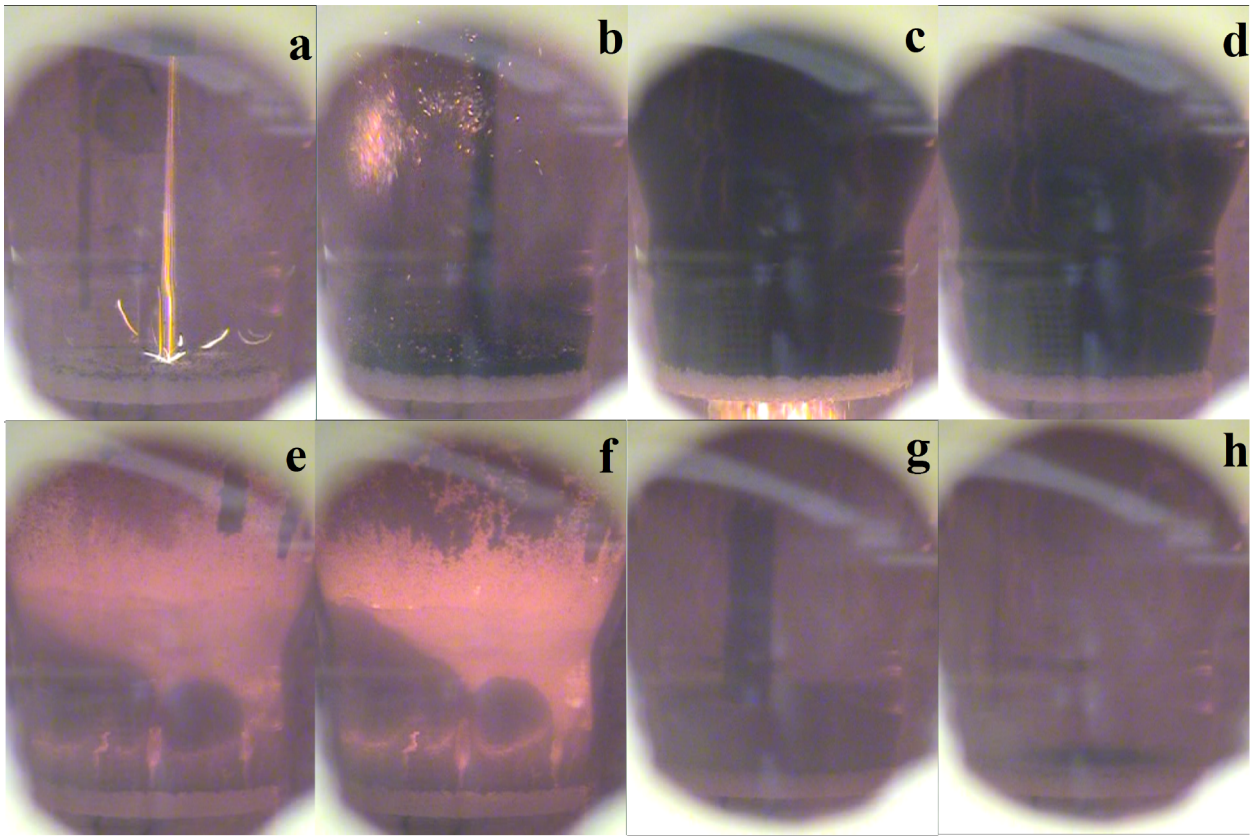

Figure 4.10. Images showing various stages of fluidized bed oxidation roasting test.

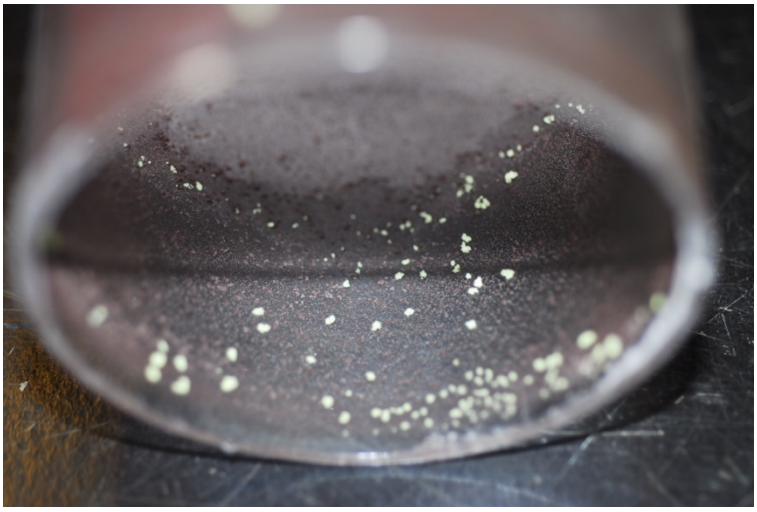

Figure 4.11. Yellowish elemental sulfur particles formed on the upper wall of the quartz tube from the condensation of the sulfur vapor.

Feeding gas _ For the calculation of the heat transfer between the feeding gas and the fluidized bed, the case is simplified by making the following assumptions: a) The feeding gas is pre-heated to the target temperature at 700 ºC when travelling in the lower portion of the quartz tube before entering the fluidized bed through the porous frit; b) The solid and gas phases are in thermal equilibrium in the fluidized bed part of the tube.

Radiation _ The calculation of the radiative heat transfer is simplified by the geometry of the system where the fluidized bed is totally surrounded by the walls of the electric furnace. Therefore, Equations (4.2) to (4.4) [13] are employed for the calculation of the radiative heat transfer rate (W) between the walls (including the heating elements) of the electric furnace and the fluidized bed. It is necessary to make several reasonable assumptions to render the calculation possible. Because the fluidized bed is totally surrounded by the walls of the electric furnace, and the surface area of the fluidized bed is much smaller compared with that of the walls, any radiation emitted from the surface of the fluidized bed will mostly be absorbed by the furnace walls after several consecutive reflections among the furnace walls. With this particular set of geometry, the furnace walls could be considered as a *black body* with an emissivity of 1 as far as the fluidized bed is concerned. The emissivity of the fluidized bed would change during the progression of the roasting due to the change of the surface chemistry and morphology of the particles as well as the temperature change. Due to the selective oxidation behavior of the iron-containing sulfide minerals (i.e. pyrrhotite and pentlandite), the surface would be iron oxide most of the time during roasting. The emissivity of Fe_2O_3 varies from 0.82 to 0.87 in the temperature range from around 400 K to 1400 K [14]. The emissivity of the fluidized bed (ε_{bed}) is assumed to be constant at 0.9, which is higher than the above mentioned emissivity range of Fe_2O_3 because of the powder nature of the fluidized bed. Also we assume that both the furnace walls and the fluidized bed are grey bodies, meaning their absorptivities are independent of the incoming spectral energy distribution. For the calculation of the surface area of the fluidized bed which is exposed to the walls of the electric furnace, assumptions are made that the geometry of the fluidized bed is a column and the average porosity of the fluidized bed is 0.7, which is a reasonable number because the measured porosity of the fix bed of mixture of 20 g sand and 5 g Raglan concentrate is 0.49. Based on these necessary assumptions, the heat transfer rate (W) at any given time during roasting could be calculated.

$$q_{furnace-bed} = A \cdot \left(e_{b,furnace} - e_{b,bed}\right) \frac{1}{1/\varepsilon_{furnace} + 1/\varepsilon_{bed} - 1} \quad (4.2)$$

$$e_{b,furnace} = \sigma \cdot T_{furnace}^4 \quad (4.3)$$

$$e_{b,bed} = \sigma \cdot T_{bed}^4 \quad (4.4)$$

where $q_{furnace\text{-}bed}$ is the heat transfer rate in W; A is the area of the fluidized bed which is exposed to the electric furnace; $\varepsilon_{furnace}$ is the emissivity of the furnace wall; ε_{bed} is the emissivity of the fluidized bed; σ is a constant which is 5.669×10^{-8} $W\cdot m^{-2}\cdot K^{-4}$; $T_{furnace}$ is the furnace temperature; T_{bed} is the fluidized bed temperature.

Reactions _ The heat generated from the roasting reactions is calculated based on the SO_2 profile in Figure 4.9 and the mineralogical composition of the Raglan concentrate in the following way. Three main reactions are taken into consideration for the calculation, which are Reactions (4.5) to (4.7). These three reactions all result in the formation of SO_2, which is shown quantitatively in Figure 4.9 as the SO_2 concentration in the offgas. Assume at any temperature, the contribution of each reaction to the concentration of SO_2 in the offgas is determined by the molar ratio of these three minerals in the Raglan concentrate. Then the amount of the oxidation occurring in any given period of time is determined by the amount of SO_2 formed from the fluidized bed. However, the SO_2 profile in Figure 4.9 does not represent the SO_2 concentration in the offgas immediately produced from the fluidized bed because of the relatively large volume of freeboard in the upper part of the quartz tube where the offgas produced from a certain period of time mix together. This back-mix phenomenon results in the delay of reading as well as the deviation of SO_2 concentration measured from that of the offgas just produced from the fluidized bed. The assumption is made that the gas in the freeboard is well mixed due to the convection resulting from the temperature variation. The corrected SO_2 profile can be calculated from the measured SO_2 profile, both of which are plotted in Figure 4.12. Three partly overlapped peaks appear in the corrected SO_2 profile, representing three predominant reactions within certain temperature ranges. In order to calculate the enthalpy for these reactions at a certain temperature, the standard enthalpy of formation and heat capacity at that temperature for all the species involved in Reactions (4.5)–(4.7) are required. The standard enthalpy of formation for pentlandite is -(837.37±14.59) kJ/mol [15]. The heat capacity of pentlandite at

298.15 K is 442.7 J/mol·K [16], which is used for the calculation at high temperatures since no heat capacity at higher temperature is available. Standard enthalpy of formation and heat capacity of other species are cited from the HSC Chemistry [17]. Please refer to the Appendix 01 which is written in C language for the whole calculation process.

$$Fe_{4.5}Ni_{4.5}S_8 + 6.875O_2 = 2.25Fe_2O_3 + 4.5NiS + 3.5SO_2 \quad (4.5)$$

$$2FeS + 3.5O_2 = Fe_2O_3 + 2SO_2 \quad (4.6)$$

$$2CuFeS_2 + 6.5O_2 = 2CuO + Fe_2O_3 + 4SO_2 \quad (4.7)$$

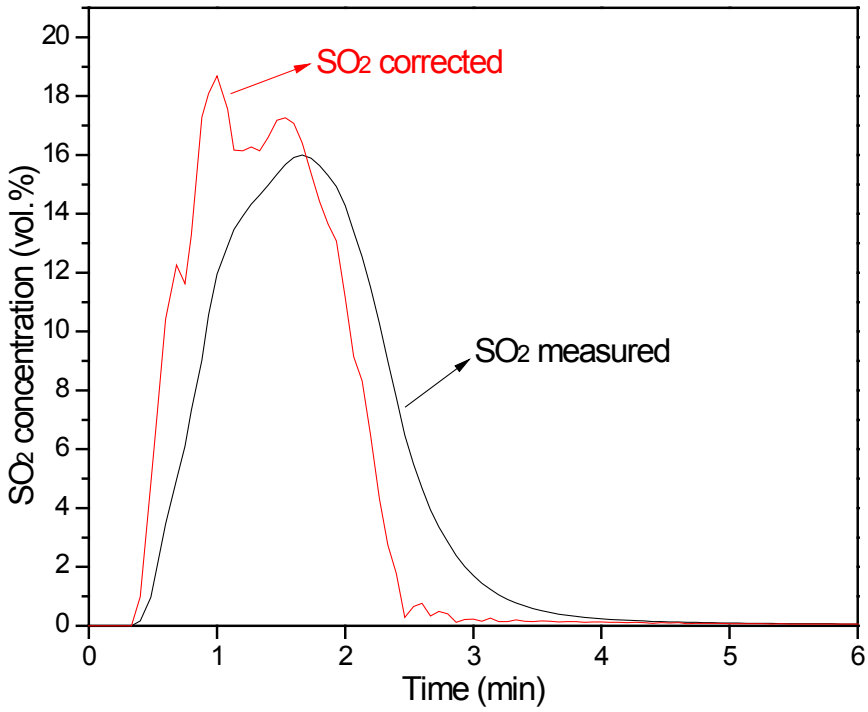

Figure 4.12. SO_2 concentration right above the fluidized bed calculated from the measured SO_2 concentration.

Conduction _ The heat transfer between the wall of the quartz tube and the fluidized bed via conduction involves three components in series: heat transfer from the fluidized bed to the inner wall of the quartz tube; conductive heat transfer in the quartz tube; and heat transfer from the outer wall of the quartz tube to the air in the furnace at 700 ºC. These three components are illustrated schematically in Figure 4.13. The inner wall of the quartz tube can be treated as the

immersed surface in the fluidized bed. As a result, the calculation of the heat transfer between the quartz tube and the fluidized bed could be performed using Equation (1.11). Thermal conductivity and heat capacity of quartz are required for the calculation of heat transfer through the quartz, which are given as Equations (4.8) [18] and (4.9) [19]. Natural convection takes place in the air near the outer surface of the quartz tube. Equations (4.10) to (4.12) are used for the calculation. These three conductive heat transfer components are interdependent in terms of their individual contribution to the total heat transfer because the thermal properties of the air, quartz and even the fluidized bed are dependent on their individual temperatures. Due to the relative complexity, three iteration processes are required, which are shown in Figure 4.14 as the flow chart for the calculation process. Please refer to the Appendix 02 for the whole calculation process.

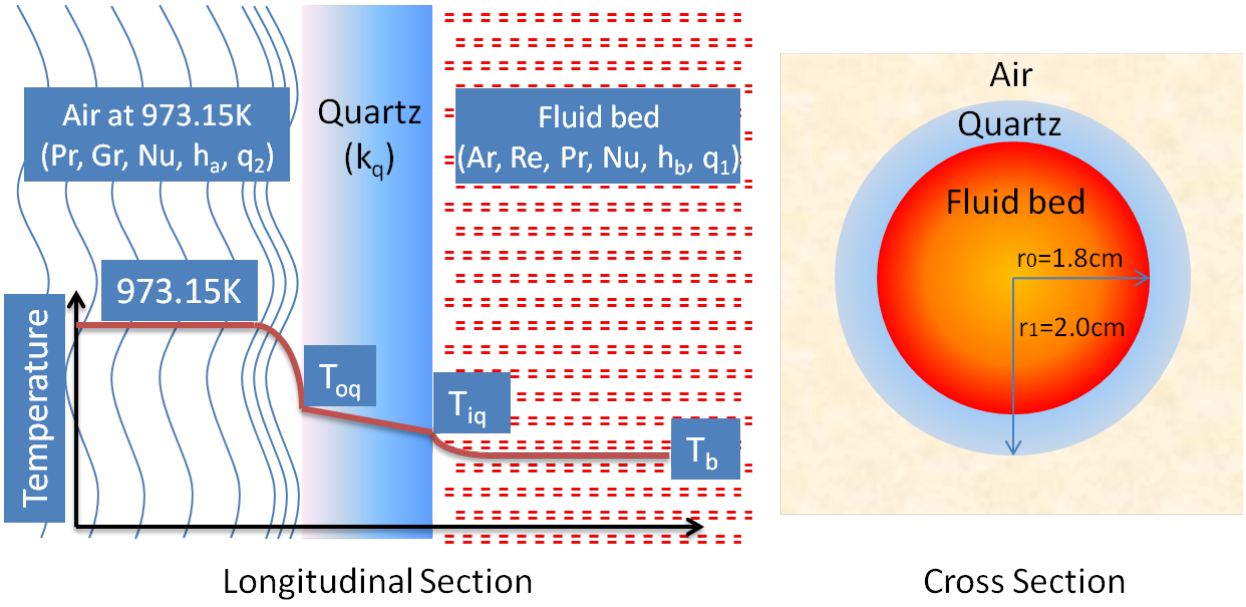

Figure 4.13. Longitudinal and cross sections of the fluidized bed system showing the temperature gradient.

$$k\ (W/(m\cdot K)) = 418.4*(3.83*10^{-6}T+0.00163) \quad (4.8)$$

$$C_p^{o}\ (J/(mol\cdot K)) = 81.1447+0.0182834T+5.4058*10^{-6}T^{2}-698.458T^{-0.5}-180986T^{-2} \quad (4.9)$$

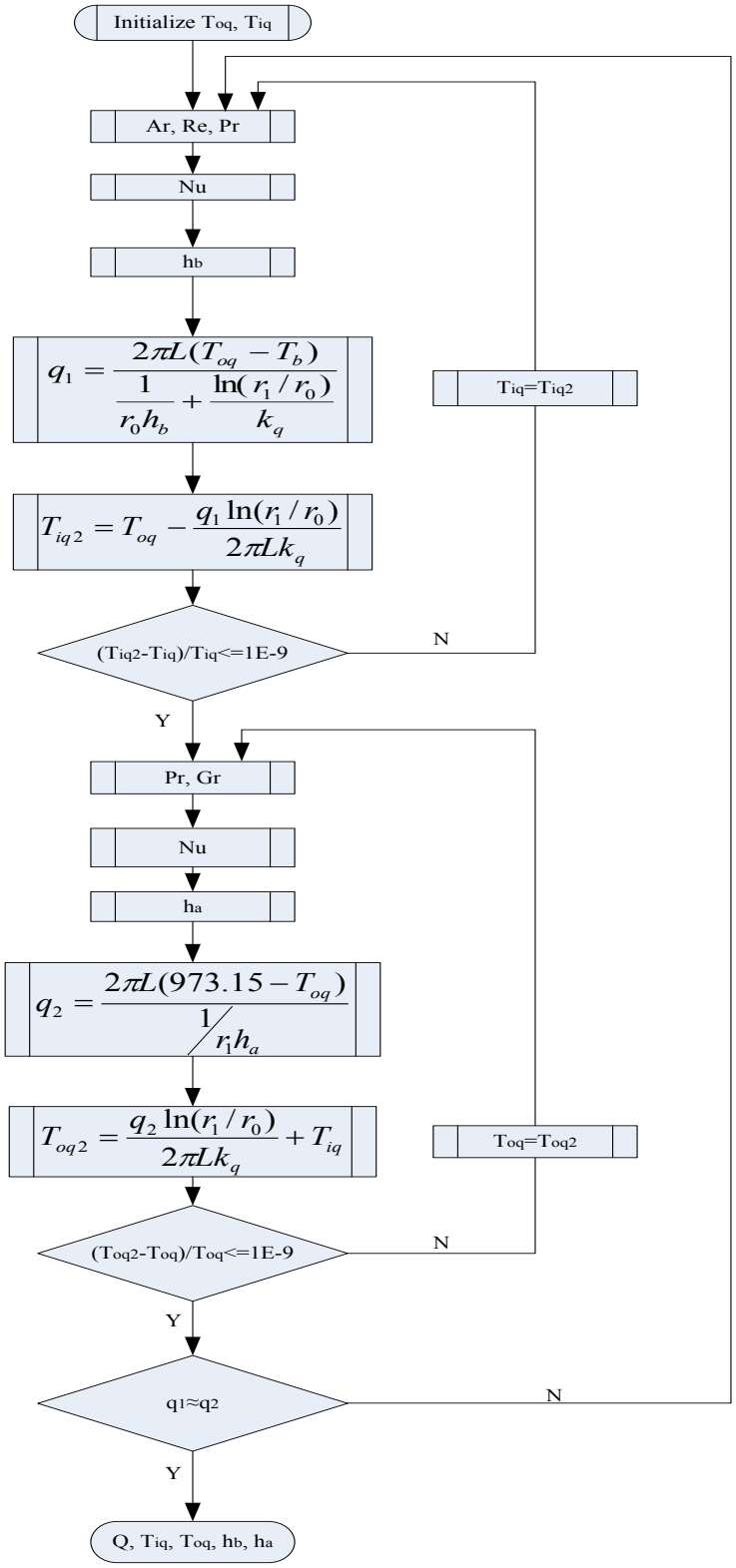

Figure 4.14. Flow chart for the calculation of the heat transfer rate through the wall of quartz tube (please refer to Figure 4.13 and Appendix 02 for the meanings of the terms).

$$Nu_L = \frac{hL}{k_f} \tag{4.10}$$

$$Pr \equiv \frac{\nu_f}{\alpha_f} = \frac{C_p \eta_f}{k_f} \tag{4.11}$$

$$Gr_L \equiv g \frac{L^3 \rho_f^2 \beta_f (T_0 - T_\infty)}{\eta_f^2} \tag{4.12}$$

Some calculation results are plotted in Figure 4.15 and Figure 4.16. The heat transfer coefficients of the fluidized bed and the air around the quartz tube (taking into account its natural convection), as well as the thermal conductivity of the quartz tube are plotted against the fluidized bed temperature in Figure 4.15. The heat transfer coefficient of the fluidized bed is much higher than that of the air around the quartz tube due to the turbulent nature of the fluidized bed. The thermal conductivity of the quartz tube increases with the increase of the fluidized bed temperature. Due to the natural convection of the air which contributes to its heat transfer, the heat transfer coefficient of the air reaches a valley at 973 K which is the furnace temperature. In order to quantitatively study the relative thermal resistivity of these three components, the temperature drops within these three components, which are proportional to their individual thermal resistivity, are plotted in Figure 4.16 as a function of the fluidized bed temperature. Note that the total temperature drop at a specific fluidized bed temperature is normalized to 100%. As can be seen, the air around the quartz tube accounts for more than 94% of the total thermal resistivity when the fluidized bed temperature is below 973 K. The quartz tube accounts for less than 1%, which is shown as the red stripe. Above 973 K, the temperature drop within the fluidized bed is around 80% of the total temperature drop, meaning that the thermal resistivity of the fluidized bed prevails. The heat transfer rate (in W) is also plotted, revealing that the heat transfer via conduction mainly occurs when the fluidized bed temperature is below 973 K.

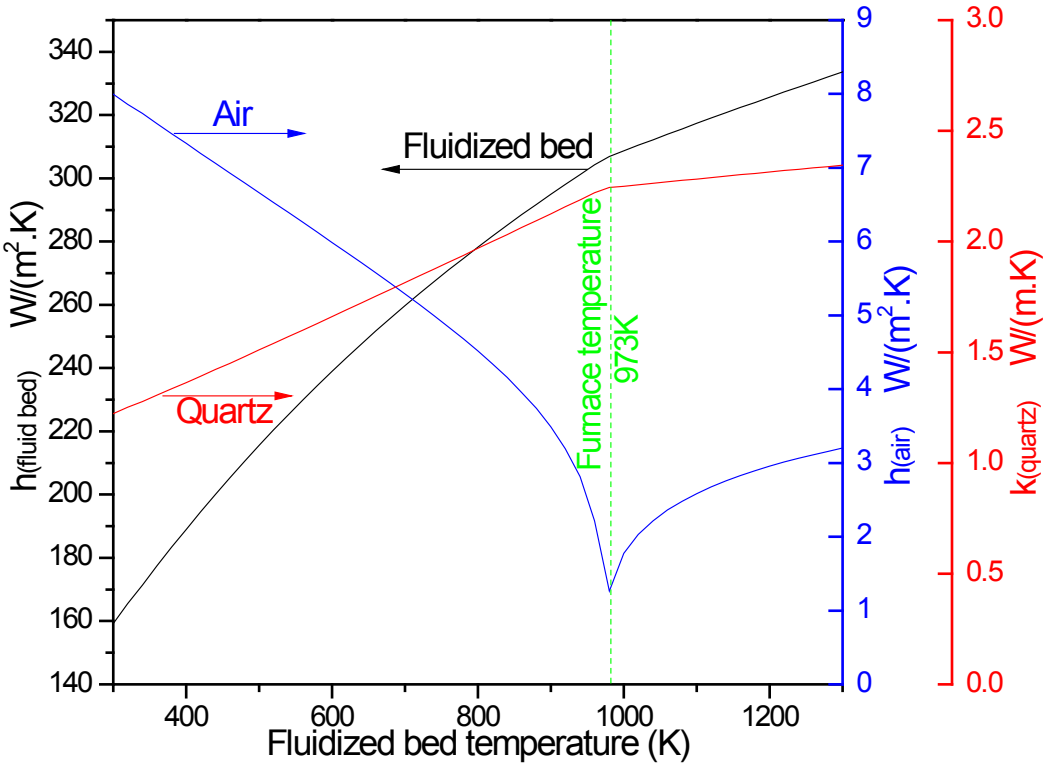

Figure 4.15. Heat transfer coefficients (h) of the fluidized bed and the air around the quartz tube, and the thermal conductivity (k) of the quartz tube as a function of the fluidized bed temperature.

The heat transfer rates associated with reactions, radiation, feeding air and conduction are plotted in Figure 4.17 against the roasting time for comparison. As can be seen, at the beginning when the concentrate is just fed to the quartz tube, the main source of heat is the radiation due to the large temperature difference between the furnace and the fluidized bed. Radiative heat transfer gradually decreases due to the temperature increase of the fluidized bed. Exothermic oxidation reactions prevail as the main source of heat afterwards due to the high temperature of the fluidized bed as the main contributing factor. As a result of the reactions occurring in the fluidized bed, the temperature increased above the furnace temperature. The radiation becomes the main channel for the heat release out from the fluidized bed to the furnace until the temperature gradually drops back to the furnace temperature. The feeding air and the conduction contribute much less to the heat transfer compared with the other two means.

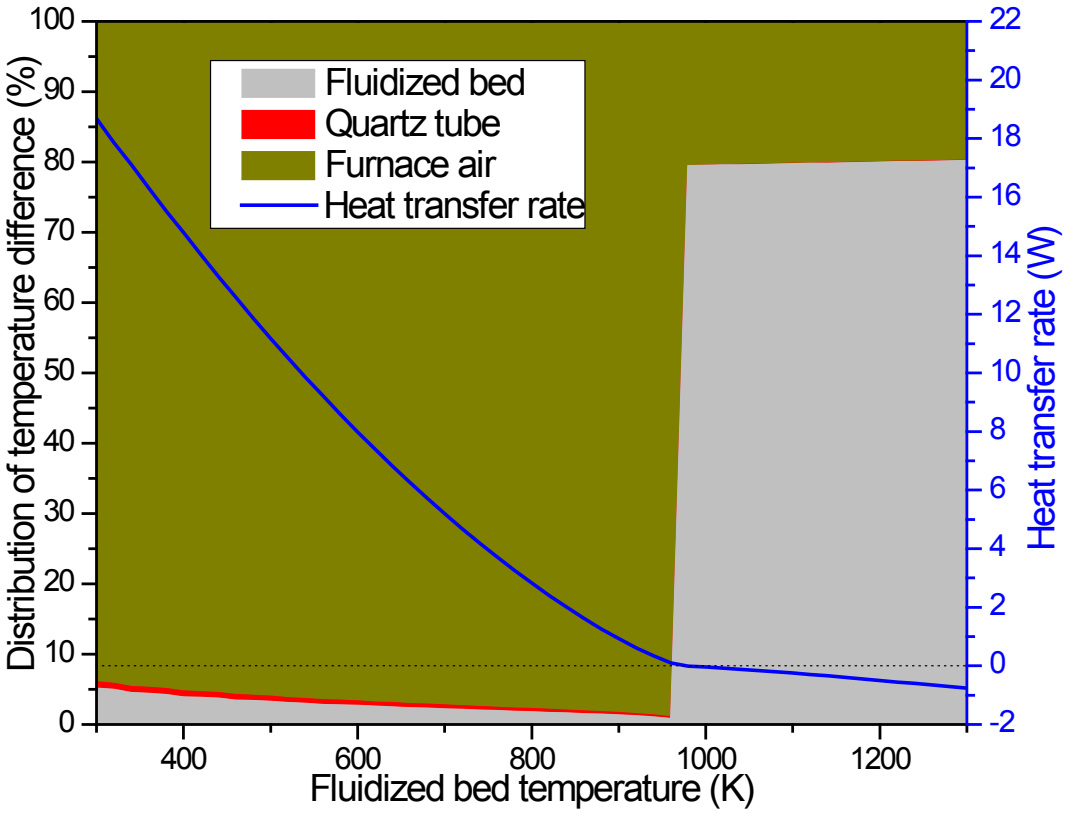

Figure 4.16. Temperature differences (in percentage) between the main body of the fluidized bed and the inner wall of the quartz tube (labeled as Fluidized bed), between the inner wall and outer wall of the quartz tube (labeled as Quartz tube), and between the outer wall and the furnace wall (labeled as Furnace air), against fluidized bed main temperature, shown as the stacked areas. Conductive heat transfer rate through the quartz tube is plotted as the blue curve.

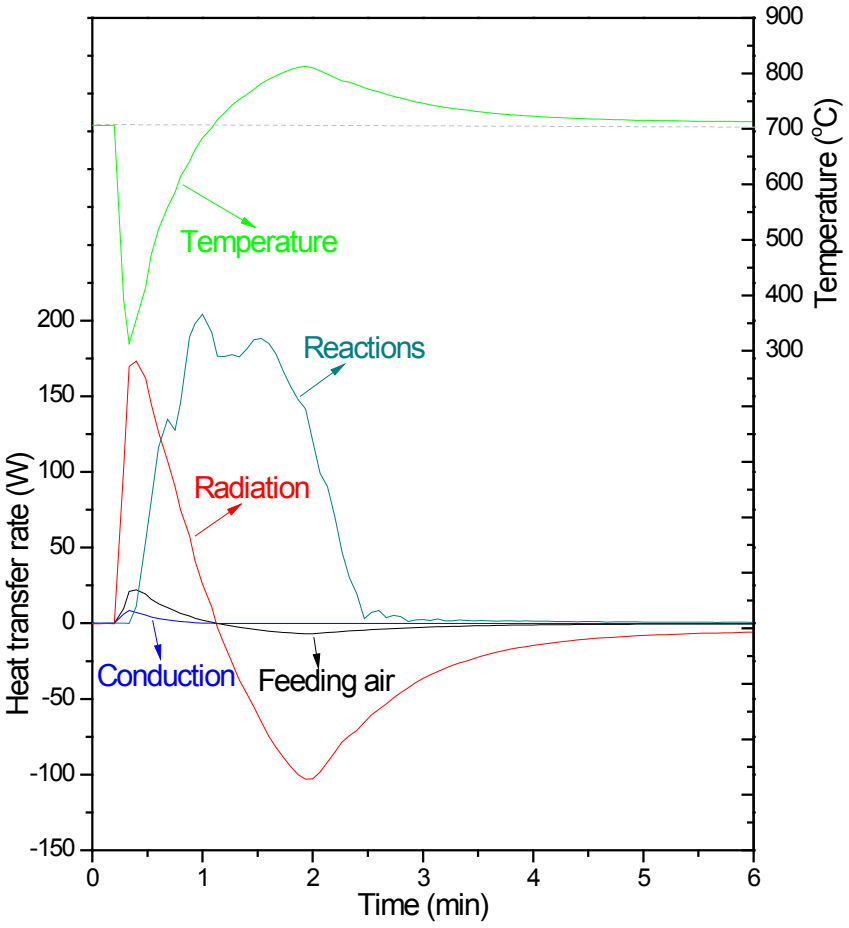

Figure 4.17. Temperature profile and the heat transfer rates by reactions, radiation, feeding air and conduction through the quartz wall.

4.3.1.4 Cooling Method

From Figure 4.17 it is apparent that the temperature will increase above the furnace set point to a great extent due to the extremely exothermic reactions occurring in the fluidized bed. Therefore, it is mandatory to apply a cooling method to absorb the heat released from the roasting reactions because the formation of nickel ferrite is favorable at higher temperatures, which is detrimental to the sulfation roasting process. Several cooling methods were tried. One method is to apply compressed cool air around the quartz tube with high velocity. Cooling efficiency is quite low because this method only enhanced the heat transfer through the air

around the quartz tube. However, the main thermal resistivity comes from the fluidized bed above 973 K, not from the air around the quartz tube, which can be seen in Figure 4.16. Another cooling method is to add drops of water into the fluidized bed. This is effective because the vaporization of water is fast, ensuring a quick heat absorption. However, the addition of water causes a serious problem that the water tends to condense on the upper part of the quartz tube, which results in the adhesion of the calcine powders on it. Another potential issue is the removal of sulfates from the calcine due to their dissolution into water, which is detrimental to the kinetic study on sulfate formation. The last cooling method is to add a stream of sand into the fluidized bed, which is proven to be the most effective way. The sand is firstly added in the sand feeder (Figure 4.1) before roasting. During roasting, when the temperature exceeds the target temperature, a stream of sand with controlled flow is applied to absorb the extra heat.

4.3.1.5 Temperature Gradient of the Fluidized Bed

As mentioned above, the temperature of the fluidized bed will be controlled by introducing a stream of sand into the fluidized bed while maintaining the muffle furnace temperature. The temperature gradient of the fluidized bed should be as small as possible in order to achieve a uniform roasting condition. This might be challenging because of the complex heat transfer mechanisms involved which was discussed in Section 4.3.1.3. The feeding of sand as the method for temperature control adds to this complexity.

The temperature gradient was quantitatively evaluated by measuring the temperatures at various locations in the fluidized bed during oxidation roasting. A mixture of 5 g Raglan concentrate and 20 g sand was roasted at 700 ºC with the introduction of sand for temperature control. Temperatures at three locations were measured by three thermocouples: Temperature#1, center of the fluidized bed; Temperature#2, between the fluidized bed center and the wall of the quartz tube; Temperature#3, close to the wall of the quartz tube. Temperature profiles are illustrated in Figure 4.18. In this figure, the quick temperature drop after 1min is a result of the feeding of the sample into the quartz tube. Because thermocouple #3 is close to the wall of the tube, Temperature#3 is higher than the other two due to the radiation received from the muffle furnace in this period of time. Fluctuation occurred after 2.5 min resulting from the manual

discontinuous addition of sand to suppress the overheating. Between 2.5 and 10 min, the magnitudes of temperatures are in the order: Temperature#1 < Temperature#2 < Temperature#3, meaning that higher temperature is observed at locations which are closer to the wall of the tube. The highest temperature difference between Temperature#1 and Temperature#3 is roughly 20 ºC, which is observed at 3 min when the rate of sand addition is at its maximum. With the progress of roasting, the temperature gradient in the fluidized bed became smaller. Based on this evaluation, the temperature gradient in the fluidized bed can be considered insignificant and a relatively uniform temperature could be achieved during roasting experiment.

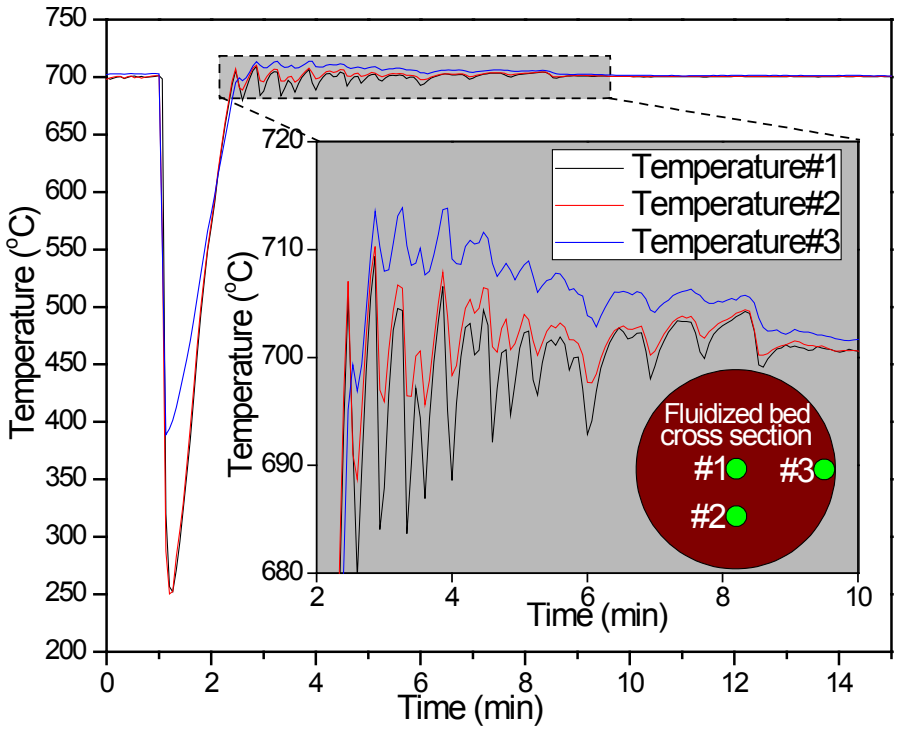

Figure 4.18. Temperatures measured at three locations in the fluidized bed.

4.3.2 Effect of Roasting Temperature

The effect of oxidation roasting temperature was evaluated from 650 °C to 775 °C with temperature increments of 25 ºC. During the start of testing, when the temperature of the fluidized bed tends to exceed the target temperature due to the exothermic roasting reactions, a stream of sand was applied to suppress the overheating. Temperature of the fluidized bed, offgas

SO_2 and O_2 contents, and pressure drop across the porous frit and the fluidized bed were continuously measured, and have been plotted in Figure 4.19, for the roasting test at 650 °C as an example. Similar plots were obtained for the roasting tests at other temperatures, exhibiting similar trends. As seen in Figure 4.19, at around 0.5 min, a rapid temperature drop and a corresponding ΔP increase were recorded, marking the start of feeding. The temperature recovered after reaching a low of around 300 ºC. The temperature rise corresponds with a decline in O_2 and an increase in SO_2 indicating the progress of roasting reactions. The low in the O_2 curve is around 2 vol%, corresponding to the SO_2 peak of around 13 vol%. The volume of the freeboard, which is the volume above the fluidized bed in the quartz tube, is relatively large compared with that of the fluidized bed. Therefore, the offgas was held up and mixed to some extent in the freeboard during roasting before reaching the gas analyzer. As a result, the offgas O_2 content recorded in Figure 4.19 lags the actual value in the fluidized bed, as does the measured SO_2. It is believed that the lowest O_2 content in the fluidized bed was below 2 vol%. This indicates that at the time when the fluidized bed atmosphere was relatively starved of O_2, the roasting reactions were so fast that the O_2 in the roasting gas was consumed immediately when passing through the fluidized bed. The roasting rate controlling step would be the supply of O_2 to the fluidized bed, rather than the roasting reactions or the gaseous diffusion through the oxide layers. At later roasting stage when the partial pressure of O_2 in the fluidized bed was high, the gas diffusion through the oxide layers could dominate and control the overall roasting rate. The offgas SO_2 profiles for all roasting tests with temperature variation are plotted in Figure 4.20, which exhibits the similarities in terms of the progress of roasting at different temperatures.

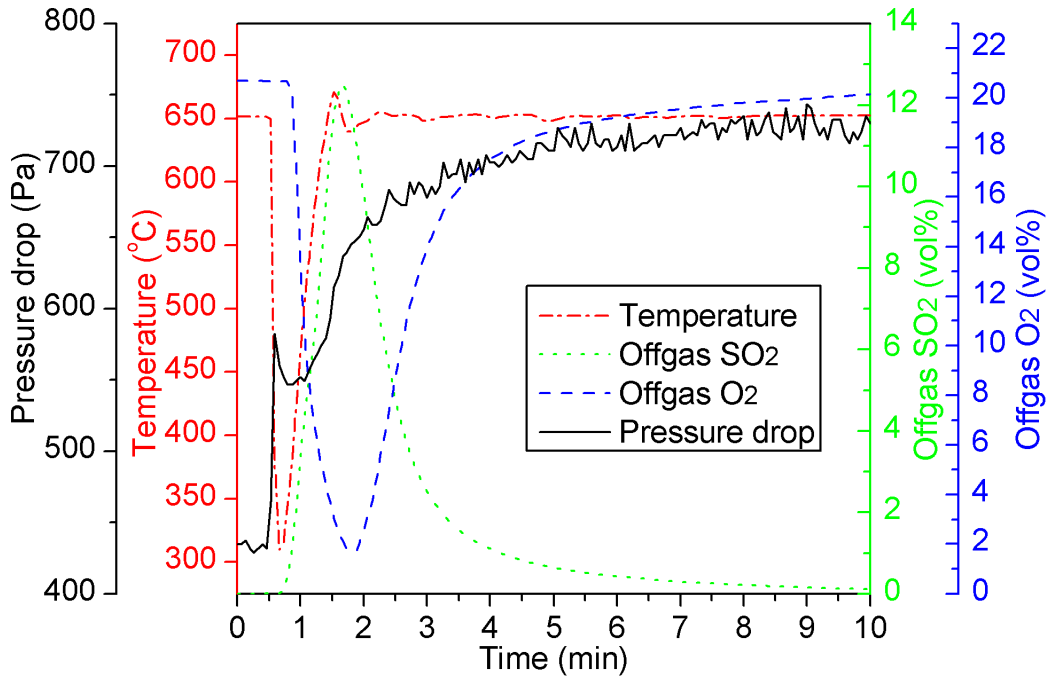

Figure 4.19. Temperature, offgas SO_2 and O_2 concentrations, and pressure drop for roasting test at 650 °C.

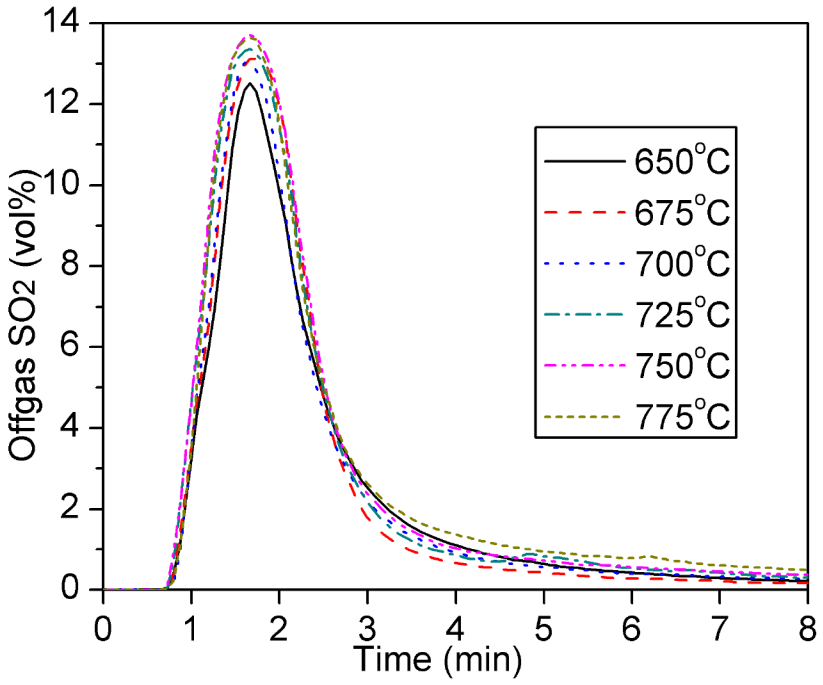

Figure 4.20. Offgas SO_2 profiles for the fluidized bed roasting tests by air with roasting temperature variation.

For oxidation roasting with air under normal roasting temperatures, the equilibrium phases are always oxides of various metals (Fe, Ni, Cu, Co) from a thermodynamic point of view. However, due to the limitations imposed by kinetics (e.g. gas/solid diffusion, chemical reactions) and the varying local gas environment, sulfides and even sulfates could be present in the calcine products. XRD analysis was employed to evaluate the mineralogical composition of the calcine products. Their XRD patterns are presented in Figure 4.21. As can be seen, the main compounds in these calcines are hematite (Fe_2O_3), trevorite ($Ni_xFe_{3-x}O_4$), nickel oxide (NiO), monosulfide solid solution (mss), and heazlewoodite (Ni_3S_2). There is no pentlandite, chalcopyrite, or pyrrhotite in the calcines. The content of hematite in the calcines does not change much with the increase of roasting temperature from 650 °C to 775 °C since there is little difference with regards to its peak intensities. This is because iron sulfide species in the form of pyrrhotite, pentlandite or chalcopyrite could be preferentially oxidized at lower temperatures [20]. Reaction (4.13) represents the complete oxidation of pyrrhotite below 650 °C. Figure 4.22 illustrates the morphology of partly oxidized pentlandite particles roasted at 650 °C. Iron sulfide was preferentially oxidized from pentlandite particles forming a hematite shell around the nickel sulfide core (mss). The partial oxidation of pentlandite could be represented by Reaction (4.14). Concentration profiles of a roasted pentlandite particle along the arrow in Figure 4.22 were measured by EPMA and are illustrated in Figure 4.23. Gradients of the Fe and Ni concentrations can be observed in the sulfide core. The centre of the sulfide core has higher Fe concentration (7.5 at%) and lower Ni concentration (41.5 at%) than the its edge (approximately 5 at% Fe, 44 at% Ni). These gradients indicate the outward diffusion of Fe to the surface of sulfide core where oxidation occurred. The hematite layer formed on the surface has approximately 2 at% Ni, suggesting that a small portion of Ni was also oxidized along with the preferential oxidation of Fe species. Co was oxidized at a faster rate than Ni, resulting in the co-presence of Co in the hematite layer.

The formation of trevorite and NiO is obvious at temperatures higher than 700 °C. Monosulfide solid solution disappears at temperatures higher than 700 °C, which could be represented by Reaction (4.15), and heazlewoodite becomes the only sulfur-containing species. The amount of heazlewoodite in the calcines becomes smaller with the increase of roasting temperature, which can be seen by the decreasing intensities of the heazlewoodite peak at 31.2° with the increase of temperature. This suggests the oxidation of heazlewoodite forming NiO according to Reaction

(4.16). Based on the XRD analysis, more species in the calcine appear in the form of oxides at higher temperatures and in the form of sulfides at low temperatures.

$$2Fe_{1-x}S(s) + (3.5-1.5x)O_2(g) = (1-x)Fe_2O_3(s) + 2SO_2(g) \quad (4.13)$$

$$(Fe,Ni)_9S_8(s) + O_2(g) \rightarrow (Ni,Fe)_{1-x}S(s) + Fe_2O_3(s) + SO_2(g) \quad (4.14)$$

$$(Ni,Fe)_{1-x}S(s) + O_2(g) \rightarrow Ni_3S_2(s) + Fe_2O_3(s) + SO_2(g) \quad (4.15)$$

$$Ni_3S_2(s) + 3.5O_2(g) = 3NiO(s) + 2SO_2(g) \quad (4.16)$$

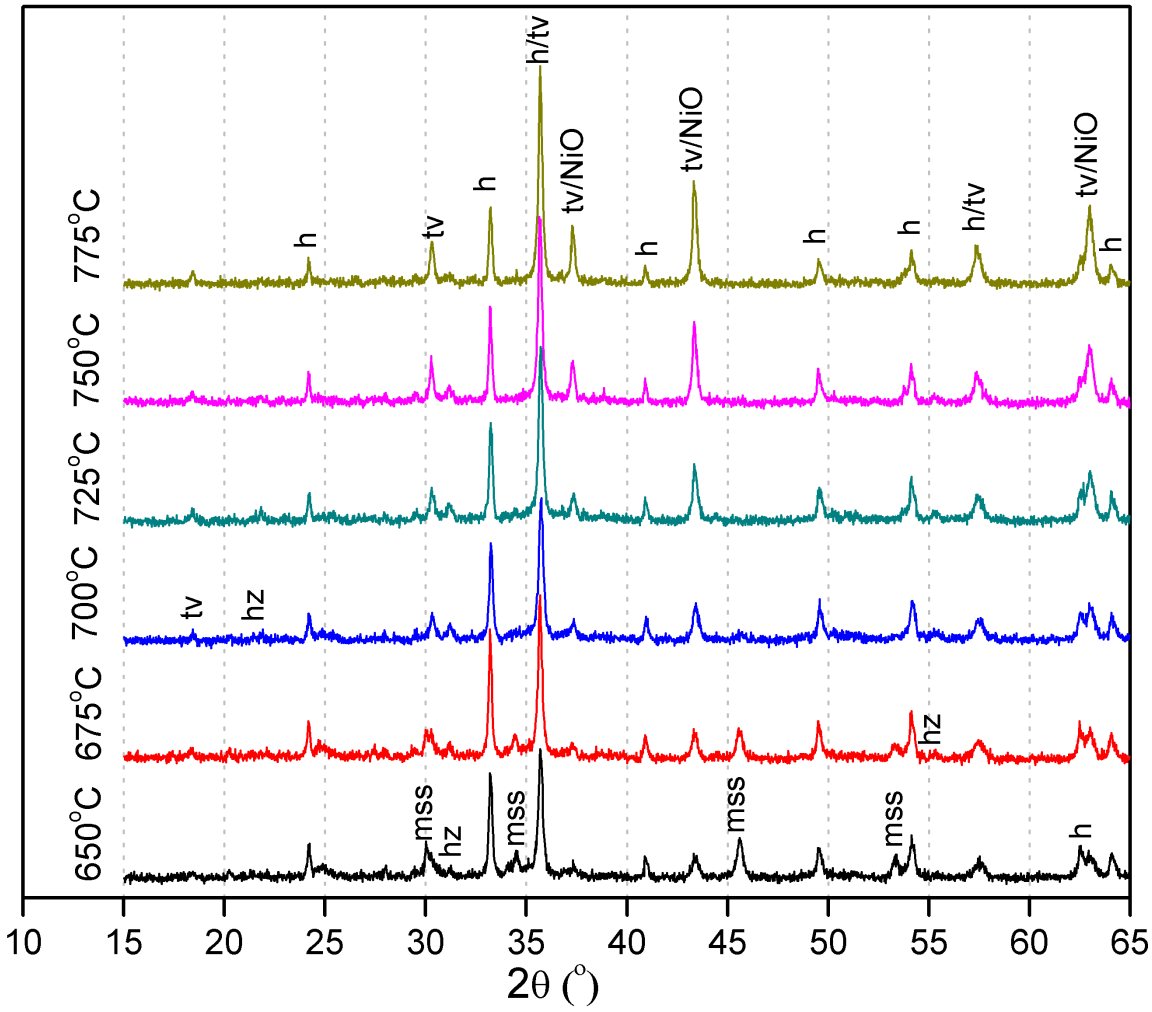

Figure 4.21. XRD patterns of the calcines for various temperatures (tv-trevorite, $NiFe_2O_4$; mss-monosulfide solid solution, $(Ni,Fe)_{1-x}S$; h-hematite, Fe_2O_3; NiO-nickel oxide; hz-heazlewoodite, Ni_3S_2).

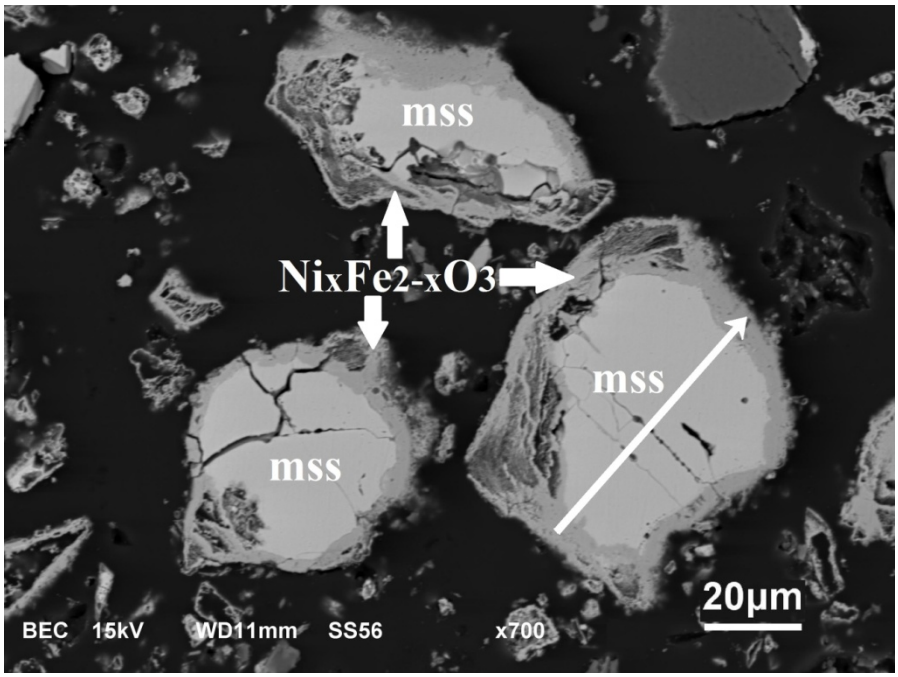

Figure 4.22. Roasted pentlandite particles at 650 °C with 3 L/min air (mss: monosulfide solid solution).

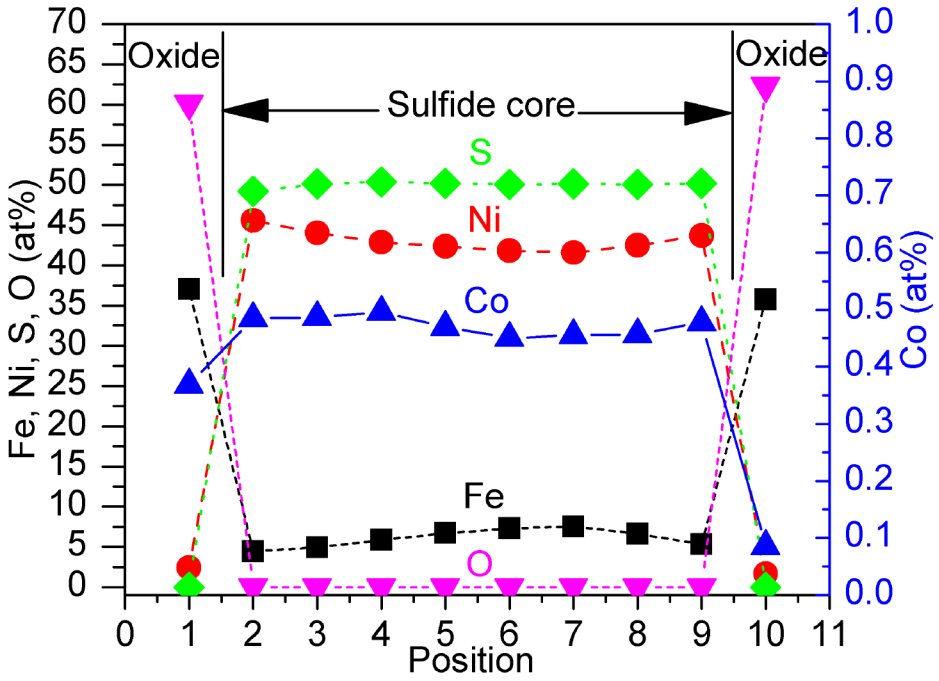

Figure 4.23. Concentration profiles in a cross section of a roasted pentlandite particle (650 °C) along the arrow in Figure 4.22 measured by EPMA.

Figure 4.24 reveals the degree of sulfur elimination as a function of roasting temperature. A previous study [21] shows that the roasting rate was limited by the mass transfer of O_2 to the reaction interface through the oxide rims which were formed upon oxidation. Considering this, the increase of sulfur elimination with the increasing roasting temperature is possibly caused by the acceleration of O_2 diffusion through the porous oxide layers at higher temperatures. A previous study [20] has shown that different sulfide species in the Ni concentrate were oxidized at various temperature ranges. Some sulfides were oxidized with a multi-step mechanism, which is also temperature dependent. This temperature dependency of oxidation roasting reactions could be another important factor that causes the dependency of the degree of sulfur elimination on temperature.

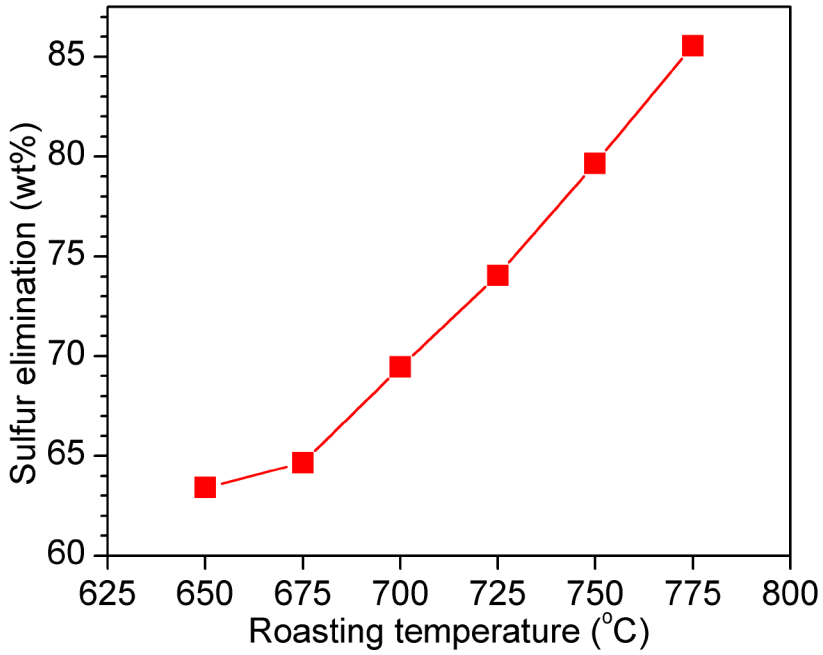

Figure 4.24. Degree of sulfur elimination as a function of roasting temperature.

In order to further understand the roasting behavior of the concentrate under different roasting temperatures, roasted pentlandite sulfide cores were analyzed by EPMA for their chemical compositions, which are shown in Figure 4.25 and Figure 4.26. Figure 4.25 illustrates the chemical composition change in a ternary diagram. As can be seen, Fe contents of most of the pentlandite derived particles are around 2 at%, i.e. they do not change with the increase of roasting temperatures. This value appears to represent the lowest iron concentration in the

pentlandite by preferential oxidation. The Fe concentration reported in Figure 4.23 is approximately 6 at%, which is much higher. This is because of its relatively large particle size (~70 µm) and the relatively low roasting temperature (650 °C) employed. Our previous study [20] has shown that smaller pentlandite particles have higher preferential oxidation rate of Fe species, which is in good agreement with the results from this study. Sulfur content decreases from around 50 at% to 44 at% when temperature increases from 650 °C to 700 °C, with a corresponding increase in Ni contents from 48 at% to 54 at%. This change in sulfur contents coincides well with the disappearance of mss with the general formula $(Fe,Ni)_{1-x}S$ above 675 °C, which is illustrated in Figure 4.21 and represented by Reaction (4.15). Further temperature increase above 700 °C does not contribute to an obvious change in composition.

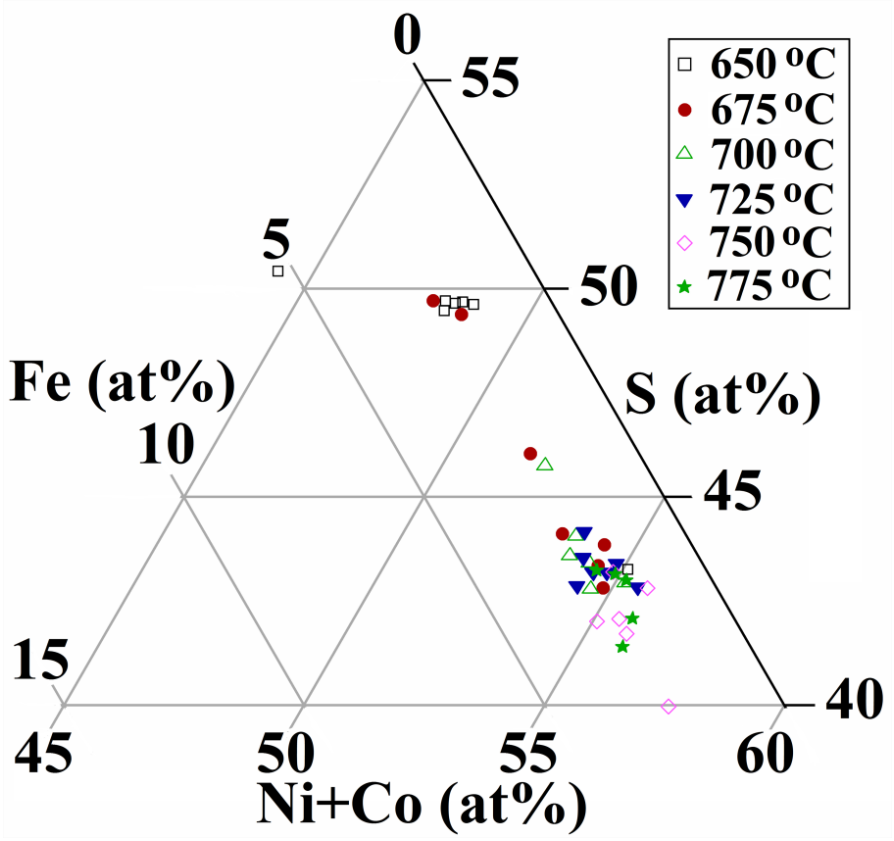

Figure 4.25. Change of the pentlandite sulfide core compositions as a function of fluidized bed roasting temperatures.

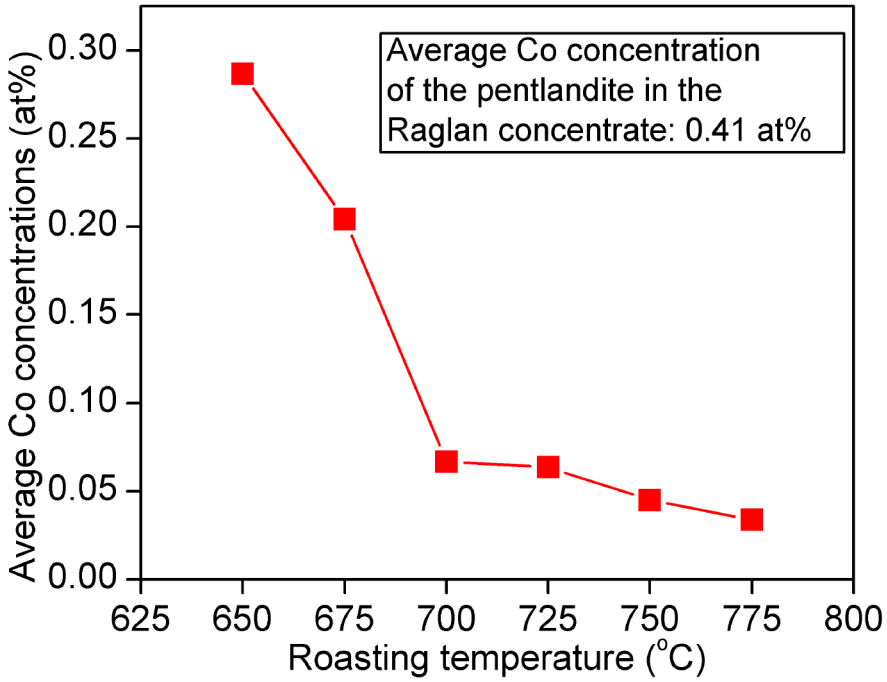

Figure 4.26. Average Co contents of the roasted pentlandite sulfide cores as a function of the fluidized bed roasting temperatures by EPMA.

During the oxidation roasting of the nickel concentrate, Co species were also partially oxidized and removed from the sulfide cores along with the oxidation of the Fe species. Figure 4.26 indicates the Co content of the roasted pentlandite sulfide cores as a function of roasting temperature. The average Co content in the pentlandite particles prior to roasting is 0.41 at%. After roasting the concentrate at 650 °C, the Co content in the pentlandite sulfide cores dropped to 0.29 at%. A substantial decrease in Co content in the roasted pentlandite particles can also be observed between 650 °C and 700 °C. Above 700 °C, the Co content dropped at a much lower rate.

A roasting sequence of metal species in the pentlandite can thus be tentatively suggested as follows. Preferential oxidation starts with the oxidation of iron sulfide from the pentlandite ($Fe_{4.5}Ni_{4.5}S_8$) forming $Fe_xNi_{1-y}S$ with around 2 at% Fe. Further roasting leads to the oxidation of nickel sulfide species towards $Fe_xNi_{3-y}S_2$, which is a more sulfur deficient phase. During the decrease in sulfur content, substantial percentages of Co in the pentlandite is oxidized and removed from the sulfide cores. For complete/dead roasting, the final oxidation should be the oxidation of the remaining nickel sulfide to form nickel oxide.

In the industrial oxidation roasting practice, the oxygen utilization efficiency is close to 100%. However, excessive amount of air was used for roasting in this study, resulting in high partial pressure of O_2 in the fluidized bed and in the offgas. This provides more favorable conditions for sulfate formation compared with the industrial roasting practice. In order to evaluate metal sulfate formation during oxidation roasting of this study, calcines were leached with hot water for 30 minutes to produce leachates for ICP analysis. Results are plotted in Figure 4.27 as percent extraction of elements from the calcines by water as a function of the roasting temperature calculated based on Equation (4.1). As can be seen, iron sulfate extraction is close to nil under these temperatures. Copper sulfate formation drops to close to zero at 675 °C. Nickel as sulfate stays at around 20 wt% when the temperature is below 700 °C, above which it drops substantially. Cobalt sulfate content drops continuously from 650 °C to 775 °C, but a substantial drop occurs when the roasting temperature is above 700 °C. The magnesium sulfate content remains relatively constant, at around 27 wt%. Soluble silicon content is constant as well, at around 5 wt% of silicon in the feed. Smaller amounts of sulfates were formed at higher temperatures because oxides were preferentially formed rather than sulfates.

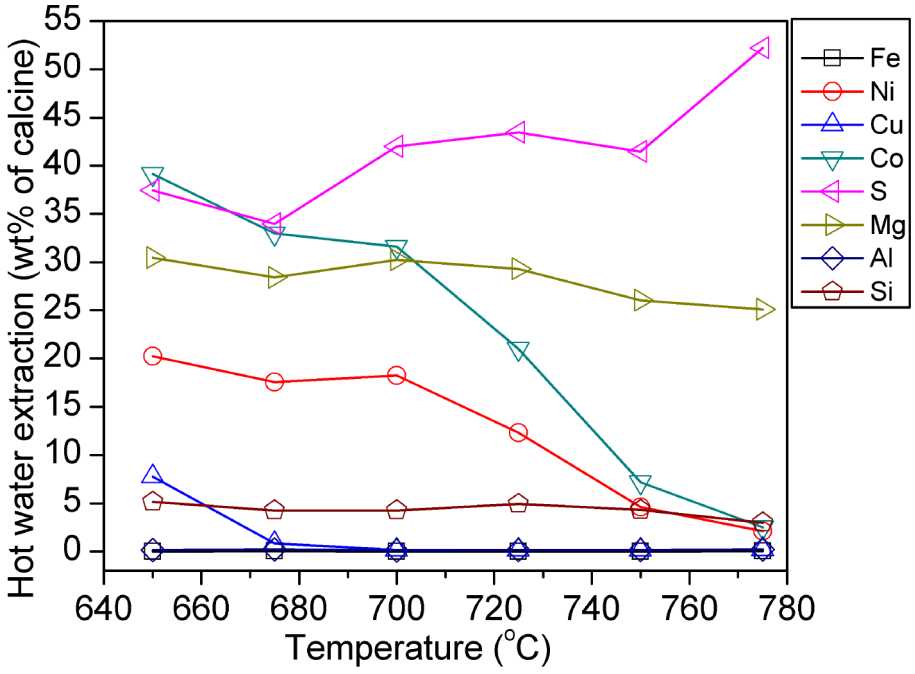

Figure 4.27. Water soluble species (%) in the roasted calcines vs. roasting temperature.

4.3.3 Effect of Roasting Time

Another series of roasting experiments was performed at 750 °C to evaluate the effect of the roasting time. Calcines were analyzed with XRD for their qualitative mineral compositions, and their XRD patterns are provided in Figure 4.28. As expected and can be seen from this figure, considerable roasting took place within one minute, resulting in the disappearance of all the original sulfide minerals and formation of various oxidized phases, i.e. trevorite ($NiFe_2O_4$), hematite (Fe_2O_3), mms ($(Fe,Ni)_{1-x}S$), NiO, and heazlewoodite (Ni_3S_2). The preferential oxidation of iron sulfide species forming iron oxides occurred within this first minute. Roasting reactions could be represented by Reactions (4.13) and (4.14). Further roasting led to the disappearance of mss after 4 min (Reaction (4.15)), as well as the formation of more oxides, i.e. hematite, trevorite, and NiO.

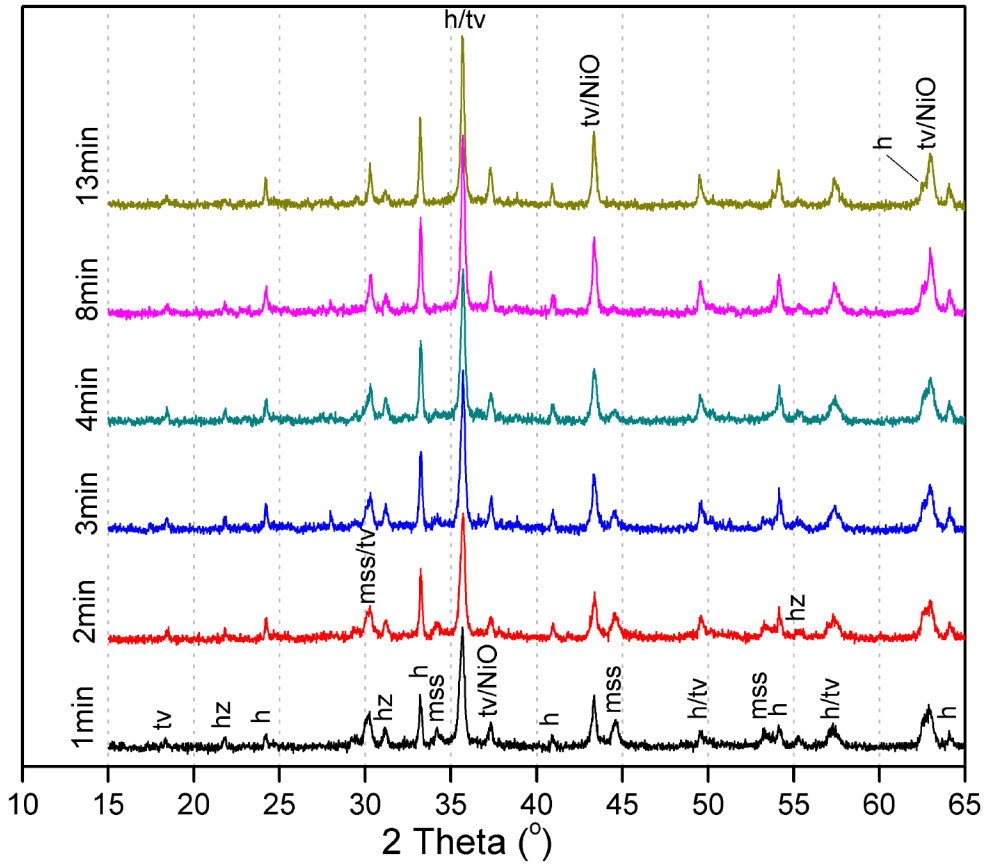

Figure 4.28. XRD patterns for the fluidized bed roasting tests at 750 °C with roasting time variation (tv-trevorite, mss-monosulfide solid solution, h-hematite, NiO-nickel oxide, hz-heazlewoodite).

Figure 4.29 illustrates the degree of sulfur elimination as a function of roasting time at 750 °C. Within 1min the sulfur removal reached 63%, indicating a high roasting rate at the beginning. The rate of sulfur elimination then decreased until it becomes practically zero after around 8 min, where the curve reaches a plateau at around 79%. The remaining 21% sulfur in the calcine is in the form of heazlewoodite based on the XRD analysis shown in Figure 4.28. Figure 4.30 shows the chemical composition change of the roasted pentlandite sulfide cores as a function of roasting time. As can be seen, the iron content in the pentlandite particles is reduced to the minimum 2 at% after 1 min (Reaction (4.14)). Longer roasting time leads to the further oxidation of nickel sulfide (NiS) to form Ni_3S_2 (Reaction (4.15)). In Figure 4.31, the average Co content of roasted pentlandite sulfide cores is plotted as a function of roasting time. As observed, the oxidation rate of cobalt from pentlandite is relatively high at the beginning of roasting then slows down as the roasting proceeds. The average Co content dropped to around 0.05% after 13 min.

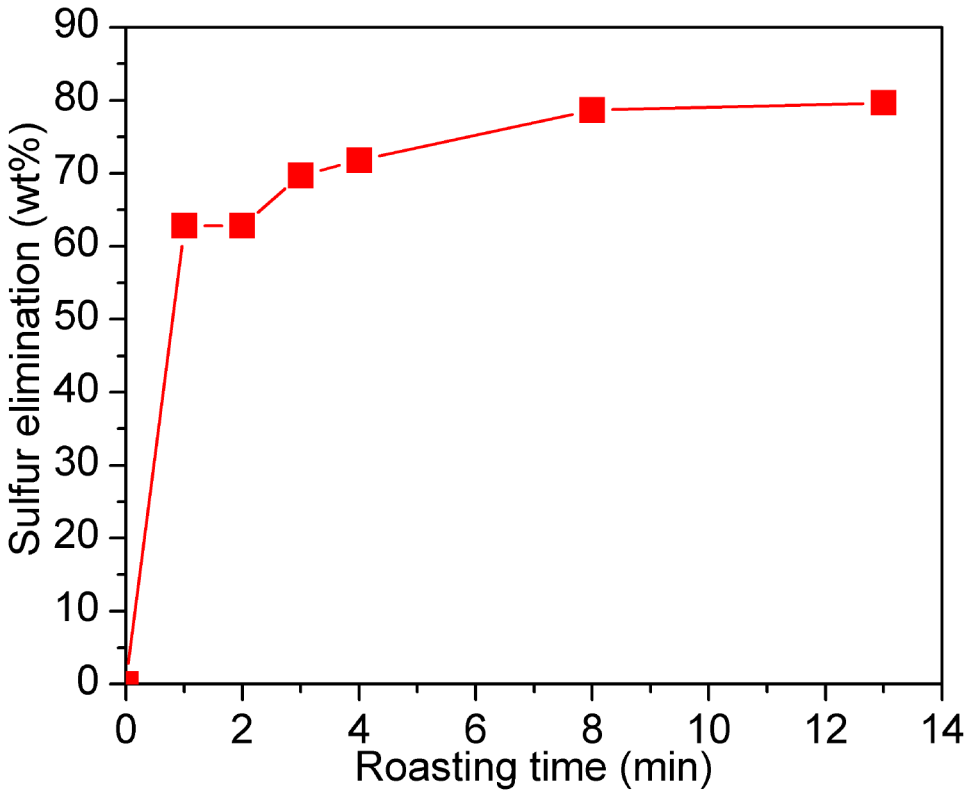

Figure 4.29. Degree of sulfur elimination as a function of roasting time at 750 °C.

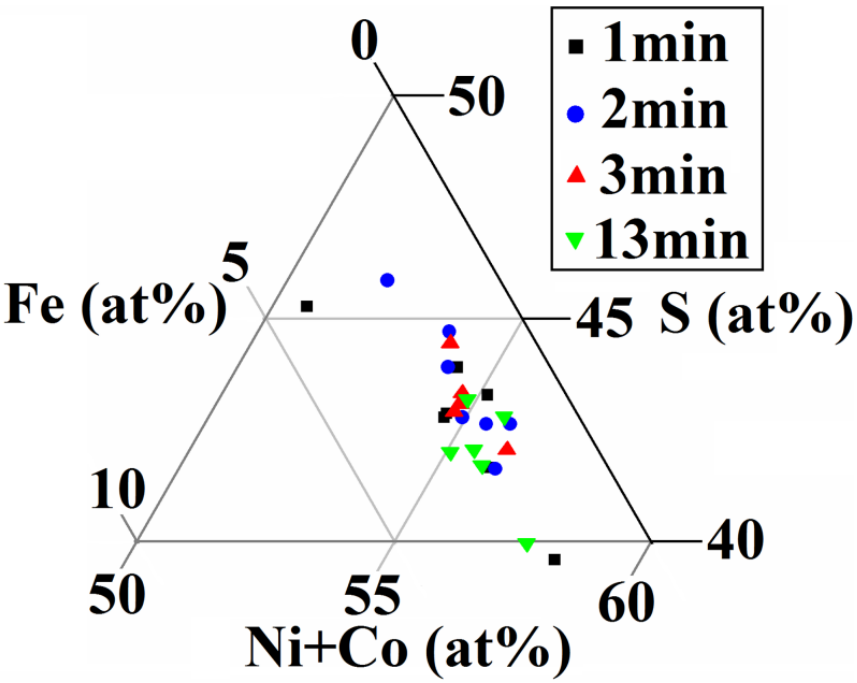

Figure 4.30. Fe-(Ni+Co)-S ternary diagram shows the composition change of the pentlandite sulfide cores as a function of fluidized bed roasting time measured by EPMA.

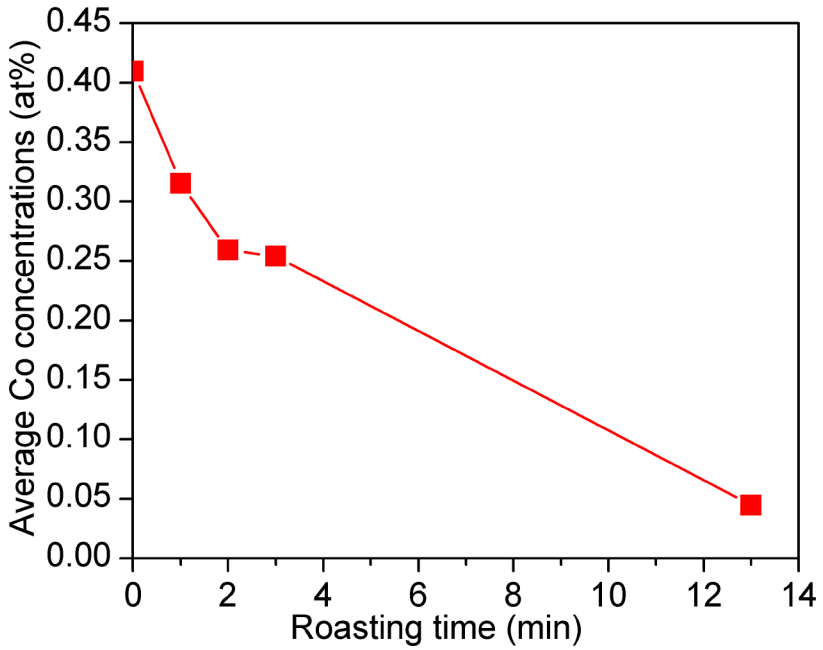

Figure 4.31. Average Co concentrations of the roasted pentlandite sulfide cores as a function of the fluidized bed roasting time measured by EPMA.

Calcines from these tests were also subjected to water leaching and ICP analysis. The results are presented in Figure 4.32. An interesting observation is that within the first two minutes, only Mg and Si were dissolved among all the metal elements. The formation of $NiSO_4$ started after 2 minutes. This is possibly because within the first two minutes iron from the pentlandite particles was preferentially oxidized, and the nickel sulfide would not likely be sulfated before the iron content in the pentlandite reaches its minimum, i.e. 2 at%. Figure 4.32 also illustrates that no sulfates of iron or copper could be formed at the temperatures as high as 750 °C under the current roasting conditions.

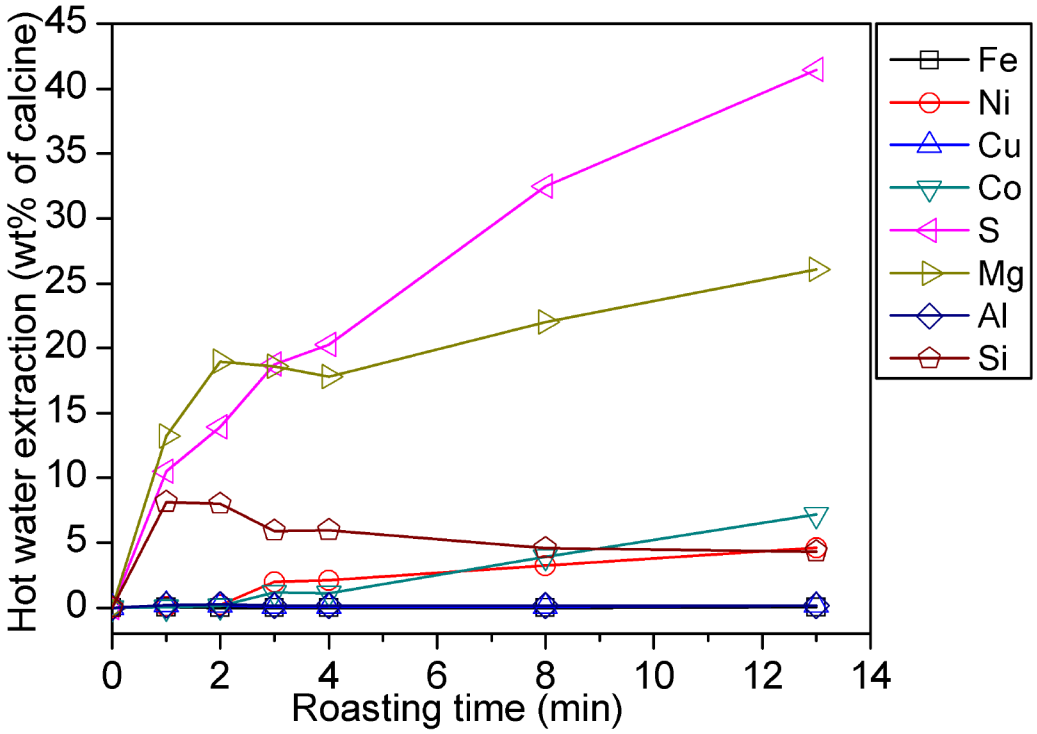

Figure 4.32. Water soluble species (wt%) in the roasted calcines vs. roasting time at 750 °C.

4.4 Conclusions

A laboratory scale, batch fluidized bed roaster was constructed to study the oxidation roasting of nickel sulfide concentrate. Roasting tests were carried out at temperatures between 650 °C and 775 °C. At all temperatures, oxidation roasting reactions mainly occurred within the first minute and usually lasted no longer than 10 minutes. Roasting reactions proceed as following: The

reactions start with the preferential oxidation of iron sulfide species forming iron oxides until the content of Fe in the pentlandite sulfide cores drops to 2 at%. The remaining nickel sulfide core in the pentlandite particles is either NiS or Ni_3S_2 depending on the roasting temperature, i.e. the nickel sulfide formed tends to be more sulfur deficient at higher temperatures. Formation of sulfates of Ni and Co occurs after the oxidation of iron sulfide. Low temperature (e.g. 650 °C) is favorable for the preferential oxidation of iron sulfide species while minimizing the formation of nickeliferous oxides, i.e. trevorite and NiO. The formation of these phases is inevitable for the roasting at temperatures higher than 700 °C. In the range of 650−775 °C no iron sulfate was formed. A higher degree of sulfur elimination could be achieved at higher temperatures. Sulfate formation was inhibited at higher temperatures at the cost of forming more oxides. Unlike the oxidation of iron sulfide, the oxidation of Co species through diffusion is a slow process. The oxidation of the nickel sulfide core Ni_3S_2 is the last step if the roasting temperature is high enough.

4.5 References

[1] J.R. Boldt, Jr., Falconbridge Pyrrhotite Process, in: P. Queneau (Ed.) The Winning of Nickel, Longmans Canada, Toronto, 1967, pp. 331-336.

[2] A.W. Fletcher, K.D. Hester, A New Approach to Copper-Nickel Ore Processing, AIME Transactions, (September 1964) 282-291.

[3] A.W. Fletcher, M. Shelef, A Study of the Sulfation of a Concentrate Containing Iron, Nickel, and Copper Sulfides, Transactions of the Metallurgical Society of AIME, 230 (1964) 1721-1724.

[4] A.W. Fletcher, M. Shelef, The Role of Alkali Sulphates in Promoting the Sulphation Roasting of Nickel Sulphides, in: Unit Process in Hydrometallurgy. Group C: Plant Operating Practice - Economics - General, New York Gordon and Breach Science Publishers, 1963, pp. 946-970.

[5] T.C. Frankiewicz, U.S. Patent 4,110,106, Selective Sulfation Process for Partitioning Ferrous and Non-Ferrous Values in an Ore, United States, 1978.

[6] M.C.B. Hotz, R.C. Kerby, T.R. Ingraham, The sulphation of nickel and cobalt ferrites and sulphides by molten sodium pyrosulphate and sodium bisulphate, Canadian Metallurgical Quarterly, 7 (1968) 205-210.

[7] P.J. Saikkonen, U.S. Patent 4,464,344, Process for Recovering Non-ferrous Metal Values From Ores, Concentrates, Oxidic Roasting Products or Slags, United States, 1984.

[8] P.J. Saikkonen, J.K. Rastas, The Role of Sulfate Melts in Sulfating Roasting, in: 25th Annual Conference of Metallurgists, Toronto, Ontario, Canada, 1986, pp. 278-290.

[9] P.G. Thornhill, U.S. Patent 2,813,015, Method of Roasting Metal Sulfide Concentrates in a Fluidized Bed, United States, 1957.

[10] P.G. Thornhill, U.S. Patent 2,813,016, Method of Roasting Nickeliferous Sulfide Concentrates in a Fluidized Bed, United States, 1957.

[11] H.Y. Sohn, R.P. Goel, Principles of Roasting, Minerals Sci.Engng, 11 (1979) 137-153.

[12] W. Curlook, Third Tutorial Symposium on Extractive Metallurgy, Pyrometallurgy: Roasting and Conversion, Toronto, 1973.

[13] D.R. Poirier, G.H. Geiger, Transport Phenomena in Materials Processing, The Minerals, Metals and Materials Society, Pennsylvania, 1994.

[14] G.G. Gubareff, J.E. Janssen, R.H. Torborg, Thermal Radiation Properties Survey, Honeywell Research Center, Minneapolis, MN, 1960.

[15] L. Cemič, O.J. Kleppa, High temperature calorimetry of sulfide systems, Phys Chem Minerals, 14 (1987) 52-57.

[16] G.A. Berezovskii, V.A. Drebushchak, T.A. Kravchenko, Low-temperature heat capacity of pentlandite, American Mineralogist, 86 (2001) 1312-1313.

[17] A. Roine, HSC Chemistry, Outokumpu Research Oy, Pori, Finland, 2007.

[18] H.E. Seemann, The Thermal and Electrical Conductivity of Fused Quartz as a Function of Temperature, Physical Review, 31 (1928) 119-129.

[19] B.S. Hemingway, Quartz; heat capacities from 340 to 1000 K and revised values for the thermodynamic properties, American Mineralogist, 72 (1987) 273-279.

[20] D. Yu, T.A. Utigard, TG/DTA study on the oxidation of nickel concentrate, Thermochimica Acta, 533 (2012) 56-65.

[21] M. Zamalloa, T.A. Utigard, The behaviour of Ni-Cu concentrate in an industrial fluid bed roaster, Canadian Metallurgical Quarterly, 35 (1996) 435-449.

5 Fluidized Bed Selective Sulfation Roasting

5.1 Introduction

A two-stage oxidation-sulfation roasting process for treatment of nickel sulfide concentrate is proposed. The previous chapter covered the first step, the oxidation roasting with an aim to maximize oxidation of iron while minimizing the formation of nickel ferrite. In this chapter, the second stage, the sulfation roasting step, is discussed with the evaluation of several parameters that may affect the sulfate formation, including the roasting gas flowrate, sulfation roasting temperature, the addition of Na_2SO_4, the sulfation roasting time, and the oxidation roasting temperature.

5.2 Materials and Methods

5.2.1 Sample

Raglan nickel concentrate was received from Xstrata Nickel's smelter in Sudbury, Ontario, Canada. Please refer to Section 2.2.1 for more details about the Raglan concentrate.

5.2.2 Experimental

The same fluidized bed roaster described in the previous chapter was employed. For sulfation roasting experiments, a column of alumina pellets coated with platinum was mounted beneath the porous frit to catalyze the oxidation of SO_2 by O_2, forming SO_3.

5.2.3 Analytical Methods

The products of the sulfation roasting were leached by water at 90 °C for 30 min to produce leachate and leach residues. The leach residues were fully digested using sodium peroxide (Na_2O_2) fusion technique. After proper dilution, solutions from both leaching and digestion were analyzed by ICP-OES (PerkinElmer Optima 7200 DV) for the determination of the percentages

of the water-soluble species in the calcines after roasting. Details of the sodium peroxide fusion technique and the calculation of the percentages of the water-soluble species are provided in Section 4.2.3.

Calcines were also mounted in the resin, then ground and polished with oil-based diamond suspension for examination under a SEM (JEOL JSM6610-Lv) which was equipped with an EDS detector (Oxford/SSD).

5.3 Results and Discussion

Since the objective of the proposed process was to preferentially oxidize the iron species by oxidation roasting prior to sulfation roasting, sufficient oxidized calcine needed to be prepared as the starting material for the sulfation roasting experiments. Based on the investigation on the oxidation roasting of the nickel concentrate discussed in the previous chapter, low temperature is preferable to minimize the formation of nickel ferrite ($NiFe_2O_4$). As a result, the Raglan concentrate was first oxidized in the fluidized bed roaster at 650 °C with an air stream of 3 L/min which gave an apparent gas velocity of 0.17 m/s for 10 minutes. SEM/EDS analysis on the calcine particles revealed a sulfide core surrounded by porous hematite rim with small amounts of nickel oxide as impurities based on EDS analysis.

5.3.1 Effect of the Sulfation Roasting Gas Flowrate

The effect of the sulfation roasting gas flowrate on sulfate formation was firstly examined. The gas composition was fixed at 5% SO_2, 19.95% O_2 and 75.05% N_2 which was achieved by mixing air with SO_2 at the ratio of 19:1. The reason for selecting this gas composition was that it falls into the favorable region for selective sulfation in Figure 1.11. Furthermore, this gas composition was roughly expected for sulfation roasting in an industrial fluidized bed roaster, because excessive air is used industrially for sulfation roasting, thus a lower SO_2 concentration of the roasting gas than that from the oxidation roasting (approximately 12%) is expected. For each test, a mixture of 5 g oxidation roasted calcine and 20 g sand was maintained at 700 °C for 30 minutes. Results are plotted in Figure 5.1 as the percentages of sulfate formation for different

elements based on the analysis of the products as described earlier. Sulfate formation results for the oxidation roasted calcine before sulfation roasting are also plotted at the flowrate of zero. As can be seen, formation of non-ferrous metal sulfates increased substantially after the sulfation roast. Sulfate formation for most of the elements analyzed reached a plateau at gas flowrates above 1 L/min, which is also the minimum flowrate to achieve fluidization. Therefore, a gas flowrate of 1 L/min was applied for further sulfation roasting tests. Formation of $CoSO_4$ and $CuSO_4$ reached 81% and 78%, respectively. $NiSO_4$ formation was still very low, at around 38%. The formation of iron sulfate remains constant at 2%. SEM/EDS analysis was performed on these sulfation roasted calcines. Figure 5.2 shows the micrographs of the sulfation roasted pentlandite particles with a gas flowrate of 1 L/min. The pores between the sulfide cores and the oxide layers were formed due to the volume reduction during the preferential oxidation of iron species from the pentlandite as well as the formation of SO_2. Most of the $NiSO_4$ appears to have formed as a thin layer on the surface of the nickel sulfide cores below the porous oxide layer. The slow kinetics of the $NiSO_4$ formation is probably due to the impervious nature of the $NiSO_4$ formed which inhibits further sulfation. Sulfate formation is first promoted by the presence of entrapped gases (SO_2 and O_2) in the pockets under the oxide layer, and then slowed down as the dense layer becomes thicker. In some particles, a dense iron nickel oxide ($Ni_xFe_{2-x}O_3$) layer, rather than $NiSO_4$, was formed on the sulfide core (e.g. Figure 5.2, bottom right corner). This layer of iron nickel oxide which covered the sulfide core has most likely been formed during the oxidation roasting stage. By examining the morphologies of the particles presented in Figure 5.2, it is apparent that the formation of $NiSO_4$ only occurred on the gas-sulfide interface (bare sulfide surface) in the gas pockets, and no $NiSO_4$ was formed on the gas-oxide interface or oxide-sulfide interface. The gas-sulfide and oxide-sulfide interfaces in the roasted pentlandite particles are formed through different oxidation mechanisms, which are suggested by other researchers [1]. Localized bare sulfide surface would form due to the outward elimination of sulfur by dissociation from the sulfide surface [1]. Gas channels must have formed through the oxide layer(s) to the outer gas environment for the escape of sulfur vapor or SO_2 from the shrinkage gap. The formation and growth of the oxide layer on the sulfide surface is due to metal elimination by cation migration through the sulfide to a region of close contact with the oxide layer, through which they further diffuse to the gas-oxide interface [1]. Suitable conditions for $NiSO_4$ formation (Reactions (1.14)-(1.16)) is provided on the bare sulfide surface

which has access to the sulfation gas through the gas channels in the oxide layer(s). The formation of sulfate on the sulfide surface is inhibited if there is a firm contact of the relatively dense oxide layer which isolates the sulfation gas. The oxide layer(s) ($Ni_xFe_{2-x}O_3$) formed is thermodynamically stable under the current sulfation roasting conditions, which would not be converted to sulfate. Based on the above discussion, the formation of $NiSO_4$ is dependent on the access of the sulfide surface to the sulfation gas, which is further determined by the porosity of the oxide layer(s) and the spatial relation between the sulfide surface and the oxide layer(s). Figure 5.3 illustrates the water leach residue of the sulfation roasted calcine. The sulfate layers were removed after leaching, leaving large gaps between the oxide layer and the nickel sulfide core.

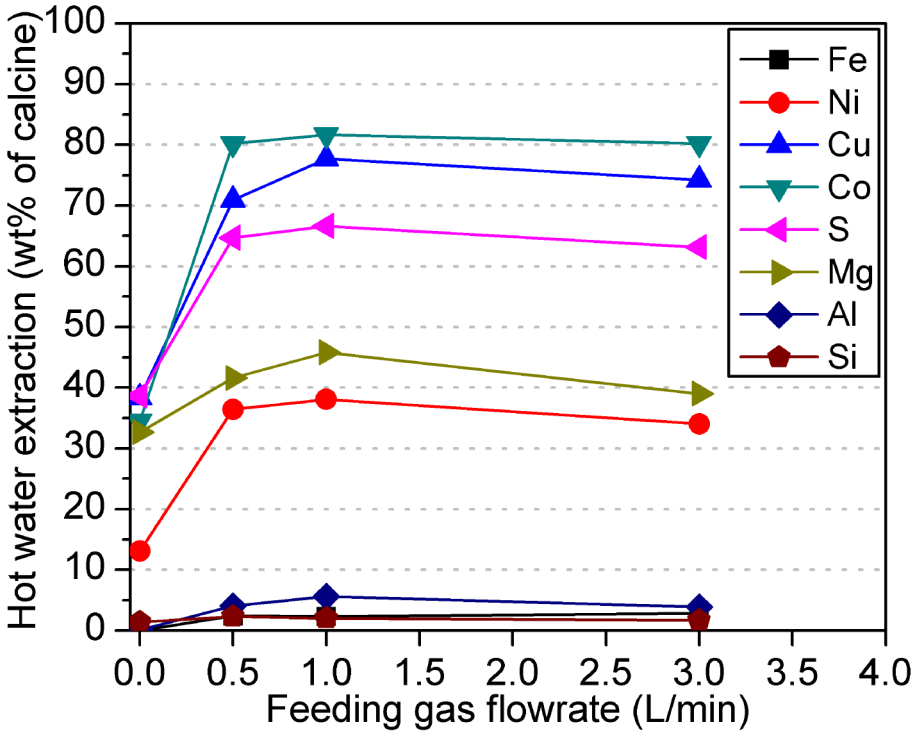

Figure 5.1. Effect of the sulfation roasting gas flowrate on the formation of sulfates.

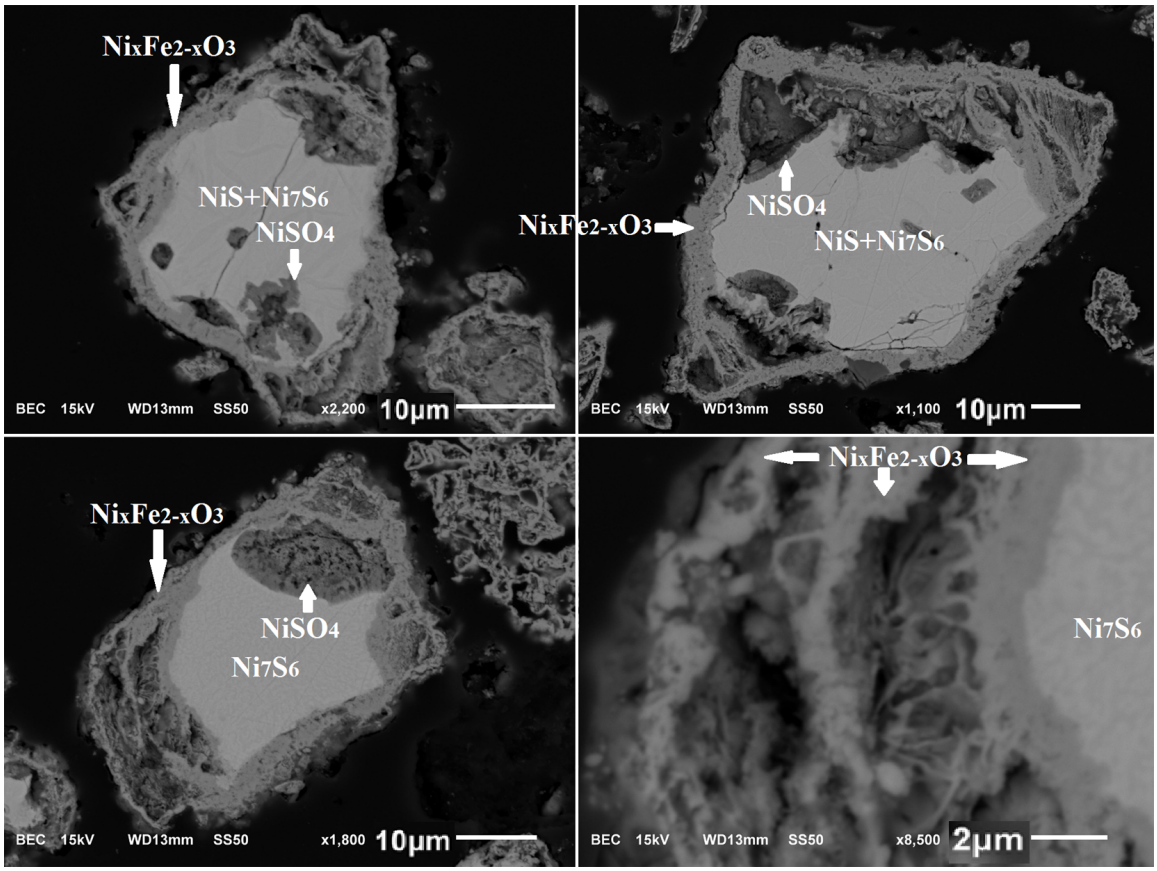

Figure 5.2. Sulfation roasted pentlandite particles with 1 L/min sulfation gas, exhibiting the formation of thin $NiSO_4$ layers on the nickel sulfide cores, and the formation of nickel iron oxide.

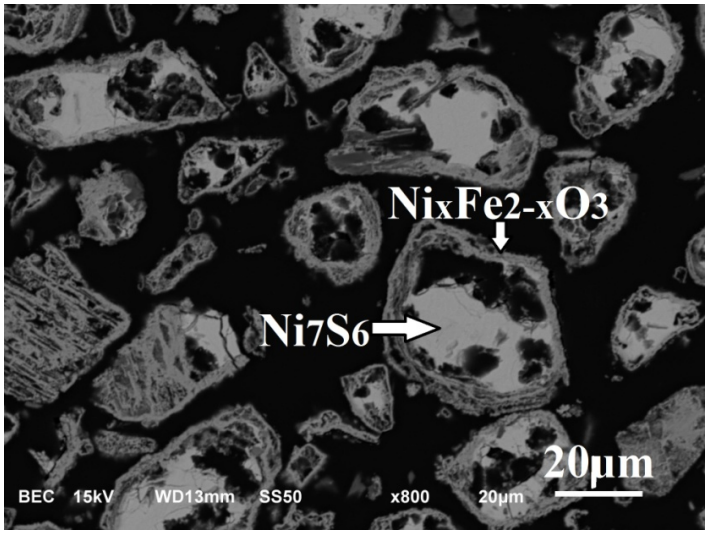

Figure 5.3. Leach residue of the sulfation roasted calcine with sulfation gas flowrate of 1 L/min.

5.3.2 Effect of the Sulfation Roasting Temperature

The dependence of the sulfate formation on the sulfation roasting temperature was investigated. For each test, a mixture of 5 g oxidation roasted calcine and 20 g sand was roasted in 1 L/min of the sulfation gas (5% SO_2, 19.95% O_2, and 75.05% N_2) at different temperatures, for 30 minutes. The sulfate formation results are shown in Figure 5.4. It is evident that the temperature dependency varies for elements. Formation of $CuSO_4$ shows a decreasing trend with the increase of sulfation roasting temperature from 660 °C up to 740 °C. $CoSO_4$ formation reaches a peak at 700 °C, while $NiSO_4$ does so at 720 °C. No appreciable iron sulfate formation is observed in the temperature range of investigation. The effect of the roasting temperature on sulfate formation is two-fold. On one hand, the temperature increase would enhance the kinetics for sulfate formation, especially for the formation of $NiSO_4$ which has been shown to be slow. On the other hand, the sulfates are less stable at higher temperatures, indicating that higher temperature favors more oxidation rather than sulfation from a thermodynamic point of view. As a result, the temperature preferable for the sulfation roasting would be the ones high enough to render fast kinetics for the sulfates formation but not excessive as to cause substantial oxidation. High temperature is not preferable for the sulfation of nickel species due to the higher tendency for formation of nickel ferrite. The optimum sulfation roasting temperature based on this series of experiments is 700 °C, which was adopted for further sulfation roasting experiments.

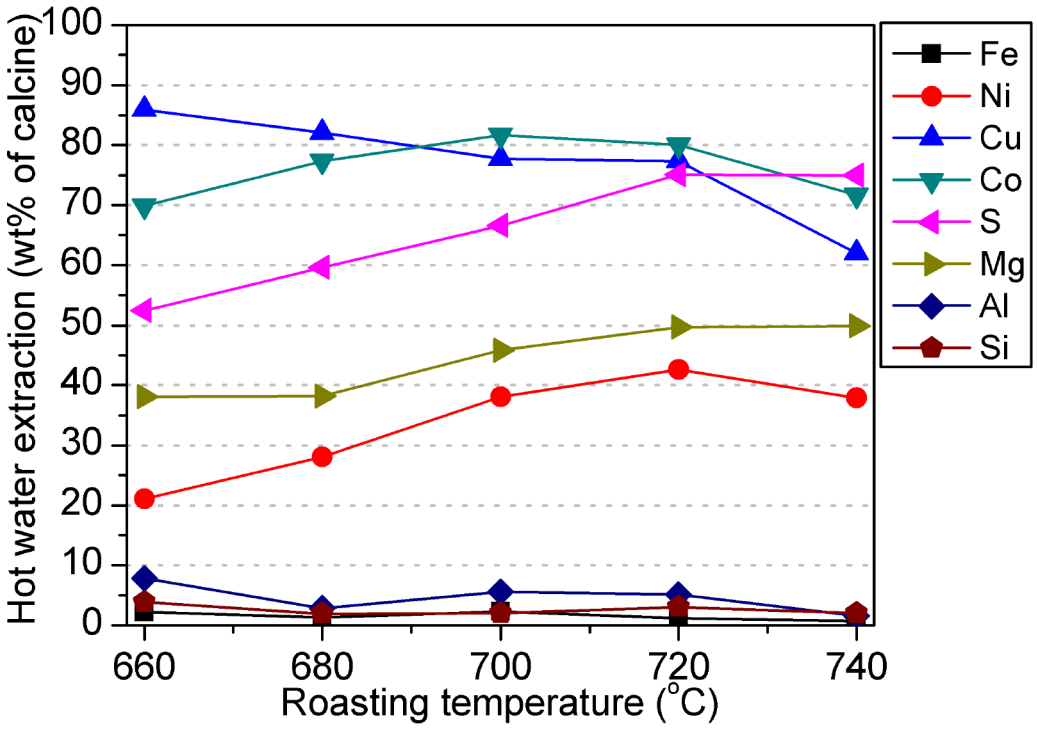

Figure 5.4. Effect of the sulfation roasting temperature on the formation of sulfates.

5.3.3 Effect of the Addition of Na_2SO_4

As discussed earlier, Na_2SO_4 has proven to be an effective promoter for the sulfation roasting. Therefore, the addition of Na_2SO_4 was studied for its effects on sulfate formation. For each experiment, a specific amount of Na_2SO_4 was firstly dissolved in 2.5 g water. Then the Na_2SO_4 solution was blended with 5 g oxidation roasted calcine to make a slurry. The slurry was then dried on a hot plate. The agglomerate formed was crushed to pass the 140 mesh sieve. It was then mixed with 20 g sand and roasted at 700 °C using 1 L/min sulfation gas for 30 min. The percentages of sulfate formation were plotted against the weight ratio of Na_2SO_4 to calcine in Figure 5.5. It can be seen that the formation of $NiSO_4$ was substantially promoted from 38% to 66% with the increase of the weight ratio of Na_2SO_4 to the calcine. Formation of $CuSO_4$ and $CoSO_4$ was also enhanced by approximately 5%. There was no increase in the iron sulfate formation because iron sulfate is not stable at this temperature. Sulfate formation levels off when the addition of $NaSO_4$ exceeds 10 wt% of calcine. As a result, the optimum $NaSO_4$

addition for the sulfation roasting under the current experimental conditions would be 10% of the weight of the calcine.

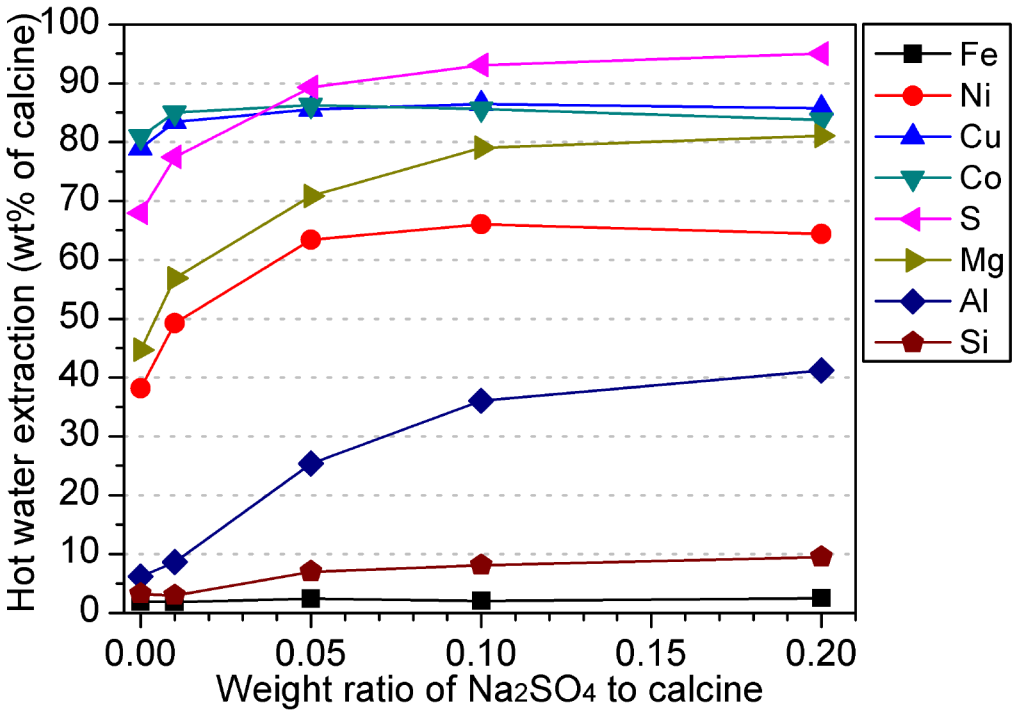

Figure 5.5. Effect of the addition of Na_2SO_4 on the formation of sulfates.

The calcines were analyzed with SEM/EDS. Figure 5.6 gives the BSE images of the sulfation roasted calcines with the weight ratios of Na_2SO_4 to calcine of 0.02, 0.05 and 0.10. The mixture of the oxidation roasted calcine and 10% Na_2SO_4 prior to sulfation roasting is shown on the top left corner for comparison. Nickel sulfide cores in the images can be distinguished by their brightness. The sulfide cores are monosulfide solid solution (mss, $(Ni,Fe)_{1-x}S$) with approximately 2 at% Fe before sulfation roasting (top-left image). This phase will further be represented by $Ni_{1-x}S$ for simplification since there is very little Fe in the phase. After sulfation roasting, the sulfide cores are primarily a non-stoichiometric sulfur-deficient phase which can be represented by Ni_7S_6 on average. This phase also has around 2 at% Fe. By comparison, it is obvious that more nickel sulfide cores were converted to $NiSO_4$ with the addition of higher amounts of Na_2SO_4. In the bottom right image which shows the sulfation roasted calcine with 10% Na_2SO_4 addition, the conversion of nickel sulfide cores to $NiSO_4$ is near completion. Figure 5.7 shows a sulfation roasted pentlandite particle with incomplete conversion of the

sulfide core to $NiSO_4$ (left) and one with complete conversion (right). Each $NiSO_4$ core is composed of large amounts of small grains, in which no Na_2SO_4 was detected. This suggests that the effect of the addition of Na_2SO_4 on the conversion of nickel sulfide to $NiSO_4$ must be indirect, meaning it takes place without physical contact. One possible mechanism is that the Na_2SO_4 acts as reservoir of SO_3 by forming $Na_2S_2O_7$ which is a strong sulfating agent, represented by Reaction (1.19). If the Na_2SO_4 in the fluidized bed happened to have physical contact with other sulfates, they would preferably form solid solution and/or binary sulfates, resulting in a lowered melting temperature. Such phases could melt in the fluidized bed if their melting point is below the roasting temperature, leading to the agglomeration of particles. For example, Figure 5.8 illustrates a cluster of particles agglomerated by a complex mixture of binary sulfates and sulfate solid solutions (Na, Ni, Mg, Cu, and Fe).

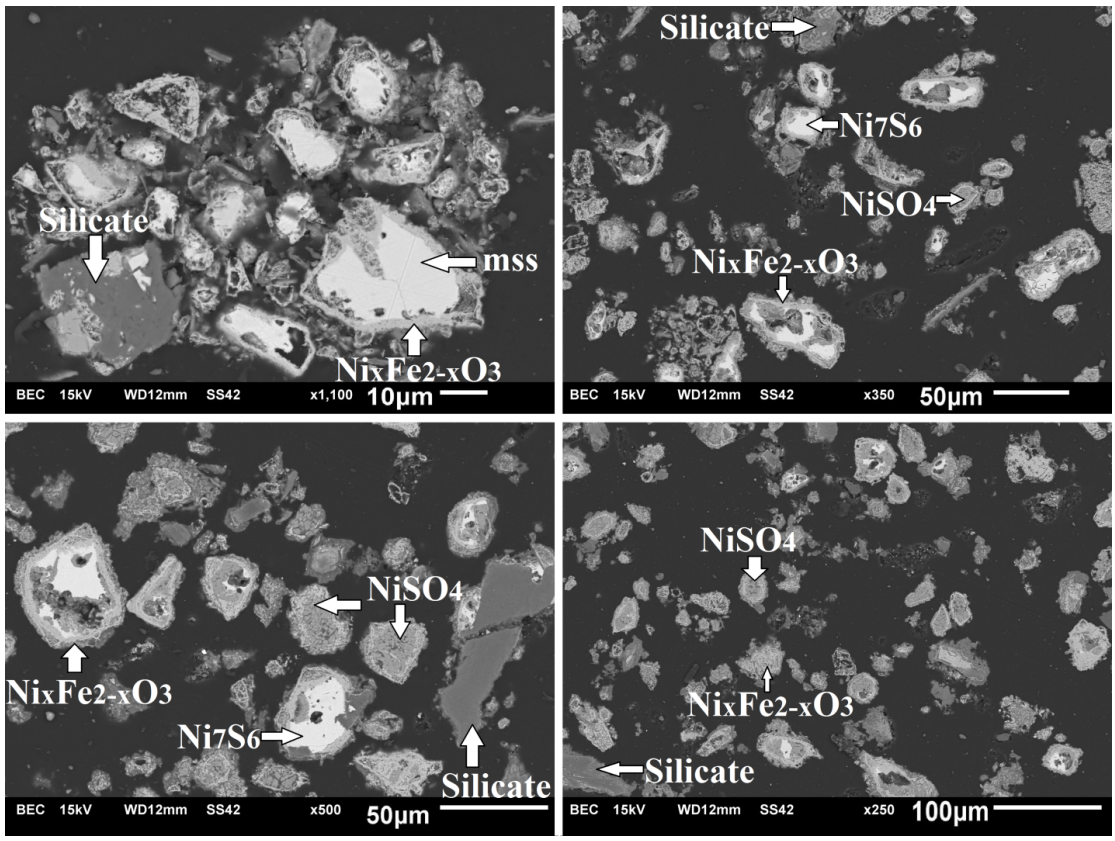

Figure 5.6. SEM images of the oxidation roasted calcine blended with 10 wt% Na_2SO_4 (top-left), and sulfation roasted calcines with the addition of Na_2SO_4 of 2% (top-right), 5% (bottom-left), and 10% (bottom-right) with regard to the weight of the calcine (mss: monosulfide solid solution).

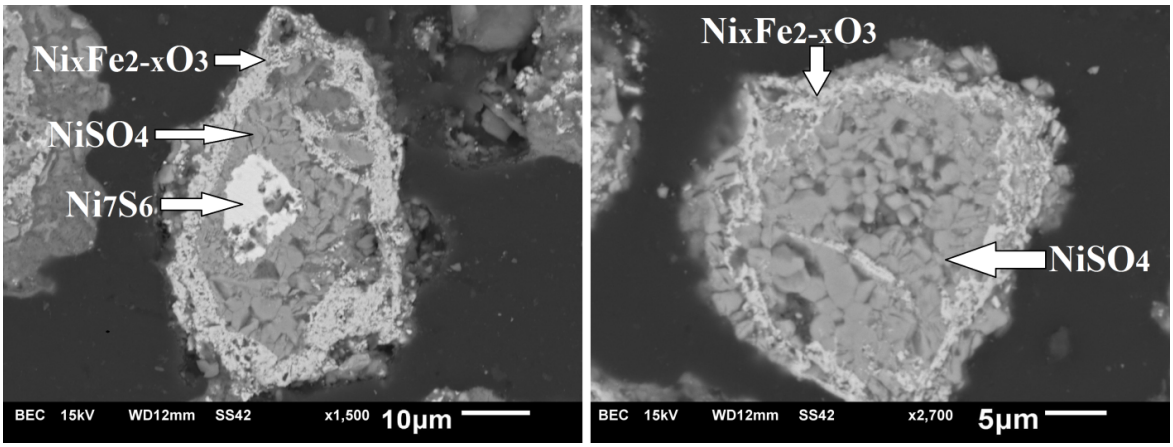

Figure 5.7. Incomplete (left) and complete (right) conversion of nickel sulfide cores to $NiSO_4$ with the addition of Na_2SO_4.

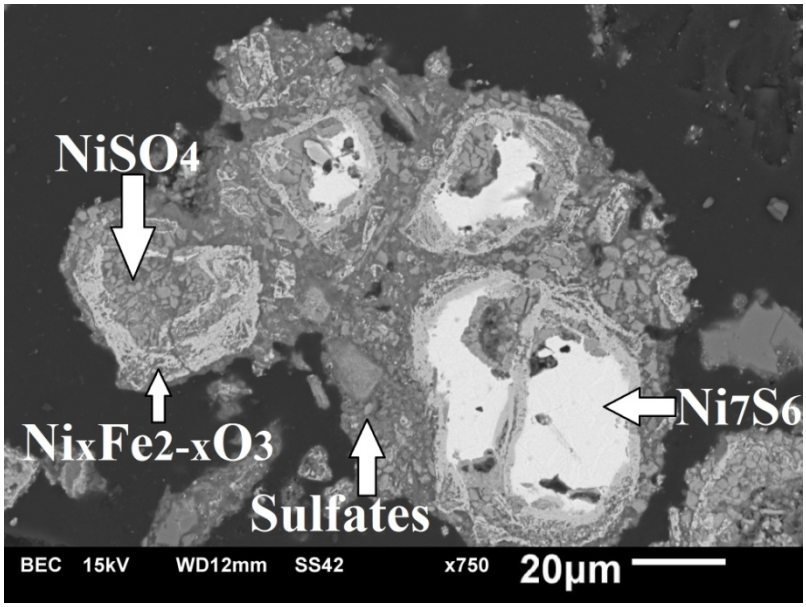

Figure 5.8. Cluster of calcine particles agglomerated by sulfate mixtures with 5% Na_2SO_4 addition.

5.3.4 Effect of the Sulfation Roasting Time

The effect of the sulfation roasting time on sulfate formation was also investigated. Mixtures of 5 g oxidation roasted calcine and 20 g sand with the addition of 10% Na_2SO_4 were sulfation roasted at 700 °C for 10 to 360 min. The results are shown in Figure 5.9. As can be seen, most

of the sulfation occurred in the first 10 min with a plateau reached after 150 min. The degrees of sulfation of Co and Cu species are the highest, at 92% and 89% respectively, after 150 min roasting. Iron sulfate formation is constant at around 2 to 3%. $NiSO_4$ formation reaches 75%, which is still relatively low. It is of interest to know the type of Ni species that are present in the leach residue. Figure 5.10 shows the relative amount of the Ni existing as sulfide and oxide in the water leach residues based on chemical analysis. It indicates that the sulfation of nickel sulfide is faster than nickel oxide, as the ratio of oxide/sulfide is larger at longer roasting times. After 150 min, the content of Ni existing as oxide in the residue exceeds 80%. This nickel should be associated with iron in the form of nickel ferrite which could have been formed during the oxidation roasting stage. To lower the formation of nickel ferrite, lower oxidation roasting temperatures were attempted with the results presented in the next section.

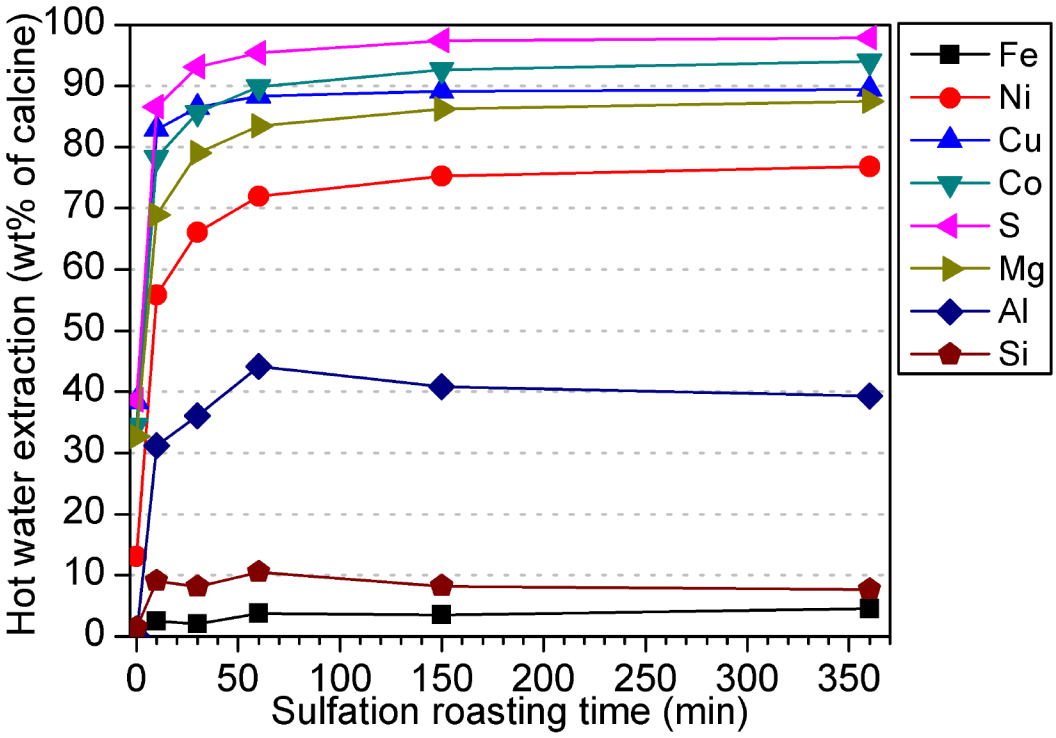

Figure 5.9. Effect of the sulfation roasting time on the formation of sulfates.

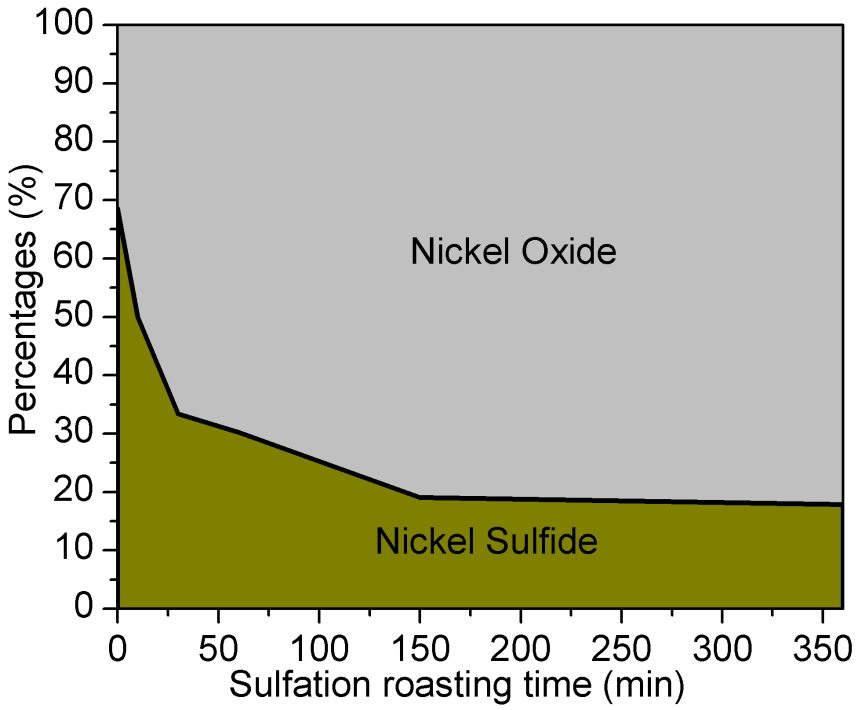

Figure 5.10. Calculated relative amount of Ni existing as sulfide and oxide (%) in the leach residue against sulfation roasting time.

5.3.5 Effect of the Oxidation Roasting Temperature

In this series of experiments, the temperature of the first stage oxidation roasting was investigated for its effect on the final formation of sulfates after the second stage sulfation roasting with the addition of Na_2SO_4. Oxidation roasting tests were performed at 500 °C, 550 °C, 600 °C and 650 °C for 10 min with 3 L/min air. Figure 5.11 illustrates four partly roasted pentlandite particles treated in different temperatures. At these low temperatures, iron sulfate(s) are stable. A relatively thick (2–3 μm) layer of $FeSO_4$ or $Fe_2(SO_4)_3$ was formed on the surface of each particle. The sulfide cores are rich in sulfur and some of them even contains substantial amount of iron, indicating a very low degree of oxidation at these temperatures. Because of the excessive amount of sulfur and iron left in the sulfide core, little nickel ferrite or other nickel iron oxide were formed. Afterwards, these calcines went through sulfation roasting under the following conditions: 10% Na_2SO_4 addition; roasting time 150 min; temperature 700 °C; feeding gas 5% SO_2, 19.95% O_2 and 75.05% N_2; 1 L/min. In order to investigate the necessity

of the first oxidation roasting stage, another test was conducted in which the Raglan concentrate was directly sulfation roasted at 700 °C without going through the first oxidation roasting stage, all other conditions remaining identical. The results of these experiments are plotted in Figure 5.12. It is clear that it is necessary to have the first oxidation roasting stage since the $NiSO_4$ formation is much lower (64%) without the conduction of the oxidation roasting stage. The $NiSO_4$ curve reaches a peak of 79% at 600 °C. The formation of $CuSO_4$ and $CoSO_4$ are also slightly higher at 600 °C. Therefore, the optimum oxidation roasting temperature appears to be 600 °C.

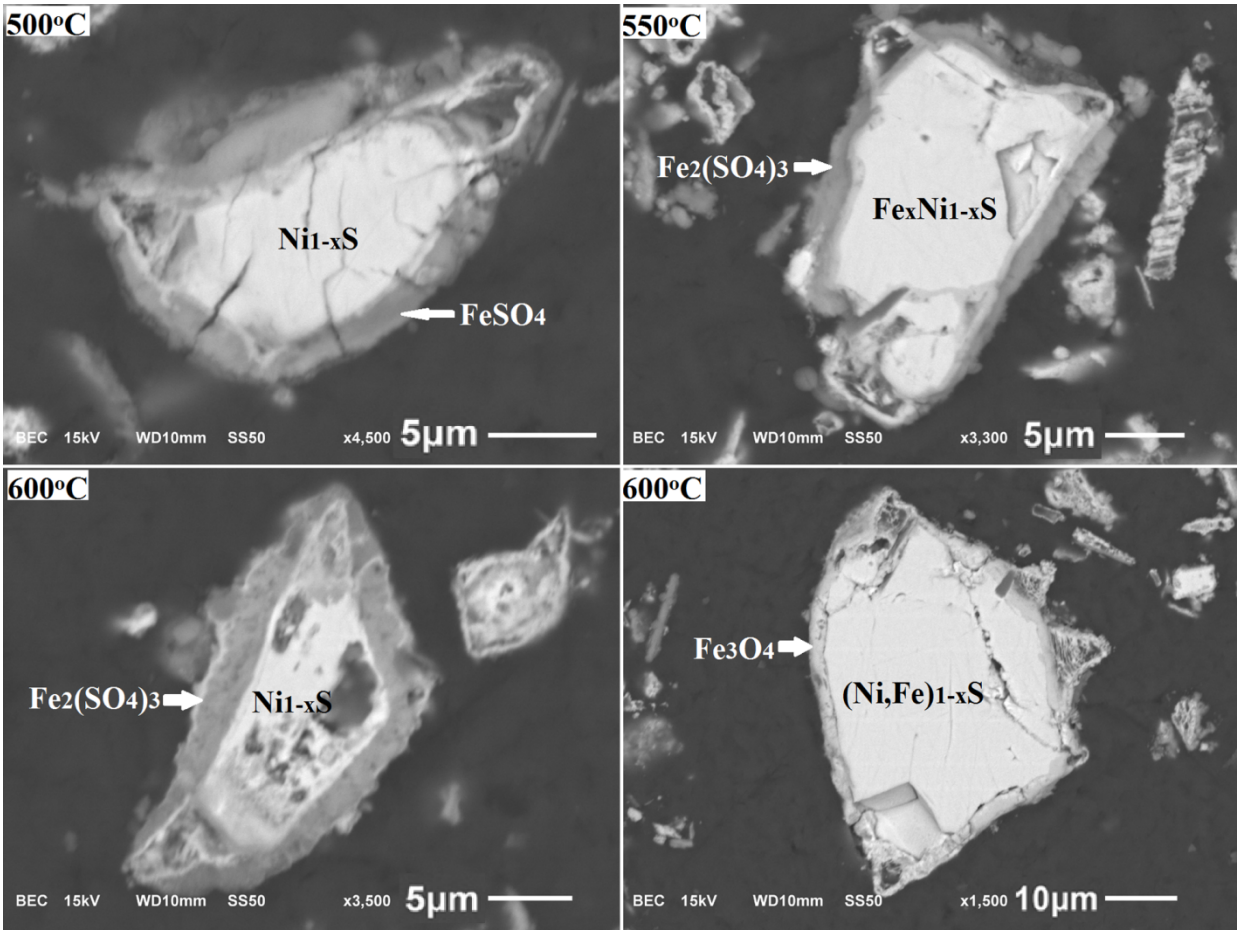

Figure 5.11. Partly oxidation roasted pentlandite particles under 500 °C, 550 °C and 600 °C.

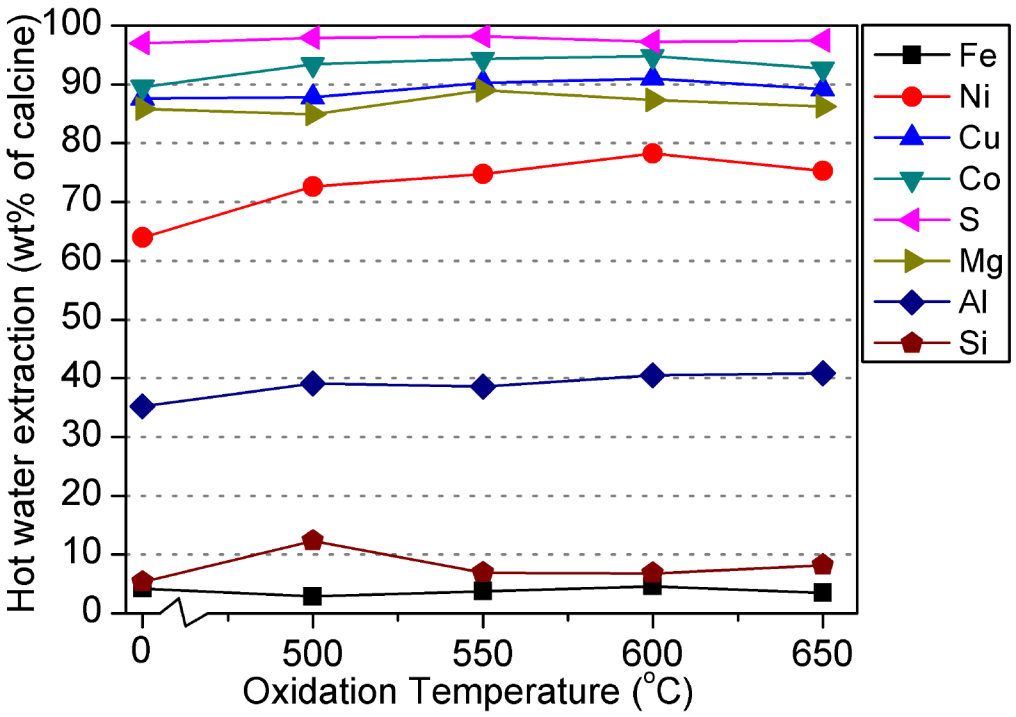

Figure 5.12. Effect of the temperature of the oxidation roasting stage on the formation of sulfates in the sulfation roasting stage at 700 °C.

The sulfation roasted calcines were examined with SEM/EDS. Results indicate the near-complete conversion of nickel sulfide cores to $NiSO_4$. However, a substantial amount of non-stoichiometric nickel ferrite with varying Fe/Ni ratio was found in all samples. Since no appreciable nickel ferrite was formed during the oxidation roasting stage at relatively low temperature, it must have been formed in the sulfation roasting stage along with the formation of sulfates, given a long roasting time (150 min) and relatively high temperature (700 °C). Figure 5.13 shows the morphologies of the sulfation roasted pentlandite particles. The top-left image shows the calcine produced by direct sulfation of the Raglan concentrate, in which the iron nickel oxide is evenly spread in the nickel sulfate matrix. This morphological feature is much different from that of the other three images, in which the oxide and the sulfate are concentrated in different regions with a defined boundary. This morphological difference is caused by the effect of the first oxidation roasting stage. Most of the iron would be preferentially oxidized to form layer(s) of iron oxides during the oxidation roasting stage, resulting in the physical separation of Fe from Ni through chemical reactions and ion diffusion. On the other hand, one-step direct sulfation roasting of the concentrate results in simultaneous formation of oxide and

sulfate, hence their inter-mixed distribution. The side effect is formation of a larger amount of nickel ferrite. This explains why the nickel sulfate formation is relatively low by direct sulfation roasting as shown in Figure 5.12.

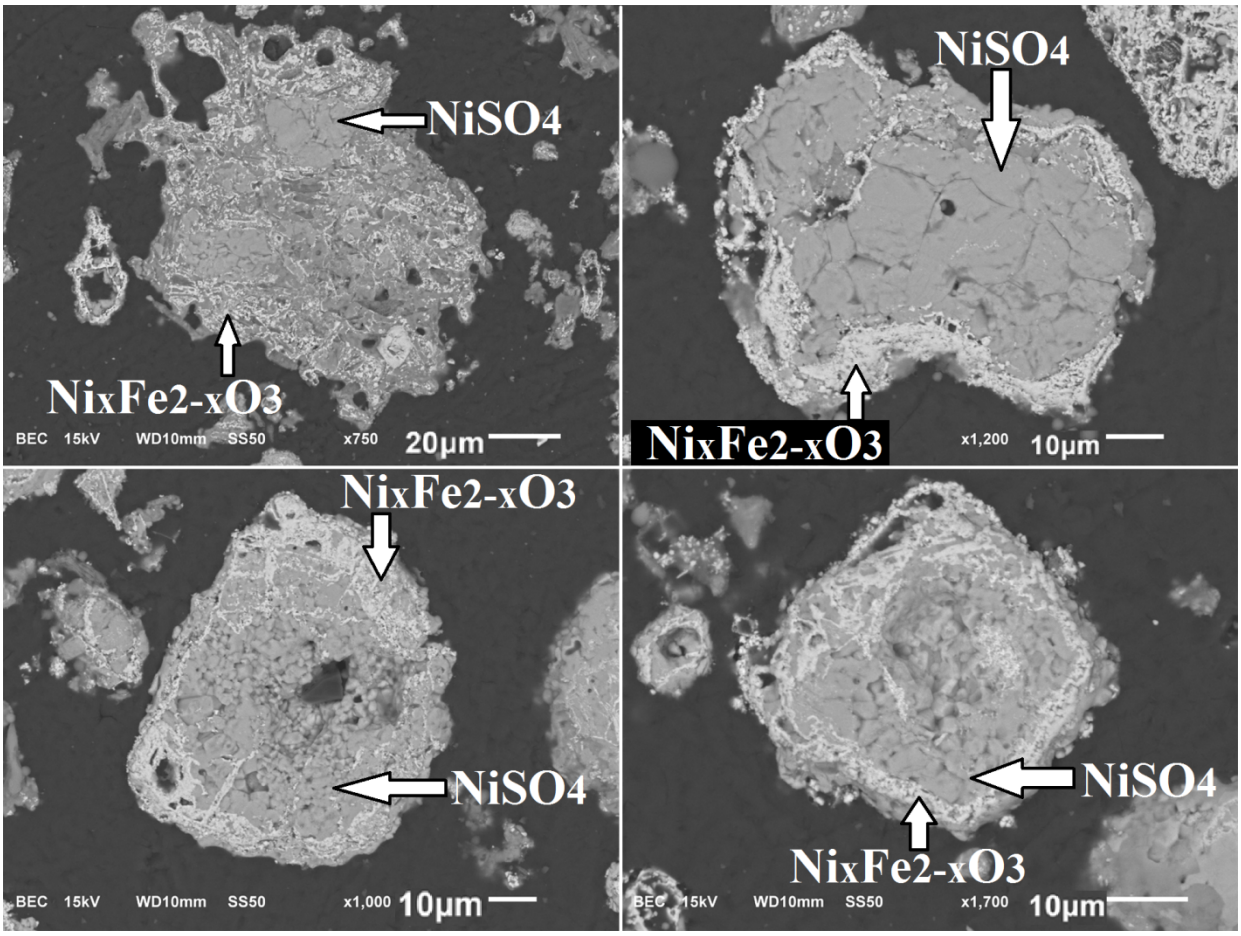

Figure 5.13. Sulfation roasted pentlandite particles: single stage sulfation roasting at 700 °C (top-left); two-stage roasting with the oxidation roasting temperature of 500 °C (top-right), 550 °C (bottom-left) and 600 °C (bottom-right).

5.3.6 Repeated Sulfation Roasting Tests

Five (5) sulfation roasting tests were repeated under optimized conditions to evaluate its uncertainty. Percentages of sulfate formation for various elements in these five tests were

plotted in Figure 5.14. Uncertainty limits based on 95% confidence level as well as the mean values (average) are reported in Table 5.1.

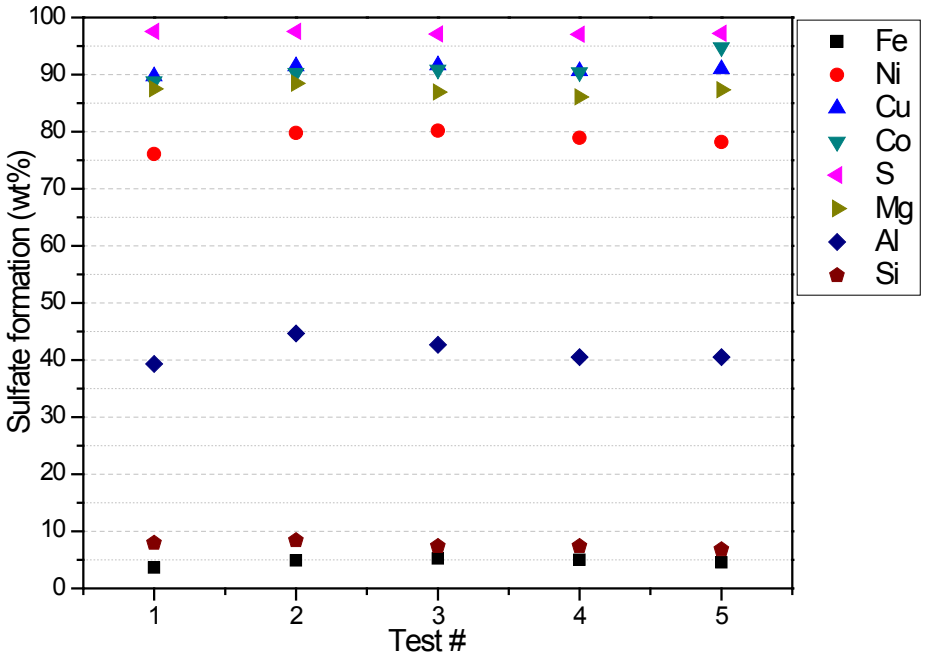

Figure 5.14. Repeated sulfation roasting tests conducted under optimized conditions.

Table 5.1. Sulfate formation (%) and uncertainty limits for sulfation roasting tests under optimized conditions.

Elements	Sulfates formation mean value	Uncertainty limits (95% confidence level)
Fe	4.66%	±1.22%
Ni	78.6%	±3.22%
Cu	90.9%	±1.54%
Co	91.0%	±4.48%
S	97.3%	±0.48%
Mg	87.3%	±1.74%
Al	41.5%	±4.27%
Si	7.59%	±1.22%

5.3.7 Mechanism of Sulfation

It is evident from the above results that the addition of Na_2SO_4 enhances the sulfation. Other researchers have shown that the enhancement of sulfation results from the destruction of the impervious $NiSO_4$ film by Na_2SO_4, thus creating new reaction sites for sulfate formation [2]. In the present study, no Na_2SO_4 was present in the sulfate cores of the sulfation roasted pentlandite particles, based on the SEM/EDS analysis. Instead, the sulfate cores were almost pure $NiSO_4$. Na_2SO_4 was only observed in the sulfate mixture as the outer layer of each particle, which is peripheral to the iron oxide layer that was formed during the oxidation roasting stage, as can be seen in Figure 5.13. Since the way the Na_2SO_4 was mixed with the oxidation roasted calcine was by making a slurry, the small amount of sulfates ($NiSO_4$, $MgSO_4$) that was formed during the oxidation roasting stage was probably dissolved into the Na_2SO_4 solution and formed a sulfate mixture of low melting temperature after drying during the sample preparation. At the initial stage of sulfation roasting, this sulfate mixture would melt immediately and dissolve any $NiSO_4$ that is formed. However, during the progression of the sulfation roasting, it would eventually reach a saturation point beyond which the sulfate melt could no longer dissolve more $NiSO_4$ (e.g. once the composition crossed the liquidus line with a negative slope in the $NiSO_4$-Na_2SO_4 phase diagram, Figure 1.12). The formation of $NiSO_4$ beneath the oxide layer of each roasted pentlandite particle requires SO_3 as a reactant. SO_3 has to first diffuse though the sulfate melt on the surface of each particle via the $S_2O_7^{2-}$-SO_4^{2-} exchange reaction and the counter diffusion of these two ions, then passing through the porous oxide layer. As could be clearly seen from Figure 5.7 and Figure 5.13, the sulfate cores formed within the particles are composed of large amounts of micro grains with cracks and crevices which provide channels for quick gas transport. As a result, through these cracks and crevices, the SO_3 could reach the surface of the sulfide core where the sulfation reactions would take place.

Figure 5.15 shows the BSE image of another partly roasted pentlandite particle with a nickel sulfide core. This sulfide core is composed of two phases, which can be seen as areas with two gray levels after contrast enhancement as shown in the top-right corner. The darker inner core is sulfur-rich and nickel-deficient monosulfide solid solution ($Ni_{1-x}S$ with 2 at% Fe), while the brighter outer phase is Ni_7S_6. This indicates that the conversion of the sulfide core from $Ni_{1-x}S$

to Ni_7S_6 accompanies $NiSO_4$ formation, which could be represented by Reaction (5.1). In the previous chapter, it has been shown that the sulfide cores of the partly roasted pentlandite particles in the calcines are more sulfur-deficient at higher roasting temperatures. Therefore, the driving force for Reaction (5.1) is likely the higher sulfation roasting temperature (700 °C) compared with the oxidation roasting temperature (650 °C). Sulfur elimination from sulfide as represented by Reaction (5.1) is achieved by first migration of sulfur ions from the interior of the sulfide to the surface [1] where it could combine with O_2. During the conversion of the sulfide cores to Ni_7S_6, the sulfation reaction would proceed according to Reaction (5.2). The SO_2 required for the sulfation reaction could be provided from Reaction (5.1). Furthermore, Reaction (5.1) would also result in the shrinkage of the sulfide core, which provides more space for the formation of $NiSO_4$ on the sulfide surface beneath the oxide layers. Evidence for this could be found in Figure 5.15, in which the large shrinkage gaps between the sulfide core and the oxide layers are filled with $NiSO_4$. The oxygen required for the sulfation reactions could be supplied by either the decomposition of SO_3 or the inward diffusion of O_2 from the gas. The overall sulfation mechanism by diffusion could be schematically represented by Figure 5.16.

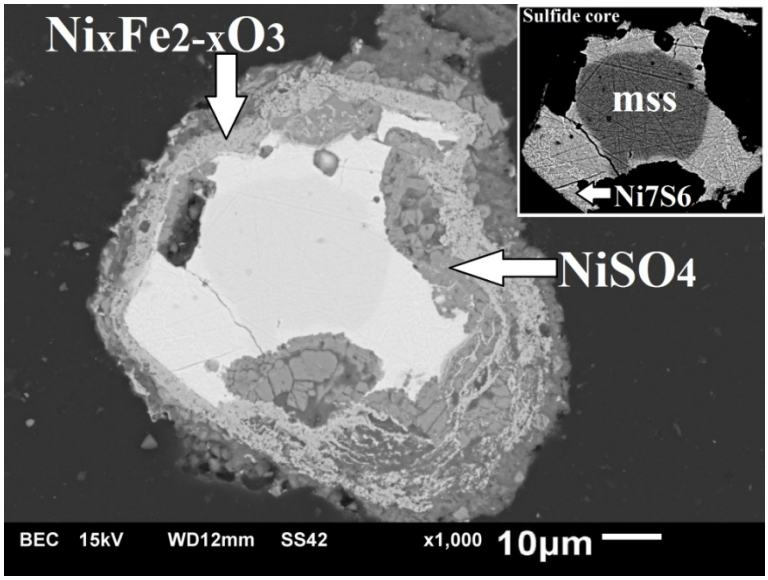

Figure 5.15. Sulfation roasted pentlandite particle with 20% addition of Na_2SO_4 at 700 °C for 30min. The sulfide core was isolated and shown in the top-right corner with enhanced contrast illustrating the presence of two sulfide phases.

$$7Ni_{1-x}S(s) + (1+6x)O_2(g) = (1-x)Ni_7S_6(s) + (1+6x)SO_2(g) \quad (5.1)$$

$$Ni_7S_6(s) + SO_2(g) + 13O_2(g) = 7NiSO_4(s) \quad (5.2)$$

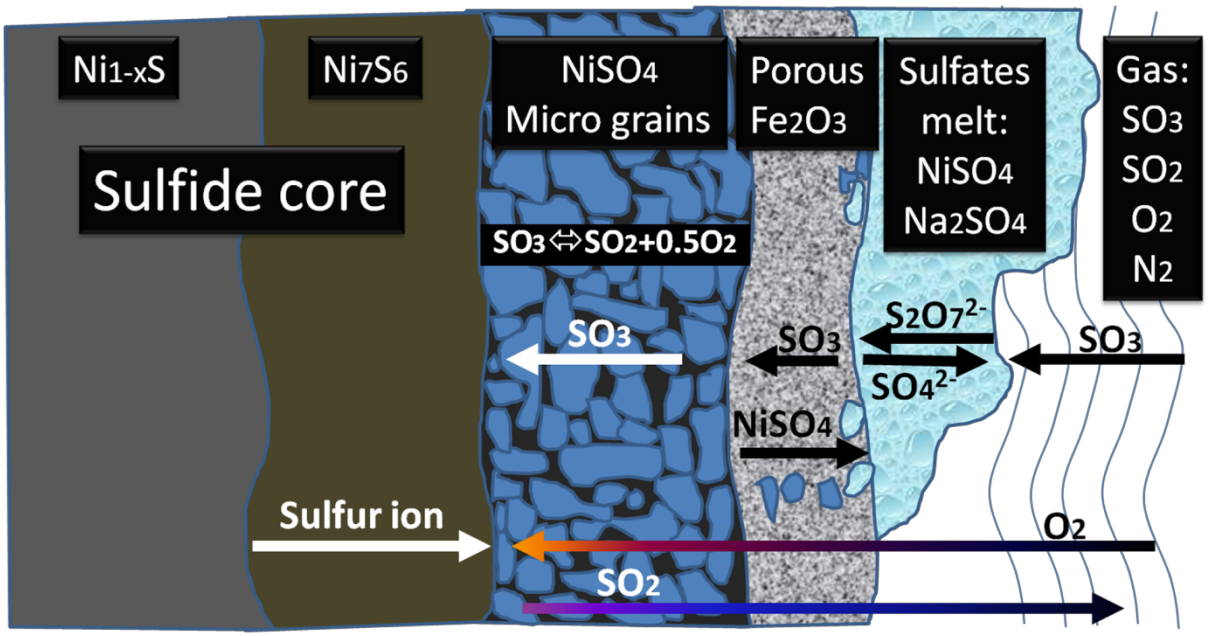

Figure 5.16. Schematic representation of the sulfation mechanism.

As represented by Reactions (5.1) and (5.2), the sulfation reactions are straightforward and do not involve oxide(s) as intermediate product(s) based on the observation by SEM. This is contradictory to the mechanism proposed by earlier researchers [2, 3]. In order to further investigate this, another series of tests was performed. Two samples of nickel sulfide (main phases: NiS, Ni_3S_2) were ground and polished to make flat surfaces. An appropriate amount of Na_2SO_4 solution was then sprayed onto the surface of one sulfide sample and dried to have a layer of Na_2SO_4 deposited on the sulfide with an average thickness of 10–20 μm. For comparison, the other sulfide sample was not coated with Na_2SO_4. Both of these specimens were suspended with the flat surfaces facing downwards in the roaster at 700 °C. Sulfation gas (5% SO_2, 95% air) of 3 L/min was introduced to the flat surfaces. Both of these two sulfide samples were pulled out from the roaster after 30 min. They were then cut and prepared for observation under SEM/EDS. Their morphologies are shown in Figure 5.17. As could be seen, without the Na_2SO_4 coating, NiO was formed on the surface and propagated into the sample for hundreds of micrometers. The black areas in the sulfide sample are crevices believed to have formed due to the volume reduction during the oxidation of nickel sulfide. No $NiSO_4$ was formed, indicating that $NiSO_4$ is thermodynamically unstable under the current sulfation

roasting conditions. For comparison, $NiSO_4$ was formed on the surface of the sulfide cores beneath the oxide layer as shown in Figure 5.2 during the sulfation roasting with the same sulfation gas composition and temperature. This indicates that the presence of the porous oxide layer maintains a stronger sulfation gas environment, i.e. higher partial pressure of SO_3, beneath the oxide layer. And the presence of the Na_2SO_4-$NiSO_4$ sulfates melt as an outer layer as shown in Figure 5.6 and Figure 5.7 further enhanced this effect. The other three images in Figure 5.17 illustrate the direct interaction between Na_2SO_4 and the sulfide sample under sulfation conditions. In the top-right and bottom-left images, only a layer of sulfate(s) with varying Na/Ni ratio was formed on the sulfide sample. There exists a layer of Ni_2O_3 in between the sulfide core and the sulfates layer in the bottom-right image. The formation of Ni_2O_3 with a valence state of Ni^{3+} could not possibly result from the oxidation of nickel sulfides, as it is thermodynamically unstable under the present experimental conditions. The oxidation product would be NiO rather than Ni_2O_3, if any. Misra and Whittle [4] studied the effects of SO_2 and SO_3 on the Na_2SO_4 induced hot corrosion of nickel. They also found the formation of a layer of Ni_2O_3 beneath the porous NiO scale in the presence of Na_2SO_4 at 750 °C. They proved the formation of the metastable Ni_2O_3 was from the decomposition of the $NiSO_4$ component of the Na_2SO_4-$NiSO_4$ melt, which was then slowly converted to NiO. As a result, it is believed that in the present study as shown in the bottom-right corner of Figure 5.17, the layer of Ni_2O_3 was also from the decomposition of the $NiSO_4$ component of the outermost layer of Na_2SO_4-$NiSO_4$ melt. It is therefore evident that the sulfation of NiS does not involve the preliminary formation of NiO as an intermediate compound. The NiS could be directly converted to $NiSO_4$ by the sulfation gas given favorable sulfation conditions. The role of the Na_2SO_4 in the sulfation is to quickly dissolve the $NiSO_4$ formed to form a sulfate melt and expose new sites on the sulfide for sulfation. Also it accelerates the transportation of the sulfation gas (SO_3) to the sulfide with the $S_2O_7^{2-}$-SO_4^{2-} equilibrium in the sulfate melt.

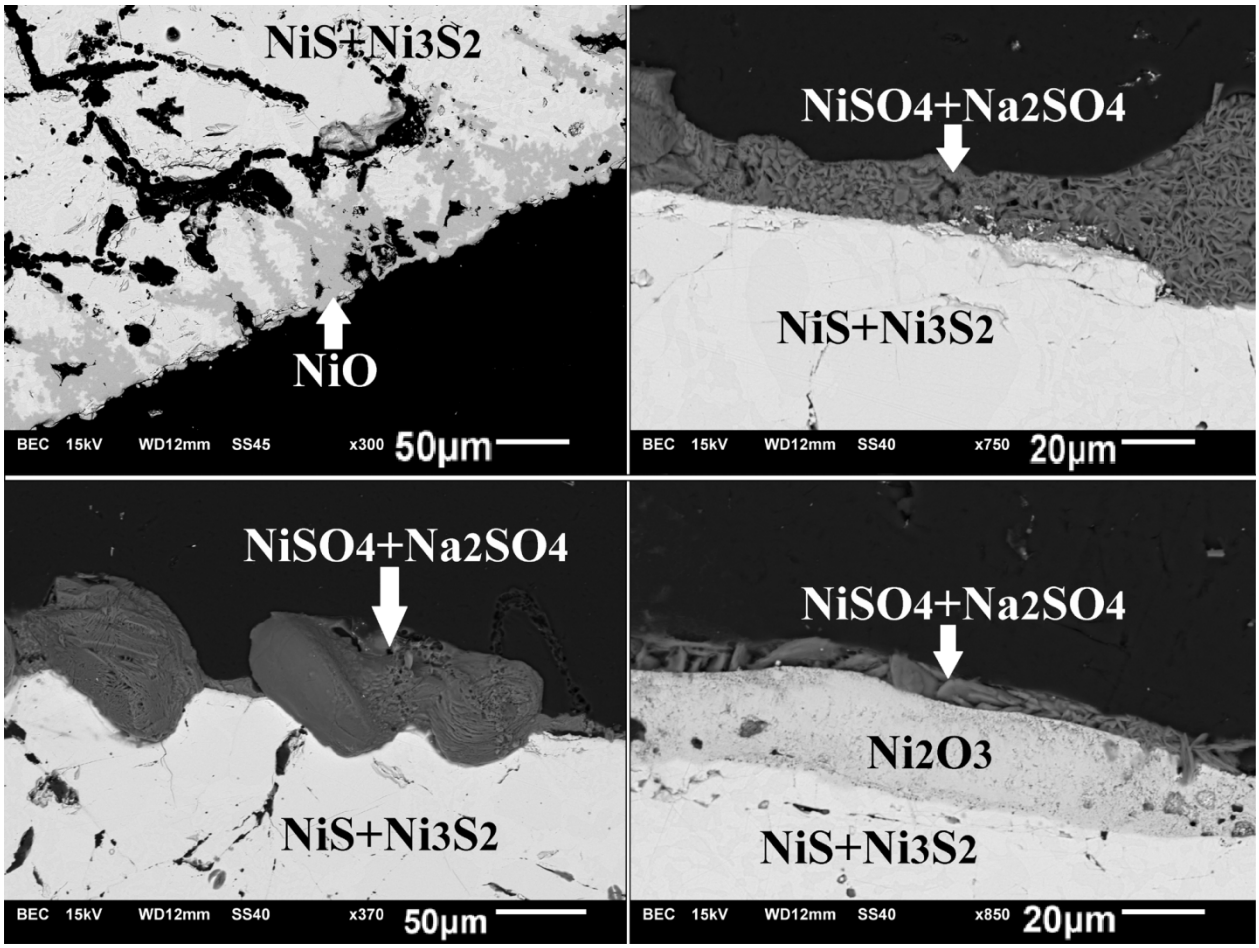

Figure 5.17. Nickel sulfide samples uncoated (top-left) and coated with Na_2SO_4 (the other three), sulfation roasted at 700 °C for 30 min.

One important observation of the present study is the formation of micro grains of $NiSO_4$ with cracks and crevices in the pentlandite particles which facilitate the formation of $NiSO_4$ by providing channels for the access of the sulfation gas. Those cracks and crevices are suggested to have formed due to the combination of several factors: 1) The high temperature (700 °C) that results in high kinetics for reactions; 2) The double sulfates melt-porous oxide layers surrounding the sulfide core that maintain a very favorable gas environment for sulfate formation; 3) The volume increases by approximately 150% as nickel sulfide (NiS) is converted to sulfate, which introduces significant stresses into the sulfate formed; 4) Quick formation of $NiSO_4$ due to the easy access of sulfation gas to the sulfide surface through the already-formed

cracks and crevices so that more stress is added to the sulfate particle before the stress in the particle is relieved by atomic rearrangement, resulting in crack formation; 5) Such cracks provide more channels for the migration of sulfation gas to the surface of the sulfide. As a result, the sulfation is self-sustained by the development of cracks and crevices.

5.3.8 Leach Residue

Under the optimum roasting conditions as suggested by the present study, 79% Ni, 91% Cu and 91% Co could be recovered by leaching with water after sulfation roasting. Fe can be effectively rejected by forming iron oxides, and the soluble Fe is only 5% during leaching. The Ni recovery is still relatively low due to the formation of nickel ferrite during the sulfation roasting stage, which ends up in the leach residue. Leach residue from the optimized two-stage sulfation roasting test is mainly composed of hematite (Fe_2O_3) and nickel ferrite ($NiFe_2O_4$) analyzing 49% Fe, 10% Ni, 1% Cu, 1% S, and 5% Si. In the smelting of nickel laterite ores to ferronickel, the dried and partially reduced calcine for smelting in the electric furnace contains 1.5−3% Ni and 15% Fe [5]. By comparison, the leach residue could be a superior feedstock for the production of ferronickel, because the concentrations of the valuable metals (Ni and Fe) in the leach residue are more than three-fold, meaning the energy consumption per tonne of ferronickel produced would be reduced tremendously. In addition, the ratio of Ni/Fe is higher in the leach residue, indicating higher value of this material. Production of ferronickel from this leach residue by reduction with H_2, CO and graphite was studied and reported in the next chapter.

5.3.9 Platinum Group Metals after Sulfation Roasting

Members of the platinum Group Metals (PGM) are ruthenium (Ru), rhodium (Rh), palladium (Pd), osmium (Os), iridium (Ir), and platinum (Pt). They can be by-products of important economical value from the smelters which process sulfides to produce base metals (e.g. Ni, Cu, Zn, and Pb). Some of the major deposits of PGM are Bushveld igneous complex (South Africa), the Ni-Cu-PGM sulfide deposits in Russian Arctic and placer deposits in the Ural mountains (Russia), Sudbury (Ontario, Canada) [6]. The Raglan concentrate which is used in this study is

produced from the ores mined from the Raglan mine located in the Nunavik region of northern Quebec, Canada. It also contains PGM values as well as other precious metals such as rhenium (Re), gold (Au) and silver (Ag) which are economically beneficial to recover as by-products. As a result, it is essential to study whether these metals can be recovered into the leach solution after water-leaching of the sulfation roasted calcine or they prefer to stay in the leach residue. This is performed by analyzing several solid samples from the experiments by Inductively Coupled Plasma Mass Spectrometry (ICP-MS). Three samples were analyzed, which are the Raglan concentrate, the sulfation roasted calcine, the leach residue from the water-leaching of the sulfation roasted calcine. Each powder sample was compressed with a die to form a pellet before analysis. Figure 5.18 illustrates the results (counts per second) of a line scan on the Raglan concentrate for different elements. The X-axis of the graphs in Figure 5.18 represents the relative location on the scanned line. The large flutuation of the curves suggests the inhomogeneity of the concentrate, meaning these elements are concentrated in some of the particles in the concentrate. This indicates that the measurements should be repeated on different locations of each sample for a large number of times and averages should be taken to represent the bulk concentrations. Due to limited time available, four (4) replicates were performed on different locations of each sample with the results plotted in Figure 5.19. The scattered data for each replicate also indicates the inhomogenious nature of the sample. Averages of the repeated measurements are also shown in the diagonal band for each element and each sample. The analysis for Ru, Os and Ir failed and their results are not shown. The mass of solid increases by 30% when the concentrate is converted to sulfation roasted calcine (See Section 7.1. Mass and Heat Balance), meaning a slight decrease by 23% in the concentrations of these elements in the calcine is expected. The mass of the leach residue is only 60% of the original concentrate (See Section 7.1. Mass and Heat Balance), meaning the concentrations of the precious metals should increase by 67% if they all remain in the residue. From the results shown in Figure 5.19, it is inconclusive to determine how much of the precious metals are leached into solution due to the poor reproducibility of the measurements. However, the results could suggest a substantial portion of the precious metals remain in the leach residue. The portion of these precious metals that was leached into solution could be concentrated in the precious metal sludge during the electrowinning process, which facilitates further recovery in the refineries. The precious metals in the leach residue also necessitates further possible recovery.

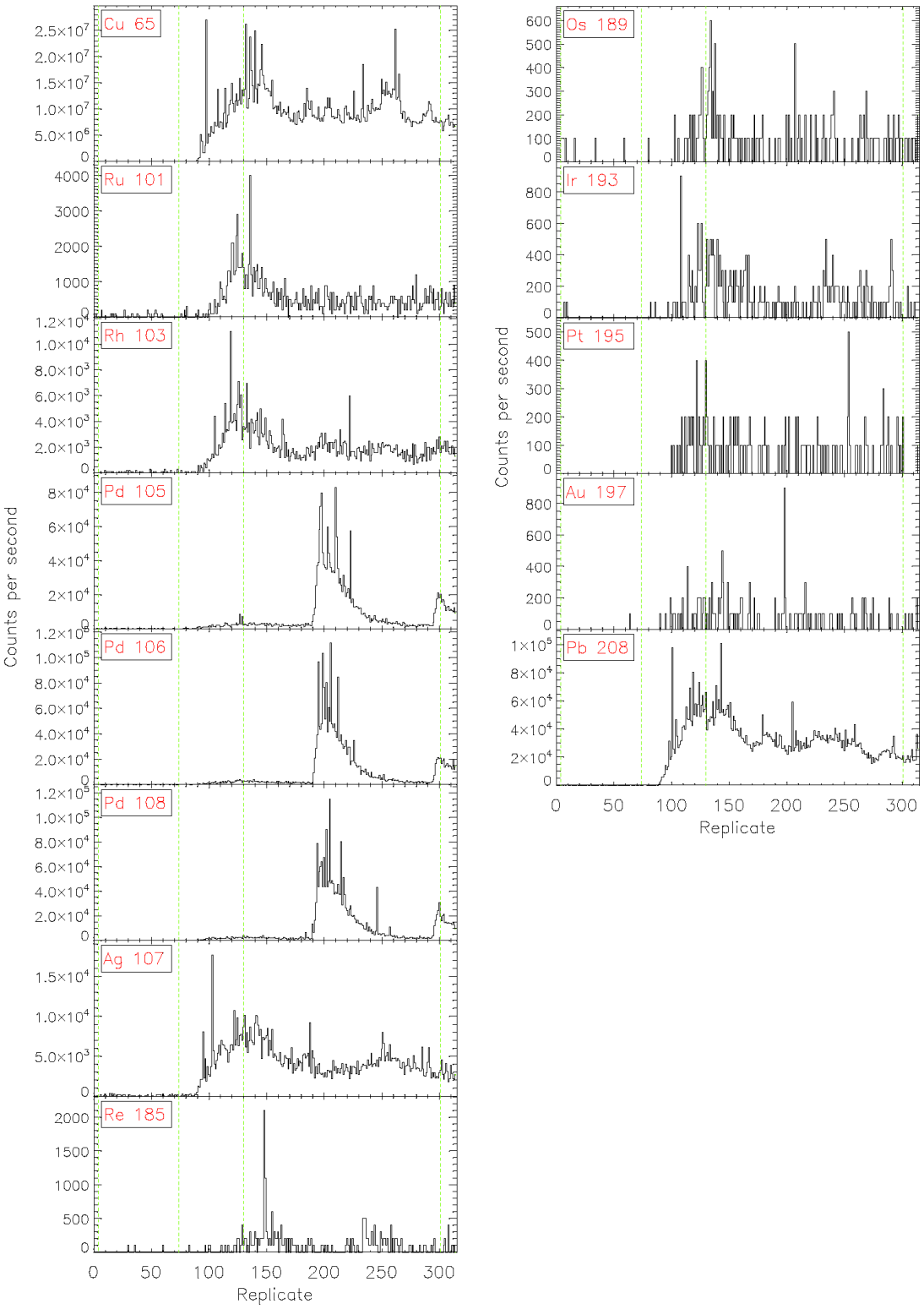

Figure 5.18. ICP-MS measurements of some of the precious metals in the Raglan concentrate by line scan.

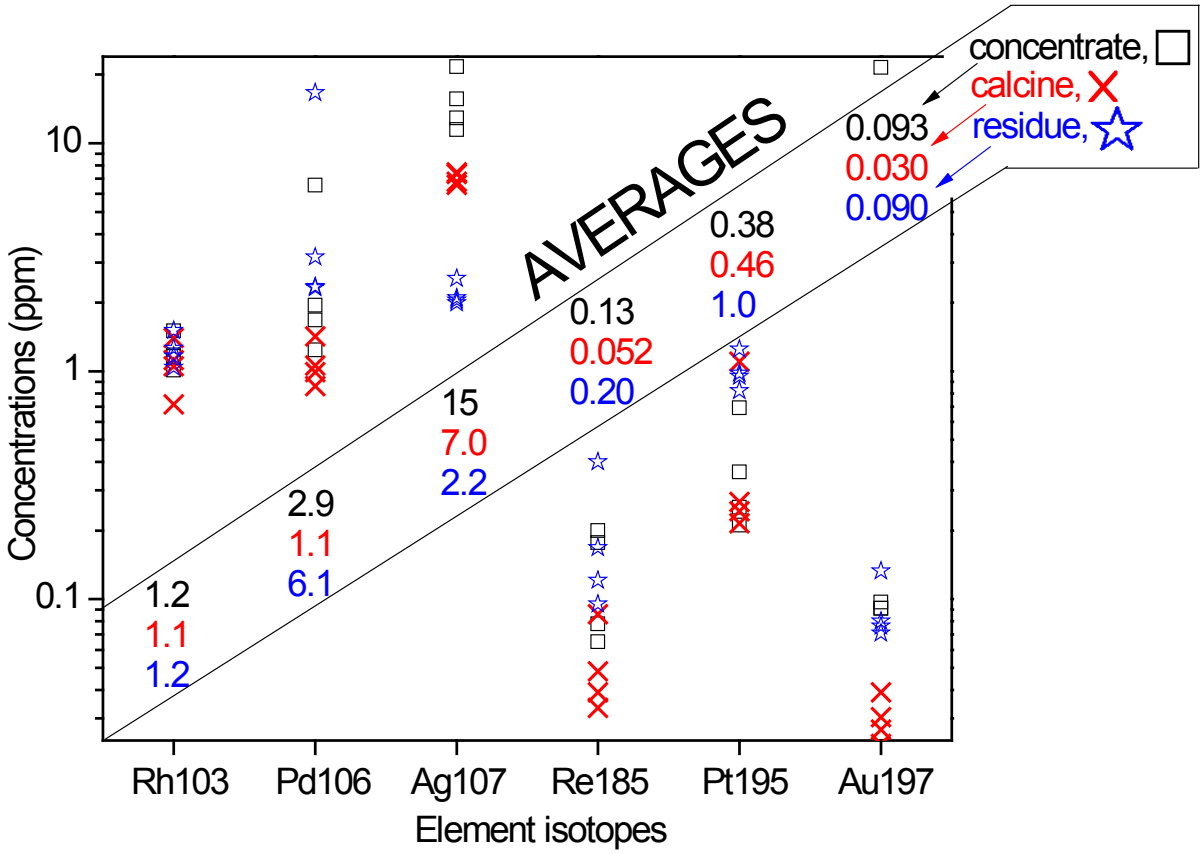

Figure 5.19. Four (4) repeated measurements of the concentrations of some precious metal isotopes by ICP-MS in three samples: Raglan concentrate (black square); sulfation roasted calcine (red cross); and leach residue of the sulfation roasted calcine (blue star). Averages of the repeated measurements are shown in the diagonal band for each element and each sample.

5.4 Conclusions

A two-stage selective oxidation-sulfation roasting process was investigated as an alternative nickel production method from nickel sulfide concentrate using a batch fluidized bed roaster. Several parameters were studied, i.e. the sulfation gas flowrate, sulfation roasting temperature, the addition of Na_2SO_4, sulfation roasting time, and the oxidation roasting temperature. The following conclusions were drawn.

(1) Under the optimized conditions of sulfation gas composition (95% air, 5% SO_2), temperature (700 °C), Na_2SO_4 addition (10 wt%) and time (150 min), the recoveries of valuable metals are 79% Ni, 91% Cu, and 91% Co. Only 5% Fe forms water-soluble sulfate.

(2)The residue from the leaching of calcine in water contains 49% Fe and 10% Ni.

(3) The Na_2SO_4 forms a melt with other sulfates on the surface of particles during sulfation roasting which is believed to have maintained a high partial pressure of SO_3 within each particle, thus facilitating sulfate formation.

(4) Conversion of sulfide cores from $Ni_{1-x}S$ to Ni_7S_6, which resulted from the outer diffusion of sulfur ions, accompanied the $NiSO_4$ formation. Shrinkage gaps formed from this conversion provided more space for further formation of $NiSO_4$.

(5) The sulfation of the nickel sulfide is direct without preliminary formation of NiO as an intermediate product.

(6) The $NiSO_4$ formation is accompanied by the creation of cracks and crevices which allowed the sulfation to proceed to near completion by providing channels for the inner diffusion of sulfation gas to the sulfide surface.

(7) A large portion of the precious metals (PGM, Re, Au, Ag) remains in the leach residue.

5.5 References

[1] P.G. Thornhill, L.M. Pidgeon, Micrographic Study of Sulfide Roasting, Journal of Metals, 9 (1957) 989-995.

[2] A.W. Fletcher, M. Shelef, The Role of Alkali Sulphates in Promoting the Sulphation Roasting of Nickel Sulphides, in: Unit Process in Hydrometallurgy. Group C: Plant Operating Practice - Economics - General, New York Gordon and Breach Science Publishers, 1963, pp. 946-970.

[3] M.C.B. Hotz, T.R. Ingraham, Fused Sodium Pyrosulphate as a Sulphation Catalyst for NiO and Co_3O_4, Canadian Metallurgical Quarterly, 5 (1966) 237-244.

[4] A.K. Misra, D.P. Whittle, Effects of SO_2 and SO_3 on the Na_2SO_4 Induced Corrosion of Nickel, Oxidation of Metals, 22 (1984) 1-33.

[5] F.K. Crundwell, M.S. Moats, V. Ramachandran, T.G. Robinson, W.G. Davenport, Smelting of Laterite Ores to Ferronickel, in: Extractive Metallurgy of Nickel, Cobalt and Platinum-Group Metals, Elsevier Ltd., Great Britain, 2011, pp. 67-83.

[6] C.R.M. Rao, G.S. Reddi, Platinum group metals (PGM); occurrence, use and recent trends in their determination, TrAC Trends in Analytical Chemistry, 19 (2000) 565-586.

6 Reduction of the Leach Residue

6.1 Introduction

An integrated pyro- and hydro-metallurgical approach to treat nickel concentrates through sulfation roasting followed by leaching is investigated [1, 2] as an alternative processing route with potential environmental benefits. In this process, the majority of the non-ferrous valuable metals are leached with water after sulfation roasting, leaving iron in the leach residue as oxides. However, approximately 20% of the nickel reports to the leach residue due to the inevitable formation of nickel ferrites ($NiFe_2O_4$) during sulfation roasting [3]. This leach residue, which is mainly composed of hematite (Fe_2O_3), nickel ferrite, and siliceous gangue, can be a high-grade source of Ni (10 wt%) and Fe (50 wt%) for the production of ferronickel. As a result, the reduction of the leach residue to produce ferronickel becomes an integral part of the sulfation roasting route and was studied.

The reduction of hematite (Fe_2O_3) with H_2 has been widely studied due to its role in production of directly reduced iron. The temperature dependence of the reduction reactions has been investigated extensively, indicating that depending on temperature, the reduction could adopt a two-step mechanism, which is $Fe_2O_3 \rightarrow Fe_3O_4 \rightarrow Fe$ [4-9], or a three-step mechanism, which is $Fe_2O_3 \rightarrow Fe_3O_4 \rightarrow FeO \rightarrow Fe$ [7, 8]. Direct formation of Fe from the reduction of hematite could also take place below 450 ºC [8]. The multi-step reduction mechanism is also affected by the X_{H2O}/X_{H2} ratio of the gas phase [10]. The effect of the partial pressure of H_2 on the reduction rate of iron oxides has been studied by previous researchers. It has been reported that for the reduction of hematite to magnetite, the order of reaction with respect to H_2 pressure was 0.036. The reaction orders were 0.09 and 1.89 for the reduction of magnetite to wustite and wustite to iron, respectively [11]. The reduction reaction is more likely controlled by interfacial chemical reactions at low temperatures. An example of this is the reduction from hematite to magnetite under fluidized bed conditions, which was limited by the gas-solid reaction in the temperature range of 400–500 ºC [12]. Reduction at high temperatures tends to be governed by diffusion especially when a substantial amount of reduction product is present. Reduction behavior is greatly affected by the particle size, crystallinity and the conditions of reduction [7, 13]. Apparent activation energies for the reduction of hematite have been reported in literature,

showing that they depend not only on the purity and physical state of the raw material, but also on the experimental conditions employed [8]. Generally the reduction rate of iron oxide with H_2 is higher than that obtained by CO [8, 14].

Bahgat et al. [15] studied the H_2 reduction of synthesized $NiFe_2O_4$ in the temperature range between 800 ºC and 1100 ºC for the generation of nanocrystalline Fe-Ni alloy and found that the reaction was governed by the combined gaseous diffusion and interfacial chemical reaction mechanisms. The apparent activation energies were reported to be 31.85 and 24.57 kJ/mol for the initial and latter reduction stages, respectively. $NiFe_2O_4$ compacts were sintered at 1000–1200 ºC and were reduced at 900–1100 ºC by pure hydrogen by Khedr [16]. It was found that a dense metallic layer (Fe_xNi_y) was formed surrounding the wustite layer which prevents gas diffusion, resulting in incomplete reduction. A conclusion was also made that its reduction rate was greatly influenced by both the firing and reduction temperature. Multi-step reduction of synthetic $NiFe_2O_4$ was also observed to have a dependence on the reduction temperature [17]. In the temperature range of 500–700 ºC, the rate controlling step was found to be the chemical reaction at the metal-oxide interface.

Figure 6.1 displays the stability diagram of iron oxides in CO/CO_2 atmosphere, as well as the CO partial pressure in the $CO\text{-}CO_2\text{-}C$ equilibrium, which can be represented by the Boudouard reaction (Eq. (6.1)) [18]. This figure illustrates that depending on the reduction temperature, the reduction of Fe_2O_3 to metallic Fe could adopt a two-step (<550 ºC) or three-step mechanism (>550 ºC) with the increase of the partial pressure of CO, admitting that in an actual Fe_2O_3 reduction process, the reduction mechanism could be largely different from the thermodynamic prediction and be more complicated due to the contributing factors mentioned above. It has generally been accepted that the indirect reduction of iron oxides with CO dominates the reduction in a blast furnace as well as in the direct reduction processes producing sponge iron, with solid-solid direct reduction playing only a minor role [19]. A conclusion has been made that for those reduction processes with carbon or carbon monoxide as the reductant, the reversible Boudouard reaction could exert a strong controlling influence on the reaction kinetics and mechanism [20-22]. However, there are studies [23-25] in which NiO was reduced by pyrolytic and natural graphite showing that the direct reduction played a major role, and the reaction occurred mostly at the edge surface rather than at the cleavage surface of the graphite

due to the much higher number of active carbon sites on the former where reduction took place preferably. This suggests that the nature of the carbon source (graphite, charcoal, coke, etc.) could also have a significant impact on the kinetics and mechanism of reduction.

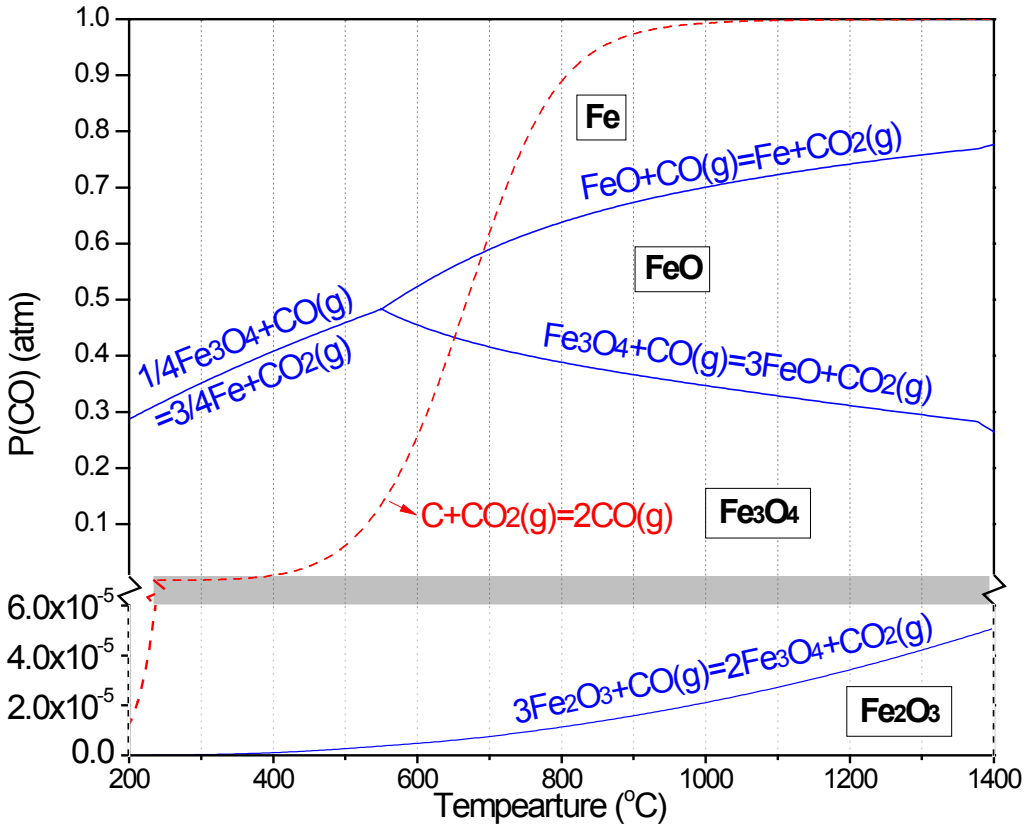

Figure 6.1. Stability diagram for Fe-O system under CO-CO_2 atmospheres (solid lines) and CO partial pressure established by the Boudouard reaction (dashed line) (Calculated using thermodynamic data from HSC Chemistry [26]).

$$C(s) + CO_2(g) = 2CO(g) \quad (6.1)$$

6.2 Experimental

6.2.1 Materials

The leach residue is primarily composed of hematite (Fe_2O_3 with varying concentrations of Ni as impurities), nickel ferrite ($NiFe_2O_4$) and siliceous gangue. Table 6.1 shows the chemical and

mineralogical compositions of the material. Figure 6.2 displays the backscattered electron (BSE) image of the leach residue [3]. It is comprised of three types of particles: (1) hematite particles (e.g. particle a in Figure 6.2) originated from the oxidation of the pyrrhotite with its characteristic columnar structure [27, 28]; (2) ring-shaped particles which are composed of hematite and nickel ferrite, originated from the oxidation of pentlandite (e.g. particle b in Figure 6.2; Ni_3S_2 resides within some of the ring-shaped particles shown as bright areas); and (3) silicate particles containing Fe, Mg, Al (e.g. particle c in Figure 6.2). Sulfur in the residue exists in the form of nickel sulfide which is shown as the bright area within some of the ring-shaped particles.

Table 6.1. Chemical and mineralogical compositions of the leach residue.

Chemical composition (wt%)	Fe	Ni	S	Cu	Co	Mg	Al	Si	O
	49.3	10.5	1.1	1.0	0.06	1.1	0.9	5.1	30.94
Mineralogical composition (wt%)	Fe_2O_3	$NiFe_2O_4$	NiS	CuO	CoO	MgO	Al_2O_3	SiO_2	
	47.4	33.7	3.1	1.2	0.08	0.8	1.8	10.8	

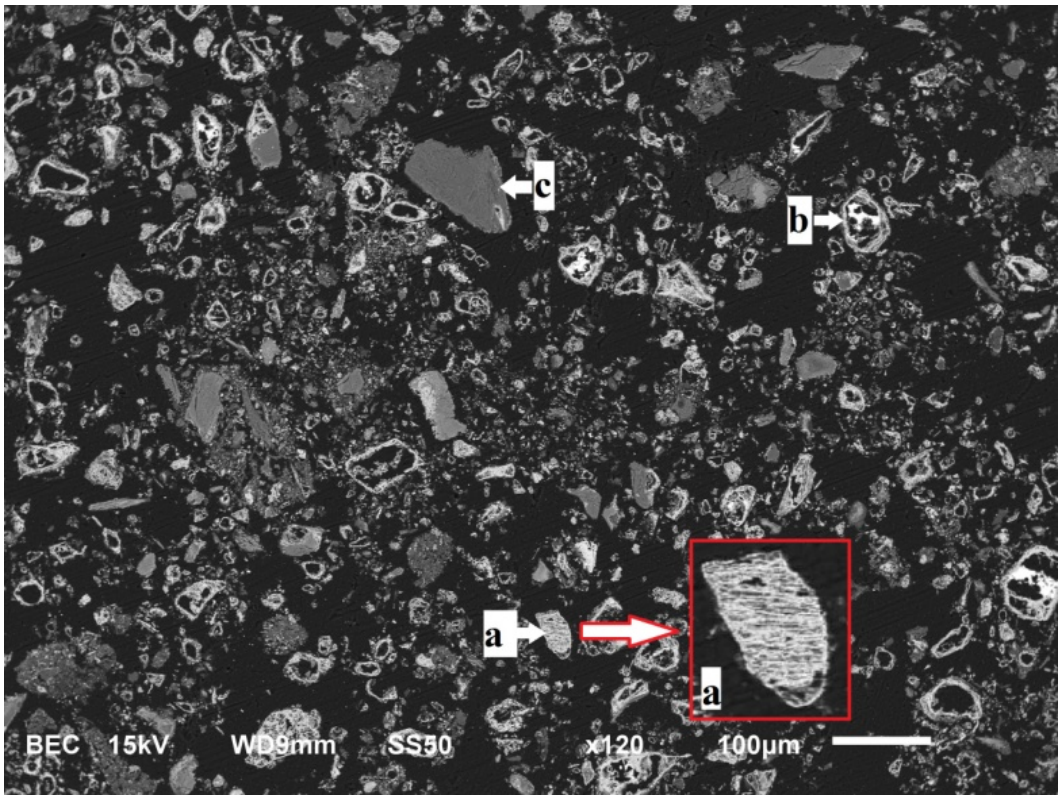

Figure 6.2. BSE image of the leach residue [3].

6.2.2 TG/DTA Study

6.2.2.1 Reduction with H_2

Thermogravimetric analysis (TGA) and differential thermal analysis (DTA) were performed with a Setaram TG–DTA 92 unit (SETARAM Inc., Newark, CA). For the reduction of the leach residue, 15% H_2 and 40% H_2 gases (balance N_2) were used at a flowrate of 1 L/min unless specified otherwise. Two series of tests were performed: 1) continuous heating at 15 ºC/min from room temperature up to 1400 ºC; 2) isothermal reduction tests with temperatures ranging from 350 ºC to 1500 ºC. Sample size of typically 50 mg was used for each run. One objective of the current study was to investigate the feasibility of producing ferronickel alloy for the steel industry using this leach residue, thus it was of interest to eliminate sulfur as much as possible during the pyro-reduction process. As a result, the sulfur elimination was evaluated by continuously analyzing the offgas for its SO_2 content using a gas analyzer (ABB EL3020). Argon was purged during the cool down period for each run. For the DTA runs, a sample size of 15 mg was used. Calcined alumina powder of 15 mg was used as the reference material.

6.2.2.2 Reduction with CO

For the reduction with CO, continuous heating tests at 15 ºC/min from room temperature to 1400 ºC were performed in both TGA and DTA modes in 1 L/min pure CO gas (CO_2<100 ppm, O_2<100 ppm). Leach residue of typically 50 mg was loaded into an alumina crucible (I.D. 7.2 mm) for TGA runs, whereas the sample size was 15 mg for DTA runs using alumina crucibles (I.D. 4.1 mm). Calcined Al_2O_3 powder of 15 mg was used as reference for the DTA runs. The gaseous reduction product CO_2 was continuously swept away by the flow of CO, and the offgas was continuously analyzed for its CO_2 concentration using a gas analyzer. Isothermal reduction tests in the temperature range from 400 ºC to 1300 ºC were also carried out using CO. For each isothermal test, the sample was heated at 15 ºC/min to the target temperature in 1 L/min argon, followed by reduction using 1 L/min CO gas.

6.2.2.3 Reduction with Graphite

Two series of reduction tests were also performed using graphite as the reductant. The graphite powder was produced by grinding a purified (ash content <50 ppm) graphite rod and the fraction below 25 μm was used. The powder and the leach residue were blended with the weight ratio of 2:5 to provide excess carbon for complete reduction. 70 mg of the mixture (50 mg residue + 20 mg graphite) was used for each TGA run, whereas the sample size for the DTA run was 21 mg (15 mg residue + 6 mg graphite). Continuous heating of the mixture was conducted in both TGA and DTA modes at 15 ºC/min to 1500 ºC in 1 L/min argon flow. The offgas was continuously analyzed for its CO and CO_2 content. The isothermal reduction tests were performed for a temperature range of 800–1400 ºC in the following manner: The sample mixture was loaded in an alumina crucible, and was first suspended from the micro balance well above the hot zone of the TGA chamber. The chamber was then heated to the target temperature at the rate of 15 ºC/min while being purged with argon (1 L/min), to prevent air ingress. After the target temperature was reached, the sample was quickly lowered into the chamber with continued purge of 1 L/min argon. Because of the small sample size used, the sample was instantly heated to the target temperature by radiation received from the chamber and the reduction was initiated. Trial experimental results showed that due to the quick evolution of gaseous product (CO and CO_2) during the reduction process, samples could be blown out of the crucible by the gas and cause an unexpected large mass loss. A thin layer of alumina wool was then used to cover the sample in the crucible to prevent this.

Another issue identified in the trial experiments was that some ambient air was inevitably introduced along with the sample into the chamber. The oxygen in the introduced air could oxidize the graphite powder in the TGA crucible during reduction process and lead to unexpected mass loss. Therefore, the oxygen has to be removed before it oxidizes the graphite powder. This was performed by modifying the TGA setup by mounting two graphite tubes on the ceramic tube and above the TGA crucible, which is shown in Figure 6.3. Due to the larger surface area of the graphite tubes compared with that of the graphite powder in the crucible, the oxygen in the chamber could be mostly removed by reacting with the tubes forming CO or CO_2, which would then be quickly removed from the chamber with the purge of argon. Isothermal experiments at 800 ºC were performed to evaluate the effectiveness of the addition of the graphite tubes in terms of the removal of oxygen from the chamber, the results of which are

shown in Figure 6.4. In this figure, test #1 shows the evolution of CO and CO_2 in the isothermal tests with empty crucible. The CO and CO_2 peaks are from the removal of O_2 by the graphite tubes. Test #2 is the isothermal test with 20 mg graphite powder in the crucible. When compared with test #1, the amount of CO_2 evolved in test #2 is roughly the same, and there is a slight increase in the evolution of CO. This indicates that the O_2 mostly reacted with the graphite tubes rather than the graphite powder, which illustrates the effectiveness of the graphite tubes in terms of O_2 removal. Test #3 is an isothermal test with a mixture of 20 mg graphite powder and 50mg residue in the crucible. Much larger peaks of CO and CO_2 appeared from the reduction of the residue with graphite powder. The relatively small CO and CO_2 peaks from the removal of O_2 by the graphite tubes indicate that they would have negligible effect on the actual reduction reactions.

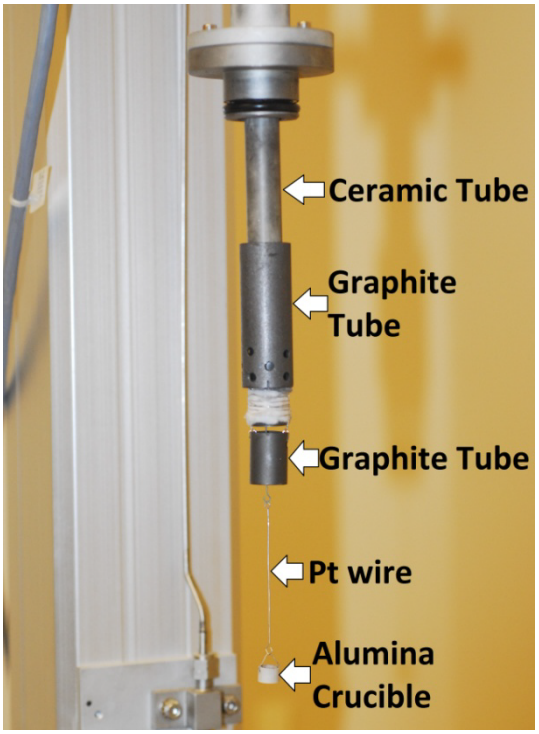

Figure 6.3. Modification of the TGA setup by mounting graphite tubes on the ceramic tube.

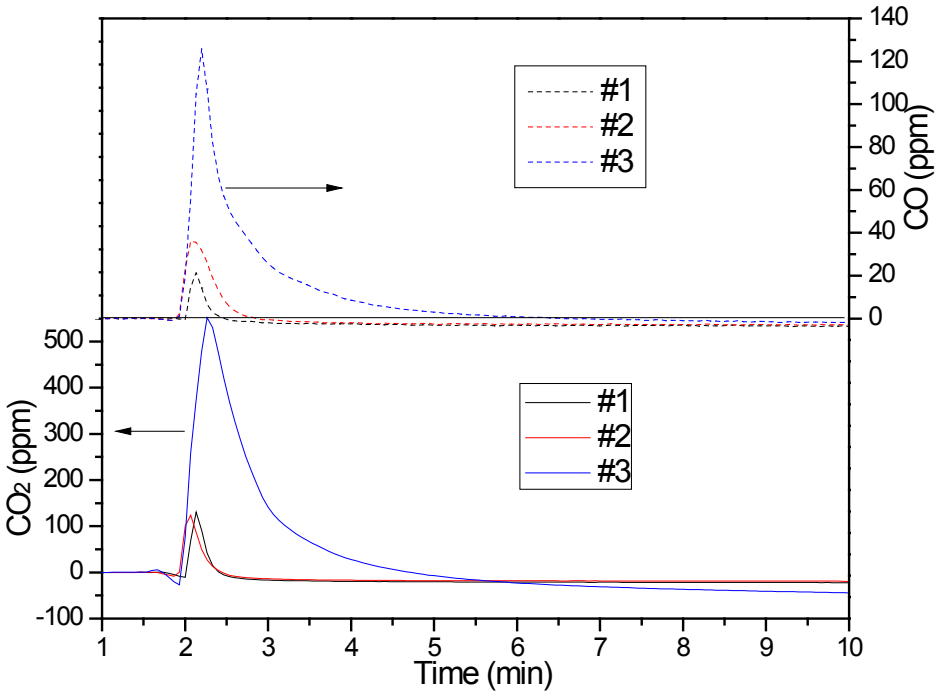

Figure 6.4. CO and CO_2 evolution during the isothermal tests at 800 ºC with empty crucible (#1), 20 mg graphite powder in the crucible (#2), and a mixture of 20 mg graphite powder and 50 mg residue in the crucible (#3), after the modification of the TGA setup.

6.2.3 Analytical Methods

Reduced products from the experiments were mounted into epoxy, ground and polished for the observation of their microstructures and for phase identifications using SEM-EDS. Elemental analysis of the phases in the reduced samples was conducted using EPMA. Samples were also analyzed by XRD using Cu-K_α radiation for their qualitative mineralogical composition.

6.3 Results and Discussion

6.3.1 Reduction with H_2

6.3.1.1 Continuous Heating

A sample was heated from room temperature up to 1400 ºC at 15 ºC/min with a controlled gas flow of 1 L/min 15% H_2 in both TGA and DTA tests. Mass change (wt%), rate of mass change (wt%/min), offgas SO_2 concentration (ppm) and heat flow (μV) are plotted as a function of temperature in Figure 6.5. Due to the geometrical difference of the crucibles used for TGA and DTA runs as well as the porous nature of the sample which tends to delay heat transfer, the temperature at which a specific thermal event occurs in DTA mode does not exactly correspond with that in the TGA mode. No remarkable mass change was observed until the temperature reached 415 ºC, where a SO_2 peak appeared and quick mass loss was initiated. This SO_2 peak and the corresponding mass loss correlated with a small endotherm peaking at 430 ºC. This endotherm represents the reduction of the remaining $NiSO_4$ in the residue as shown in Eq. (6.2). The rate of mass loss is even higher when the temperature exceeded 550 ºC until 790 ºC, where most of the reduction reactions take place. They could be represented by Eqs. (6.3) and (6.4). These reduction reactions revealed themselves in the DTA curve as a wide endotherm peaking at 630 ºC. A wide SO_2 peak appeared after this mass loss, peaking at 955 ºC. This evolution of SO_2 is possibly caused by the melting of the Ni_3S_2 present in the residue, because Ni_3S_2 was observed to have a melting temperature of 813 ºC [27]. The silicate material in the residue gradually melted above 1200 ºC, leading to an endotherm at 1370 ºC as well as another SO_2 peak. There is only a slight mass decrease after 800 ºC since most of the oxides have already been reduced.

$$NiSO_4 + 2H_2(g) = Ni + SO_2(g) + 2H_2O(g) \quad (6.2)$$

$$Fe_2O_3 + 3H_2(g) = 2Fe + 3H_2O(g) \quad (6.3)$$

$$NiFe_2O_4 + 4H_2(g) = Ni + 2Fe + 4H_2O(g) \quad (6.4)$$

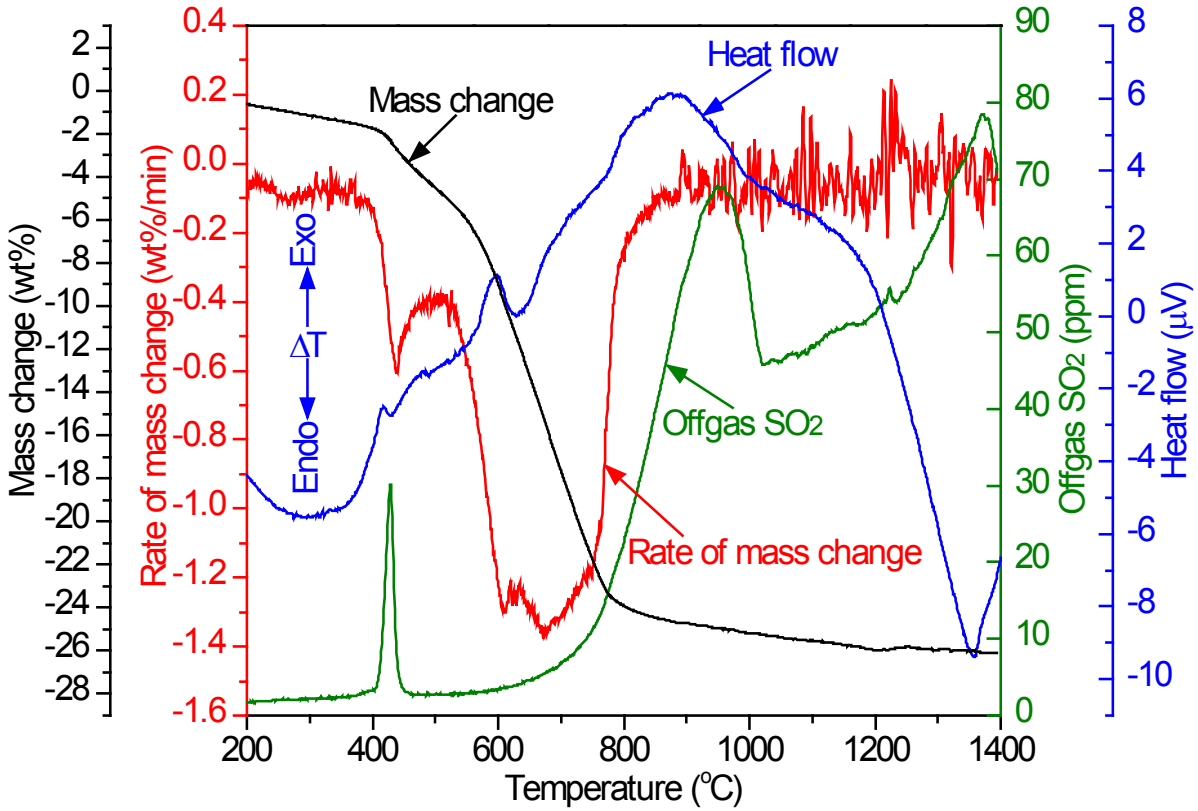

Figure 6.5. TGA/DTA results of the continuous heating tests at 15 ºC/min for the reduction with 15% H_2.

6.3.1.2 Isothermal Reduction

As an effort to further investigate the kinetics of H_2 reduction of the leach residue, a series of isothermal reduction tests were performed with temperatures ranging from 350 ºC to 1500 ºC. The TGA results are plotted in Figure 6.6 and Figure 6.7. For quantitative analysis of the kinetic data, Eq. (6.5) [29] is introduced to describe the rate of reaction, where α is the extent of reduction; t is time; k is the rate constant which is a function of temperature (T); f(α) is a function of differential form which has its particular expression for different reaction models; h(P) is function of pressure of the gas that is involved in the reaction. For the present study, P is the partial pressure of H_2. The temperature dependence of the reaction rate could be described by the Arrhenius equation which is expressed as Eq. (6.6), in which A is the pre-exponential factor; E_a is the activation energy; R is the universal gas constant; and T is temperature. The

dependence of rate on gas pressure can be expressed in the form of the power law, which is shown as Eq. (6.7) [29]. Substituting Eqs. (6.6) and (6.7) in Eq. (6.5) yields Eq. (6.8).

$$\frac{d\alpha}{dt} = k(T) * f(\alpha) * h(P) \tag{6.5}$$

$$k(T) = A * \exp(\frac{-E_a}{RT}) \tag{6.6}$$

$$h(P) = P^n \tag{6.7}$$

$$\frac{d\alpha}{dt} = A * \exp(\frac{-E_a}{RT}) * f(\alpha) * P^n \tag{6.8}$$

For the complete reduction of the oxides in the leach residue, the corresponding mass loss should be 25.5 wt%. As can be seen from Figure 6.6 and Figure 6.7, the overall reduction rate keeps increasing all the way from 350 ºC up to 1100 ºC, indicated by the larger slope of the mass loss curve at higher temperatures. For the isothermal tests at 350 ºC, 400 ºC, 450 ºC and 500 ºC in Figure 6.6, a linear region appears right after the initial quick mass loss, indicating that the reduction rate is constant and independent of the extent of reaction. This suggests that the reduction rate is controlled by the zero-order chemical reaction. The differential form for the zero-order reaction model is f(α)=1 [30]. From these isothermal reduction data, the apparent activation energy was calculated to be 64.7 kJ/mol. Figure 6.8 illustrates the morphology of the residue after 22% reduction at 400 ºC. It was observed that there was no apparent morphological change compared to the leach residue before reduction. Little morphological change suggests a non-topochemical reaction mode for the reduction at low temperatures.

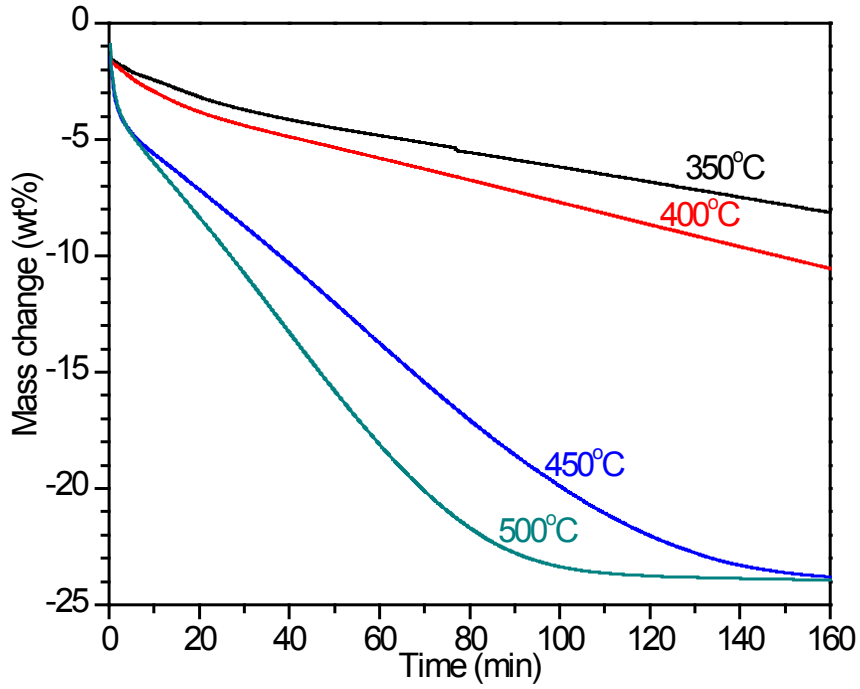

Figure 6.6. Isothermal H_2 (15%) reduction of the leach residue at 350 ºC, 400 ºC, 450 ºC and 500 ºC.

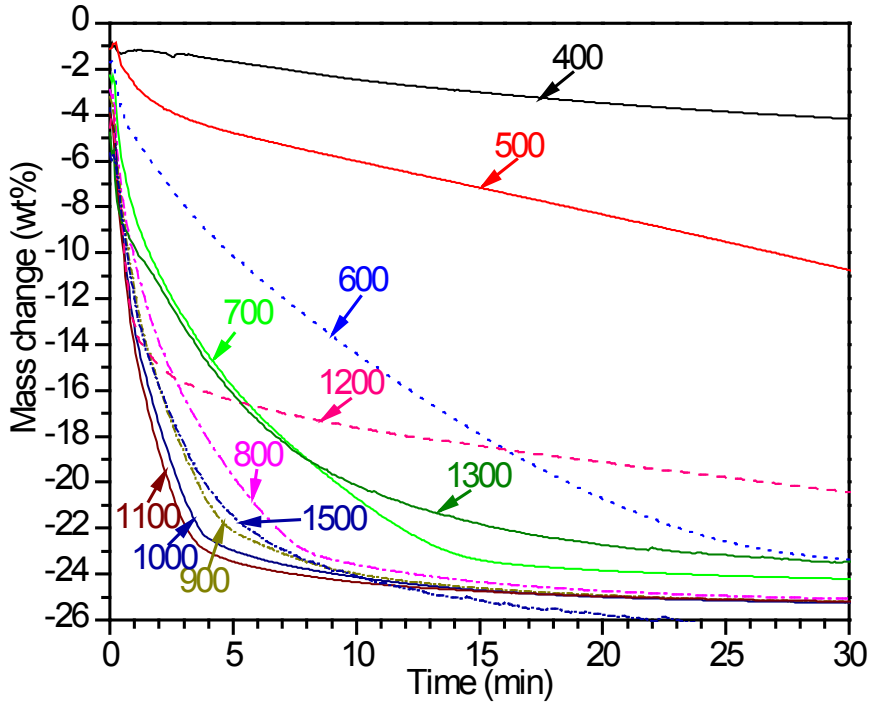

Figure 6.7. Mass change (wt%) during the isothermal reduction of the leach residue by 15% H_2 at various temperatures.

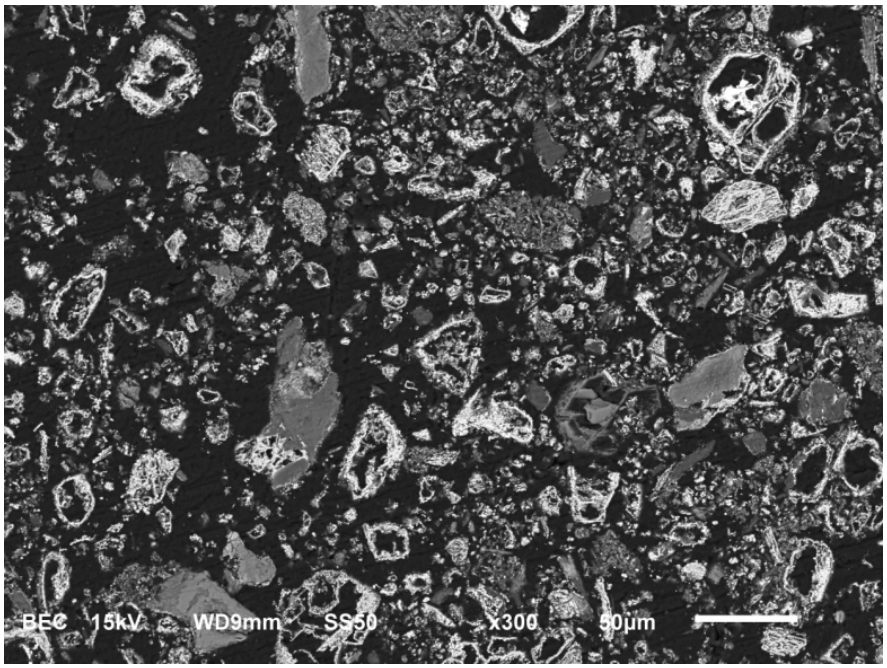

Figure 6.8. BSE image of the residue partly reduced (22%) at 400 ºC with 15% H_2.

No linear region could be observed for the plots above 600 ºC in Figure 6.7, indicating that the reaction rate changed with the progress of reduction. The overall reaction rate increased with the increase of temperature until a transition temperature of 1200 ºC is reached. For the isothermal test at 1200 ºC, the initial reduction rate is comparable to that at 1100 ºC. However, the reaction slowed down dramatically after reduction for 90 seconds, compared with the reduction at lower temperatures. For the isothermal tests at 1300 ºC and 1500 ºC, the initial quick mass loss can also be observed, and the reduction after the initial period is faster compared to the one at 1200 ºC. The effect of the temperature on the reduction rate could be more easily observed by plotting the time required for 90% reduction of the leach residue as a function of temperature, which is illustrated in Figure 6.9. As can be seen, the time needed for 90% reduction continued to decrease with the increase of temperature before the temperature reached 1200 ºC. 1200 ºC is the transitional temperature at which the time needed for 90% reduction reached a maximum.

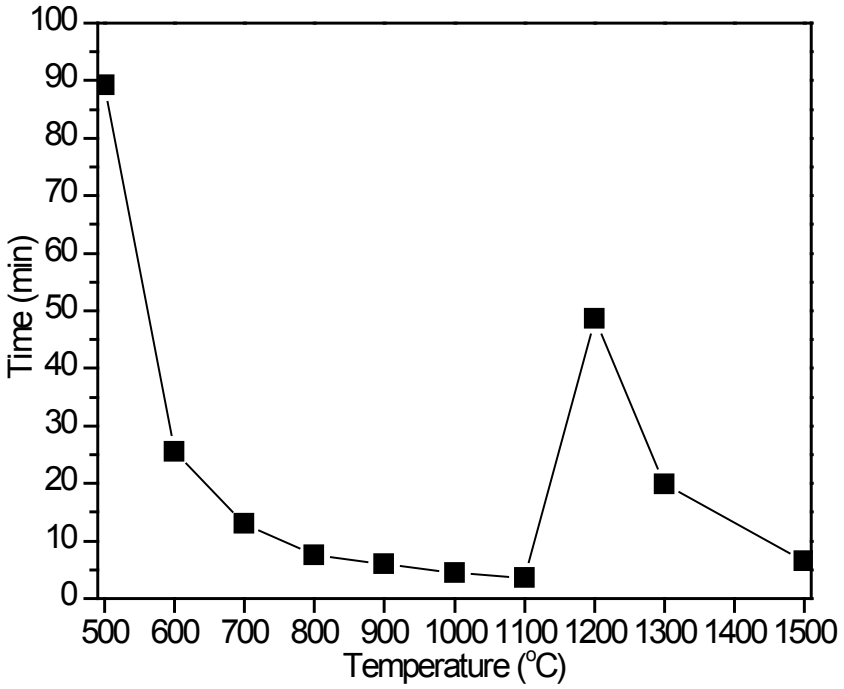

Figure 6.9. Time required to reach 90% reduction of the leach residue with 15% H_2 as a function of temperature.

In order to determine the rate controlling step for the isothermal tests in the temperature range between 600 ºC and 1100 ºC, a model fitting method was adopted. According to Eq. (6.5), the rate of reaction $d\alpha/dt$ should have a linear relationship with $f(\alpha)$, since k_T and h_P are constant for a particular isothermal reduction test with fixed H_2 concentration. This linear relationship is only observed when applying the 2D diffusion model, which is expressed as Eq. (6.9) [30] and plotted in Figure 6.10. The trend of the reaction rate for the initial quick reduction within 90 seconds at 1200 ºC also shows a linear relationship in Figure 6.10. The slopes of these plots give $k_T \cdot h_P$ according to Eq. (6.5). Eq. (6.10) was derived from Eqs. (6.5)–(6.8). According to this equation, a linear trend would be observed by plotting $\ln(k_T \cdot h_p)$ vs. the reciprocal of temperature, which is shown in Figure 6.11. As can be seen from Figure 6.11, the Arrhenius plot for 600 ºC deviated from the linear trend. This is possibly because the reduction at 600 ºC was in the transition stage, i.e. reduction rate could be controlled by a combination of chemical reaction and diffusion. Apparent activation energy could be calculated from the slope of this linear trend, which is 34.1 kJ/mol. This value is much smaller compared with the apparent activation energy for the zero–order chemical reactions below 600 ºC, i.e. 64.7 kJ/mol. The

values are however in good agreement with the activation energies measured by Shimakage et al. [17]. They studied the hydrogen reduction of synthetic nickelferrite pellets and reported activation energies of 66.1 kJ/mol below 600 ºC and 38.1 kJ/mol above 600 ºC.

$$f(\alpha) = [-\ln(1-\alpha)]^{-1} \tag{6.9}$$

$$\ln(k_T * h_P) = \ln(A * h_P) - \frac{E_a}{RT} \tag{6.10}$$

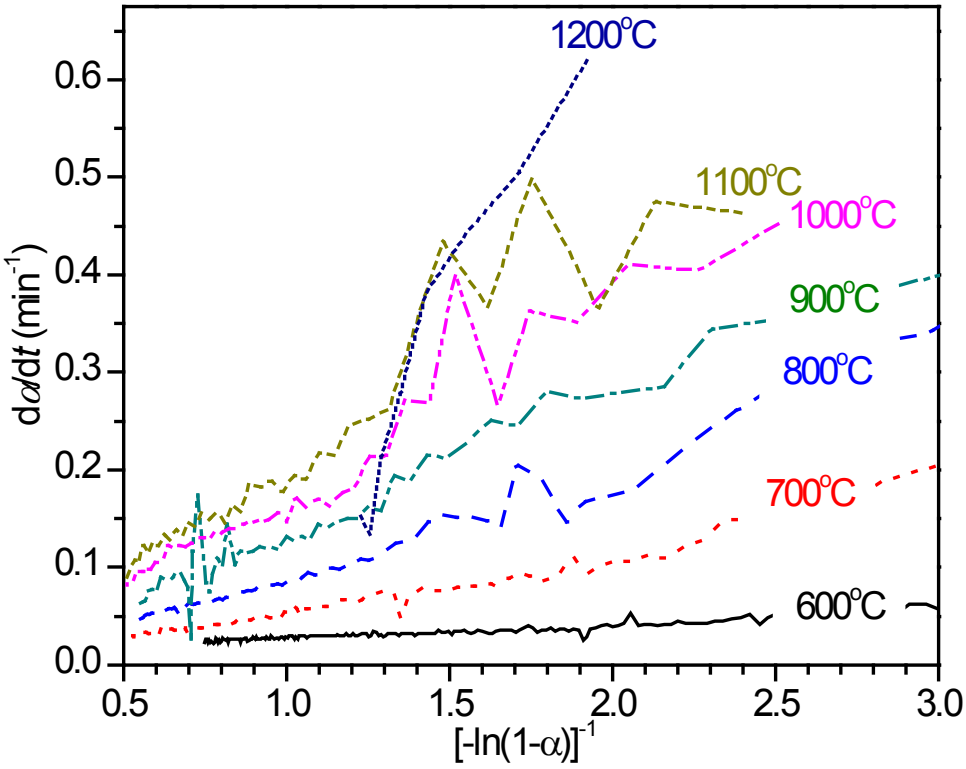

Figure 6.10. Linear relations between the rate of reaction and the differential form of the 2D diffusion model which is $f(\alpha)=[-\ln(1-\alpha)]^{-1}$ for the isothermal tests from 600 ºC to 1200 ºC.

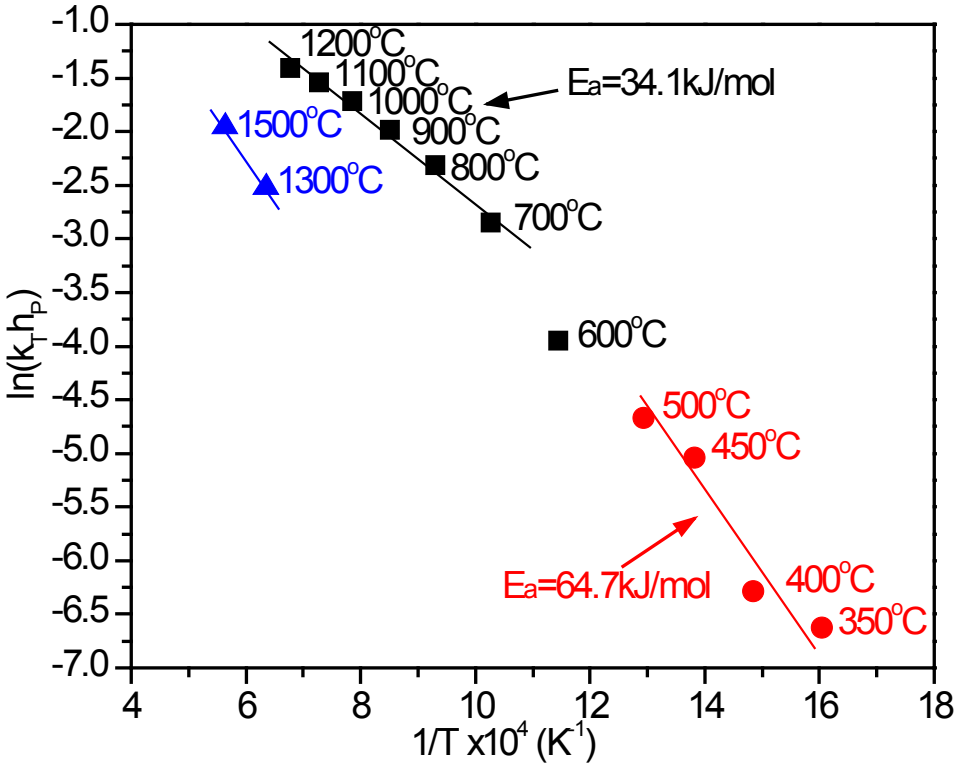

Figure 6.11. Arrhenius plot for the isothermal reduction tests from 350 ºC to 1500 ºC (Data for 1200 ºC was calculated based on the initial reduction period).

Figure 6.12 exhibits the surface morphology of the fully reduced residue produced from the isothermal tests at 900 ºC. It shows that the sample is still rather porous after reduction. Figure 6.13 shows the XRD pattern of the fully reduced residue, indicating the formation of mainly two alloy phases, which are Fe_3Ni_2 and $Fe_{10.8}Ni$. As mentioned earlier, the rate of reduction fits the 2D diffusion model, thus the gas diffusion through the solid product layer in each individual particle has to be the rate controlling step for the isothermal tests between 600 ºC and 1100 ºC as well as the quick initial reduction period of the isothermal test at 1200 ºC. Two other series of isothermal tests at 800 ºC were performed with the evaluation of the effects of the gas flowrate and sample size. Figure 6.14 illustrates the effect of the change of the gas flowrate on the reduction of the residue. It appears that there is little effect on the mass loss of sample by lowering the reducing gas flowrate from 1000 mL/min to 100 mL/min, meaning that the supply of H_2 to the sample with the flowrate of 1000 mL/min is large enough. The effect of sample size on the rate of reduction at 800 ºC is illustrated in Figure 6.15. It is evident that the rate of

reduction (%) is slower for the larger sample. This indicates that the reduction reactions did not take place uniformly in the whole sample in the TGA crucible, but a reaction front progressed from the top to the bottom, which is the consequence of the reaction rate partially governed by H_2 gas diffusion through the sample bed. From the discussion above, the isothermal reduction is most likely controlled by the combination of the gas diffusion through the pores of the sample bed and gas diffusion through the solid product layer of individual particles (mixed control).

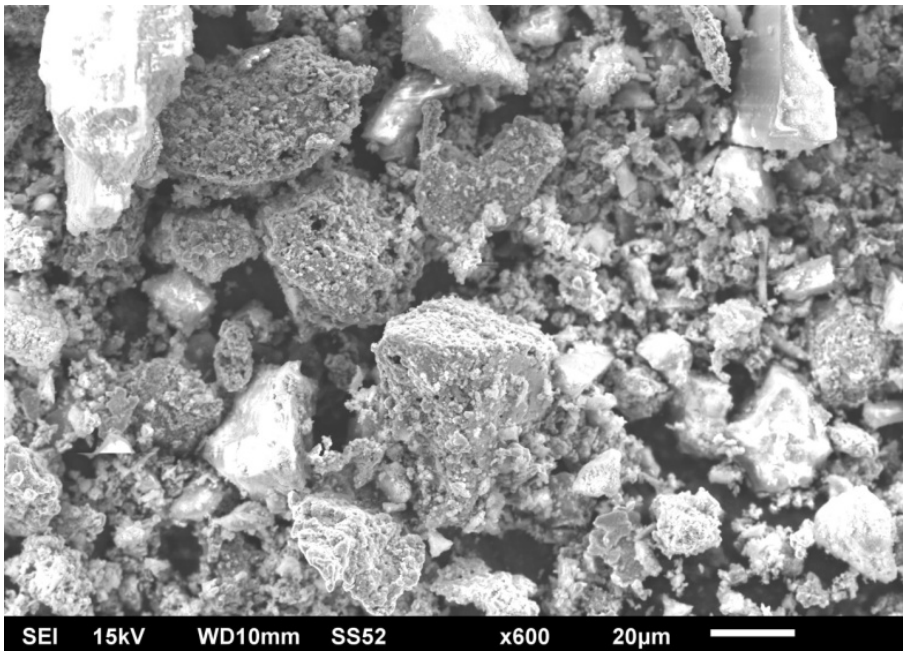

Figure 6.12. Morphology of the fully reduced residue (900 ºC with 15% H_2).

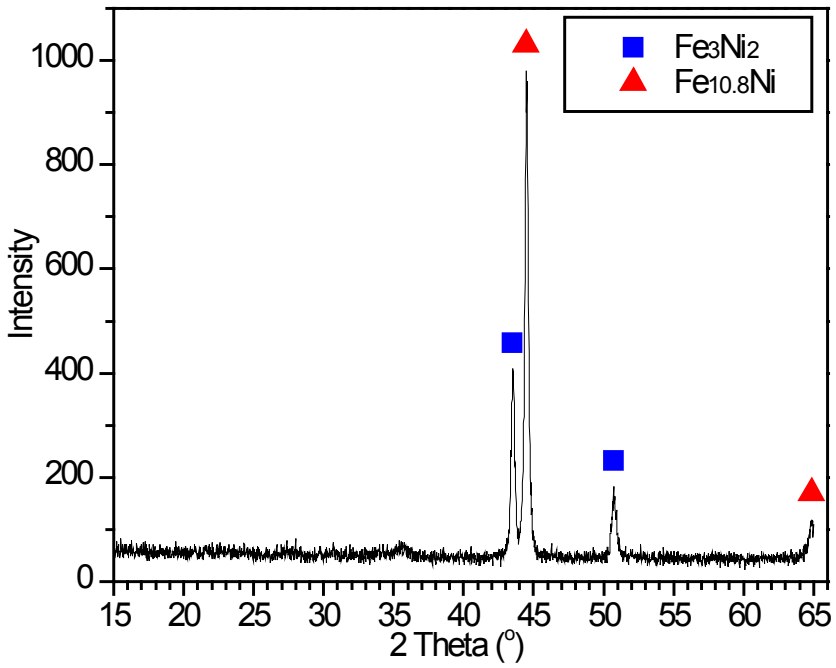

Figure 6.13. XRD pattern for the fully reduced residue (900 ºC with 15% H_2).

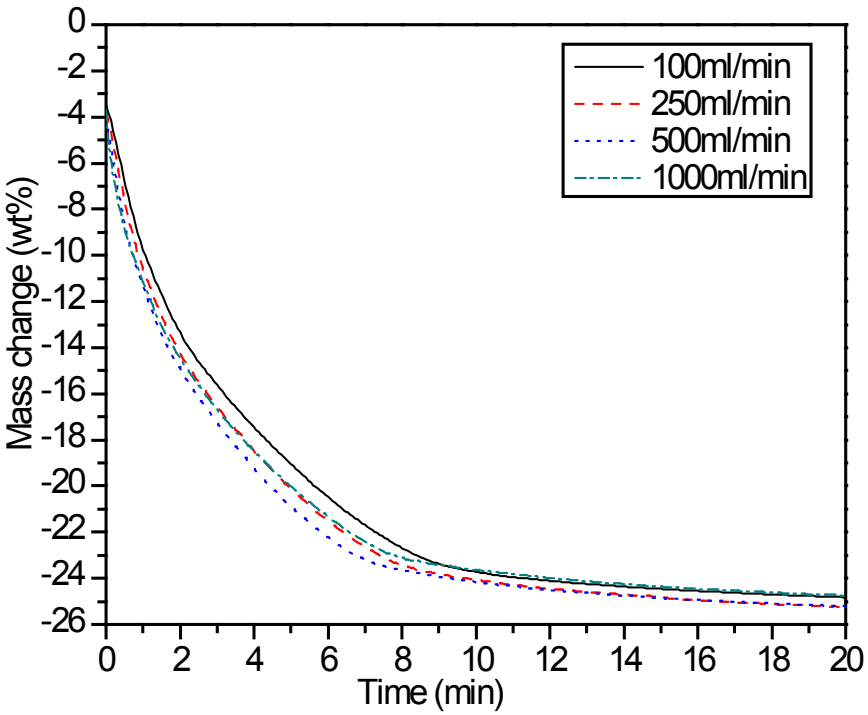

Figure 6.14. Effect of gas flowrate on the isothermal reduction of the leach residue at 800 ºC (15% H_2).

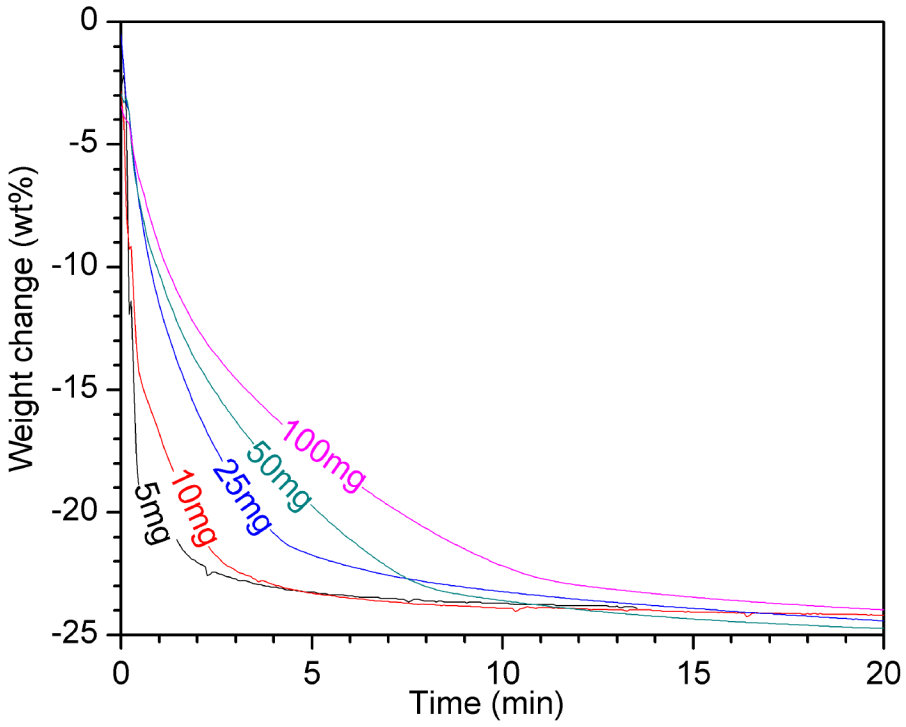

Figure 6.15. Effect of sample mass on the isothermal reduction of the leach residue at 800 ºC.

At 1100 ºC, the ferronickel alloy that was produced would partly melt and sinter, illustrated by the cross section of the alloy particles in Figure 6.16. But it was still rather porous, which provided channels for the gas diffusion through the sample bed in the TGA crucible. However, when the temperature reached 1200 ºC, the silicate material melted and sintered with the alloy that was formed, which is shown in Figure 6.17. The sample became non-porous, thus the reducing gas had to diffuse through the molten sample bed in order for the reduction reactions to proceed. This physical transition explains the two different stages occurring during the isothermal reduction at 1200 ºC. When the temperature was raised to 1200 ºC, the silicate materials in the sample melted immediately. However, the sample was still rather porous at the initial stage of reduction because of the presence of a large amount of solid oxides. As a result, during the initial reduction stage, the rate controlling step was the gas diffusion into the sample bed through the pores, leading to a quick initial mass loss. As the reduction proceeded, the alloy and silicates began to melt, leading to substantial shrinkage. The porosity of the sample bed would eventually reduce to a critical point where gas diffusion became very limited. This would in turn result in a much slower reduction rate. As a result, the reduction rate decreased substantially after 90 seconds reduction at 1200 ºC. At the latter stage, the rate controlling step

would be the gas diffusion through the molten sample. This transition of the rate controlling mechanisms was also observed in the isothermal tests at 1300 ºC. A 2D diffusion model was applied to the isothermal tests at 1300 ºC and 1500 ºC. Arrhenius plots for these two temperatures were also calculated and shown in Figure 6.11 for comparison with those for other temperatures. Due to the insufficient data for this high temperature range, calculation of the apparent activation energy was not possible.

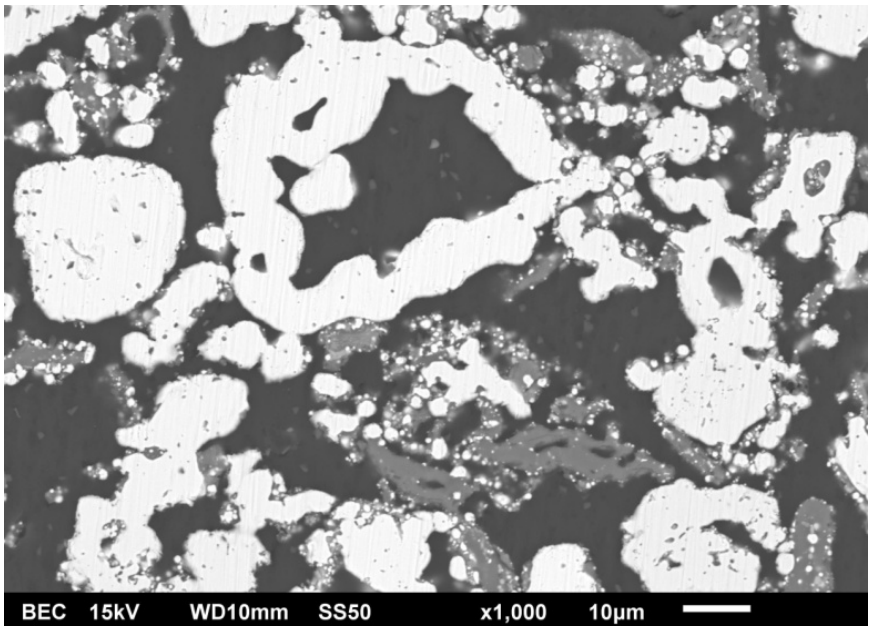

Figure 6.16. Morphology of the residue fully reduced at 1100 ºC with 15% H_2.

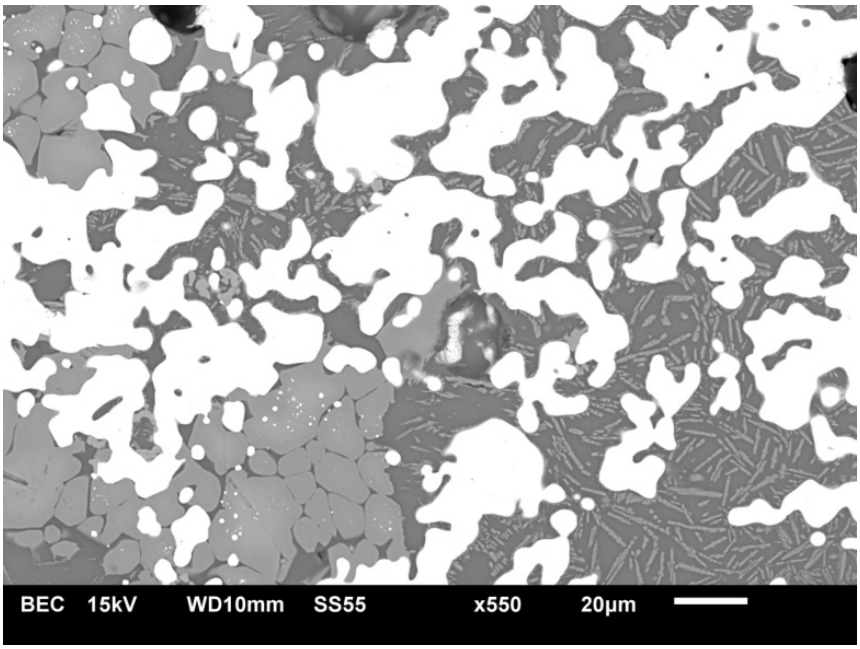

Figure 6.17. BSE image of the fully reduced residue from the isothermal test at 1200 ºC with 15% H_2 (white area is the ferronickel alloy, grey areas are silicates with varying Fe contents).

6.3.1.3 Effect of the Partial Pressure of H_2

The effect of the partial pressure of the reducing gas on the reduction rate could be expressed in the form of the power law which is shown as Eqs. (6.7) and (6.8). In order to evaluate this, 40% H_2 gas was used for the reduction of the leach residue for comparison with the 15% H_2 reduction trends. Comparison was made on the reduction of the leach residue during continuous heating from room temperature up to 1400 ºC, which is illustrated in Figure 6.18. It is apparent that by increasing the partial pressure of H_2 the reduction rate increased and the curve shifted to lower temperatures. Most reduction was achieved at 600 ºC with 40% H_2 as opposed to at 800 ºC with 15% H_2. The effect of the change of partial pressure of H_2 is also obvious even at low temperatures, e.g. in the range of 400 ºC to 600 ºC, where the reduction rate controlling step is the zero-order chemical reaction based on the previous discussion. This appears to contradict with the zero-order chemical reaction mechanism discussed earlier. This is because the partial pressure of H_2 was fixed in the previous isothermal reduction tests. Therefore, it may be concluded that the reaction is only zero-order with respect to the mass of the oxides during the reduction, whereas its order with respect to H_2 pressure is higher.

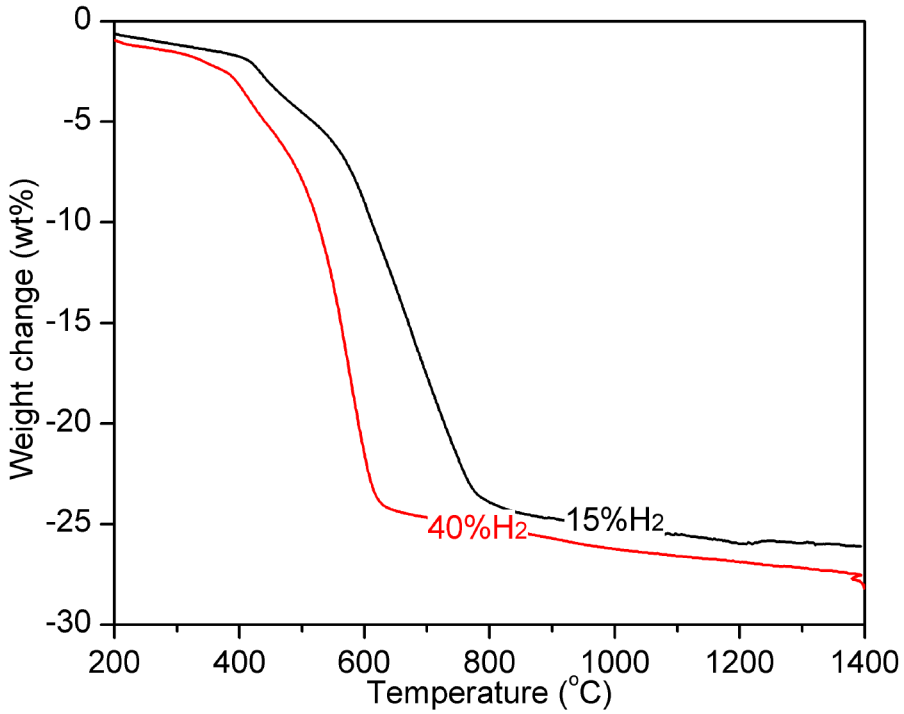

Figure 6.18. Comparison of the continuous heating reduction with 15% H_2 and 40% H_2 at 15 ºC/min.

In order to evaluate the order of reaction with respect to the partial pressure of the reducing gas (n) in Eq. (6.7), one isothermal test was performed at 800 ºC with 40% H_2 for comparison with the isothermal reduction with 15% H_2. The results are shown in Figure 6.19. The reduction rate is much higher with 40% H_2. A linear relationship was also obtained by plotting the rate of reduction ($d\alpha/dt$) as a function of $[-\ln(1-\alpha)]^{-1}$, meaning that this isothermal reduction was also controlled by gas diffusion. The order of reaction (n) was calculated to be 1.4. The pre-exponential factors (A) could also be solved for different temperature ranges after n is obtained. Accordingly, two empirical correlations for the reaction rates in the two regimes could be established as shown in Table 6.2.

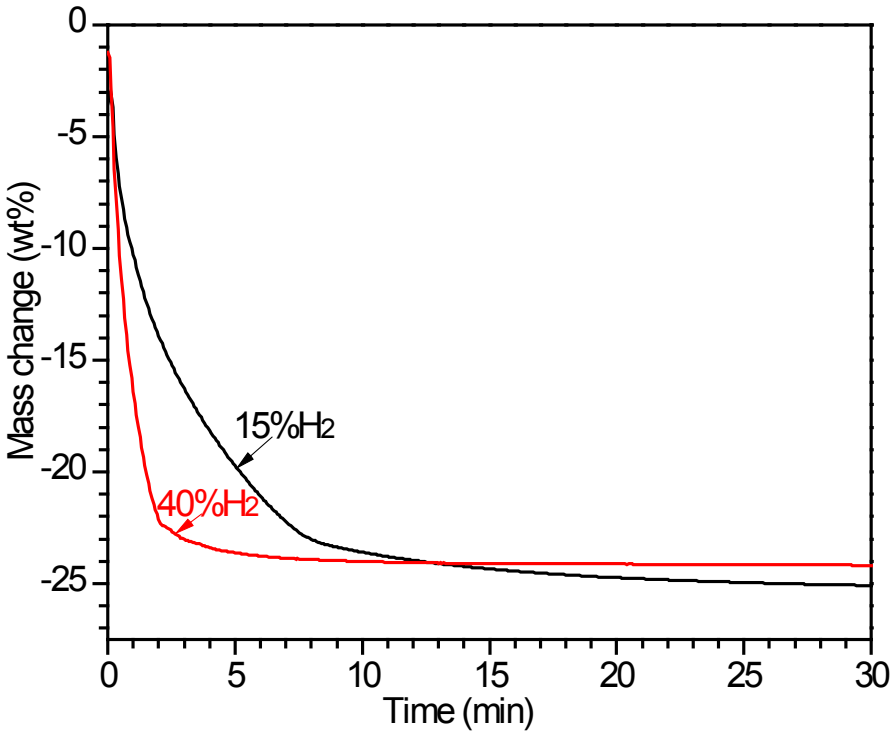

Figure 6.19. Comparison of the isothermal reduction with 15% H_2 and 40% H_2 at 800ºC.

Table 6.2. Overall reaction rate expressions for different temperature ranges.

Temperature ranges	Rate-controlling mechanisms	Rate of reaction equations
350 ºC–600 ºC	Pseudo-zero-order chemical reactions	$\frac{d\alpha}{dt} = 4012 * \exp(\frac{-64673}{RT}) * P^{1.4}$
600 ºC–1200 ºC	Mixed control of gas diffusion through product layer of individual particles and gas diffusion through pores of sample bed	$\frac{d\alpha}{dt} = 66 * \exp(\frac{-34093}{RT}) * [-\ln(1-\alpha)]^{-1} * P^{1.4}$
1200 ºC–1500 ºC	Gas diffusion through the molten sample bed	———

6.3.2 Reduction with CO

6.3.2.1 Continuous Heating

The leach residue was firstly reduced with CO in both TGA and DTA mode, the results of which are plotted in Figure 6.20 as a function of temperature. As can be seen, the reduction is negligible below 400 ºC. Most reduction occurred in the temperature range 400–800 ºC. In this temperature range, two stages of reduction could be identified. The first stage reduction is denoted by the initial quick mass loss between 400 and 520 ºC, corresponding to two partly overlapped CO_2 peaks at 424 ºC and 455 ºC. There is an endotherm at 405 ºC shown on the DTA curve (heat flow curve). This endotherm should represent the first reduction stage. The second reduction stage occurred between 520 and 800 ºC which is characterized by a quicker mass loss to reach -23.5 wt% with a corresponding large CO_2 peak and an endotherm at 593 ºC.

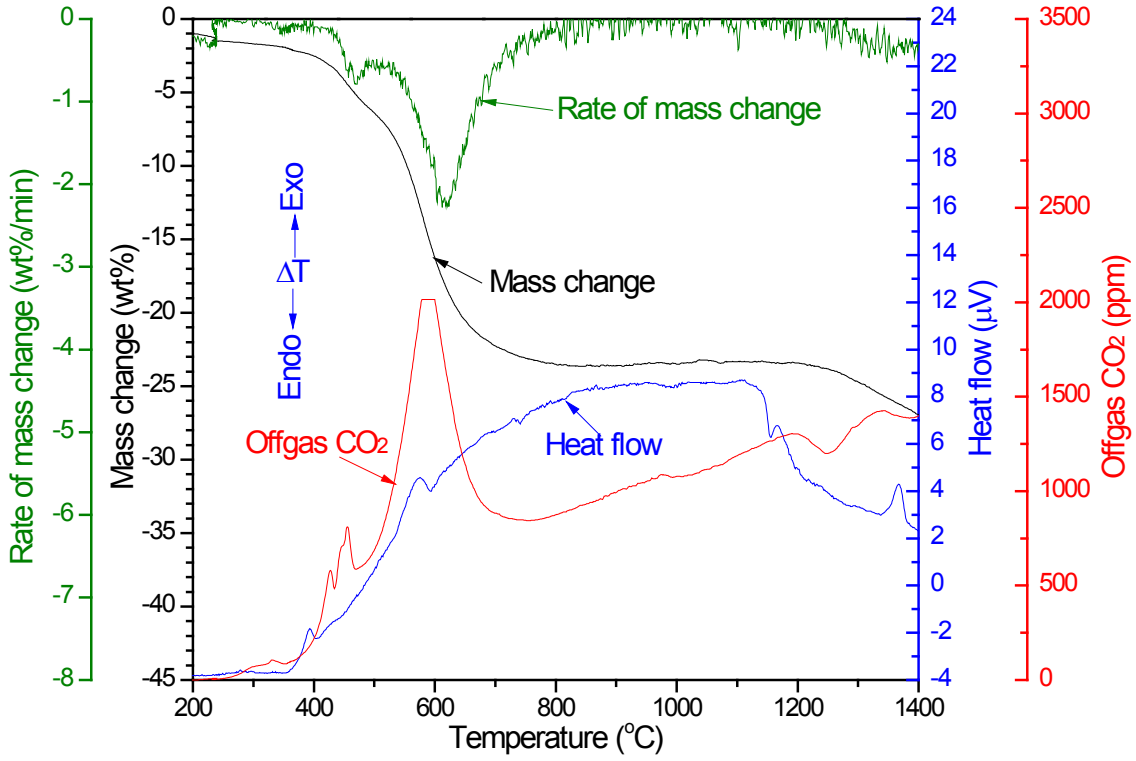

Figure 6.20. Continuous heating (15 ºC/min) of the leach residue in CO.

In order to identify what reduction reactions occurred in these two stages, samples were collected from intermediate temperatures of 520 ºC and 800 ºC and were subject to XRD

analysis. Their XRD patterns are plotted in Figure 6.21 along with the pattern for the original leach residue for comparison. As can be seen, the phases identified in the original leach residue are hematite and nickel ferrite. Hematite disappeared after the sample was heated to 520 ºC with the formation of substantial amount of magnetite (Fe_3O_4). The formation of an alloy phase $Fe_{10.8}Ni$ is also observed. It becomes evident that one of the reactions in the first stage is the reduction of hematite by CO to magnetite, which could be represented by Eq. (6.11). By calculation, Eq. (6.11) could only cause 1.5 wt% mass loss. This suggests that the first small CO_2 peak at 424 ºC is most likely caused by this reduction reaction. The second reaction which is represented by Eq. (6.12) is responsible for the formation of the alloy $Fe_{10.8}Ni$ and the appearance of the second CO_2 peak at 455 ºC. Due to the presence of Ni as impurities of varying concentrations in the original hematite phase, reduction via Eq. (6.11) would result in the formation of an iron-nickel oxide ($Ni_xFe_{3-x}O_4$) instead of magnetite (Fe_3O_4). As a consequence, the reduction product of Eq. (6.12) is an Fe-rich alloy phase ($Fe_{10.8}Ni$) instead of pure Fe. Iron oxide reduction is not complete at 520 ºC as suggested by the presence of substantial amount of magnetite at this temperature, Figure 6.21. Relatively broad peaks for magnetite phase, which partly overlap with those for $NiFe_2O_4$, can be seen at 520 ºC in Fig. 4. This is due to the presence of various amounts of Ni in this phase ($Ni_xFe_{3-x}O_4$) which caused the distortion of the lattice structure to varying degrees, thereby shifting and/or broadening the XRD peaks. The completion of iron oxide reduction is marked by the disappearance of the magnetite peak at 800 ºC, indicating that magnetite reduction proceeds in both reduction stages (400–520 ºC, 520–800 ºC). This is probably caused by the presence of two morphologies of the original hematite phase which gives rise to the difference in their reduction kinetics. The first type has a rather porous columnar structure (e.g. Particle *a* in Figure 6.2), which has easy access to the reduction gas. The second type is relatively dense and co-exists with nickel ferrite in the ring-shaped particles (e.g. Particle *b* in Figure 6.2). The reduction of the latter particles should be slower because of the dense nature of solid phase(s). As a result, it is tentatively suggested that the reduction of the porous magnetite occurred at around 455 ºC, and the denser magnetite in the ring-shaped particles was reduced between 520 and 800 ºC.

$$3Fe_2O_3(s) + CO(g) = 2Fe_3O_4(s) + CO_2(g) \quad (6.11)$$

$$Fe_3O_4(s) + 4CO(g) = 3Fe(s) + 4CO_2(g) \quad (6.12)$$

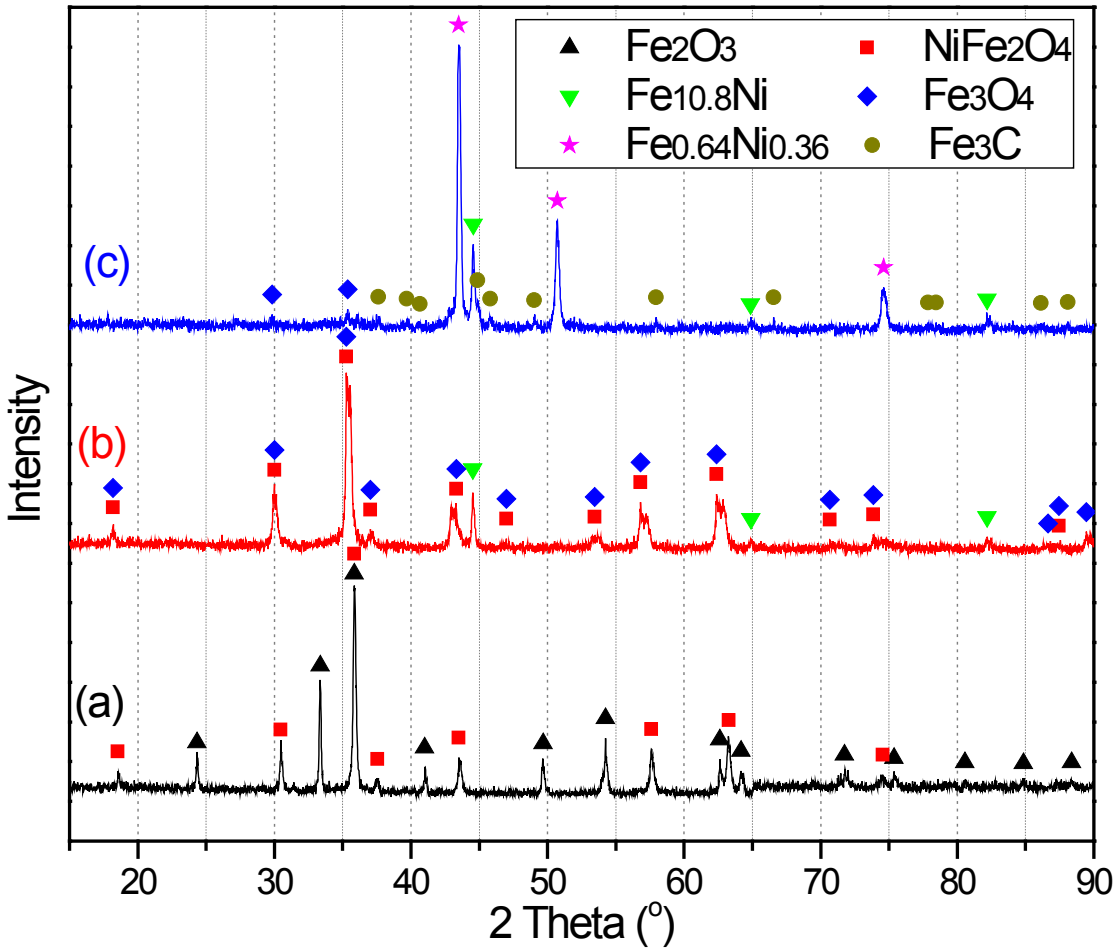

Figure 6.21. XRD patterns for the leach residue (a), and samples collected after continuous heating in CO to 520 ºC (b) and 800 ºC (c).

In the second reduction stage (520–800 ºC), nickel ferrite is also reduced, as indicated by the disappearance of nickel ferrite and the formation of an alloy phase $Fe_{0.64}Ni_{0.36}$ in Figure 6.21. The reduction of nickel ferrite could be represented by Eq. (6.13).

$$NiFe_2O_4 + 4CO = Fe_2Ni(alloy) + 4CO_2 \quad (6.13)$$

Further increase in temperature above 800 ºC caused little mass loss before 1200 ºC. On the contrary, a slight mass gain is observed in this temperature range, which is believed to be caused by the carbon deposition onto the sample and the crucible by the reverse Boudouard reaction (Eq. (6.1)). The gradual drift of the base of the CO_2 curve in Figure 6.20 also indicates the occurrence of the reverse Boudouard reaction. The base of the heat flow curve in Figure 6.20

has drifted, which is caused by the physical changes of the sample during the course of reduction, i.e. decrease in the heat capacity of the sample and/or increase in its thermal conduction rate partly due to the shrinkage of the sample bed.

Further mass loss occurred after 1200 ºC, following an endothermic peak. A previous study on the reduction of the leach residue by H_2 showed that the silicate materials in the sample melted at around 1200 ºC, suggesting that the reduction of the Fe from the molten silicates (Eq. (6.14)) should be responsible for this mass loss. The reduced product Fe should be in the form of an alloy by merging with the existing alloy phases.

$$Fe_2SiO_4(l) + 2CO = 2Fe\ (alloy) + SiO_2 + 2CO_2 \quad (6.14)$$

6.3.2.2 Isothermal Reduction

Isothermal tests were performed to evaluate the reduction kinetics at various temperatures in the range 400–1300 ºC. The mass changes were plotted in Figure 6.22. As can be seen, the reduction rate increased with the increase of temperature from 400 to 1100 ºC indicated by the greater slope of the mass change curve at higher temperatures. At 1100 ºC, the reduction was complete within around 3 min. The occurrence of the reverse Boudouard reaction (Eq. (6.1)) is seen in the isothermal reduction runs in the temperature range 800–1100 ºC which is revealed by the slight mass gain after the reduction is complete or near complete. Two distinct reduction stages could be clearly identified for the isothermal run at 1200 ºC. At this temperature, the reduction rate is high and comparable to those at 1000 and 1100 ºC in the first 45 seconds. A sudden drop in the reduction rate took place at 45 seconds, after which the reduction is slow and only comparable to that at 400 ºC. This drop in the reduction rate is believed to be caused by the melting of the silicates in the sample. As discussed earlier, the silicate material in the sample begins to melt at around 1200 ºC. In the first stage where the reduction is fast, the sample is rather porous due to the presence of large volume percentage of oxides as solid particles even though the silicates may have melted. Substantial melting of silicates at around 45 seconds results in the collapse of the porous structure, as well as pore blockage by liquid, both of which lead to significant reduction in the reactive surface area. The diffusion through the molten silicates can soon become the rate controlling step, hence the sudden drop in the reduction rate.

This sequence of events resembles the reduction of iron ore in the blast furnace when fayalitic liquid is formed as a coating layer on the ore surface, severely limiting the reduction rate in a phenomenon known as *slag blocking* [31]. At 1300 ºC, the quick reduction stage is even shorter. But due to the higher diffusion rate in the silicate melt, the reduction is faster compared with the reduction at 1200 ºC in the second reduction stage.

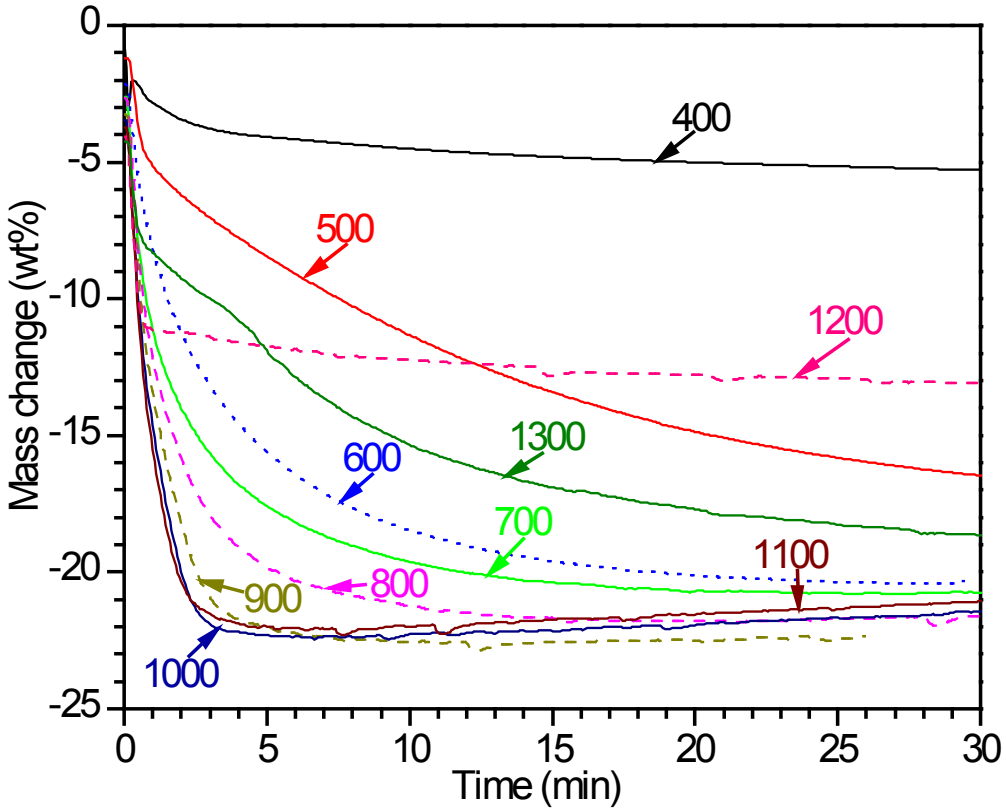

Figure 6.22. TGA isothermal reduction of the leach residue with CO.

The kinetics of the isothermal reduction was evaluated by analyzing the mass change curves in Figure 6.22. Eq. (6.15) [29] was adopted for this purpose. The Arrhenius equation (Eq. (6.6)) was used to describe the temperature dependence. The dependence of reduction rate on the extent of reduction is represented by the kinetic model $f(\alpha)$, the form of which is determined by the rate controlling mechanism. For an isothermal reaction, the integral form of the kinetic model $g(\alpha)$ has the relationship with temperature (T) and time (t) as expressed by Eq. (6.16) [29]. Isoconversional (model-free) method was firstly employed to calculate the apparent activation energies without determining the kinetic models. Eq. (6.17) can be easily derived from Eq. (6.16), in which $t_{\alpha,i}$ represents the time required to reach a certain extent of reduction

(α) at temperature (T_i). The apparent activation energy at certain extent of reduction can be calculated from the slope of the plot $\ln t_{\alpha,i}$ vs. $1/T_i$. The mass change curves for the isothermal reduction tests at 700–1100 ºC were evaluated by applying Eq. (6.17) at various extents of reduction (α, 0.2–0.9). The evaluation was not performed for $\alpha<0.2$ because of the relatively large error arising from the ambiguity in determining the starting time of the reduction from the TGA curves. The apparent activation energies were calculated and plotted against α in Figure 6.23. The plot of $\ln t_{\alpha,i}$ vs. $1/T_i$ is also shown in Figure 6.23 as an inset. As can be seen, the apparent activation energy increases from 6.7 kJ/mol to 41.1 kJ/mol with the progress of the reduction. This large variation of apparent activation energy suggests that these E_a are composite values resulting from the tangled interplay of different steps/processes. These steps/processes could be species-dependent chemical steps, gaseous reactants/products diffusion through a solid product/reactant, adsorption–desorption of gaseous products/reactants on the surface of the reacting solid, etc. [32, 33]. The apparent activation energies are relatively low, indicating the rate controlling mechanism is very likely diffusion control rather than chemical control. In order to determine whether the diffusion of CO through the pores of the sample bed is the rate-controlling factor, two series of TGA experiments were performed. In the first series of experiments, 50 mg leach residue was isothermally reduced at 800 ºC with varying flowrates of CO. The results are plotted in Figure 6.24. As can be seen, three mass change curves overlap, indicating that the transfer of CO to the surface of sample bed at 1 L/min was high enough and did not adversely affect the reduction rate. The variation of sample size was then evaluated in the second series of isothermal experiments at 800 ºC, the results of which are shown in Figure 6.25. A higher reduction rate can be observed with smaller sample size especially within the first minute of reduction, indicated by the varying slopes of the mass change curves. This suggests that the reduction did not take place uniformly in the sample bed, which resulted from the limited mass transfer (gaseous transfer) in the pores of the sample bed during reduction. The effect of this rate controlling mechanism gradually diminished with the progress of reduction, as suggested by the parallel curves after approximately 1 minute.

$$\frac{d\alpha}{dt} = k(T) * f(\alpha) \tag{6.15}$$

$$g(\alpha) \equiv \int_0^{\alpha} \frac{d\alpha}{f(\alpha)} = A * \int_0^{t} \exp(\frac{-E_a}{RT})dt = A * \exp(\frac{-E_a}{RT}) * t \tag{6.16}$$

$$\ln t_{\alpha,i} = \ln\left[\frac{g(\alpha)}{A_\alpha}\right] + \frac{E_a}{RT_i} \tag{6.17}$$

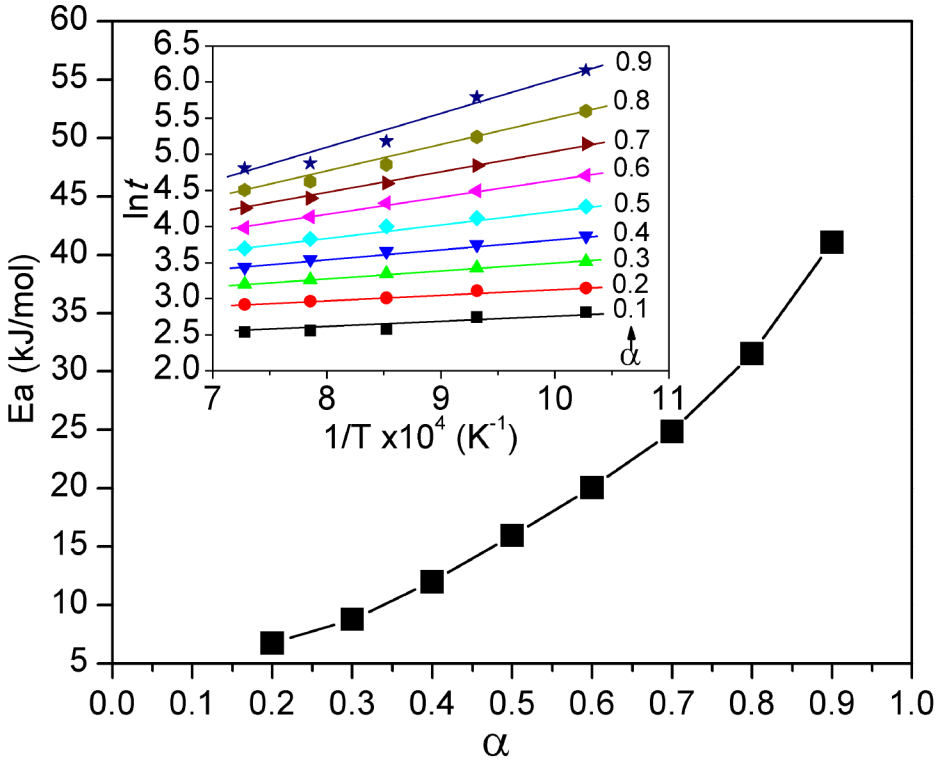

Figure 6.23. Variation of apparent activation energies as a function of extent of reduction (α) for the isothermal reduction tests. ln*t* vs.1/T $\times 10^4$ (isoconversional method) is also plotted as an inset.

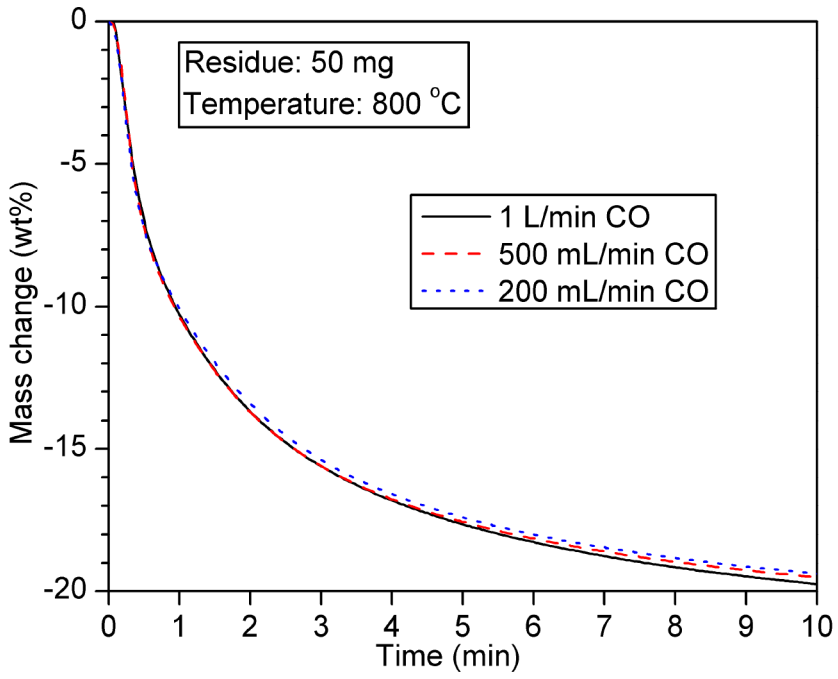

Figure 6.24. Effect of the variation of the flowrates of CO on the isothermal reduction of the leach residue.

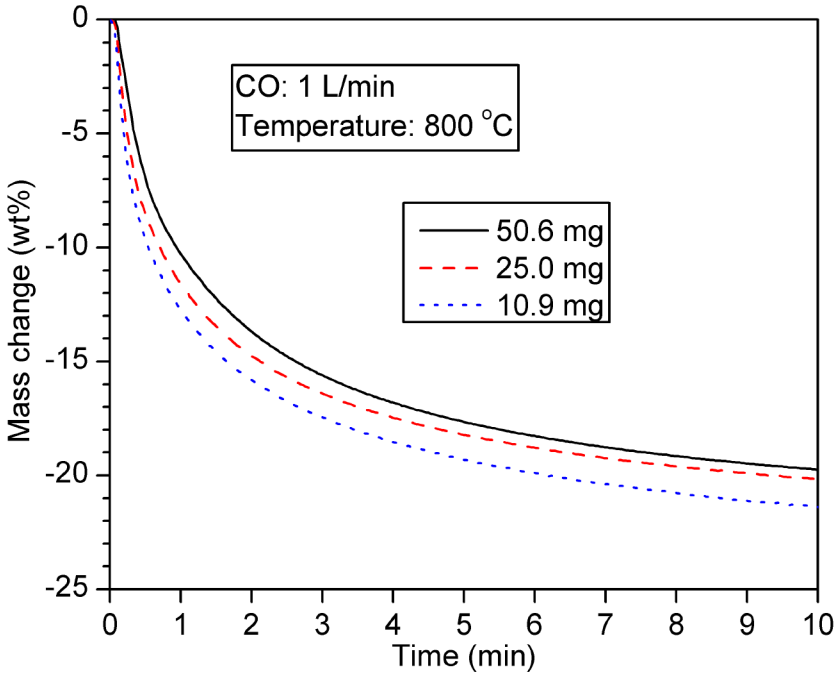

Figure 6.25. Effect of the variation of sample sizes on the isothermal reduction of the leach residue.

Model fitting method was also used to further determine the rate controlling mechanism. Linear trends are obtained between the reduction rate and $f(\alpha)$ for the isothermal tests in the temperature range 500–1100 ºC by employing the 2D diffusion model, which is represented by Eq. (6.9) [29]. These linear trends are exhibited in Figure 6.26 as an inset. For each individual test, the 2D diffusion model applies only when α is higher than a certain value, which is shown in Figure 6.26. This is because in the lower range of α, the reduction rate is predominantly controlled by the gaseous diffusion in the pores which is discussed earlier. Since the 2D diffusion model represents the diffusion in the solid product layer [34], this indicates that in the higher range of α where the 2D diffusion model applies, diffusion of reactive species through metallic alloys in individual particles controls the reduction rate. An Arrhenius plot is also shown in Figure 6.26 yielding the apparent activation energy of 31.8 kJ/mol based on the slope of the line for the temperature range 600–1100 ºC. This value is very close to that obtained with hydrogen as the reductant, which is 34.1 kJ/mol for 600–1200 ºC. The plot for 500 ºC deviated from the linear trend in Figure 6.26. This deviation is possibly caused by the partial reduction at low temperatures due to the stepwise reduction mechanism (Eqs. (6.11)–(6.13)), whereas at other higher temperatures the reduction is near completion. From the above discussion, gaseous diffusion through the pores of the sample bed mainly controls the reduction rate at the lower range of α, and the rate controlling factor gradually shifts to diffusion through the layer of alloy products in individual particles at a higher range of α. A large variation of activation energies with α in Figure 6.23 is a result of the combining effect of the two rate-controlling mechanisms as well as their varying contributions to the overall reduction rate.

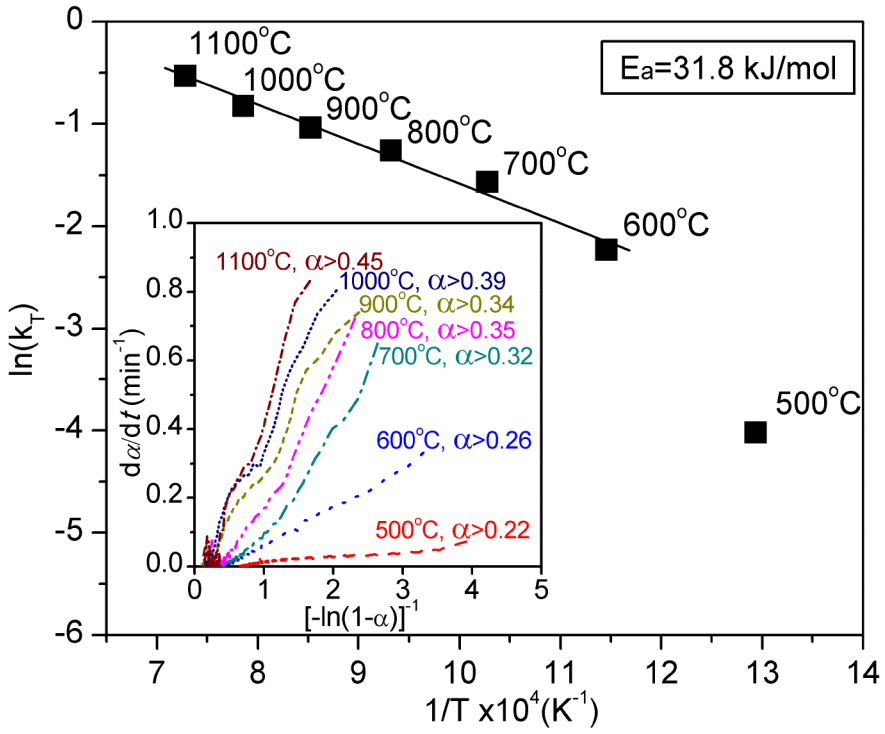

Figure 6.26. Arrhenius plot for the isothermal reduction tests between 500 and 1100 ºC. The relationship between the reduction rate and the 2D diffusion model ($f(\alpha)=[-\ln(1-\alpha)]^{-1}$) is also plotted as an inset.

The reduction products from the isothermal tests were examined by SEM/EDS. Figure 6.27 illustrates the microstructures of the porous hematite particles after reduction by CO at various temperatures. The hematite was not reduced at 400 ºC and its columnar porous structure was preserved (top-left). At 500 ºC, the hematite was reduced to form highly porous Fe particles with submicron grains (top-right). The grains grow coarser and further apart when reduced at higher temperatures (bottom-left and bottom-right). Some sintering could be observed in the reduced hematite particles at 900 ºC.

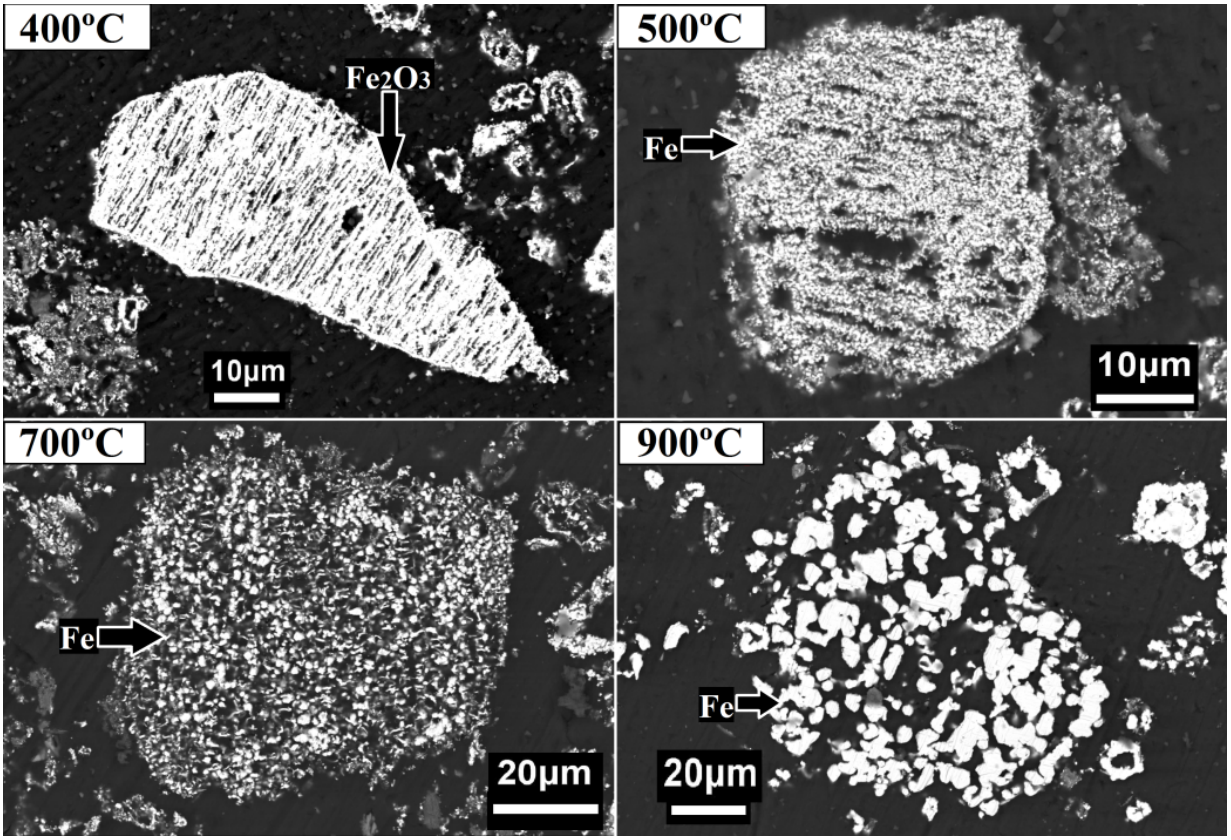

Figure 6.27. Isothermal reduction of the porous hematite particles with CO at various temperatures.

The change of morphologies of the ring-shaped particles reduced at various temperatures was also examined and is presented in Figure 6.28. Nickel sulfide resided within some of the ring-shaped particles, which can be seen in Figure 6.28. The particle at 400 ºC in Figure 6.28 was not reduced, and the oxide ring is much denser compared with the hematite particle in Figure 6.27. Reduction was obvious when the temperature reached 500 ºC and the ring formed Fe-Ni alloy with micron-sized pores. At 600 and 700 ºC, the alloy rings were still rather porous, and the residual nickel sulfide was partly converted to nickel-rich Ni-Fe alloy. This reaction is tentatively suggested as the reduction of the nickel sulfide to form alloy with carbonyl sulfide (COS) as the gaseous product, which is represented by Eq. (6.18). Crowe and Utigard [35] have reported this reaction as being responsible for the reduction of Ni, Cu, and Co sulfides by CO. Above 800 ºC in Figure 6.28, substantial sintering took place, and the degree of sintering is greater at higher temperatures. For the sample reduced at 900 ºC, some Fe_3O_4 was found locked in the alloy phase. This was caused by the immediate sintering of the alloys that were formed on

the surface of the oxide which limited the reduction rate of the oxide. The residual nickel sulfide was fully reduced to nickel-rich alloy which sintered on the alloy ring. At 1100 ºC, the reduced ring was adequately densified and formed a uniform alloy particle.

$$Ni_3S_2 + 2CO = 3Ni(alloy) + 2COS(g) \quad (6.18)$$

The silicates melted at 1200 ºC and all pores were removed. The alloy phase formed during this process was distributed in the silicate melt as small particles of various shapes. Two silicates were formed from the exsolution of the melt upon cooling, i.e. pyroxene which is rich in Fe and Al, and olivine which is rich in Fe and Mg. The silicates phases formed were found to have higher Fe content than the original silicates in the leach residue before reduction. This suggests that part of the iron oxide in the leach residue must have dissolved into the silicate melt. This is further supported by the fact that a large number of small regular-shaped Fe_2O_3 particles were exsolved from the silicate melt upon cooling, which could be seen in the BSE image at 1200 ºC in Figure 6.28. The partial dissolution of the hematite into the silicate melt which substantially lowers the activity of hematite might be another critical factor that leads to the slow reduction rate at 1200 ºC (Figure 6.22). In this case, the reduction is better represented by Eq. (6.14) in which Fe is formed from the reduction of the silicate melt and merges with the existing alloy particles. At 1300 ºC, more alloy was formed and the two silicate phases (pyroxene and olivine) which were exsolved from the melt formed a laminar structure with no exsolution of Fe_2O_3 particles. This is probably caused by the greater degree of reduction at higher temperature which results in an iron-deficient silicate melt. During reduction, gas bubbles of CO_2 are formed, which on solidification leave behind features such as those seen in Figure 6.29. Upon cooling the melt, the gas bubbles shrink in volume, drawing the still-liquid silicate phase from the already sintered alloy particles. On complete solidification, a spherical void and an alloy-free halo remain at the bubble site. Because the exsolved pyroxene phase has a higher freezing temperature than the olivine phase, the pyroxene solidifies before olivine, creating the unique laminar structure with parallel plates of olivine separated by a gap, Figure 6.29.

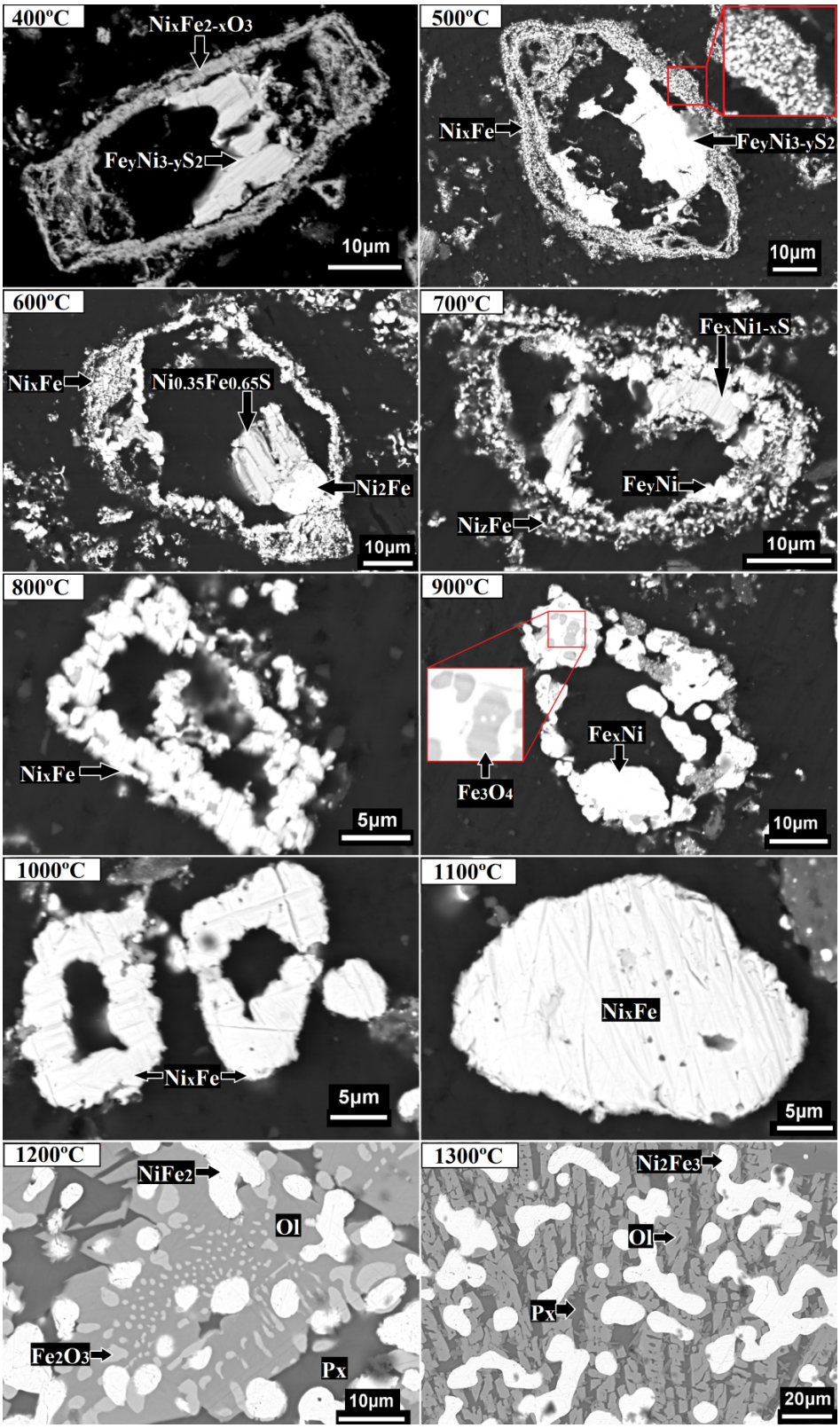

Figure 6.28. Microstructure of particles reduced by CO under isothermal conditions (Px: Pyroxene, silicate containing Fe, Al, Na; Ol: Olivine, silicate containing Fe, Mg).

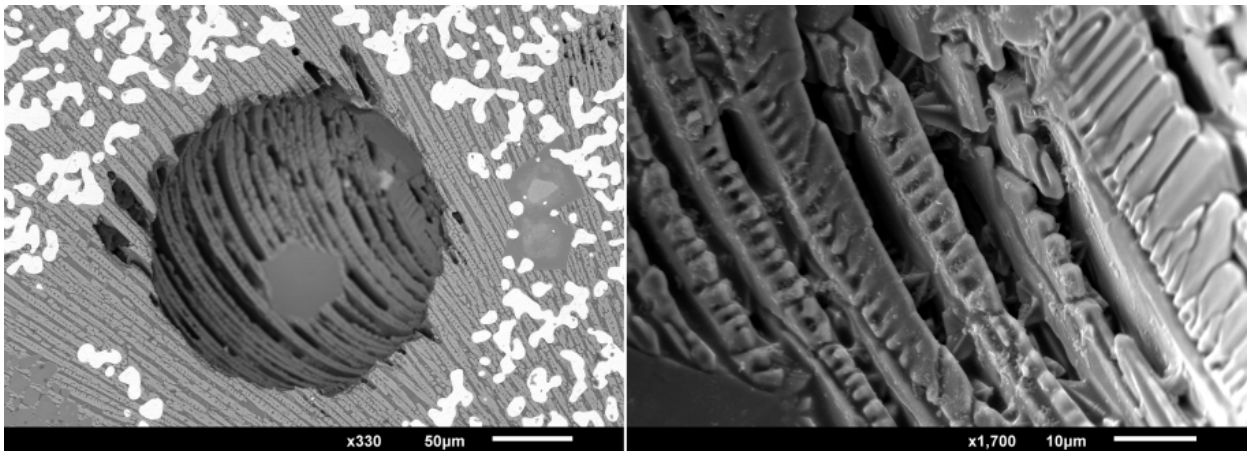

Figure 6.29. Laminar structure of the silicates formed upon cooling the reduced residue from 1300ºC with a gas bubble formed in the melt (left) and interior of the bubble (right).

6.3.3 Reduction with Graphite

6.3.3.1 Continuous Heating

Figure 6.30 shows the results for the reduction of the leach residue with excess amount of graphite powder by continuously heating the mixture at 15 ºC/min to 1500 ºC under an argon atmosphere. As can be seen, little reduction occurred below 800 ºC. A higher temperature (>800 ºC) is required to initiate the reduction using graphite as reductant compared with the reduction using CO (>400 ºC). This is possibly due to the different reduction mechanisms involved: initial reduction of the oxides by graphite is solid-solid reaction which has very limited reaction sites, with much smaller rate than the gas-solid reaction involving CO. Moreover, even with the same area of reaction sites for the two cases, the different reduction mechanisms determine that the effect of temperature on the progress of reduction for both cases must be different. Above 800 ºC in Figure 6.30, the reduction progressed gradually, resulting in an increasing mass loss and the formation of mainly CO_2 as the gaseous product below 1000 ºC. Massive reduction took place above 1000 ºC peaking at 1050 ºC, which resulted in large emission of CO and CO_2. DTA analysis measured a large endotherm at 1020 ºC which corresponds to this stage of reduction. The main reduction reactions occurring in this stage are the reduction of hematite and nickel ferrite, represented by Eqs. (6.19)–(6.24). Gas-solid reduction reactions which are represented by Eqs. (6.21)) and (6.24)) are expected to take place due to the formation of CO from Eqs.

(6.19)) and (6.22)) as well as from the Boudouard reaction (Eq. (6.1)). The following scenario can be envisaged. The gas (CO and CO_2) formed from within the sample bed needs to diffuse upwards to the surface of the bed before it is swept away by the argon flow. As the CO and CO_2 formed diffuse upwards through the pores of the sample bed, CO could reduce oxides on its path (Eqs. (6.21) and (6.24)), resulting in an increased partial pressure of CO_2. While the CO_2 could be reduced by the graphite particles on its path depending on the equilibrium of the Boudouard reaction (Eq. (6.1)), resulting in the increased partial pressure of CO. The reversed Boudouard reaction could also take place if the partial pressure of CO is higher than the equilibrium value. As a result, the relative partial pressure of CO and CO_2 in the offgas analyzed (Figure 6.30) is a result of the competition among the reversible Boudouard reaction (Eq.(6.1)), reduction reactions by graphite (Eqs. (6.19), (6.20), (6.22), (6.23)), and reduction reactions by CO (Eqs. (6.21) and (6.24)). Due to the complexity of the reaction system, no further effort was made to determine which type of reaction prevailed in the reduction process.

The Boudouard reaction, Eq. (6.1), was also expected to take place. The speculation is made based on the fact that in Figure 6.30, the formation of CO_2 as the gaseous reduction product predominates below around 1000 ºC, above which the formation of CO prevails. This trend is in accordance with the equilibrium of Boudouard reaction (Figure 6.1), although the offgas CO/CO_2 in Figure 6.30 did not reach equilibrium because of the non-equilibrium conditions applied. The reduction slowed down until the temperature reached 1200 ºC, above which a second stage quick reduction occurred. It peaked at 1300 ºC and ended at 1340 ºC. This second stage of reduction results in the formation of CO as the gaseous product and corresponds to an endotherm peak at 1235 ºC. This is believed to be induced by the melting of the silicates in the sample which brings about the reduction of the molten silicate by the graphite, which could be represented by Eq. (6.25).

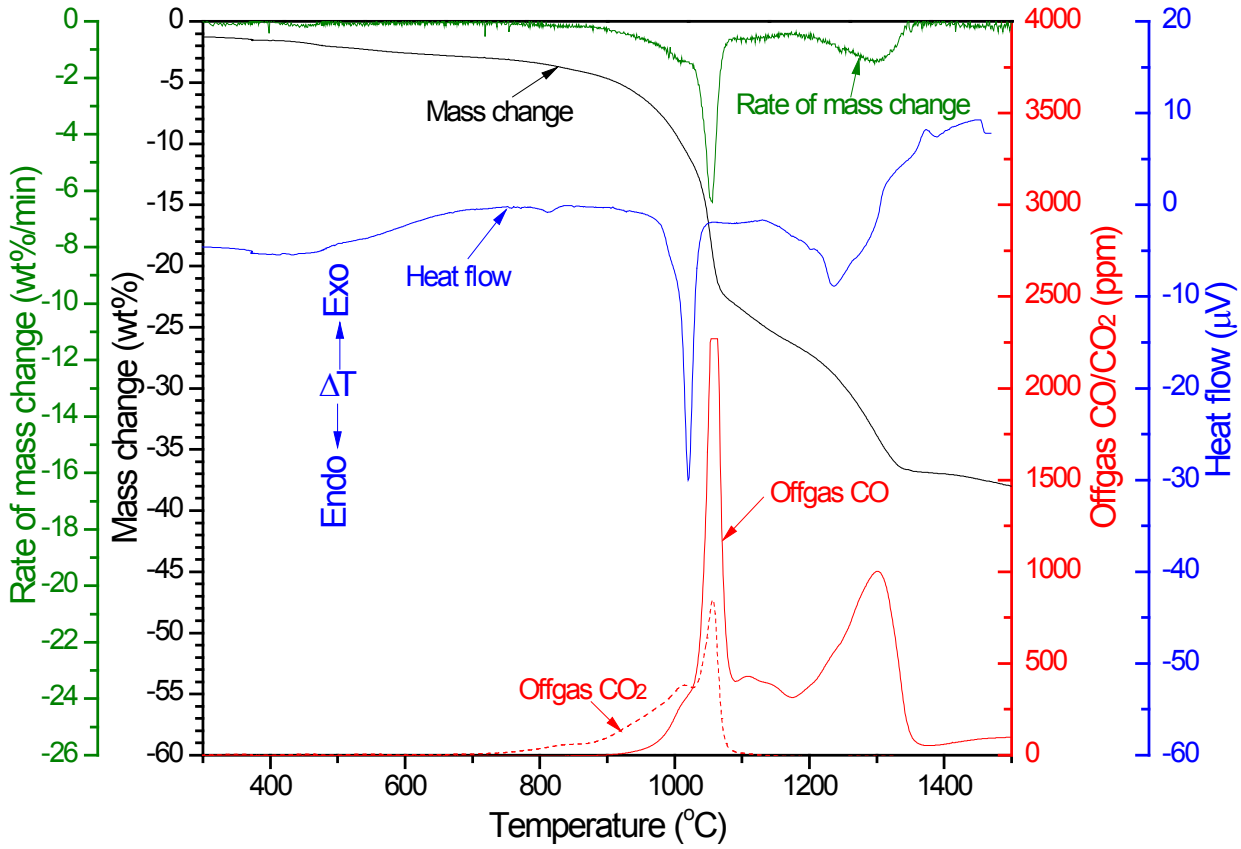

Figure 6.30. Continuous heating of the leach residue with graphite in TGA and DTA.

$$Fe_2O_3 + 3C = 2Fe + 3CO \quad (6.19)$$

$$2Fe_2O_3 + 3C = 4Fe + 3CO_2 \quad (6.20)$$

$$Fe_2O_3 + 3CO = 2Fe + 3CO_2 \quad (6.21)$$

$$NiFe_2O_4 + 4C = NiFe_2(alloy) + 4CO \quad (6.22)$$

$$NiFe_2O_4 + 2C = NiFe_2(alloy) + 2CO_2 \quad (6.23)$$

$$NiFe_2O_4 + 4CO = NiFe_2(alloy) + 4CO_2 \quad (6.24)$$

$$Fe_2SiO_4(l) + 2C(s) = 2Fe(s,l) + SiO_2(s) + 2CO(g) \quad (6.25)$$

6.3.3.2 Isothermal Reduction

In order to study the reduction kinetics at different temperatures, isothermal reduction tests were performed in the temperature range 800–1400 ºC with the results shown in Figure 6.31. The reduction products from these isothermal runs were examined by SEM/EDS, EPMA, and XRD to elucidate the reduction mechanisms. As can be seen in Figure 6.31, at low temperatures of 800 and 900 ºC, the reduction rate is slow and very limited reduction took place within 30 min. Effective reduction only occurred when the temperature is higher than 1000 ºC. Two quick reduction stages can be observed at this temperature, which took place during 0–2 min and 4–7 min, respectively. This possibly resulted from the sequential reduction of the porous hematite particles and the relatively dense ring-shaped particles which are composed of both hematite and nickel ferrite. The reduction at 1100 ºC was faster and near complete within 3 min. Two stages of reduction were also observed for the isothermal runs at and above 1200 ºC. In this case, the first stage is always the quick reduction of the oxides until approximately 25 wt% mass loss is reached, while the following second stage is the reduction of the molten silicate. It is apparent from Figure 6.31 that the molten silicate reduction stage is faster at higher temperatures, indicated by the higher slope of the curves below -25 wt% at higher temperatures.

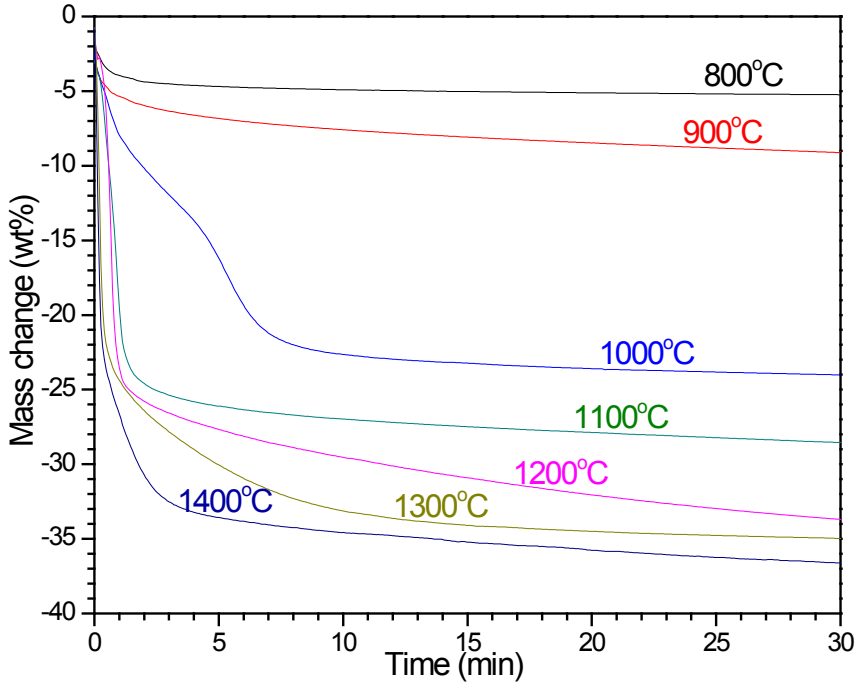

Figure 6.31. TGA isothermal reduction of the leach residue with graphite.

The alloy phases that were formed from these isothermal runs were analyzed by EPMA and the results are presented in the ternary graph in Figure 6.32. The alloy phases identified at 900 ºC under the electron probe are all nickel-rich Ni-Fe alloys, which are formed from the reduction of the nickel sulfide. Previous study showed that the nickel sulfide (Ni_3S_2) melted at 813 ºC [27]. As a result, it was in its molten state during isothermal reduction at 900 ºC. The reaction could be represented by Eq. (6.26). Figure 6.33 exhibits a partly reduced nickel sulfide particle forming nickel-rich alloy with a clear boundary between the alloy and sulfide phases. Another alloy particle is shown in Figure 6.34 as the product from the reduction of the nickel sulfide at 1000 ºC. It is evident from this particular morphology that both the alloy and the nickel sulfide were in a liquid state during reduction, the sulfide covering the surface of the alloy drop.

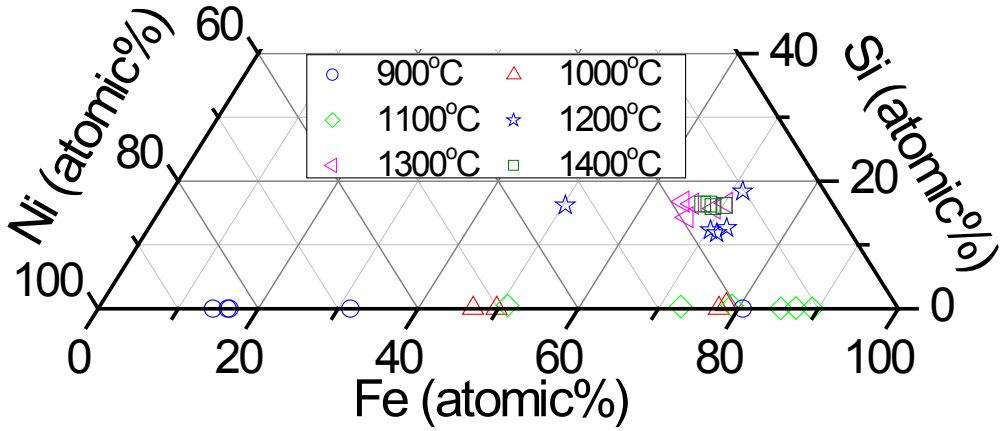

Figure 6.32. EPMA analysis on the alloy particles formed from the isothermal reduction tests by graphite.

$$Ni_3S_2(l) + C(s) = 3Ni(alloy) + CS_2(g) \quad (6.26)$$

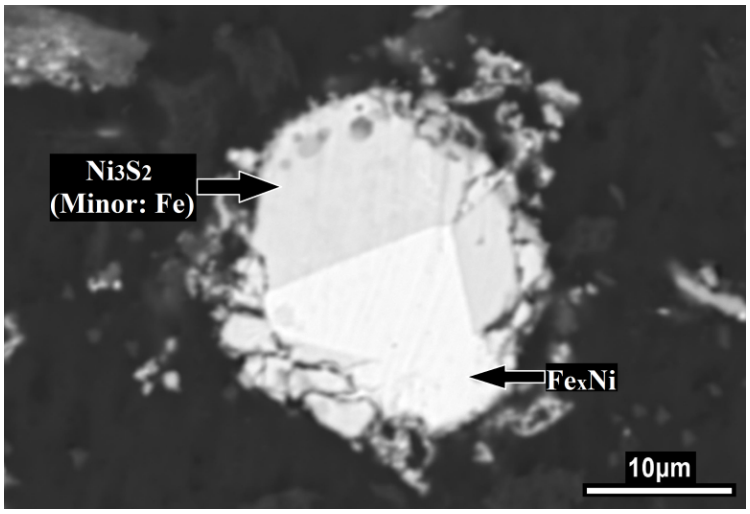

Figure 6.33. Partial conversion of the nickel sulfide to alloy at 900 ºC.

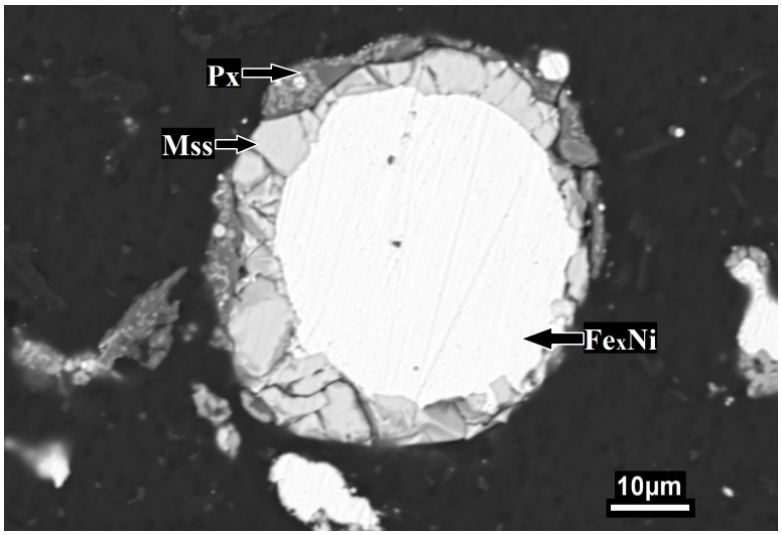

Figure 6.34. Alloy surrounded by monosulfide solid solution (Mss, (Ni,Fe)S) reduced at 1000 ºC (Px: Pyroxene, silicate containing Fe, Al).

With further increase of temperature, more iron-rich alloys were formed from the reduction of the hematite and nickel ferrite, which can be seen from Figure 6.32. Reduction of the silicates started at 1200 ºC denoted by the presence of around 15 at% Si in the alloy phase. The silicates after isothermal reduction were also analyzed by EPMA to reveal the progress of reduction, which is plotted in Figure 6.35. The low concentration of FeO in the silicates at 1200 ºC indicates that Fe is also reduced along with Si. The reduction of Fe from the silicate is more complete at 1200 ºC and higher. The SiO_2 content of the silicates also dropped with the increase

of temperature, indicating a larger extent of reduction at higher temperatures in terms of Si removal. Figure 6.36 exhibits the nucleation and growth of Fe–Si alloy particles within the silicate melt. The sizes of the particles range from nanometers to microns. The exterior Fe-Ni alloy gradually absorbs some of these Fe-Si particles, particularly from the edge of the silicate, to form a Fe-Ni-Si phase. Figure 6.37 shows a Fe-depleted silicate particle covered with a relatively thick layer of Fe-Ni-Si alloy at 1200 ºC. This suggests that the reduction of silicate melt could also proceed by the diffusion of carbon or possibly CO through the alloy.

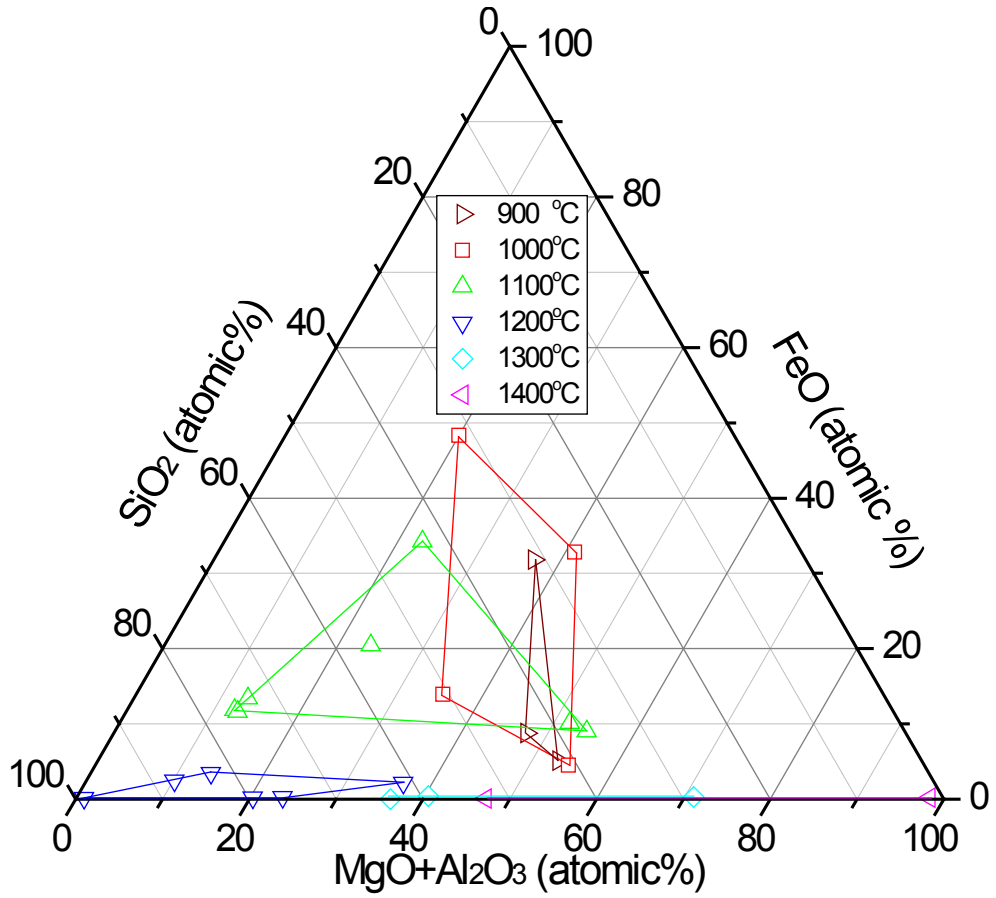

Figure 6.35. The composition of silicate phases in isothermal reduction by graphite.

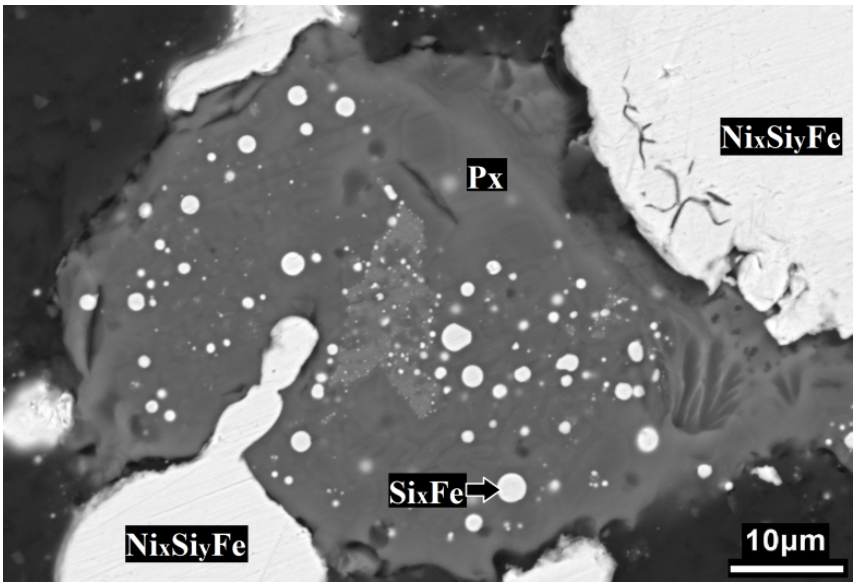

Figure 6.36. Formation of Si_xFe alloy particles from the silicate melt at 1200 ºC (Px: Pyroxene, silicate containing Al, Mg, Fe).

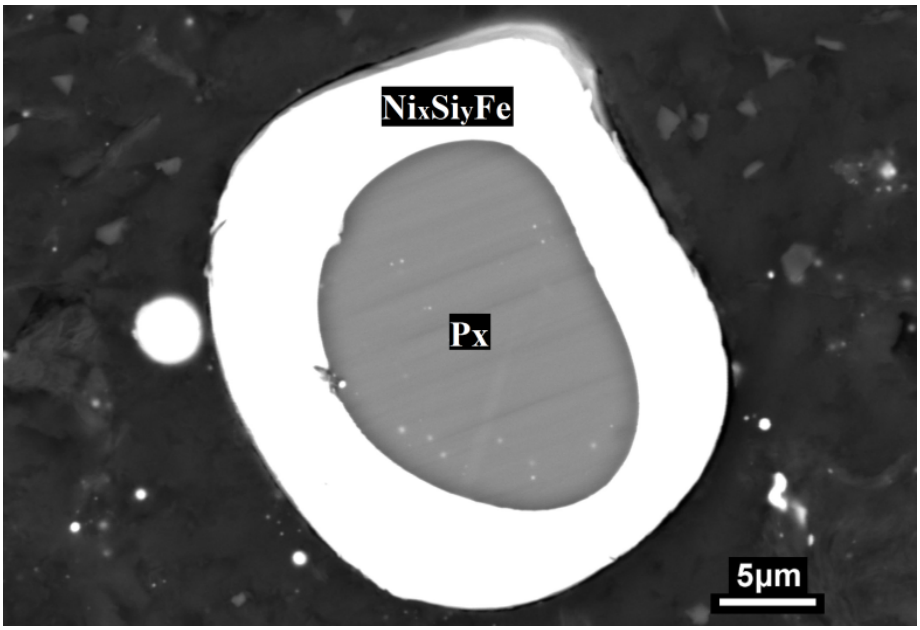

Figure 6.37. Reduction of Fe and Si from a silicate particle forming Ni-Si-Fe alloy at 1200 ºC (Px: Pyroxene, silicate containing Al, Mg, Na).

Thermodynamic evaluation of the formation of the Fe-Si alloys from the reduction of the silicate by graphite was performed using HSC Chemistry [26]. Changes in Gibbs free energy (ΔG) for the reduction of Fayalite (Fe_2SiO_4) by graphite to form various alloys and gaseous CO were

calculated. Figure 6.38 depicts the minimum temperature to initiate the reduction (ΔG=0) as a function of the molar ratio of Si/(Fe+Si) of the alloy phase formed. The solid products are indicated near each point in the graph. As can be seen, the silicate could be reduced to form Fe at temperature as low as 731 ºC from a thermodynamic point of view. Higher temperature is required to form an alloy with a higher Si content. If pure Si and Fe are formed without the formation of Fe-Si alloy, the minimum temperature to initiate the reduction is 1217 ºC. The reduction of the silicates in this study suggests 1200 ºC as the minimum temperature to form alloy phases. This is because the melting of the silicates at about 1200 ºC greatly enhances the kinetics for reduction. Below 1200 ºC, the reduction of silicates is limited due to the slow kinetics of the solid-solid reduction reactions.

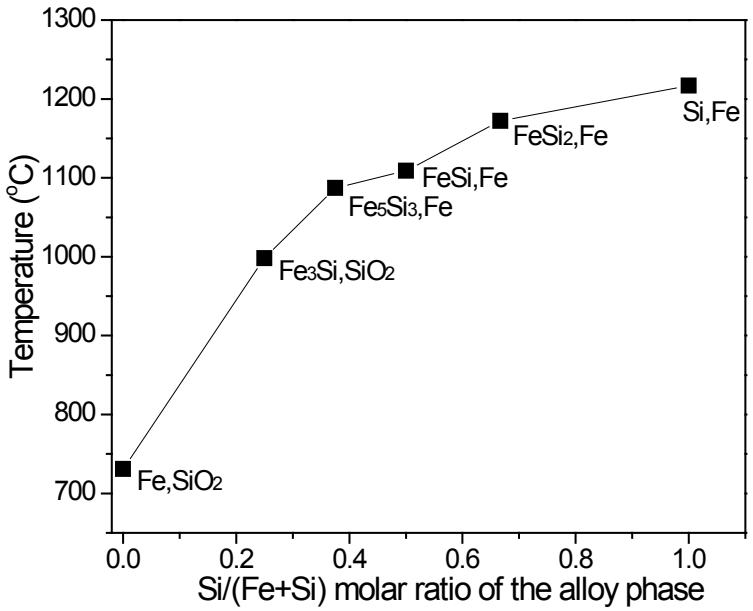

Figure 6.38. Temperatures at which ΔG=0 for the reduction of $FeSiO_4$ by graphite as a function of the molar ratio of Si/(Fe+Si) of the alloy product.

With the increase of the isothermal temperature from 1200 to 1400 ºC, the composition of the alloy particles becomes more uniform, suggested by the converging trend of the plots in Figure 6.32. This indicates that alloy particles have a greater tendency to merge and form larger and more homogenized particles at higher temperatures, which is supported by the evidence from both the SEM and XRD analysis. Figure 6.39 shows the spherical alloy particles produced at 1300 ºC. These particles could be as large as 100 μm in diameter. Figure 6.40 shows an alloy particle 175 μm in diameter. Two phases were exsolved from the alloy melt showing different

grey levels. The interior brighter phase has more Fe and less Si. XRD analysis was conducted on the samples produced from the isothermal runs at 1000 ºC, 1200 ºC and 1400 ºC with the results shown in Figure 6.41. At 1000 ºC, the main alloys are $Fe_{0.64}Ni_{0.36}$ and $Fe_{10.8}Ni$ which were produced from the reduction of the nickel ferrite and hematite, respectively. Due to the reduction of molten silicate, Fe-Ni-Si alloy was formed as the major alloy phase at 1200 ºC with little $Fe_{0.64}Ni_{0.36}$. The alloy produced at 1400 ºC is a relatively homogeneous phase of Ni-Si-Fe, showing enhanced merging of the alloy particles.

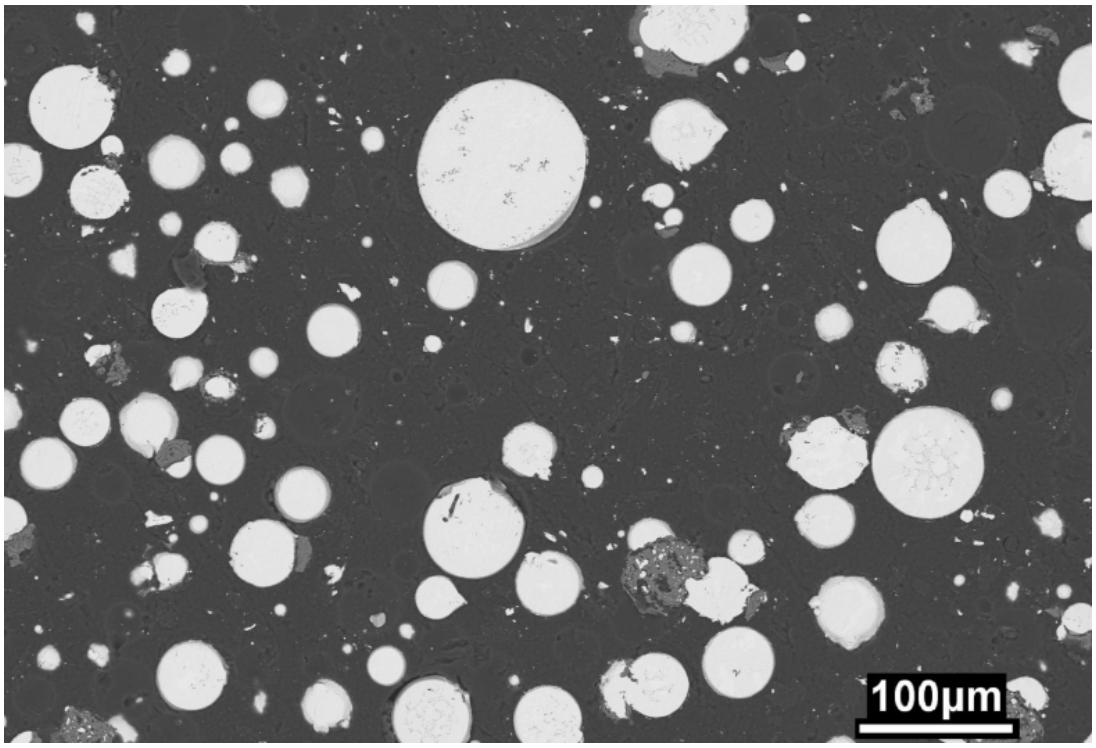

Figure 6.39. Ni_xSi_yFe alloy formed at 1300 ºC.

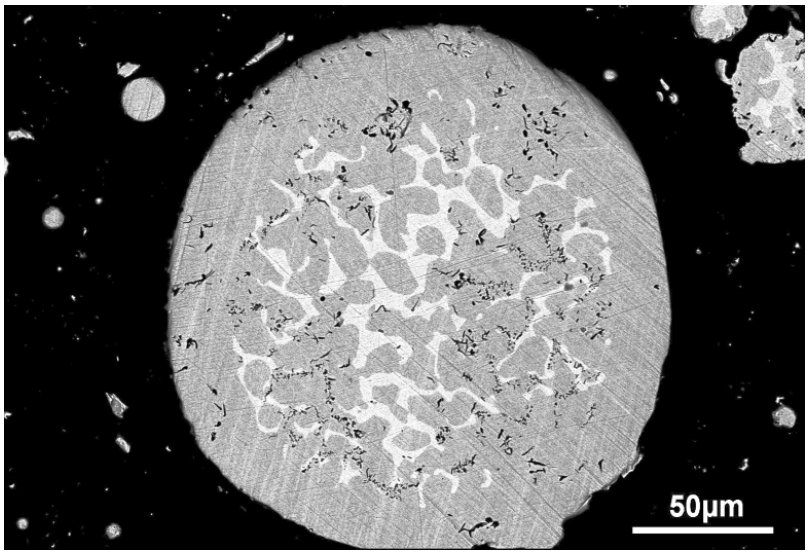

Figure 6.40. An Ni_xSi_yFe alloy particle formed from the reduction at 1400 ºC.

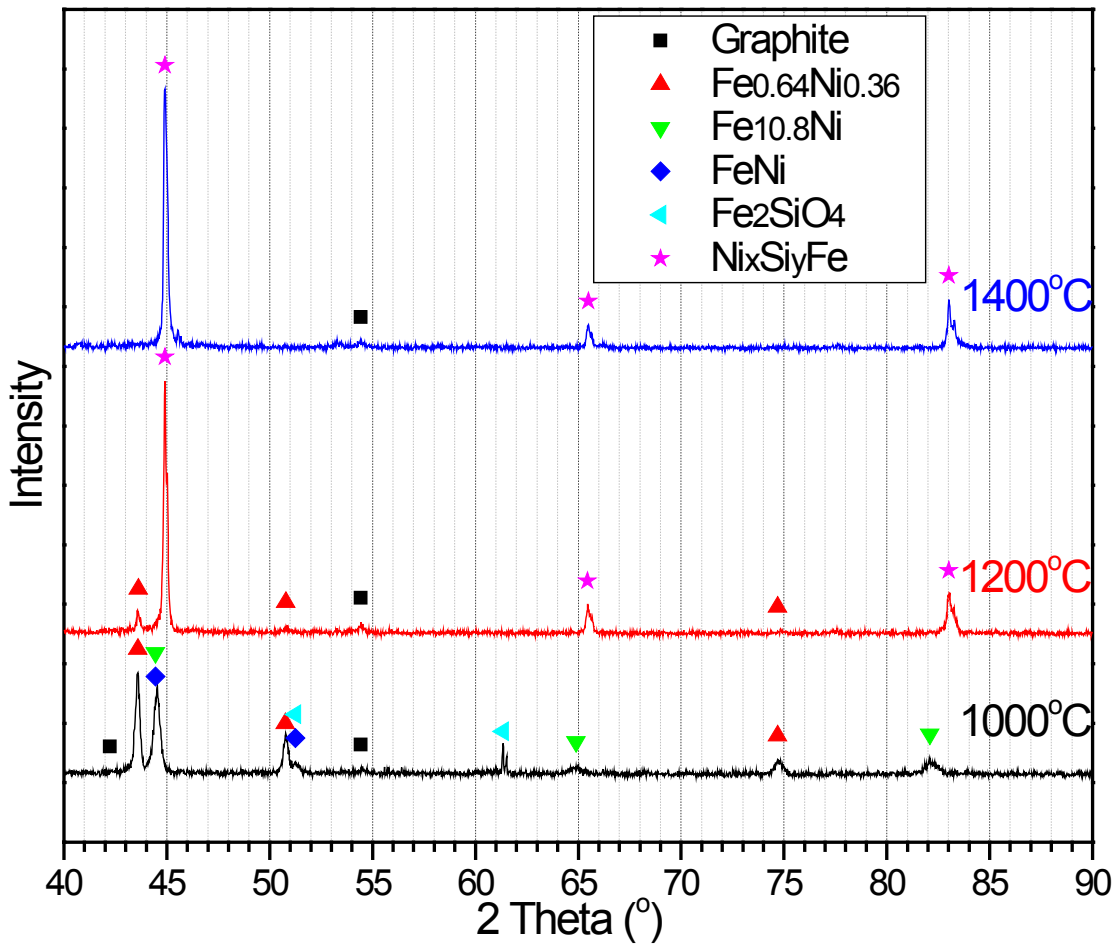

Figure 6.41. XRD analysis on the product from the reduction at 1000 ºC, 1200 ºC and 1400 ºC.

6.4 Conclusions

Reduction of the leach residue by hydrogen, carbon monoxide and graphite was conducted using TGA and DTA. The reduced products were analyzed by SEM/EDS, EPMA and XRD. Effective reduction of the residue by H_2 could only be achieved with the temperature above around 350 ºC. At low temperatures (350–600 ºC), the reduction rate is low and is controlled by the chemical reactions. Reduction occurred in a non-topochemical mode. Above 600 ºC and up to 1200 ºC, the reduction is faster and is controlled by the combination of gas diffusion through the solid product layer of individual particles and gas diffusion through the pores of the sample bed. The formed ferronickel alloy was sintered at around 1100 ºC. The silicate materials in the sample melted at 1200 ºC and greatly reduced the porosity of the sample, resulting in substantial reduction of the reaction rate. The reduction could be accelerated by increasing the partial pressure of H_2 with the reaction order (n) of 1.4. Apparent activation energies of the two reaction regimes were 64.7 kJ/mol below 600 ºC and 34.1 kJ/mol for 600–1200 ºC.

Reduction by CO initiated at around 400 ºC during the continuous heating tests. The reduction of the hematite phase took place in two stages with magnetite as the intermediate products. Nickel ferrite was reduced mostly in between 520 and 800 ºC resulting in the formation of an alloy phase $Fe_{0.64}Ni_{0.36}$. Significant sintering of the alloys was observed above 800 ºC, and the extent of the sintering was greater at higher temperatures. Below 1200 ºC, the isothermal reduction was firstly controlled by the gaseous diffusion in the pores of the sample bed. More alloy products formed with the progress of reduction, resulting in the gradual shift of the rate-controlling mechanism to the diffusion through the alloy products in individual particles. This change of rate-controlling mechanism led to the increase of the apparent of activation energies from 6.7 kJ/mol (α=0.2) to 41.1 kJ/mol (α=0.9). The siliceous gangue melted at 1200 ºC, which caused the partial dissolution of hematite into the silicate melt and removal of pores from the sample bed. This resulted in slow reduction kinetics.

Substantial reduction of the leach residue by graphite powder took place only above 1000 ºC. The formation of CO or CO_2 as the main gaseous product is largely dependent on temperature, and is suggested to be dominantly influenced by the Boudouard reaction. The Fe and Si

components of the silicates could be reduced by graphite above their melting temperature (1200 ºC) forming an Fe-Si alloy. The alloys formed from the reduction of hematite, nickel ferrite or silicates tend to be more homogeneous at higher temperatures resulting from the enhanced merging of the alloy particles.

6.5 References

[1] D. Yu, T.A. Utigard, M. Barati, Fluidized Bed Selective Oxidation-Sulfation Roasting of Nickel Sulfide Concentrate: Part I. Oxidation Roasting, Metallurgical and Materials Transactions B, 2013, DOI: 10.1007/s11663-013-9958-x.

[2] D. Yu, T.A. Utigard, M. Barati, Fluidized Bed Selective Oxidation-Sulfation Roasting of Nickel Sulfide Concentrate: Part II. Sulfation Roasting, Metallurgical and Materials Transactions B, 2013, DOI: 10.1007/s11663-013-9959-9.

[3] D. Yu, M. Zhu, T.A. Utigard, M. Barati, TGA Kinetic Study on the Hydrogen Reduction of an Iron Nickel Oxide, Minerals Engineering, 54 (2013) 32-38.

[4] O.J. Wimmers, P. Arnoldy, J.A. Moulijn, Determination of the Reduction Mechanism by Temperature-Programmed Reduction: Application to Small Fe_2O_3 Particles, Journal of Physical Chemistry, 90 (1986) 1331-1337.

[5] A.J.H.M. Kock, H.M. Fortuin, J.W. Geus, The Reduction Behavior of Supported Iron Catalysts in Hydrogen or Carbon Monoxide Atmospheres, Journal of Catalysis, 96 (1985) 261-275.

[6] H.-Y. Lin, Y.-W. Chen, C. Li, The mechanism of reduction of iron oxide by hydrogen, Thermochimica Acta, 400 (2003) 61-67.

[7] W.K. Jozwiak, E. Kaczmarek, T.P. Maniecki, W. Ignaczak, W. Maniukiewicz, Reduction behavior of iron oxides in hydrogen and carbon monoxide atmospheres, Applied Catalysis A: General, 326 (2007) 17-27.

[8] A. Pineau, N. Kanari, I. Gaballah, Kinetics of reduction of iron oxides by H_2 Part I: Low temperature reduction of hematite, Thermochimica Acta, 447 (2006) 89-100.

[9] P. Pourghahramani, E. Forssberg, Reduction kinetics of mechanically activated hematite concentrate with hydrogen gas using nonisothermal methods, Thermochimica Acta, 454 (2007) 69-77.

[10] J. Zielinski, I. Zglinicka, L. Znak, Z. Kaszkur, Reduction of Fe_2O_3 with hydrogen, Applied Catalysis A: General, 381 (2010) 191-196.

[11] B. Weiss, J. Sturn, S. Voglsam, F. Winter, J. Schenk, Industrial fluidised bed direct reduction kinetics of hematite ore fines in H_2 rich gases at elevated pressure, Chemical Engineering Science, 66 (2011) 703-708.

[12] C. Feilmayr, A. Thurnhofer, F. Winter, H. Mali, J. Schenk, Reduction Behavior of Hematite to Magnetite under Fluidized Bed Conditions, ISIJ International, 44 (2004) 1125-1133.

[13] J.-m. Pang, P.-m. Guo, P. Zhao, C.-z. Cao, D.-w. Zhang, Influence of Size of Hematite Powder on Its Reduction Kinetics by H_2 at Low Temperature, Journal of Iron and Steel Research, International, 16 (2009) 07-11.

[14] K. Piotrowski, K. Mondal, H. Lorethova, L. Stonawski, T. Szymanski, T. Wiltowski, Effect of gas composition on the kinetics of iron oxide reduction in a hydrogen production process, International Journal of Hydrogen Energy, 30 (2005) 1543-1554.

[15] M. Bahgat, M.-K. Paek, J.-J. Pak, Reduction Kinetics and Mechanisms of $NiFe_2O_4$ with Synthesis of Nanocrystalline Fe-Ni Alloy, Materials Transactions, JIM, 48 (2007) 3132-3139.

[16] M.H. Khedr, Isothermal reduction kinetics at 900-1100ºC of $NiFe_2O_4$ sintered at 1000-1200ºC, Journal of Analytical and Applied Pyrolysis, 73 (2005) 123-129.

[17] K. Shimakage, T. Ejima, S. Morioka, The Hydrogen Reduction of Synthertic Nickelferrite, Transactions of the Japan Institute of Metals, 11 (1970) 335-345.

[18] M.O. Boudouard, Recherches sur les equilibres chimiques, Annales De Chimie Et De Physique, 24 (1901) 1-85.

[19] R. Haque, H.S. Ray, Role of Ore/Carbon Contact and Direct Reduction in the Reduction of Iron Oxide by Carbon, Metallurgical and Materials Transactions B, 26B (1995) 400-401.

[20] M.S. Bafghi, M. Fukuda, Y. Ito, S. Yamada, M. Sano, Effect of CO Gas Formation on Reduction Rate of Iron Oxide in Molten Slag by Graphite, ISIJ International, 33 (1993) 1125-1130.

[21] J. Moon, V. Sahajwalla, Investigation into the Role of the Boudouard Reaction in Self-Reducing Iron Oxide and Carbon Briquettes, Metallurgical and Materials Transactions B, 37B (2006) 215-221.

[22] K. Mondal, H. Lorethova, E. Hippo, T. Wiltowski, S.B. Lalvani, Reduction of iron oxide in carbon monoxide atmosphere - reaction controlled kinetics, Fuel Processing Technology, 86 (2004) 33-47.

[23] S.K. Sharma, F.J. Vastola, J. P.L. Walker, Reduction of nickel oxide by carbon: I. Interaction between nickel oxide and pyrolytic graphite, Carbon, 34 (1996) 1407-1412.

[24] S.K. Sharma, F.J. Vastola, J. P.L. Walker, Reduction of nickel oxide by carbon: II. Interaction between nickel oxide and natural graphite, Carbon, 35 (1997) 529-533.

[25] S.K. Sharma, F.J. Vastola, J. P.L. Walker, Reduction of nickel oxide by carbon: III. Kinetic studies of the interaction between nickel oxide and natural graphite, Carbon, 35 (1997) 535-541.

[26] A. Roine, HSC Chemistry, Outokumpu Research Oy, Pori, Finland, 2007.

[27] D. Yu, T.A. Utigard, TG/DTA study on the oxidation of nickel concentrate, Thermochimica Acta, 533 (2012) 56-65.

[28] P.G. Thornhill, L.M. Pidgeon, Micrographic Study of Sulfide Roasting, Journal of Metals, 9 (1957) 989-995.

[29] S. Vyazovkin, A.K. Burnham, J.M. Criado, L.A. Perez-Maqueda, C. Popescu, N. Sbirrazzuoli, ICTAC Kinetics Committee recommendations for performing kinetic computations on thermal analysis data, Thermochimica Acta, 520 (2011) 1-19.

[30] A. Khawam, D.R. Flanagan, Role of isoconversional methods in varying activation energies of solid-state kinetics I. isothermal kinetic studies, Thermochimica Acta, 429 (2005) 93-102.

[31] G.C. Ulmer, W.C. Elliott, T. Buntin, J. Edwin S. Erickson, J.J. Friel, Role of Selected Cations and Gas Speciation on the Reduction of Fayalite at 1300ºC, Journal of the American Ceramic Society, 75 (1992) 1476-1483.

[32] S. Vyazovkin, Kinetic concepts of thermally stimulated reactions in solids: A view from a historical perspective, International Reviews in Physical Chemistry, 19 (2000) 45-60.

[33] A.K. Galwey, What is meant by the term ‘variable activation energy’ when applied in the kinetic analyses of solid state decompositions (crystolysis reactions)?, Thermochimica Acta, 397 (2003) 249-268.

[34] A. Khawam, D.R. Flanagan, Solid-State Kinetic Models: Basics and Mathematical Fundamentals, The Journal of Physical Chemistry B, 110 (2006) 17315-17328.

[35] C.J.B. Crowe, T.A. Utigard, Kinetics of Carbon Monoxide Reduction of Oxidized Calcines, Canadian Metallurgical Quarterly, 42 (2003) 447-454.

7 Summary and Conclusions

7.1 Mass and Heat Balance

A mass and heat balance calculation was performed using HSC Chemistry [1] for three stages of the process, i.e. oxidation roasting of the Raglan concentrate, sulfation roasting of the oxidation roasted calcine, and reduction of the leach residue. The results are shown in Table 7.1, Table 7.2 and Table 7.3, respectively. For the oxidation roasting stage, Raglan concentrate of 100 kg was used as the starting material. Stoichiometric amount of air was used to preferentially oxidize the Raglan concentrate at 600 ºC to produce a calcine of a similar chemical composition as that obtained in the oxidation roasting experiments. Formation of small amounts of sulfates was also taken into account in the calculation process as shown in Table 7.1. The BALANCE of mass (in kg) in Table 7.1 is zero, indicating that the mass balance was performed correctly. For the calculation of heat balance, thermodynamic data for all the species involved is available in the database of HSC Chemistry [1], except that for pentlandite. The standard enthalpy of formation for pentlandite of -(837.37±14.59) kJ/mol [2] was used. The heat capacity of pentlandite at 298.15 K is 442.7 J/mol·K [3], which was used for the calculation at high temperatures since no heat capacity at higher temperature is available. As can be seen, heat of a total of 267.79 MJ is released from the processing of 100 kg concentrate. This balance of heat should be absorbed to prevent the overheating of the fluidized bed in an industrial setting. This could be done by mixing the concentrate with water to make a slurry as the feed to the fluidized bed roaster, which has been a common practice in the industry. Such a practice could also alleviate the entrainment of dust into the offgas. By calculation, the amount of heat released from roasting of 100 kg concentrate could form 103.66 kg steam from water at 25 ºC. This suggests that the slurry of feed could be made with the concentrate to water ratio of 1:1 to achieve a constant temperature of the fluidized bed. Alternatively, the excessive amount of heat could also be absorbed by inserting water coolants into the fluidized bed to recover the heat by making steam. As to the mass balance of sulfur which accounts for 29.39 wt% of the Raglan concentrate, the degree of sulfur elimination in the oxidation roasting stage is 56.1 wt%, the remaining 43.9 wt% being in the calcine in the form of sulfides and sulfates.

Table 7.1. Mass and heat balance for the oxidation roasting of 100 kg Raglan concentrate.

INPUT						
Raglan concentrate 100kg	Temperature (ºC)	Amount (kmol)	Amount (kg)	Amount (Nm^3)	Latent H (MJ)	Total H (MJ)
$Fe_{4.5}Ni_{4.5}S_8$	25.0	0.070	53.94	0.000	0.00	-58.51
$Fe_{4.5}Co_{4.5}S_8$	25.0	0.001	1.08	0.000	0.00	-1.17
Fe_7S_8	25.0	0.025	16.11	0.000	0.00	-18.32
$CuFeS_2$	25.0	0.074	13.53	0.003	0.00	-14.04
Mg_2SiO_4	25.0	0.069	9.77	0.003	0.00	-151.17
Al_2SiO_5(S)	25.0	0.008	1.24	0.000	0.00	-19.81
SiO_2	25.0	0.072	4.33	0.002	0.00	-65.65
Air						
O_2(g)	25.0	1.147	36.69	25.700	0.00	0.00
N_2(g)	25.0	4.313	120.84	96.681	0.00	0.00
Total input	N/A	5.779	257.53	122.389	0.00	-328.67

OUTPUT						
Calcine	Temperature (ºC)	Amount (kmol)	Amount (kg)	Amount (Nm^3)	Latent H (MJ)	Total H (MJ)
Fe_2O_3	600.0	0.284	45.40	0.009	22.40	-211.59
NiS	600.0	0.252	22.83	0.004	9.40	-12.70
CoS	600.0	0.004	0.35	0.000	0.12	-0.26
Cu2S	600.0	0.034	5.40	0.001	1.93	-0.76
Mg_2SiO_4	600.0	0.049	6.84	0.002	4.28	-101.54
$NiSO_4$	600.0	0.063	9.73	0.002	4.68	-50.21
$CoSO_4$	600.0	0.002	0.38	0.000	0.19	-1.99
$CuSO_4$	600.0	0.006	0.94	0.000	0.45	-4.10
$MgSO_4$	600.0	0.042	5.02	0.002	2.99	-49.59
Al_2SiO_5(S)	600.0	0.008	1.24	0.000	0.73	-19.07
SiO_2	600.0	0.093	5.58	0.002	3.41	-81.21
Offgas						
O_2(g)	600.0	0.001	0.02	0.015	0.01	0.01
N_2(g)	600.0	4.313	120.84	96.681	74.90	74.90
SO_2(g)	600.0	0.515	32.96	11.532	14.37	-138.34
Total output	N/A	5.664	257.53	108.251	139.87	-596.46
BALANCE	N/A	-0.115	0.00	-14.138	139.87	-267.79

The calcine produced from the above oxidation roasting stage was used at 25 ºC as part of the input for the mass and heat balance calculation of the sulfation roasting stage, as shown in Table 7.2. In reality, calcine produced from the oxidation roasting stage could be directly fed to the sulfation roasting stage before its temperature drops substantially, for the sake of energy conservation. Na_2SO_4 was also added for sulfation roasting with the concentrate to Na_2SO_4 weight ratio of 10:1. The offgas from the oxidation roasting stage which has 10.7 vol% SO_2 could be used as the feed gas for the sulfation roasting stage. In order to achieve a preferable sulfation condition and to produce an offgas from the sulfation roasting stage with a SO_2 concentration high enough for acid making, this offgas is mixed with 96% oxygen (balance nitrogen) instead of air as the feed gas. Sulfation roasting was assumed to take place at 700 ºC. Solid product from the sulfation roasting is the calcine containing sulfates, oxides and silicates, the amounts of which were calculated based on the metal recoveries in the experiments. As to the balance of sulfur, 17.1 vol% of the SO_2 in the feed gas forms sulfates in the sulfation roasting stage, and 46.5 wt% of total sulfur remains as SO_2 and SO_3, the rest being in the sulfation roasted calcine. The concentrations of O_2, SO_2, and SO_3 in the offgas in the OUTPUT were calculated based on their thermodynamic equilibrium at 700 ºC. The calculated concentrations of SO_2 and SO_3 in the offgas are 4.1 vol% and 4.8 vol%, respectively. This relatively high concentration of SO_3 in the offgas will cause possible operational and maintenance problems of the offgas handling system, such as plugging and corrosion, which necessitates the special design of the offgas handling system to cope with the possible issues. In terms of heat balance, total heat of 182.37 MJ is produced from the sulfation roasting stage when 100kg concentrate is processed. This heat could be absorbed either by making slurry as the solid feed or by applying water coolants in the fluidized bed.

Table 7.2. Mass and heat balance for the sulfation roasting stage.

INPUT						
Calcine from oxidation roasting	Temperature (ºC)	Amount (kmol)	Amount (kg)	Amount (Nm^3)	Latent H (MJ)	Total H (MJ)
Fe_2O_3	25.0	0.284	45.40	0.009	0.00	-234.00
NiS	25.0	0.252	22.83	0.004	0.00	-22.10
CoS	25.0	0.004	0.35	0.000	0.00	-0.38
Cu_2S	25.0	0.034	5.40	0.001	0.00	-2.70
Mg_2SiO_4	25.0	0.049	6.84	0.002	0.00	-105.82
$NiSO_4$	25.0	0.063	9.73	0.002	0.00	-54.90

$CoSO_4$	25.0	0.002	0.38	0.000	0.00	-2.18
$CuSO_4$	25.0	0.006	0.94	0.000	0.00	-4.55
$MgSO_4$	25.0	0.042	5.02	0.002	0.00	-52.57
$Al_2SiO_5(S)$	25.0	0.008	1.24	0.000	0.00	-19.81
SiO_2	25.0	0.093	5.58	0.002	0.00	-84.62
Addition of Na_2SO_4						
Na_2SO_4	25.0	0.073	10.37	0.004	0.00	-101.34
Offgas from oxidation roasting						
$O_2(g)$	600.0	0.001	0.02	0.015	0.01	0.01
$N_2(g)$	600.0	4.313	120.84	96.681	74.90	74.90
$SO_2(g)$	600.0	0.515	32.96	11.532	14.37	-138.34
96% oxygen to be mixed with the offgas for sulfation roasting						
$O_2(g)$	25.0	0.772	24.70	17.298	0.00	0.00
$N_2(g)$	25.0	0.032	0.90	0.721	0.00	0.00
Total input	N/A	6.541	293.49	126.273	89.28	-748.38

OUTPUT						
Sulfation roasted calcine	Temperature (ºC)	Amount (kmol)	Amount (kg)	Amount (Nm^3)	Latent H (MJ)	Total H (MJ)
Fe_2O_3	700.0	0.204	32.54	0.006	19.53	-148.18
$NiFe_2O_4$	700.0	0.067	15.77	0.000	0.00	-72.75
CuO	700.0	0.007	0.53	0.000	0.23	-0.82
CoO	700.0	0.001	0.04	0.000	0.02	-0.11
Mg_2SiO_4	700.0	0.009	1.24	0.000	0.93	-18.27
$Al_2SiO_5(S)$	700.0	0.004	0.73	0.000	0.51	-11.07
SiO_2	700.0	0.136	8.16	0.003	5.92	-117.84
$Fe_2(SO_4)_3$	700.0	0.013	5.30	0.002	3.21	-31.04
$NiSO_4$	700.0	0.247	38.25	0.010	22.09	-193.65
$CuSO_4$	700.0	0.067	10.70	0.003	6.09	-45.61
$CoSO_4$	700.0	0.006	0.89	0.000	0.55	-4.53
$MgSO_4$	700.0	0.121	14.59	0.005	10.48	-142.51
$Al_2(SO_4)_3$	700.0	0.003	1.09	0.000	0.79	-10.14
Na_2SO_4	700.0	0.073	10.37	0.004	9.33	-92.00
Offgas from sulfation roasting						
$O_2(g)$	700.0	0.019	0.60	0.417	0.40	0.40
$SO_2(g)$	700.0	0.198	12.68	4.437	6.61	-52.15
$SO_3(g)$	700.0	0.228	18.28	5.118	10.42	-79.95
$N_2(g)$	700.0	4.346	121.74	97.402	89.46	89.46
Total output	N/A	5.749	293.49	107.407	186.58	-930.75
BALANCE	N/A	-0.793	0.00	-18.866	97.30	-182.37

The water-insoluble part of the sulfation roasted calcine produced from above was assumed as the water-leach residue for the mass and heat balance calculation of its reduction by CO. A stoichiometric amount of CO was used for reduction. The reduction temperature was assumed as 1250 ºC which is 33 ºC higher than the melting point of fayalite (*FeO*SiO_2). The grade of Fe-Ni alloy formed would be higher because part of the iron oxide would form molten slag phase as observed in the experiments. The reduction requires an energy input of 93.62 MJ per 100 kg concentrate processed. This energy input could be in the form of incomplete combustion of fuel (e.g. oil, coke) which provides both heat and reductant for the reduction process.

Table 7.3. Mass and heat balance for the reduction of the leach residue with CO.

INPUT						
Leach residue	Temperature (ºC)	Amount (kmol)	Amount (kg)	Amount (Nm^3)	Latent H (MJ)	Total H (MJ)
Fe_2O_3	25.0	0.217	34.66	0.007	0.00	-178.62
$NiFe_2O_4$	25.0	0.067	15.77	0.000	0.00	-72.75
CuO	25.0	0.007	0.53	0.000	0.00	-1.05
CoO	25.0	0.001	0.04	0.000	0.00	-0.13
Mg_2SiO_4	25.0	0.009	1.24	0.000	0.00	-19.20
Al_2SiO_5(S)	25.0	0.004	0.73	0.000	0.00	-11.59
SiO_2	25.0	0.136	8.16	0.003	0.00	-123.76
Reductant						
CO(g)	25.0	0.656	18.37	14.699	0.00	-72.49
Total input	N/A	1.097	79.51	14.709	0.00	-479.58

OUTPUT						
Solid	Temperature (ºC)	Amount (kmol)	Amount (kg)	Amount (Nm^3)	Latent H (MJ)	Total H (MJ)
Fe	1250.0	0.297	16.58	0.002	13.83	13.83
Ni	1250.0	0.067	3.95	0.000	2.69	2.69
Cu	1250.0	0.007	0.43	0.000	0.32	0.32
Co	1250.0	0.001	0.03	0.000	0.03	0.03
Mg_2SiO_4	1250.0	0.009	1.24	0.000	1.80	-17.39
Al_2SiO_5(S)	1250.0	0.004	0.73	0.000	1.01	-10.57
2FeOSiO_2	1250.0	0.136	27.69	0.006	42.80	-158.17
Offgas						
CO_2(g)	1250.0	0.656	28.86	14.699	41.37	-216.69
Total output	N/A	1.176	79.51	14.708	103.85	-385.96
BALANCE	N/A	0.080	0.00	-0.001	103.85	93.62

7.2 Conclusions

Selective oxidation and sulfation roasting followed by leaching was proposed and investigated as an alternative route to the conventional roasting–electric furnace smelting–converting route for nickel processing. The oxidation roasting stage of the innovative process was intended to preferentially oxidize the iron species from the nickel concentrate forming iron oxides. The sulfides of non-ferrous metals (Ni, Cu and Co) were then selectively converted to water-soluble sulfates for further leaching either by water or acid.

In order to achieve preferential oxidation of the iron species, the roasting mechanism of the nickel concentrate was firstly studied by means of TGA and DTA. Roasting products from intermediate temperatures were analyzed by various techniques, such as SEM/EDS, XRD, EPMA, and ICP, to help elucidate the reaction scheme. It was found that due to the complex mineralogy of the nickel concentrate and the heterogeneous nature of the roasting reactions, various reactions involving a large variety of intermediate compounds as well as phase changes could take place, such as the low temperature thermal decomposition of pentlandite (350–550 ºC), preferential oxidation of iron sulfide species (<700 ºC), transformation of nickel sulfide core from $Ni_{1-x}S$ to $Ni_{3\pm x}S_2$ (730 ºC), melting of nickel sulfide core (813 ºC), and sulfate formation and decomposition at various temperatures. The reaction rate was found to be controlled by the gas diffusion downward through the sample bed.

In order to gain more understanding of a possible industrial roasting practice, a laboratory scale fluidized bed roster which is operated in a batch mode was constructed for oxidation and sulfation roasting experiments. It was found that the oxidation roasting in a fluidized bed starts with the preferential oxidation of iron sulfide species forming iron oxides until the content of Fe in the pentlandite sulfide cores drops to ~2 at%. The remaining nickel sulfide core in the pentlandite particles is either NiS or Ni_3S_2 depending on the roasting temperature. Formation of sulfates of Ni and Co occurs after the oxidation of iron sulfide. Low temperature (e.g. 650 °C) is favorable for the preferential oxidation of iron sulfide species while minimizing the formation of nickel ferrite. Unlike the oxidation of iron sulfide, the oxidation of Co species through diffusion

is a slow process. The oxidation of the nickel sulfide core Ni_3S_2 is the last step if the roasting temperature is high enough.

Selective sulfation roasting of the oxidation roasted calcine was further studied in the fluidized bed roaster with the evaluation of several parameters. It was concluded that among the parameters evaluated, the addition of Na_2SO_4 as catalyst was most effective in enhancing sulfate formation. Under optimized conditions of sulfation gas composition (95% air, 5% SO_2), temperature (700 °C), Na_2SO_4 addition (10 wt%) and time (150 min), 79% Ni, 91% Cu, and 91% Co were converted to water-soluble sulfates. Iron sulfate formation was only 5%. A sulfation mechanism was suggested. A high partial pressure of SO_3 is maintained within each particle due to the formation of sulfate melt on the surface, favoring sulfate formation. The conversion of the nickel sulfide core to sulfate is direct without preliminary formation of NiO as an intermediate product. Another important finding was that the sustained conversion to $NiSO_4$ is due to the unique morphology of the $NiSO_4$ formed, which is the micro-grain structure with cracks and crevices which allowed the sulfation to proceed to near completion by providing channels for the inner diffusion of sulfation gas to the sulfide surface.

Leach residue from the optimized oxidation–sulfation roasting test is mainly composed of hematite (Fe_2O_3) and nickel ferrite ($NiFe_2O_4$), which could be a superior feedstock for the production of ferronickel. The feasibility of producing ferronickel by pyro-reduction of the leach residue with H_2, CO and graphite was evaluated by means of TGA and DTA. It was found that at low temperatures (350–600 ºC), the reduction rate is governed by chemical reactions when using H_2 as reductant. The rate controlling step becomes mixed control of gas diffusion through the solid product layer of individual particles and gas diffusion through the sample bed at higher temperatures. The formed alloys experienced significant sintering at temperatures higher than 1100 ºC. When using CO as the reductant, sintering of the products took place at temperatures as low as 800 ºC. A shift of the rate controlling mechanism from gas diffusion through the pores of the sample bed to gas diffusion through the product layer in individual particles were observed for the isothermal reduction tests below 1200 ºC, resulting in a variation of apparent activation energies with the extent of reduction. Melting of the siliceous materials in the residue at 1200 ºC greatly hindered the reduction process by substantially reducing the porosity of the sample bed. Temperatures higher than 1000 ºC are required to initiate effective

reduction by graphite. The molten silicate (>1200 ºC) can be reduced by graphite to form Si-containing alloys.

Calcines were also leached by hot water and HCl to study their leaching behavior. It was concluded that hot water leaching at 90 ºC for 30 minutes is effective to dissolve all sulfates from the calcines. In order to increase of the recovery of the non-ferrous metals, acid leaching is beneficial. However, less selectivity is observed with acid leaching because substantial iron oxides can also be dissolved.

7.3 References

[1] A. Roine, HSC Chemistry, Outokumpu Research Oy, Pori, Finland, 2007.

[2] L. Cemič, O.J. Kleppa, High temperature calorimetry of sulfide systems, Phys Chem Minerals, 14 (1987) 52-57.

[3] G.A. Berezovskii, V.A. Drebushchak, T.A. Kravchenko, Low-temperature heat capacity of pentlandite, American Mineralogist, 86 (2001) 1312-1313.

8 Proposed Flow Sheet

Based on this study, a flow sheet was proposed for the two-stage fluidized bed selective oxidation and sulfation roasting of nickel sulfide concentrate, which is illustrated in Figure 8.1. It involves two fluidized bed roasters in series, one for oxidation and the other for sulfation. As suggested from the Mass and Heat Balance Section (Section 7.1), offgas from the oxidation roasting stage could be used after mixing with 96% oxygen as the feed gas for the sulfation roasting stage. And the offgas from the sulfation roasting stage could be used for acid making. Na_2SO_4 solution which is recycled from the hydrometallurgical stream should be mixed with the oxidation roasted calcine to make a slurry before being fed to the sulfation roaster. The latent heat of the hot calcine produced from the oxidation roasting stage (600 ºC) could be utilized to concentrate the diluted Na_2SO_4 solution by vaporizing some of the water content, so that the water content of the slurry is just enough to absorb the heat released from the sulfation roasting stage (Please refer to the Mass and Heat Balance Section 7.1). Heat scavenged from the oxidation roasting stage could also be utilized for the concentration of the Na_2SO_4 solution. The hot calcine produced from the sulfation roasting stage can be quenched by water to render quick dissolution of sulfates. After leaching, valuable metals could be separated and recovered by standard hydrometallurgical methods, e.g. ion exchange, solvent extraction, and electrowinning, after Fe removal. The portion of the precious metals that is leached into water could form concentrated precious metal sludge during electrowinning. The method for the recovery of these precious metals from the sludge has been well established in the industry. The diluted sulfuric acid produced from the electrowinning process could be neutralized by adding limestone to make gypsum ($CaSO_4 \cdot 2H_2O$). Na_2SO_4 could be recovered from the solution and recycled back to the sulfation roasting stage. The leach residue which contains mainly hematite and nickel ferrite is used for the production of ferronickel alloys by pyro-reduction. One possible way of recovering the precious metals from the leach residue is by partial reduction of the leach residue so that the precious metals could be enriched in the metallic part.

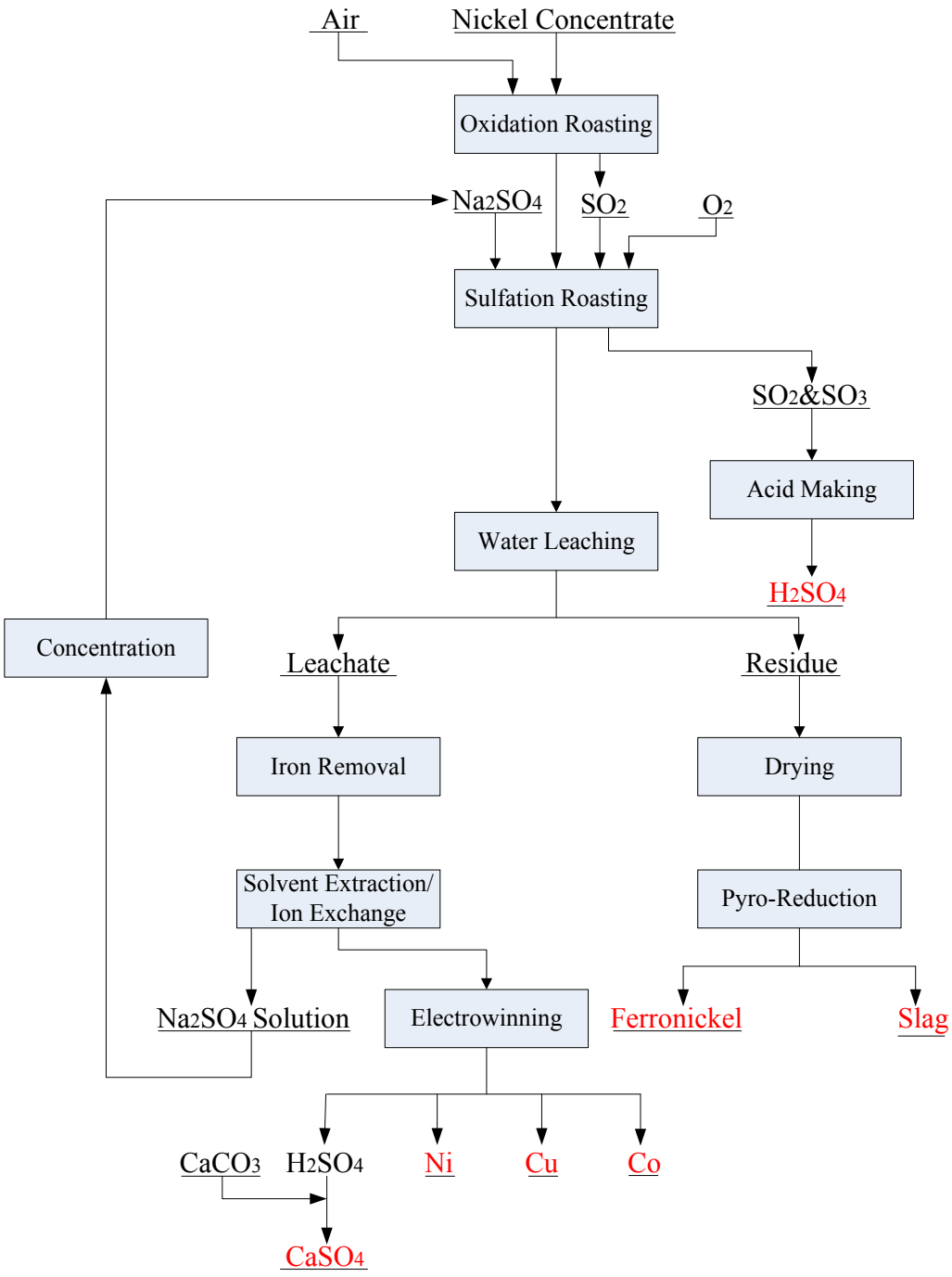

Figure 8.1. Proposed flow sheet for the selective oxidation and sulfation roasting of nickel concentrate.

In the conventional pyrometallurgical process to treat nickel concentrate, the iron species end up in molten slags in various stages. In comparison, the iron component of the nickel concentrate is utilized to form final product, i.e. ferronickel alloy, in this proposed process. Thus maximum

utilization of the raw material is achieved, which is of great significance in terms of both the economic aspect and approaching sustainability of the mining and metallurgical industries. SO_2 emission from this process could be minimal since offgas with strong SO_2 is produced from the sulfation roaster, which makes it suitable for acid making. The consumption of electric energy could also be greatly reduced. Pyro-reduction of the leach residue requires energy input, either from electric energy or from combustion of fossil fuels. However, this energy input should be much lower compared with the energy requirement of an electric furnace (EF) in the conventional roasting–electric furnace smelting–converting process. This is because it can be operated at much lower temperatures (~800 ºC) compared with the conventional EF smelting practice (~1500 ºC). In addition, for the processing of one tonne of nickel concentrate in both the conventional route and the proposed selective oxidation-sulfation roasting route, the mass of the leach residue for reduction is much smaller than that of the feed to the EF furnace, meaning much less energy is required.

By directly addressing the sustainability issues in three aspects, i.e. materials, environment, and energy, this innovative process should be more sustainable compared with the conventional pyrometallurgical route for nickel production.

Appendices

Appendix 01: C Code for the Calculation of Enthalpy Change during the Roasting of the Raglan Concentrate as a Function of Temperature

```
/*
  This program performs the following functions:
  1. Read the csv file which contains one column of numerical values and convert them to
double values;
  2. Process the data according to the function, which calculate the enthalpy change for the
following reactions:
     1) 1Fe4.5Ni4.5S8 + 8.375O2 = 2.25Fe2O3 + 1.5Ni3S2 + 5SO2
     2) 1Fe7S8 + 13.25O2 = 3.5Fe2O3 + 8SO2
     3) 1CuFeS2 + 3.25O2 = 0.5Fe2O3 + 1CuO + 2SO2
     According to the mineralogy of the Raglan concentrate, the molar ratios of these three
minerals are:
     Pn:Py:Cpy=1 : 0.349180273 : 1.034034368
     The molar ratio of the total SO2 formed to the minerals are:
     SO2:Pn:Py:Cpy=(1*5+0.349180273*8+1.034034368*2) : 1 : 0.349180273 : 1.034034368
                =9.86151092: 1 : 0.349180273 : 1.034034368

  3. Write the data produced into a new csv file.
*/

#include <string.h>
#include <stdlib.h>
#include <math.h>
#include <stdio.h>
#include <graphics.h>
#include <conio.h>
double function(double a);
double pn(double T);
double o2(double T);
double fe2o3(double T);
double ni3s2(double T);
double so2(double T);
double py(double T);
double cpy(double T);
double cuo(double T);

void main()
{
FILE *fp, *fp2;
int i=5, indicator_row=0, indicator_column=0;
double buff;
```

```
char t, temp[50], pathread[50], pathwrite[50], *p, *end;

printf("This program performs the following functions:\n1. Read the csv file which contains one
column of numerical values and convert them to double values;\n2. Process the data according
to the function;\n3. Write the data produced into a new csv file.\n--Dawei Yu, March 3rd,
2012\n");
looppath:
printf("Please input the path of the source file here.\n You have %d time(s):",i);
scanf("%s",pathread);
clrscr();
fp=fopen(pathread,"r");
if(fp!=NULL)
printf("\n\n\nFile is opened successfully!\n");
else
  {i--;
   printf("File is not open! Please check the path!\n");
   if(i>=1) goto looppath;
   else goto end;
  }

printf("Please input the directory of the csv file which contains the results:");
scanf("%s",pathwrite);

fp2=fopen(pathwrite,"w");

FLAG:

/*initialize the temp[50]*/
for(i=0;i<50;i++)
 temp[i]='\0';

  for(i=0,t=fgetc(fp);!feof(fp)&&i<50;t=fgetc(fp),i++)
    {

     if(t!=','&&t!='\n') temp[i]=t;
     if(t==',') {indicator_column=1; break;}
     if(t=='\n') {indicator_row=1; break;}

    }

buff=function(strtod(temp,&end));

/*initialize the temp[50]*/
for(i=0;i<50;i++)
 temp[i]='\0';

sprintf(temp,"%lf",buff);
```

```
p=temp;

while((*p!='\0')&&fputc(*(p++),fp2)!=EOF);

if(indicator_column==1) fputc(',',fp2);
else if(indicator_row==1) fputc('\n',fp2);

indicator_column=0;
indicator_row=0;

if(!feof(fp)) goto FLAG;
else goto end;

end: fclose(fp);
    fclose(fp2);
    printf("\nDONE!\n");
    getch();
}


double function(double T)
{
double Enthalpy;
/*
    1) 1Fe4.5Ni4.5S8 + 8.375O2 = 2.25Fe2O3 + 1.5Ni3S2 + 5SO2
    2) 1Fe7S8 + 13.25O2 = 3.5Fe2O3 + 8SO2
    3) 1CuFeS2 + 3.25O2 = 0.5Fe2O3 + 1CuO + 2SO2
    Pn:Py:Cpy=1 : 0.349180273 : 1.034034368
*/

Enthalpy=1*(2.25*fe2o3(T)+1.5*ni3s2(T)+5.0*so2(T)-1.0*pn(T)-
8.375*o2(T))+0.349180273*(3.5*fe2o3(T)+8.0*so2(T)-1.0*py(T)-
13.25*o2(T))+1.034034368*(0.5*fe2o3(T)+1.0*cuo(T)+2*so2(T)-1.0*cpy(T)-3.25*o2(T));

return Enthalpy;
}

double pn(double T)
{
 double En;
 En=-837.37+0.4427*(T-298.15);
 return En;
}

double o2(double T)
{
```

```
  double T2, En, a[2][6]={{22.060,20.887,1.621,-8.207,298.150,700.0},{29.793,7.910,-6.194,-
2.204,700,1200}};
int i, flag=0;

En=0.00;
 for(i=0;i<2;i++)
  {
   if(T<=a[i][5])T2=T, flag=1;
   else T2=a[i][5];
  En=En+1e-3*((a[i][0]*T2+a[i][1]*1e-3/2*pow(T2,2)-a[i][2]*1e5/T2+a[i][3]*1e-
6/3*pow(T2,3))-(a[i][0]*a[i][4]+a[i][1]*1e-3/2*pow(a[i][4],2)-a[i][2]*1e5/a[i][4]+a[i][3]*1e-
6/3*pow(a[i][4],3)));
if(flag==1) break;
else ;
  }

return En;
}

double so2(double T)
{
  double T2, En, a[2][6]={{29.134,37.222,0.058,-2.885,298.15,500},{54.779,3.350,-24.745,-
0.241,500,5000}};
int i, flag=0;

En=-296.813;
 for(i=0;i<2;i++)
  {
   if(T<=a[i][5])T2=T, flag=1;
   else T2=a[i][5];
  En=En+1e-3*((a[i][0]*T2+a[i][1]*1e-3/2*pow(T2,2)-a[i][2]*1e5/T2+a[i][3]*1e-
6/3*pow(T2,3))-(a[i][0]*a[i][4]+a[i][1]*1e-3/2*pow(a[i][4],2)-a[i][2]*1e5/a[i][4]+a[i][3]*1e-
6/3*pow(a[i][4],3)));
if(flag==1) break;
else ;
  }

return En;
}

double fe2o3(double T)
{
  double T2, En, a[4][6]={{143.556,-36.323,-31.433,71.792,298.15,700},{637.809,-963.532,-
447.383,560.951,700.0,950.0},{-220672.038,290104.570,378928.406,-
107181.103,950.0,1050.0},{80.217,55.974,167.385,-12.403,1050.0,1812}};
int i, flag=0;
```

```
En=-823.00;
 for(i=0;i<4;i++)
  {
   if(T<=a[i][5])T2=T, flag=1;
   else T2=a[i][5];
  En=En+1e-3*((a[i][0]*T2+a[i][1]*1e-3/2*pow(T2,2)-a[i][2]*1e5/T2+a[i][3]*1e-
6/3*pow(T2,3))-(a[i][0]*a[i][4]+a[i][1]*1e-3/2*pow(a[i][4],2)-a[i][2]*1e5/a[i][4]+a[i][3]*1e-
6/3*pow(a[i][4],3)));
if(flag==1) break;
else ;
  }

return En;
}

double ni3s2(double T)
{
  double T2, En, a[3][6]={{113.202,48.626,-8.858,-
0.008,298.15,829.0},{188.615,0.0,0.0,0.0,829.0,1062},{191.790,0.0,0.0,0.0,1062.0,3800.0}};
int i, flag=0;

En=-216.313;
 for(i=0;i<3;i++)
  {
   if(T<=a[i][5])T2=T, flag=1;
   else T2=a[i][5];
  En=En+1e-3*((a[i][0]*T2+a[i][1]*1e-3/2*pow(T2,2)-a[i][2]*1e5/T2+a[i][3]*1e-
6/3*pow(T2,3))-(a[i][0]*a[i][4]+a[i][1]*1e-3/2*pow(a[i][4],2)-a[i][2]*1e5/a[i][4]+a[i][3]*1e-
6/3*pow(a[i][4],3)));
if(flag==1) break;
else ;
  }
if(T>1062) En=En+19.748+56.233;
else if(T>829) En=En+56.233;

return En;
}


double py(double T)
{
  double T2, En, a[1][6]={{398.568,0.0,0.0,0.0,298.150,1500}};
int i, flag=0;

En=-736.384;
 for(i=0;i<1;i++)
  {
```

```
   if(T<=a[i][5])T2=T, flag=1;
   else T2=a[i][5];
  En=En+1e-3*((a[i][0]*T2+a[i][1]*1e-3/2*pow(T2,2)-a[i][2]*1e5/T2+a[i][3]*1e-
6/3*pow(T2,3))-(a[i][0]*a[i][4]+a[i][1]*1e-3/2*pow(a[i][4],2)-a[i][2]*1e5/a[i][4]+a[i][3]*1e-
6/3*pow(a[i][4],3)));
if(flag==1) break;
else ;
  }

return En;
}


double cpy(double T)
{
  double T2, En, a[3][6]={{86.985,53.555,-5.607,0.0,298.15,830},{-
1441.974,1844.977,0.0,0.0,830,930},{172.464,0.0,0.0,0.0,930.0,1200.0}};
int i, flag=0;

En=-190.372;
 for(i=0;i<3;i++)
  {
   if(T<=a[i][5])T2=T, flag=1;
   else T2=a[i][5];
  En=En+1e-3*((a[i][0]*T2+a[i][1]*1e-3/2*pow(T2,2)-a[i][2]*1e5/T2+a[i][3]*1e-
6/3*pow(T2,3))-(a[i][0]*a[i][4]+a[i][1]*1e-3/2*pow(a[i][4],2)-a[i][2]*1e5/a[i][4]+a[i][3]*1e-
6/3*pow(a[i][4],3)));
if(flag==1) break;
else ;
  }
if(T>830.0) En=En+10.083;

return En;
}

double cuo(double T)
{
  double T2, En, a[1][6]={{48.591,7.198,-7.500,0.001,298.15,1500}};
int i, flag=0;

En=-155.800;
 for(i=0;i<1;i++)
  {
   if(T<=a[i][5])T2=T, flag=1;
   else T2=a[i][5];
```

```
  En=En+1e-3*((a[i][0]*T2+a[i][1]*1e-3/2*pow(T2,2)-a[i][2]*1e5/T2+a[i][3]*1e-
6/3*pow(T2,3))-(a[i][0]*a[i][4]+a[i][1]*1e-3/2*pow(a[i][4],2)-a[i][2]*1e5/a[i][4]+a[i][3]*1e-
6/3*pow(a[i][4],3)));
if(flag==1) break;
else ;
  }

return En;
}
```

Appendix 02: C Code for the Calculation of the Heat Transfer Rate through the Quartz Tube from the Air in the Electric Furnace to the Fluidized Bed

/*C code for the calculation of the heat transfer rate through the quartz tube from the air in the electric furnace to the fluidized bed.*/

/*
Conditions: The temperature of the air in the furnace is known to be 973.15K. And the temperature of the fluidized bed is also known at specific time to be represented by Tb. There are three layers to be considered: 1. the natural convection of the air near the outer surface of the quartz tube; 2. the heat conduction in the quartz; 3. the heat transfer from the fluidized bed to the inner wall of the quartz tube.

1. Thermal conductivity of the quartz tube: kq=418.4*(3.83e-6*Temperature+0.00163) with the unit of W/(m·ºC)

2. For the calculation of the heat transfer coefficient for natural convection, the following equations are used:

Tf=1/2*(Toq+973.15) where Toq is the temperature of the outer surface of the quartz tube.
Pr=nv/alfa, where Pr is Prandtl number, nv is kinematic viscosity of air, alfa is thermal diffusivity of air.
Gr=9.81*pow(L,3)*pow(rho,2)*beta*(Tf-973.15)/pow(nv,2), where L is the height of the fluidized bed; rho is the density of the air at the temperature Tf, beta is 1/Temperature for ideal gases.
Nu=0.902*sqrt(Pr)*pow(Gr/4,1/4)/pow(0.861+Pr,1/4), where Nu is the Nusselt number.
Nu=ha*L/k, where ha is the heat transfer coefficient, L is the height of the fluidized bed, k is the thermal conductivity of the air at temperature Tf.

Please refer to Pages 258-259 in Transport Phenomena in Materials Processing.

3. For the calculation of the heat transfer coefficient for the fluidized bed, the following equations are used:

Ar=9.81*pow(D,3)*rho*(2872-rho)/pow(nv,2), where Ar is the Archimedes number, D is the mean diameter of the fluid particle, rho is the density of air at Fluidized bed temperature Tb, nv is the kinematic viscosity of air at Tb, 2872 is the weight average density of the fluid particle.

Radiation of the fluidized bed can be neglected since the quartz tube is transparent.

Tf2=(Tb+Tiq)/2, where Tf2 is the average, Tb is the temperature of the fluidized bed, Tiq is the temperature of the inner wall of the fluidized bed.

Re=D*V*rho/nv

where D is the mean diameter of the fluid particle, V is the superfacial velocity of the feeding gas,rho is the density of the air,nv is the kinematic viscosity of the air at Tf2.

Pr=nv/alfa, where Pr is the Prandtl number, nv is kinematic viscosity of the air at Tf2, alfa is the thermal diffusivity of air.

Nu=0.85*pow(Ar,0.1)*pow(2872/rho,0.14)*pow(Cp/Ca,0.24)*pow(1-omega,2/3)+0.046*Re*Pr*pow(1-omega,2/3)/omega,
where rho is the density of air at Tf2, Cp is the heat capacity of sand(quartz) at Tb, Ca is the heat capacity of air at Tb, omega is the porosity of the fluidized bed, which is assume to be 0.7.

Nu=hb*D/k, where k is the thermal conductivity of air at Tf2, hb is the heat transfer coefficient of the fluidized bed, D is the mean particle size.

Please refer to Page 271 in Transport Phenomena in Materials Processing.

*/

```
#include<string.h>
#include<math.h>
#include<stdio.h>
#include<conio.h>
  double kq(double T);
  double Cp(double T);
  double nv(double T);
  double alfa(double T);
  double rho(double T);
  double k(double T);
  double Ca(double T);

void main()
{
Start:

int i;
char a;
double Flag1=1, Flag2=1, Gr, Nu, Re, Pr, Tf, Tf2, Ar, ha, hb, Tb, Tiq=1.0, Tiq2=1.0, Toq=1.0, Toq2=1.0, D, V, r0=0.018, r1=0.020, omega=0.7, Q1=1, Q2, Q10, Q20, L=0.0294, beta;

printf("\nPlease input the fluidized bed temperature in Kelvin:");
scanf("%lf",&Tb);

D=(150.0+212.0)/2.0*1e-6;

/*initialize the temperature Toq and Tiq*/
  if(Tb<973.15)
    {Toq=973.15-0.001;
```

```
    Tiq=Tb+0.001;
   }
  else
   {Toq=973.15+0.001;
    Tiq=Tb-0.001;
   }

for(Q2=2.0*Q1, i=0;Flag2*Flag1>=0;i++)
  {
   if(i>0) Flag2=Flag1;
   else ;

   /*Fix Toq, and correct Tiq by performing the loop:*/

   for(;;)
     {
         Tf2=(Tiq+Tb)/2.0;

         Ar=9.81*pow(D,3.0)*rho(Tf2)*(2872.0-rho(Tf2))/pow(nv(Tf2),2.0);

         V=3.0*1e-3/60.0/(3.141592653*r0*r0)*Tf2/298.15;
         Re=D*V*rho(Tf2)/nv(Tf2);

         Pr=nv(Tf2)/alfa(Tf2);

         Nu=0.85*pow(Ar,0.1)*pow(2872.0/rho(Tf2),0.14)*pow(Cp(Tf2)/Ca(Tf2),0.24)*pow(1.
0-omega,2.0/3.0)+0.046*Re*Pr*pow(1.0-omega,2.0/3.0)/omega;

         hb=Nu*k(Tf2)/D;

         Q1=2.0*3.141592653*L*(Toq-Tb)/(1.0/(r0*hb)+log(r1/r0)/kq(Tf2));
         Tiq2=Toq-Q1*log(r1/r0)/kq(Tf2)/2.0/3.141592653/L;
         if(fabs((Tiq2-Tiq)/Tiq)>=1e-9) Tiq=Tiq2;
         else break;
     }

   /*Fix Tiq, and correct Toq by performing the loop:*/

   for(;;)
     {
         Tf=1.0/2.0*(Toq+973.15);
         beta=1.0/Tf;

         Pr=nv(Tf)/alfa(Tf);
         Gr=9.81*pow(L,3.0)*pow(rho(Tf),2.0)*beta*fabs(Tf-973.15)/pow(nv(Tf),2.0);
         Nu=0.902*sqrt(Pr)*pow(Gr/4.0,1.0/4.0)/pow(0.861+Pr,1.0/4.0);
         ha=Nu*k(Tf)/L;
```

```
        Q2=2.0*3.141592653*L*(973.15-Toq)/(1.0/(r1*ha));
        Toq2=Q2*log(r1/r0)/kq(Tf)/2.0/3.141592653/L+Tiq;
        if(fabs((Toq2-Toq)/Toq)>=1e-9) Toq=Toq2;
        else break;
    }
    Flag1=Q1-Q2;
    if(i=0) Flag2=Flag1;
    else ;

  }

  printf("\nQ=%lf J\nTiq=%lf K\nToq=%lf K\nhb=%lf W/(m.K)\nha=%lf W/(m.K)\nPress 'c' to
continue...",Q2*4.0,Tiq,Toq,hb,ha);
  if(getch()=='c') goto Start;

}

  double kq(double T) /*thermal conductivity of quartz, unit W/(m.oC)*/
  {
  double k;
  k=418.4*(3.83e-6*T+0.00163);
  return k;
  }

  double Cp(double T) /*heat capacity of quartz(sand), unit J/(mol.K)*/
  {
  double C;
  C=81.1447+0.0182834*T+5.4058e-6*pow(T,2.0)-698.458*pow(T,-0.5)-180986.0*pow(T,-
2.0);
  return C;
  }

  double nv(double T) /*kinematic viscosity of air, unit kg/m*s*/
  {
  double n;
  n=-1.14681e-14*pow(T,3.0)+8.87916e-11*pow(T,2.0)+4.55037e-8*T-5.43395e-6;
  return n;
  }

  double alfa(double T) /*thermal diffusivity of air, unit m^2/s)*/
  {
  double a;
  a=-1.28870e-14*pow(T,3.0)+1.03146e-10*pow(T,2.0)+8.99405e-8*T-1.29867e-5;
  return a;
  }

  double rho(double T) /*density of air, unit kg/m^3*/
```

```
{
double d;
d=353.179/T;
return d;
}

double k(double T) /*thermal conductivity of air, unit W/m.K*/
{
double k;
k=6.56677e-12*pow(T,3.0)-3.38667e-8*pow(T,2.0)+9.42622e-5*T+7.50556e-4;
return k;
}

double Ca(double T) /*heat capacity of air, unit J/kg.K)*/
{
double C;
C=1.12295e-10*pow(T,4.0)-5.35621e-7*pow(T,3.0)+8.27169e-4*pow(T,2.0)-
0.295423*T+1032.1;
return C;
}
```

Appendix 03: Photos of the Fluidized Bed Experimental Setup

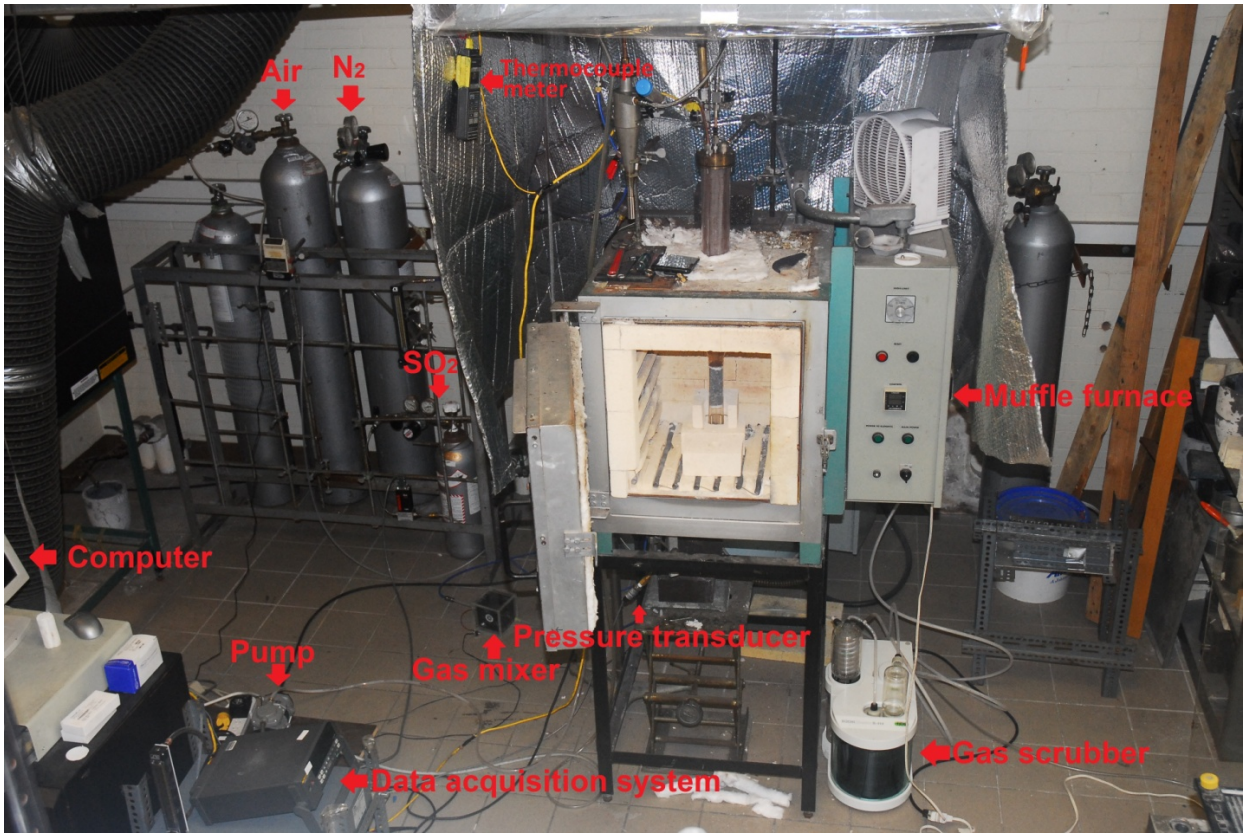

Figure A 1. Fluidized bed experimental setup.

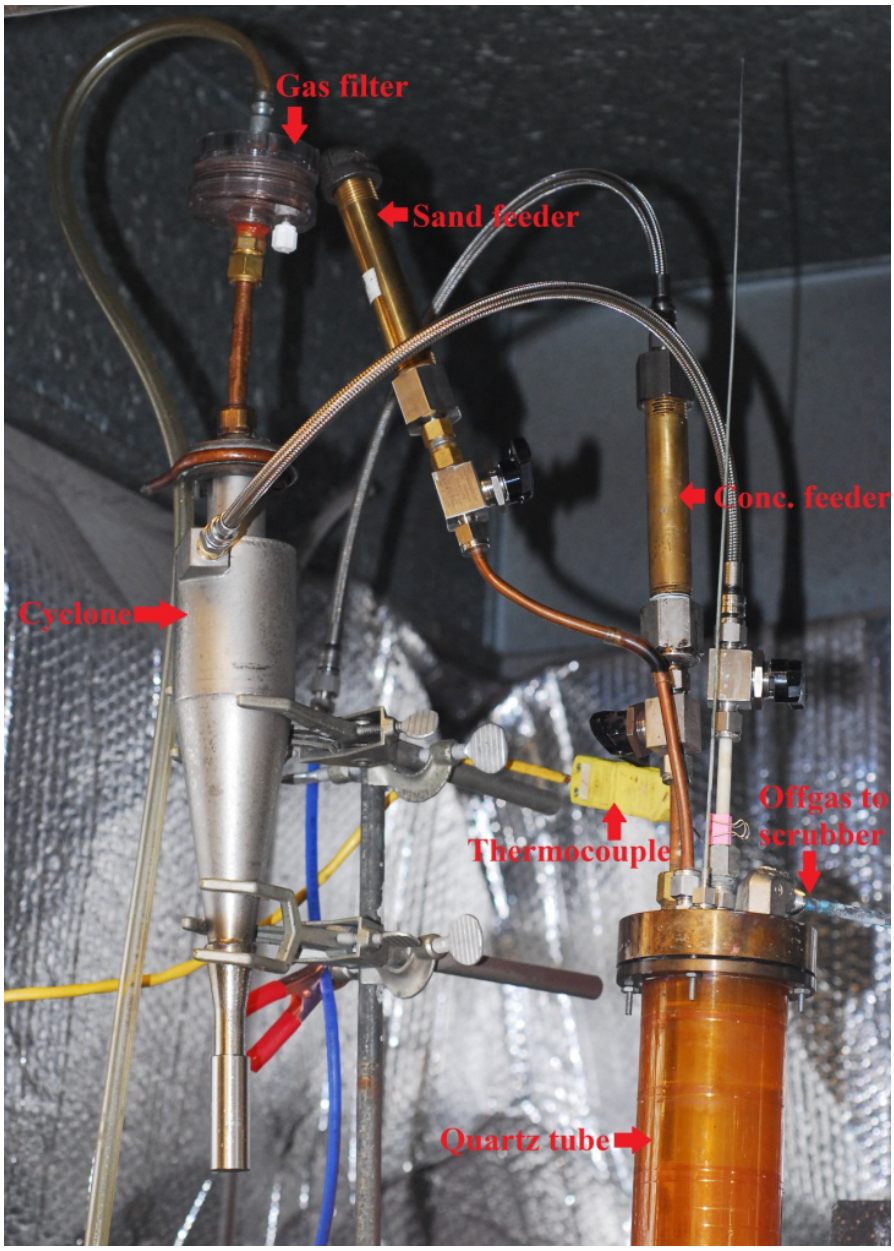

Figure A 2. Sample feeding and collection systems of the fluidized bed setup.

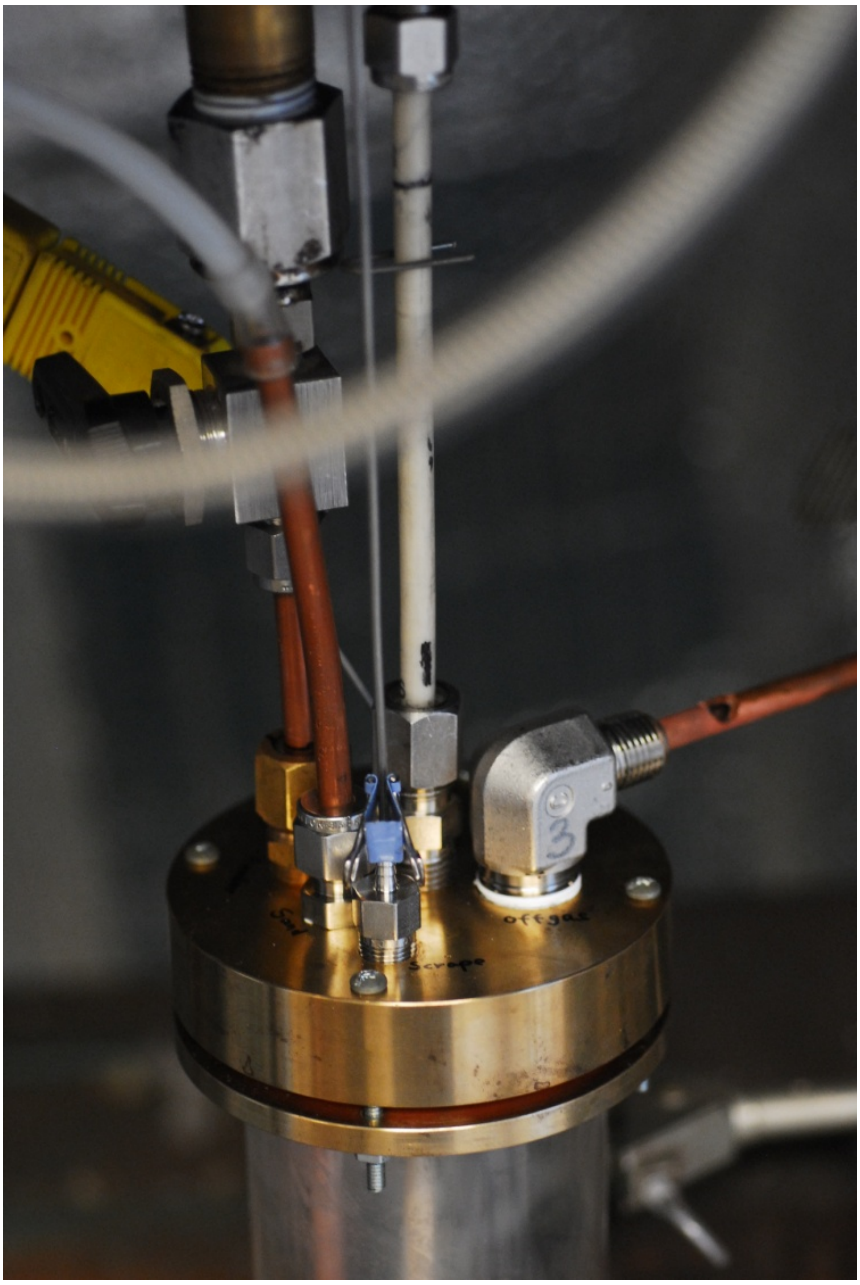

Figure A 3. Brass cap and its fittings on the quartz tube.

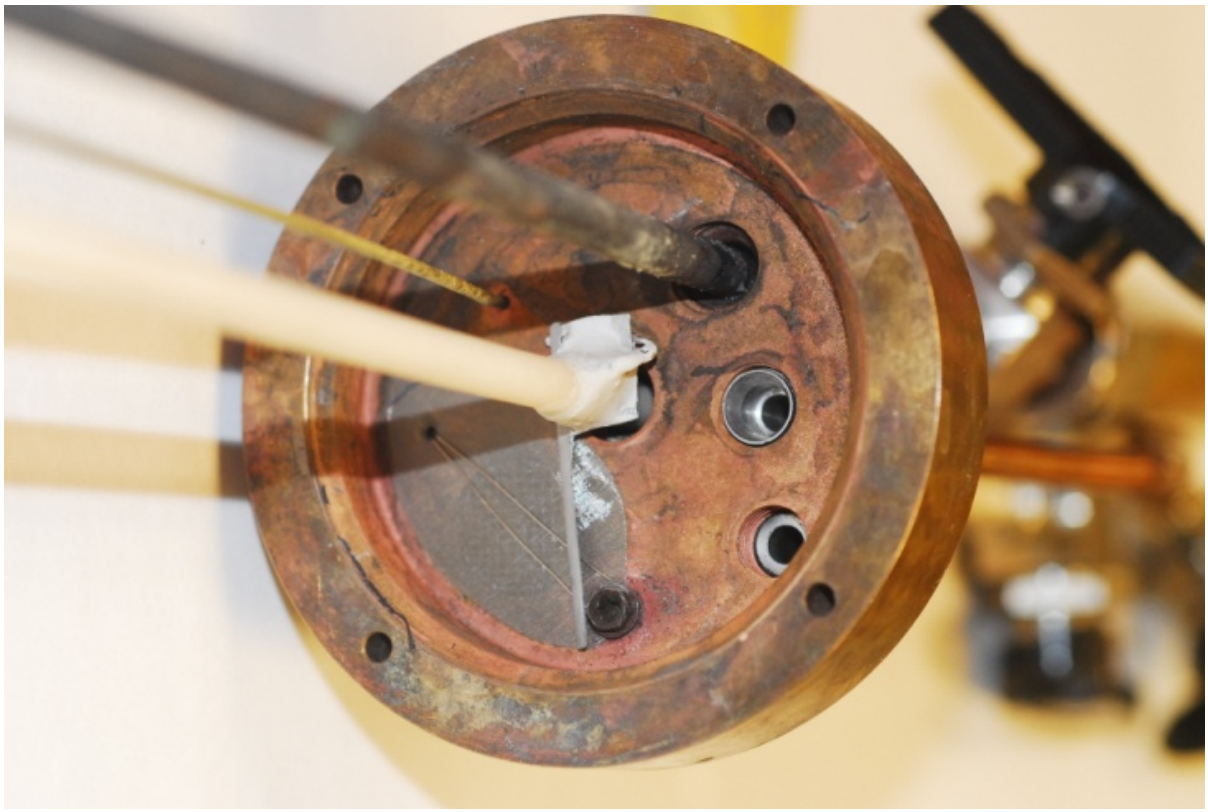

Figure A 4. Interior of the brass cap. The gas outlet is covered with a piece of stainless steel mesh to filter the dust from the offgas. A thin steel blade is fixed on the rotatable ceramic tube by cement. During roasting, the dust accumulated on the mesh is periodically scraped by the rotating blade and falls into the fluidized bed.

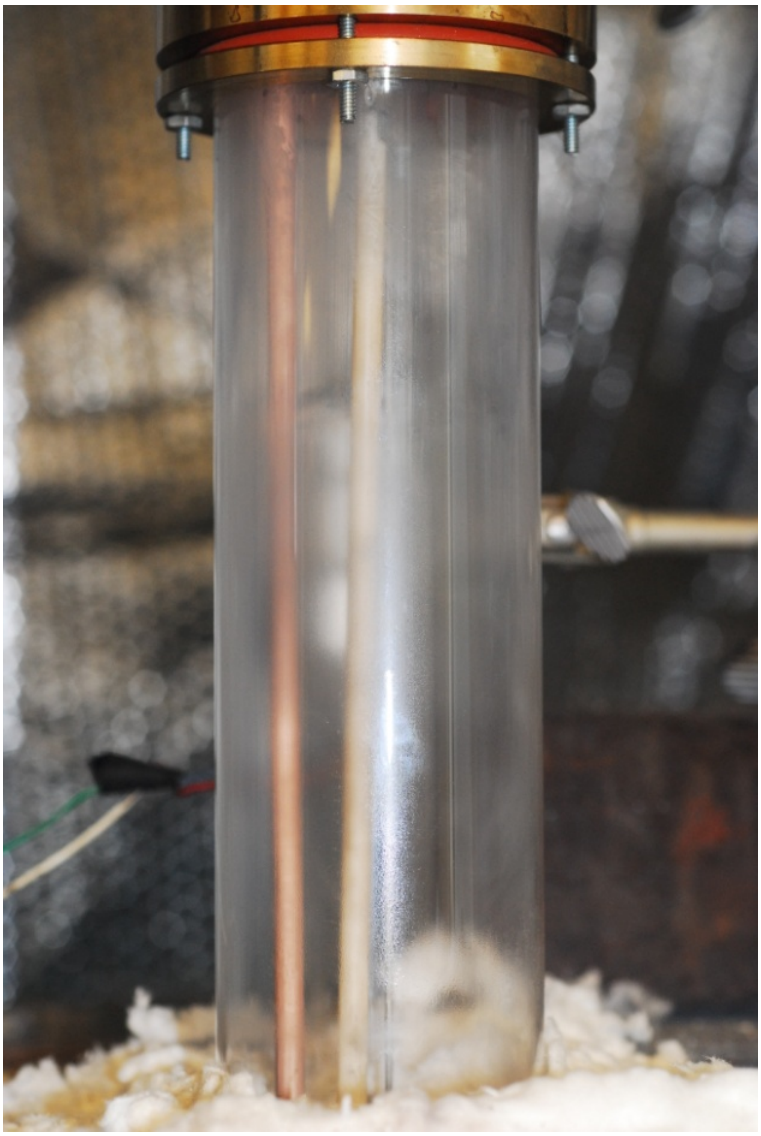

Figure A 5. Upper part of the clear quartz tube showing the SO_3 fume formed during roasting and the condensed SO_3 on the inner wall.

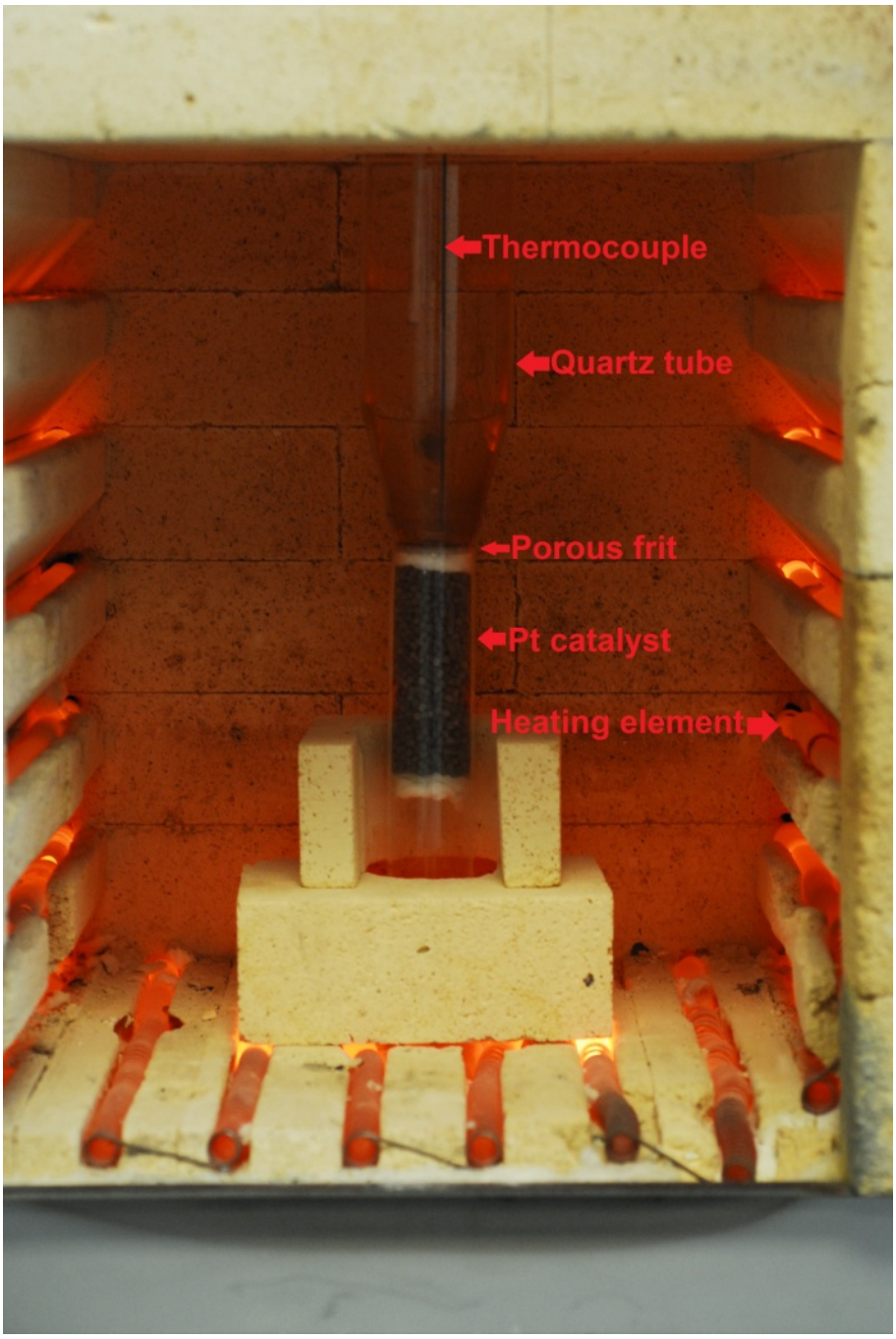

Figure A 6. Interior of the muffle furnace.

Appendix 04: Related Publications

(i) R. Pandher, S. Thomas, D. Yu, M. Barati, T. Utigard, Sulfate Formation and Decomposition of Nickel Concentrates, Metallurgical and Materials Transactions B, 42 (2011) 291-299.

(ii) D. Yu, T.A. Utigard, TG/DTA study on the oxidation of nickel concentrate, Thermochimica Acta, 533 (2012) 56-65.

(iii) D. Yu, T. Utigard, M. Barati, Fluidized Bed Selective Oxidation-Sulfation Roasting of Nickel Sulfide Concentrate: Part I. Oxidation Roasting, Metallurgical and Materials Transactions B, 2013, DOI: 10.1007/s11663-013-9958-x.

(iv) D. Yu, T. Utigard, M. Barati, Fluidized Bed Selective Oxidation-Sulfation Roasting of Nickel Sulfide Concentrate: Part II. Sulfation Roasting, Metallurgical and Materials Transactions B, 2013, DOI: 10.1007/s11663-013-9959-9.

(v) D. Yu, M. Zhu, T.A. Utigard, M. Barati, TGA kinetic study on the hydrogen reduction of an iron nickel oxide, Minerals Engineering, 54 (2013) 32-38.

(vi) D. Yu, M. Zhu, T.A. Utigard, M. Barati, TG/DTA study on the carbon monoxide and graphite thermal reduction of a high-grade iron nickel oxide residue with the presence of siliceous gangue, Thermochimica Acta, 575 (2014) 1-11.

(vii) D. Yu, T.A. Utigard, M. Barati, Leaching behavior of the roasted nickel calcine, in: 51st Annual Conference of Metallurgists, Niagara Falls, Ontario, Canada, 2012, pp. 275-289.

(viii) D. Yu, M. Zhu, T.A. Utigard, M. Barati, TGA Kinetic Study on the H_2 Reduction of an Iron Nickel Oxide, in: The 3rd International Symposium on Processing of Nickel Ores & Concentrates, Cape Town, South Africa, 2012.